Characterization of organelle morphology and DNA repair in replicatively aging yeast

Jessica Hsu

A dissertation

submitted in partial fulfillment of the

requirements for the degree of

Doctor of Philosophy

University of Washington

2013

Reading Committee:

Daniel Gottschling, Chair

Susan Biggins

Lawrence Loeb

Program Authorized to Offer Degree:

Molecular and Cellular Biology

University of Washington

Abstract

Characterization of organelle morphology and
DNA repair in replicatively aging yeast

Jessica Hsu

Chair of Supervisory Committee:
Professor Daniel E. Gottschling
Department of Molecular and Cellular Biology

Aging is one of the most ubiquitous processes in biology, and yet, how the aging process is initiated and the mechanisms that govern how an organism ages remain largely unknown. The study of human aging has been impeded by its inherent complexity. Consequently, simpler model organisms such as the unicellular eukaryote budding yeast *Saccharomyces cerevisiae* have been employed to better understand the aging process at a cellular level. We performed a novel cell biological screen of ~80 fluorescently tagged proteins corresponding to ~20 cellular structures to identify organelles that exhibited altered morphology with replicative age, as changes in organelle morphology likely reflect changes in cellular function. The screen revealed that the morphologies of several organelles changed in an age-dependent manner. Of those, the four most robust phenotypes - fragmentation of the nucleolus, increased peroxisome number and decreased peroxisome size, fragmentation of the vacuole, and missegregation of the mitotic spindle and other mitotic abnormalities - were further characterized to determine the relative timing and relationship of each event. These phenotypes were compared to age-associated mitochondrial fragmentation, as it is a well-established early event in the aging process. Finally, each phenotype was examined in mutant backgrounds and conditions that confer longevity to determine the contribution of known lifespan-extending pathways on these organelles with age.

Further characterization demonstrated a strict association between mitochondrial fragmentation, which occurred first, followed by vacuolar fragmentation. In addition, nucleolar fragmentation and mitotic abnormalities were often coexistent in aging cells. Because of their association with replicative age and the nature of these morphological changes, these phenotypes were all presumed to reflect events detrimental to the cell. Surprisingly, deletion of *UBR2*, which extends replicative lifespan by increasing proteasome activity, actually accelerated mitochondrial and vacuolar fragmentation. Furthermore, both nuclear and nucleolar phenotypes were also suppressed in *ubr2Δ* cells. These findings suggest that mitochondrial and vacuolar fragmentation in wildtype and *ubr2Δ* cells likely occur by two different mechanisms and that the proteasome has a role in limiting extrachromosomal rDNA circle accumulation or enhancing cell cycle progression in replicatively old cells. Taken together, these phenotypes may indicate the important targets of proteasome-dependent degradation necessary for extended lifespan in *ubr2Δ* cells. Finally, no lifespan-extending pathways significantly affected the age-associated change in peroxisome number and size suggesting that a yet undiscovered aging pathway may govern this phenotype. This screen and its subsequent characterization represent an unprecedented effort, which uncovered new phenotypes and provided insights into mechanisms that underlie lifespan extension and the aging process.

Acknowledgements

I would like to thank the many people who have helped and supported me, and who have made this work possible:

First, thank you to my graduate advisor, Dan Gottschling, for mentoring me and giving me the opportunity to train in his lab. Dan's guidance, support, and encouragement helped me grow both as a person and as a budding scientist. His commitment to a collaborative training environment brings me to my next big thanks, which is to all the past and present members of the Gottschling lab who have all contributed to my education through their technical assistance, scientific discussions, and moral support.

Next, I would like to thank my committee, Sue Biggins, Stan Fields, Brian Kennedy, and Larry Loeb for all their patience, support above and beyond, and great advice over the years. Special thanks to my reading committee: Sue Biggins and Larry Loeb for their reading and comments on my thesis, not once, but twice.

Thank you to the department of molecular and cellular biology, basic science division, and the medical scientist training program and to all the many faculty, postdocs, fellow classmates, and administrative staff who have advised and supported me in so many different ways throughout my training.

Finally, I'd like to acknowledge my friends and family who have provided me with unwavering support from day one: to my dear friend and MSTP classmate Cassie Chou who is always willing to lend an ear or a hand depending on the situation; to Larry Loeb for introducing me to the laboratory and for his support, advice, and encouragement over the past decade; to my brother Albert Hsu who always has something insightful and entertaining to say; to my mother Ning Hsu who is my role model and best friend and who has always supported me unconditionally; and to my father Chin Hsu who in life always encouraged me to work hard and through his death inspired me to pursue a career in science and medicine. Last, but not least, I would like to thank my loving husband, David Patterson, who is endlessly supportive and who's love and humor carried me through even the most difficult times.

Table of Contents

List of Tables

List of Figures

Figure Number **Page**

List of Figures (cont.)

List of Figures (cont.)

List of Figures (cont.)

List of Figures (cont.)

Section One: Characterization of organelle morphology with replicative age

Chapter I: Introduction to replicative aging and organelle morphology

Aging is a universal, yet poorly understood phenomenon

Aging is one of the most ubiquitous processes in biology, and yet, how the aging process is initiated and the mechanisms that govern how an organism ages remain largely unknown. Advances in public health during the past century, such as the advent of antibiotics, have greatly extended the average human lifespan. While this has been pivotal in improving the quality of life, we now face new challenges associated with an ever-expanding aging population. Ultimately, the goal of aging research is to alleviate the burden of age-associated morbidities and diseases of aging, however, we first need to better understand the causes and consequences of the aging process.

The complexity of aging poses a significant challenge to its research

The study of human aging has been impeded by its inherent complexity and the time required to characterize changes in lifespan. Consequently, simpler, shorter-lived model organisms such as rodents, and invertebrates such as *Drosophila* and *Caenorhabditis elegans* have been used to identify exogenous and endogenous modulators of lifespan (Kim, 2007; Tissenbaum and Guarente, 2002; Tissenbaum, 2012; Vanhooren and Libert, 2013). The use of multiple diverse model organisms has been fruitful in identifying the common aging pathways that are most likely to be conserved in humans and play an important role in human aging and age-associated disease (Kim, 2007). However, the intrinsic complexity of the aging process is particularly evident in the case of *C. elegans*, whose aging phenotypes and longevity are widely variable despite a highly regimented developmental scheme (Herndon et al., 2002). The differences in how aging phenotypes are manifested between individuals, even within an isogenic population in a common environment, likely reflect innate stochasticity and the involvement of several interacting pathways in the aging process. The multicellularity of these model organisms adds to the complexity of aging studies, leading towards a shift in the past couple decades towards using an even simpler model: the aging cell.

Characterization of aging at the cellular level will provide insight into the molecular mechanisms of the aging process

The cell is the most basic unit of life that experiences aging. The current prevailing hypothesis is that aging at the tissue or organismal level is the manifestation of cellular deterioration due to the accumulation of molecular damage (Kirkwood, 2005). This is in contrast to the competing idea that aging, like development, is a purposeful and programmed biological process that occurs to ensure the death of the cell or organism (Kirkwood, 2008, 2005; Kirkwood and Melov, 2011; Austad, 2004; Kenyon, 2010). While the concept of programmed aging has recently begun to fall out of favor, there continues to be controversy surrounding why and how aging occurs. The implications of these two opposing theories bring up important considerations in the approach to studying cellular aging and the interpretation of results.

If cell or organismal death is programmed, the instructions should be genetically regulated and discrete events would be expected to occur once the aging process has been initiated. Death should occur by similar means in every cell. On the other hand, the idea that cell death is due to the accumulation of molecular damage means that there is inherent stochasticity in the aging process, and that there are likely multiple pathways that contribute to the aging phenotype. This theory also implies that altering the rate at which damage accumulates, either by changing the rate of damage accrual or removal, would also alter the course of aging. This latter theory, the non-adaptive theory of aging, has gained favor for several reasons: 1) lifespan and other aging phenotypes are highly variable even amongst an isogenic population in a common environment, implying an element of stochasticity, 2) multiple independent pathways of aging have already surfaced within a single organism, i.e. dietary restriction and ERCs in yeast (discussed later in this introduction), 3) multiple types of molecular damage are found in aging cells, and changing the kinetics of damage accumulation alters lifespan (also discussed later in this introduction), and 4) there is no evolutionary basis for a post-reproductive programmed death process (Kirkwood and Melov, 2011; Kaeberlein et al., 2004; Kruegel et al., 2011; Erjavec et al., 2007).

The idea that aging may be the result of multiple molecular mechanisms highlights the importance of exploring the aging process at the cellular level. Because different aging mechanisms will likely result in different aging phenotypes, it is important to describe cellular events observed during aging in addition to the measurement of lifespan. The temporal relationship of these events will be mechanistically important as early events may represent causes of aging and late events may represent terminal dysfunction. That multiple aging mechanisms exist also necessitates the analysis of a large population of cells in order to detect

different types of events and potentially rare events in the setting of stochasticity. Furthermore, extensive knowledge of cellular processes and pathways at the molecular level in young cells will be a prerequisite for successfully identifying, characterizing, and interpreting age-associated changes. Together these attributes of cellular aging support an unbiased cell-based approach to identify and characterize age-associated changes in a simpler single-cell organismal model, such as yeast *Saccharomyces cerevisiae*.

Saccharomyces cerevisiae **is a well-established model for studying cellular aging**

Yeast as a model organism

Budding yeast *Saccharomyces cerevisiae* is a simple unicellular eukaryotic organism that has had an integral role in our ability to understand and characterize fundamental concepts in biology. *S. cerevisiae* continues to be a widely used model organism because of its genetic tractability. Its fully annotated genome has made possible the development of gene deletion and overexpression libraries to determine the importance of various gene products in specific cellular pathways and to address other genetic questions. Additionally, systematic methods of creating genome-wide collections have been applied to create a library that expresses C-terminal GFP fusion proteins of each yeast open reading frame which allows the further characterization of yeast proteins on both a biochemical and cell biological level (Huh et al., 2003a).

Many cellular substructures, processes, and pathways are conserved from yeast to humans, and the study of yeast homologues of human proteins has led to better understanding of the mechanisms and pathophysiology of human diseases. This approach has been especially fruitful in furthering our knowledge of age-associated diseases such as cancer, neurodegenerative diseases, and premature aging (Botstein and Fink, 2011; Pereira and Yamashita, 2011; Aggarwal and Brosh, 2009; Yamagata and Kato, 1998). Because *S. cerevisiae* has been so well characterized, it provides the ideal foundation for the identification of molecular and cellular differences under altered physiological conditions such as those that occur with age.

Yeast have a limited replicative lifespan

Yeast cells divide asymmetrically producing a larger original mother cell and a smaller new daughter cell at every division (Hartwell and Unger, 1977). The number of daughter cells that

can be produced by a single mother cell is finite, and this limit is defined as the cell's replicative lifespan (Mortimer and Johnston, 1959). The limited replication potential of a yeast mother cell is analogous to the replicative senescence of human fibroblasts in culture as described by Hayflick in 1965 and to adult stem cell aging (Hayflick, 1965; Jazwinski, 2005). In contrast to the replicatively aging mother cell, most daughter cells are born young and with full replicative potential explaining how yeast cultures can appear immortal while the individual cell experiences a limited lifespan. It also emphasizes the importance of asymmetry in yeast division and replicative aging (Mortimer and Johnston, 1959; Kennedy et al., 1994). This asymmetry has led to the questions the yeast aging field has been working to answer since its inception in 1959, which is: What is different between the mother cell as she ages and her young daughter cell, how is that difference established, and what factors cause and contribute to the replicative aging process?

Methods used to identify, isolate, and monitor replicatively aging cells

Several methods have been developed to study replicative aging in yeast, and they all include ways to identify and isolate old cells, and to monitor lifespan. When Mortimer and Johnston discovered that yeast had a limited replicative lifespan in 1959, they did so by quantifying the newborn daughter cells they micro-dissected away from each mother cell until she senesced (Mortimer and Johnston, 1959). Micromanipulation has since been the gold standard method for highly accurate measurement of replicative lifespan and gross observation of single cells as they age. Although time and labor intensive, this method has been widely used to identify genes and pathways important for lifespan regulation (Kennedy et al., 1995; Sinclair and Guarente, 1997; Lin et al., 2000; Defossez et al., 1999; Steffen et al., 2008).

The primary disadvantages of micromanipulation as a replicative aging assay are that it only allows for the examination of relatively few cells and is generally limited to answering genetic questions when the phenotypic endpoint is lifespan. This was a major technical hurdle for exploring biochemical and cell biological questions, which would require the isolation of larger quantities of old mother cells from liquid culture. Because of their short division time and rapid entry of daughter cells into the replicating population, unfractionated populations of yeast cells, such as those growing in liquid culture, are predominantly young cells. To overcome this obstacle, the Gottschling lab developed the Mother Enrichment Program (MEP), a genetic system that allows for the enrichment of mother cells in liquid culture by preventing daughter cells from undergoing further division (Lindstrom and Gottschling, 2009a). This system utilizes Cre-lox conditional gene disruption to excise two essential cell-cycle genes, *CDC20* and *UBC9*,

in a daughter-specific manner. Cre-recombinase is fused with an estrogen-binding domain (EBD), and the fusion gene expressed from a daughter-specific promoter. Under normal conditions, the Cre-EBD fusion protein is expressed only in daughters and remains inactive within the cytoplasm. Addition of estradiol results in EBD binding and translocation of Cre-EBD into the nucleus where it mediates the excision of the loxP-flanked genes and cell-cycle arrest in a daughter-specific manner (**Figure 1.1**). The final result is a culture with normally dividing mother cells and daughter cells that arrest before their first division. The MEP allows for enrichment of mother cells of any replicative age.

Old mother cells can be readily identified and their replicative age determined by quantitation of their bud scars. Bud scars are chitinous rings created at the mother-daughter interface during budding, and because budding does not occur from the same site twice, the number of bud scars reflects the replicative age of the mother cell (Barton, 1950). Bud scars are visualized by fluorescence microscopy following staining with calcofluor white or fluorescence-conjugated wheat germ agglutinin (Hartwell et al., 1974).

The purity of the population of replicatively aged mother cells can be further enhanced by isolating old mother cells away from the arrested daughter cells following MEP culture. Because newly formed daughter cells synthesize their cell walls *de novo*, the mother cell retains her original cell wall and consequently any cross-linked moieties throughout replicative aging (Ballou, 1982). By biotinylating the original population of cells used to start a MEP culture, old mother cells can later be isolated with streptavidin-coated magnetic beads providing a very pure population of replicatively aged cells (Smeal et al., 1996; Park et al., 2002). Taking advantage of the same phenomenon, replicatively aging mother cells can be readily identified from bulk MEP culture by fluorescence microscopy if the cell walls of the starting population were cross-linked with a fluorescent dye.

By combining the MEP with magnetic bead separation, pure populations of aging mother cells can be isolated for use in genetic, cell biological, and biochemical studies previously impossible in old cells. Furthermore, because the MEP allows for the analysis of large numbers of old cells, it is possible to detect rare events and to begin to address the question of whether stochasticity may be contributing to the aging process. The methods discussed here have already helped the field achieve a greater understanding of the mechanisms that underlie the aging process in yeast, and how yeast can be used to better understand pathways known to modulate aging in higher organisms. The remainder of this introduction will be dedicated to describing the approaches that have been used to address lifespan and aging in yeast, how these approaches have advanced the aging field in general, how this foundation of knowledge

might be used to advance our understanding of the aging process even further, particularly as it pertains to this body of work.

Dietary restriction is a highly conserved mechanism for lifespan extension

Lifespan extension due to reduced dietary intake was first observed in the 1930's in rats by Clive McCay. To date, dietary restriction is the only non-genetic intervention to extend lifespan and promote healthy aging in organisms, from yeast to perhaps even primates or humans (Bishop and Guarente, 2007; Fontana et al., 2010; Colman et al., 2009; McDonald and Ramsey, 2010). Furthermore, some pathways important in lifespan extension through dietary restriction are also conserved among many organisms, including yeast, worms, flies, and rodents (Sinclair, 2005; Smith et al., 2008; Bishop and Guarente, 2007; Piper et al., 2011).

Dietary restriction defined

In general, the term dietary restriction (DR) means reduced calorie intake, however it can also refer to the reduction of specific nutrients. In fact, lifespan extension in flies and mice have been accomplished by altering components of diet without reduction in calories (Piper et al., 2011). The definition of dietary restriction often varies in practice from study to study even within the same model organism, which has made it difficult to compare results from different laboratories (Greer and Brunet, 2009; Piper and Partridge, 2007; Kaeberlein, 2010). In yeast, calorie restriction is usually accomplished by growing cells in media containing reduced glucose at either 0.5% (moderate DR) or 0.05% (extreme DR) instead of the routine 2%. Although both calorie restriction protocols are effective in extending replicative lifespan, the roles of mediators of yeast aging differ depending on the severity of caloric restriction (Kaeberlein et al., 2004, 2005; Easlon et al., 2007). The ideal method of calorie restriction remains controversial in both the yeast replicative aging field and in the study of higher organisms. The Gottschling lab favors the use of moderate dietary restriction as it does not result in reduced growth rates and is a level of dietary restriction that could be applied to mammalian models.

Genetic mediators of lifespan extension

The genetic mediators of lifespan extension through dietary restriction were first described in yeast (Defossez et al., 1999; Kaeberlein et al., 1999). Dietary restriction in yeast is thought to occur through several overlapping nutrient-sensing and signaling pathways: the cAMP-dependent protein kinase A (PKA) pathway, the target of rapamycin (TOR) pathway, and the

AKT homologue Sch9 kinase (Kaeberlein et al., 2005; Lin et al., 2000). These pathways were also found to mediate lifespan extension by dietary restriction in higher organisms in a parallel manner (Bishop and Guarente, 2007). Disruption of genes in these nutrient-sensing and signaling pathways mimics dietary restriction and consequently results in lifespan extension (Kaeberlein et al., 2005). In other words, dietary restriction of deletion mutants such as *tor1Δ* and *sch9Δ* does not result in additional lifespan extension.

Other genetic mimetics of dietary restriction

Other genetic mimetics of dietary restriction include the disruption of genes both upstream and downstream of PKA, Tor1, and Sch9. Upstream mimetics include deletion of *HXK2*, which encodes the major hexokinase responsible for retention of glucose in cytoplasm, and deletion of either *GPR1* or *GPA2* (Walsh et al., 1983; Lin et al., 2000). In the presence of glucose, G protein coupled receptor Gpr1 interacts with the G protein alpha subunit Gpa2 to increase cAMP levels and allow PKA activation (Yun et al., 1998). The absence of either Gpr1 or Gpa2 results in attenuation of PKA signaling and extension of lifespan (Lin et al., 2000).

The downstream mimetics of dietary restriction that have been characterized are primarily the targets of the TOR pathway. The TOR pathway is responsible for integrating nitrogen sensing information with cell growth (Loewith and Hall, 2011). The Tor1 kinase is activated by nutrient-rich conditions and acts to repress stress responses while promoting ribosome biosynthesis and protein translation (Loewith and Hall, 2011). Inhibition of 60S ribosomal subunit biogenesis extends replicative lifespan through a mechanism that is dependent on induction of the nutrient-responsive transcription factor Gcn4 (Steffen et al., 2008).

The genetic mimetics of dietary restriction play a very powerful role in dissecting the various pathways that may be causative or contributory in the aging process in that they have the advantage of clarifying the specific pathways necessary for modifying the aging process. In contrast, dietary restriction is a global environmental condition that is likely to affect many pathways simultaneously and results of studies using dietary restriction have been difficult to compare due to variations in growth conditions. These studies demonstrate the importance of using genetics to better understand the interactions between genes and cellular responses to dietary restriction. However, how dietary restriction or genetic mimetics of dietary restriction affects cellular and organelle function to extend lifespan is far from fully understood. The ability to isolate old cells for cell biological and biochemical studies will be invaluable to furthering our understanding of the functional consequences of dietary restriction.

Genetic regulation of replicative lifespan

The idea that there is a hereditary component to lifespan and age-associated diseases is not new, however the extent of genetic contribution and the specific genes and pathways involved in the aging process and in lifespan determination have not yet been completely defined (Jazwinski, 1998; Barzilai et al., 2012; Martin, 2011; Vijg and Suh, 2005). Early human twin studies suggested a possible role of genetics in longevity that was later estimated to be ~25% (Kallman and Sander, 1947; Gurland et al., 2004). Other studies in long-lived humans have attempted to identify genes associated with longevity, and while informative, have more importantly demonstrated that aging is a very complex, multifactorial process (Barzilai et al., 2010; Murabito et al., 2012; Sebastiani et al., 2012). Because of this, the use of model organisms to characterize aging on a genetic level has been the focus of the past 25 years and has proven to be a very powerful way to better understand the biological changes that occur with age. As described above, many researchers have turned to yeast as a model for aging because its genetic tractability and short lifespan make it an ideal organism for genetic studies.

The role of Sir2 and ERCs on replicative lifespan modification

The study of genetic modifiers of lifespan has had a profound impact on our understanding of the aging process both in yeast and in higher organisms. Due to the tedious nature of measuring yeast lifespan by micromanipulation, the initial experiments to identify genes that regulate replicative lifespan were directed. One early study to determine if stress resistance was associated with replicative lifespan extension led to the characterization of a long-lived sirtuin mutant, *SIR4-42* (Kennedy et al., 1995). This result ultimately opened up the aging field in many ways and lead to the wide use of genetic studies to identify mechanisms of aging.

Sir4 is part of a larger complex that includes Sir2 and Sir3, which together, acts to transcriptionally repress telomeres and the mating loci (Ivy et al., 1986; Rine and Herskowitz, 1987; Aparicio et al., 1991). It was later found that Sir2, a NAD-dependent histone deacetylase, could act independently to suppress recombination at the rDNA locus and maintain rDNA repeat stability, and that this promoted replicative longevity (Blander and Guarente, 2004; Kaeberlein et al., 1999).

The yeast rDNA locus consists of 100-200 copies of a 9.1 kb DNA segment arranged head-to-tail in a tandem array on chromosome XII. Each unit consists of two transcribed genes encoding the 35S rRNA and 5S rRNA, and two non-transcribed regions, an origin of replication

or autonomously replicating sequence (ARS) and a replication fork block site. Importantly, these repeats do not contain any centromeric sequence. Aberrant intrachromosomal recombination events at this site generate small extrachromosomal rDNA circles (ERCs) capable of autonomous replication, but incapable of faithful segregation (Kobayashi, 2011).

ERCs have long been implicated as an aging factor with a role for limiting replicative lifespan. Once present, ERCs increase in copy number as a function of replicative age, and are retained in the mother cell due to their lack of centromere (Sinclair and Guarente, 1997). Artificial ERCs introduced at high copy number in young cells significantly decrease the replicative lifespan of these cells (Sinclair and Guarente, 1997). Furthermore, mutants that act at the rDNA to either promote or suppress rDNA recombination and ERC formation also decrease or increase replicative lifespan, respectively. For example, *SIR2* overexpression decreases rDNA recombination and ERC formation and results in lifespan extension (Kaeberlein et al., 1999); conversely, deletion of *SIR2* increases ERC formation and consequently shortens lifespan (Kaeberlein et al., 1999). Another important player in this cellular process is the replication fork block protein Fob1, which promotes rDNA recombination and ERC formation, and thus deletion of *FOB1* delays ERC accumulation and extends lifespan (Defossez et al., 1999).

Despite this being perhaps the most characterized theory of yeast aging, the mechanisms by which ERCs limit replicative lifespan are still unknown. Several hypotheses have been proposed and include the presence of ERCs destabilizing the rDNA locus, ERCs sequestering factors required for replication and/or transcription, and disruption of cellular homeostasis due to over-production of rRNA (Steinkraus et al., 2008). While the mechanism of ERC-dependent aging deserves further study, the association between a sirtuin and replicative aging in yeast launched an entire field of study across all model organisms and humans. ERCs as a cause of aging is likely to be yeast specific, however an ERC-independent role for sirtuins in aging has been described in yeast and in higher organisms (Longo and Kennedy, 2006).

The role of sirtuins in the aging process, particularly as it relates to dietary restriction, has been the topic of much active research and controversy at all organismal levels (Kaeberlein, 2010; Longo and Kennedy, 2006; Guarente, 2012). In yeast, the role of Sir2 and other yeast sirtuins in lifespan extension by dietary restriction is debated (Kaeberlein, 2010; Guarente, 2005; Kaeberlein and Powers, 2007). The contention hinges on whether Sir2 activity increases during caloric restriction as attempts to determine this has been hampered by sub-optimal assays, strain background differences, and varied execution of moderate and extreme calorie restriction (Kaeberlein et al., 2004; Lin et al., 2000; Kaeberlein, 2010). That dietary restriction at

least partially extends lifespan independent of Sir2 is supported by the find that calorie restriction extends the lifespan of the *sir2Δ fob1Δ* double mutant (Kaeberlein et al., 2004). The possible involvement of sirtuins in lifespan extension through dietary restriction must be kept in mind when testing for changes in age-associated phenotypes in the presence of either moderate or extreme calorie restriction. Furthermore, it highlights the importance of strain and media choices in study design.

The existence of at least one other aging pathway that is Sir2-dependent but ERC-independent is suggested by the finding that the *sir2Δ fob1Δ* double mutant has a decreased lifespan compared to the *fob1Δ* single mutant despite similar age-associated ERC accumulation (Defossez et al., 1999; Kaeberlein, 2010). Because an ERC-dependent and Sir2-dependent aging pathway has been established, it will be important to determine whether any newly identified aging pathways and age-associated phenomena occur independent of this pathway.

Increased proteasome activity extends replicative lifespan

Genetic analyses have yielded much of what we currently know about lifespan regulation. Due to the difficult nature of measuring yeast lifespan, there has only been one unbiased genetic screen for genes that alter lifespan (Kruegel et al., 2011; Kaeberlein et al., 2005). This was carried out using the yeast haploid ORF deletion library to identify genes, that when deleted, alter replicative lifespan. Approximately 2% of the deletion mutants extended lifespan, where as ~20% mutants were short-lived (Smith et al., 2008). Interpreting data from short-lived strains has proven difficult because cells die prematurely from causes other than accelerated aging. In contrast, long-lived mutants from this and previous genetic studies have provided insight into how at least three independent pathways might modulate the aging process. The first, the effects of ERCs on replicative aging, and the second, dietary restriction and genetic mimetics of dietary restriction, have already been discussed.

The third independent pathway for replicative lifespan extension in yeast is through increased proteasome activity. The ubiquitin/proteasome system is one of two degradative pathways (the other is degradation via the vacuole) in the cell responsible for the clearance of misfolded and damaged proteins (Finley et al., 2012). The proteasome is localized in both the cytoplasm and the nucleus, and is a large, evolutionarily conserved protein consisting of many subunits. These subunits are organized into two major components, the core particle and the regulatory particle. The regulatory particle is further subdivided into two components, the base and the lid. The lid is responsible for recognizing polyubiquinated proteins destined for degradation and transferring them into the catalytic core for proteolysis (Finley et al., 2012).

Consistent with the hypothesis that aging is caused by cellular degeneration secondary to the accumulation of damaged biomolecules, proteasome activity has been shown to be decreased in several model organisms of aging (Jana, 2012). Additionally, increased proteasome activity was demonstrated in the fibroblasts of human centenarians and in the long-lived naked mole rat (Chondrogianni et al., 2000; Rodriguez et al., 2012). In yeast, the proteasome subunits are co-transcriptionally regulated by a common transcription factor, Rpn4. Rpn4 is only briefly active in the absence of proteotoxic stress, and is rapidly ubiquitylated by the E3 ligase Ubr2 and degraded by the proteasome (Finley et al., 2012). Deletion of *UBR2* greatly increases cellular proteasome activity, and results in increased replicative lifespan. Conversely, deletion of *RPN4* globally reduces proteasome activity, renders the cell unresponsive to proteotoxic insult, and shortens replicative lifespan. Furthermore, the lifespan extension achieved in *ubr2Δ* cells occurs independently of caloric restriction and *sir2Δ fob1Δ* (Kruegel et al., 2011).

These findings suggest that suboptimal protein homeostasis has a negative effect on lifespan. The mechanism of how increased proteasome activity extends lifespan is not known. Presumably damaged proteins may not be adequately turned over in old cells, either due to overwhelming accumulation or age-associated decrease in proteasome activity. Whether lifespan extension is the result of removing specific damaged proteins or if it results from increased turnover globally is an important question to address and would provide insight into the causative mechanism of aging.

The next step for using genetics to study replicative aging

As described above, genetics has played an important role in the identification of genes that affect lifespan. The identity of these genes has helped differentiate between three independent aging pathways thus far. The genetics that help determine the independence of these pathways will be important in determining if novel age-associated phenotypes represent new pathways of replicative aging. The use of genetics and measurement of lifespan as a terminal phenotype has been informative and relatively straightforward because it is quantitative. However, a greater challenge to the field of replicative aging will be to design experiments that characterize events that occur during the aging process from causation to consequence, and to use genetics to elucidate the mechanism of these age-associated phenotypes (Barzilai et al., 2012).

Yeast replicative aging is likely based on the establishment of asymmetric division

As previously mentioned, yeast divide asymmetrically, producing a larger mother cell and a smaller daughter cell (Hartwell and Unger, 1977). The replicative lifespan of both of these cells are finite, however, daughter cells are born with their full replicative potential whereas the mother cells approaches senescence with every daughter cell they produce (Egilmez and Jazwinski, 1989; Kennedy et al., 1994). Interestingly, the daughter cells born to old mother cells nearing the end of their replicative lifespans are not born with their full replicative potential, but instead experience up to a 75% reduction in replicative lifespan (Kennedy et al., 1994). This further supports the idea that replicative aging is somehow dependent on asymmetric cell division and suggests that this asymmetry is lost as a function of replicative age. This also emphasizes the importance of determining what is different between an old mother cell and the young daughter cells she produces.

Superficial age-associated phenotypes

Compared to their young counterparts, cells of advanced replicative age have long been observed to exhibit several phenotypes. First, cells markedly increase in size with replicative age (Mortimer and Johnston, 1959). It has been proposed that the increase in size may limit replicative lifespan or even be the cause of replicative aging (Mortimer and Johnston, 1959; Zadrag-Tecza et al., 2009; Yang et al., 2011; Bilinski et al., 2012), however these ideas have not been well-supported (Bilinski et al., 2012; Ganley et al., 2012). The cause of age-associated cell expansion is not known, however may be due to the slowing of the cell cycle with age (Delaney et al., 2011).

The presence of bud scars is another example of asymmetry between mother and daughter cells. As previously mentioned, bud scars are non-overlapping chitinous rings that form on the mother cell with every division. It has also been suggested that bud scar accumulation or even bud scars themselves are capable of limiting replicative lifespan (Mortimer and Johnston, 1959; Cabib et al., 1974). However, this theory has been discounted because the cell surface area increases to accommodate additional bud scars and because a mutant that repeatedly buds from the same bud site is not long-lived (Tong et al., 2007).

These two observations of age-associated differences between old mother cells and young daughter cells led to many experiments to derive the mechanism of each phenomenon and their impact on replicative aging. The increase in cell size and surface area, and the accumulation of bud scars could be considered the first proposed aging factors.

Theories to associate asymmetrical division with replicative aging

Several theories have been proposed to explain what is asymmetrically distributed between the mother and daughter cells and how that asymmetry is maintained (Henderson and Gottschling, 2008a). Perhaps the most studied is the idea of an aging or senescence factor that accumulates in the mother cell with replicative age, and is either absent or present in very low levels in young cells. Mother cells are capable of retaining this senescence factor until very late in the their lifespans when the mechanisms of retention are disrupted and sufficient senescence factor is conferred to the daughter cell and results in reduced replicative lifespan (Kennedy et al., 1994; Egilmez and Jazwinski, 1989).

At least three aging factors have now been proposed. The first is ERCs. ERCs occur and accumulate in aging mother cells, and increasing the level of ERCs in young cells results in reduced lifespan (Sinclair and Guarente, 1997; Kaeberlein et al., 1999). Conversely, reduction in ERC formation by deletion of *FOB1* results in lifespan extension (Defossez et al., 1999). However, two other ERC-independent pathways have been established suggesting that ERCs cannot be the only senescence factor at play during replicative aging.

Another potential aging factor is oxidatively damaged biomolecules. The free radical theory of aging was proposed over 60 years ago by Harman, and hypothesized that reactive oxygen species produced secondary to aerobic metabolism inflicted cellular damage that accumulated with age and subsequently resulted in senescence and/or death (Harman, 1956). While reactive oxygen species have not been proven to have a causative effect on the aging process, the association between oxidative damage and age has been established in many model organisms (Bokov et al., 2004). Consistent with this, yeast proteins damaged by carbonylation (a form of oxidative damage), are more abundant in old cells compared to young cells and preferentially accumulate in the mother cell compared to the daughter cell (Nyström, 2005; Aguilaniu et al., 2003). These data support the possibility that oxidatively damaged proteins might be an aging factor, however, it is not known if the damage has to be to specific proteins or if these damaged proteins play a causative or correlative role in the aging process. Furthermore, the role of reactive oxygen species in aging is one that has been hotly debated since its introduction. There is controversy in yeast because overexpression of superoxide dismutase, an enzyme required to neutralize reactive oxygen, does not consistently extend lifespan (Harris et al., 2005, 2003). The idea that damaged proteins might be the aging factor is particularly attractive given the recent finding that increased proteasome activity extends lifespan. Because carbonylated proteins likely represent a very small proportion of the total

burden of damaged proteins, globally increasing protein turnover may diminish or delay the effects of this proposed aging factor.

The third candidate aging factor, protein aggregates, was discovered based on the hypothesis that oxidatively damaged proteins often form aggregates. Nystrom's group used fluorescently-tagged Hsp104, a protein that interacts with aggregated proteins, as a marker for general protein aggregation (Glover and Lindquist, 1998). They found that Hsp104 aggregates were more abundant in replicatively old cell and asymmetrically retained in the mother cell (Erjavec et al., 2007). Interestingly, the presence of Sir2 is required for mother cell retention of both carbonylated proteins and Hsp104-GFP marked proteins aggregates, making all three potential aging factors Sir2-dependent (Erjavec et al., 2007).

That there might be one pathway of aging that is Sir2-independent, i.e. dietary restriction, allows for the possibility of additional aging factors not yet described. These may be damaged organelles or more abstract, such as loss of specific cellular functions. For instance, perhaps damaged biomolecules are equally transmitted between mother and daughter cells, however, relatively increased proteasome activity in the daughter cell allows for a reset replicative potential. Alternatively, there could be a lifespan promoting factor that is preferentially segregated to the daughter cell. These possibility leads us back to the initial question about the nature of aging cells, which is what is different between old and young cells, and how are those differences established. To better address this question, cell biological approaches have been undertaken as they allow for the monitoring of changes within the cell throughout the aging process in addition to the measurement of lifespan.

A cell-biological approach to understanding the aging process

The approaches discussed thus far have mostly been used to identify genes and their role in various replicative aging pathways with lifespan being the measured phenotype. While the several aging pathways have been discovered using these methods, the specific cellular events and changes in cellular function that contribute to and occur during replicative aging are not well understood. The yeast aging field is now poised to address this question. The development of the mother enrichment program allows for the isolation of large numbers of mother cells at any replicative age (Lindstrom and Gottschling, 2009a). The creation of GFP-tagged yeast strain collection along with the subcellular localization and abundance of the majority of proteins encoded by the yeast genome have already been defined (Ghaemmaghami et al., 2003; Huh et al., 2003a). Finally, because of yeast's long-standing history as a simple eurkaryotic organism,

the relationship between organelle morphology and function are well-characterized (Van Zutphen and Van der Klei, 2011).

Previous studies demonstrate the utility of cell biological approaches to further our understanding of the events that govern replicative aging

Initial studies using cell biology to identify age-associated changes in organelle morphology and their relationship to changes in cellular function demonstrate utility in this approach and support the use of microscopy-based screens for identifying cellular events that occur as a function of age. Two early studies by Sinclair et al. in 1997 showed that the yeast nucleolus was enlarged and fragmented in old mother cells, and that this fragmentation was associated with ERC accumulation by characterizing the localization of Sir3 and nucleolar proteins with age (Sinclair and Guarente, 1997). This finding suggested the possibility of using nucleolar morphology as a marker for ERC accumulation and for advanced replicative age.

More recently, Hughes and Gottschling discovered that early age-associated loss of vacuolar acidity in the mother cell leads to mitochondrial fragmentation and dysfunction by performing an overexpression screen for mitochondrial morphology-associated genes that suppressed age-associated mitochondrial fragmentation (Scheckhuber et al., 2007; Hughes and Gottschling, 2012). In determining how loss of vacuolar acidity and mitochondrial dysfunction is related to previously described aging pathways, they found that calorie restriction in yeast extends replicative lifespan by increasing the acidity of the vacuole, and that is was the vacuole's storage function and not its degradative function that was required for lifespan extension (Hughes and Gottschling, 2012). The mechanism of how disruption of vacuolar storage leads to mitochondrial fragmentation and dysfunction remains unknown.

These studies, particularly the study carried out by Hughes and Gottschling demonstrate how the use of a cell biological approach to characterize an age-associated change in organelle morphology can provide further insight into the cellular functions important for the aging process and lifespan regulation. Cell biology was used to identify and characterize an age-associated change in organelle morphology: mitochondrial fragmentation. Previous characterization of the relationship between organelle morphology and function revealed an age-associated change in cell function: loss of mitochondrial membrane potential (Fannjiang et al., 2004). Application of previously defined genetic modulators of the change in organelle morphology led to the mechanism of the age-associated organelle dysfunction: loss of vacuolar acidity (Altmann and Westermann, 2005; Dimmer et al., 2002). And finally, placing this discovery in the context of

the pathways known to be important for replicative aging and lifespan extension elucidated a long-anticipated mechanism for how dietary restriction extends replicative lifespan.

An unbiased cell-biological screen to identify novel age-associated changes in organelle morphology and function will identify important causative and consequential cellular events that occur during the aging process

The question posed at the beginning of this introduction is what is different between an old organism and a young one. While significant progress has been made to answer this question, one common theme that has arisen throughout each section is that there is still much to be uncovered about the aging process and the regulation of lifespan. Another common theme in the field of aging is the idea that stochasticity plays a role in the aging process. Because there are likely to be one or few initiating events and many subsequential events, it will be important to identify these pathways using an unbiased approach, and allow the kinetics and nature of each event to guide experiments to determine mechanism. Combining recent methods for large-scale isolation of replicatively aging cells with a cell biological approach offers the opportunity to monitor organelles at multiple timepoints throughout the aging process and within a large population of cells. The overarching goal of this work is to address many of the fundamental questions of aging by identifying the cellular structures and pathways that become defective with age, and by determining the role these pathways play in replicative aging.

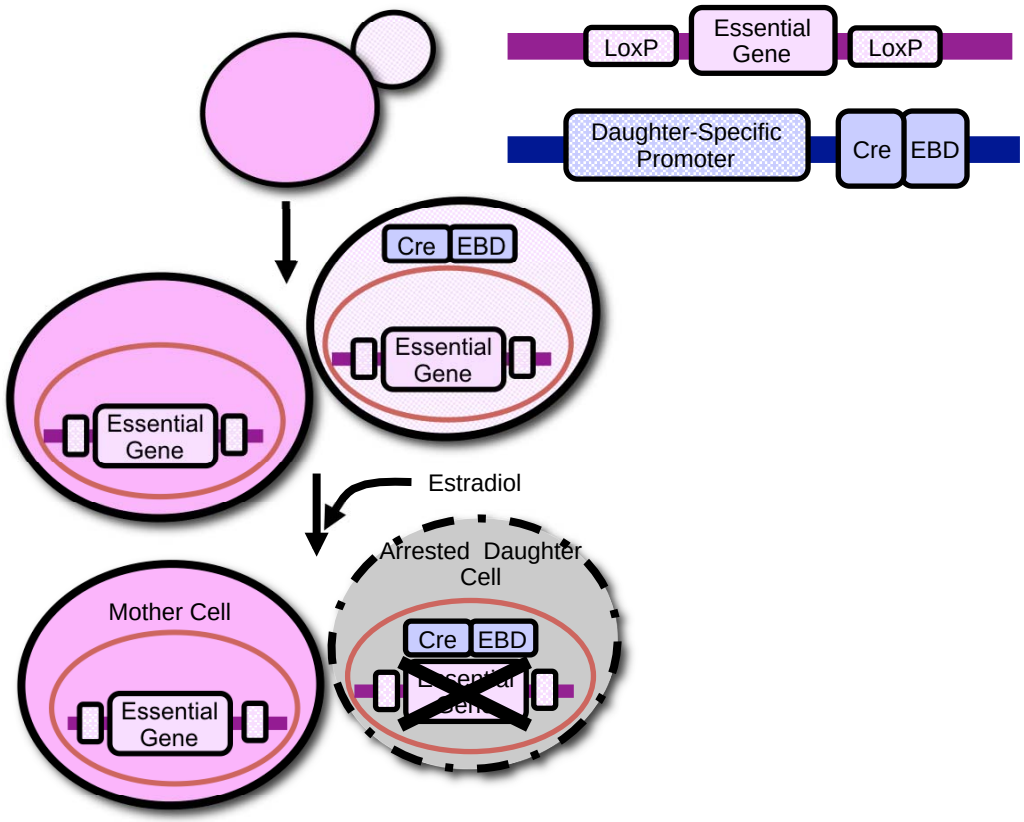

Figure 1.1. The Mother Enrichment Program allows for the enrichment of mother cells in liquid culture by preventing daughter cells from undergoing further division. Cre recombinase is fused to an estrogen-binding domain (EBD) to allow estradiol-inducible nuclear translocation of Cre. The Cre-EBD fusion gene is placed under the regulation of a daughter-specific promoter, *SCW11*pr. In the presence of estradiol, the Cre-EBD gene product translocates to the nucleus and deletes the sequences in both *CDC20* and *UBC9* genes that are flanked by loxP sites. Removal of these gene regions occurs only in daughters, and results in daughter cell-specific attenuation. Thus, the mother-enrichment program allows for the enrichment of mother cells in liquid culture by preventing daughter cells from undergoing further division. The end result is a culture that contains viable mother cells and few arrested daughters.

Chapter II: Cell-biological screens to identify age-associated changes in organelle morphology

Two independent screens for changes in organelle morphology with age – an overview

In order to identify processes that may be compromised during the aging process, I performed two independent cell-biological screens for organelle and cellular substructures that exhibit morphological changes with replicative age. To systematically and comprehensively analyze the effect of replicative aging on many different cellular structures, I generated a set of strains containing the components required for the Mother Enrichment Program (MEP) and containing a single GFP-tagged marker protein corresponding to one of over 20 different cellular structures (Appendix G) (Lindstrom & Gottschling, 2009; Niedenthal, Riles, Johnston, & Hegemann, 1996). The majority of these marker proteins were expressed from their endogenous promoters at their natural chromosomal locus. The GFP-tagged marker proteins were chosen based on their usage by other laboratories to visualize morphological changes in certain cellular structures. These markers were less likely to result in growth defects induced by fusion with a fluorescent protein, and were more likely to be an abundant protein that allowed optimal visualization of the organelle or structure of interest. References citing papers that have used each marker appear in the section they are discussed. Multiple marker proteins were selected for each organelle to reduce the possibility that the morphological changes identified could be attributed to a specific marker.

Two independent screens were done: first on fixed cells and then on living cells. The fixed-cell screen was designed to facilitate batch processing and analysis, and to maximize the number of markers that could be visualized for each organelle and cellular substructure. The brightest markers for each structure and additional markers for structures that were suggestive of age-associated changes in morphology were then analyzed in living cells. The second live-cell screen was done to ensure that results were reproducible and not due to artifacts of fixation or purification. Furthermore, a subset of GFP-tagged marker proteins, such as those that allow visualization of endosomal structures, lose their intensity and localization upon fixation. The live-cell screen allowed analysis of structures whose marker proteins were resistant to fixation.

For the first screen, cells were biotinylated, aged in culture using the MEP, harvested, fixed, purified at various replicative ages, and visualized using wide-field epifluorescence microscopy (**Figure 2.1A**). For the second screen, cells were labeled with rhodamine, aged in culture using the MEP, and visualized live using wide-field epifluorescence microscopy (**Figure 2.1B**). Rhodamine was used to permanently label the cell walls of the original population of

mother cells in the live-cell screen. While rhodamine is primarily detected using red excitation/emission filters, such as TRITC or Texas Red, it exhibits significant emission bleed-through into the FITC channel used to detect GFP. As a result, the cell wall often appears labeled in images detecting GFP-labeled marker proteins, especially when longer exposures were required.

For both screens, approximately 10-20 cells were visualized at five different timepoints: exponentially growing cells prior to labeling (log, ~1-2 divisions), at the time of MEP induction (time 0 hours, ~2-3 divisions), and at time 3 hours (~4-7 divisions), 24 hours (~16-22 divisions), and 48 hours (28+ divisions) following MEP induction. Time 48 hours also corresponds to our laboratory strain's median lifespan (Lindstrom and Gottschling, 2009b). Log-phase cells expressing each fluorescently tagged marker protein were used to confirm that the subcellular localization of the marker proteins in the MEP strains were identical to its localization as reported in the literature. Organelles and cellular substructures were monitored for changes that occurred as a function of replicative age. Each structure was scored for its number, size, sub-cellular localization, intensity, and when possible, inheritance. The marker proteins analyzed in the two screens are organized by cellular structure and listed in **Tables 2.1-2.14.**

To systematically and quantitatively characterize each organelle and cellular structure, as well as confirm the observations made in the fixed- and live-cell screens, I subjected the brightest organelle markers to three-dimensional wide-field fluorescence microscopy followed by deconvolution. The markers used for this higher-resolution secondary screen are also indicated on **Tables 2.1-2.13**.

The findings from the fixed- and live-cell screens, as well as the high-resolution secondary screen are organized by structure. The marker proteins that did not reflect any changes in the organelle, those that changed in a way that could be attributed to age-associated differences in cell size, and those exhibited significant age-dependent changes, but were not followed up in this study, are described below. The organelles and their corresponding marker proteins that changed as a function of age and were further characterized are described in Chapter III.

Most structures exhibit change with replicative age

The fixed- and live-cell screens revealed that the majority of marker proteins exhibited some change as a function of replicative age. These changes ranged from subtle to very robust. The findings from the screens are summarized below along with a brief introduction for each organelle or cellular substructure. Representative images for each of the marker proteins

visualized in both the fixed- and live-cell screens, and with higher-resolution microscopy with deconvolution are shown in **Figures 2.2-2.20**.

Structures that were not observed to change with replicative age

Bud:

Background: The bud was visualized because yeast cells divide asymmetrically, and the bud is an entity distinct from the mother cell (Amon, 1996). Cell polarity factors are important in establishing this asymmetry, and it has been proposed that a barrier exists separating the mother cell and budding daughter cell (Kang and Béven, 2010). One theory of aging suggests that mother/daughter asymmetry and the barrier is required for daughter cells to be born reset with full replicative potential (Henderson and Gottschling, 2008b). Loss of localization of a bud-specific protein would indicate a disruption in the establishment of asymmetry between the mother and daughter cells or a defect in the barrier.

Marker (**Table 2.1**): The bud was visualized using Ymr295cp-GFP, a protein of unknown function that localizes specifically to the cell periphery and bud (Huh et al., 2003b).

Results: Ymr295cp-GFP remains bud-localized at all replicative ages (**Figure 2.2**). This suggests that the mechanism that is required for targeting and retaining Ymr295cp in the bud is intact in replicatively old mother cells.

Bud Neck:

Background: The bud neck harbors many structures that are important for asymmetric division, establishment of polarity, spindle dynamics and cytokinesis (Oh and Bi, 2011; Merlini and Piatti, 2011). It has also been proposed that the mother/daughter barrier resides at the bud neck (Oh and Bi, 2011). Changes in the bud neck may suggest a loss of asymmetry, disruption of the mother/daughter barrier, or dysfunction in completing the cell cycle.

Markers (**Table 2.2**): The bud neck was visualized using several proteins, including Bni4p-GFP and GFP-tagged septins Cdc10p, Cdc11p and Cdc12ph(Huh et al., 2003a; Versele and Thorner, 2004)

Results: Bni4p-GFP was poor marker for the bud neck as it is very transiently localized to the bud neck and is weakly fluorescent (**Figure 2.3A**). Visualization of Cdc10p-GFP and Cdc12p-GFP in fixed cells (**Figures 2.3B,C**), and of Cdc11p-GFP in live cells (**Figure 2.3D**) at increasing replicative ages revealed that septin components remained localized to the bud neck throughout aging. One interesting age-dependent artifact of fixation was discovered upon visualization of Cdc10p-GFP and Cdc12p-GFP (**Figures 2.3B,C**). In time 24 and 48 cells, the septin ring is slightly shifted away from the bud neck, primarily into the bud, following fixation with paraformaldehyde diluted with water. Because this phenotype was only observed in older cells, it may suggest an age-dependent change in the cell's physical and/or mechanical ability to tolerate osmotic stress. Additionally, it is apparent from both fixed- and live-cell screens that cells with abnormal and/or elongated buds often have wider bud necks. In cells with normal buds, the increasing diameter of the bud neck with age may scale with the increasing size of the aging cell.

The bud necks of replicatively aged cells were also visualized by high-resolution microscopy using the septin ring component Cdc11p C-terminally fused to GFP as a marker (**Figure 2.3E**). The width of the bud neck and septin ring were only notably greater in cells that appeared to be defective or delayed in mitosis, as evidenced by an abnormally elongated or enlarged bud. The localization of bud neck markers was only altered in the context of fixation with paraformaldehyde and water, and in the context of mitotic delay, both in old time 24- and 48-hour cells. Thus, morphological changes of the bud neck were not further characterized. Mitotic delay in replicatively aging cells is discussed in Chapter III.

Microtubules and microtubule-related structures:

Background: Microtubules in yeast can be divided into two classes: cytoplasmic and nuclear. The primary roles for the nuclear microtubules are to ensure the proper attachment of kinetochores to the spindle pole bodies, and to provide the structure necessary for proper spindle orientation, elongation, and segregation. The cytoplasmic microtubules also play a role in spindle dynamics and provide additional cytoskeletal support for the cell (Saunders, 1999).

Markers (**Table 2.3**): The markers used to visualize microtubules and microtubule-related structures are the kinesin motor protein Cin8p, the cytoplasmic dynein heavy

chain Dyn1p, the kinesis-related motor protein Kip3p, and α-tubulin Tub1p (Tanaka et al., 2007).

Results: Except for GFP-Tub1p, the microtubule markers were fairly weak. Cin8p-GFP localization was similar to that of the spindle pole body markers, showing spindle position defects at time 24 hours. Cin8p-GFP was not detected at time 48 (**Figure 2.4A)**. Dyn1p, which marks the cytoplasmic microtubules, was extremely faint at log, and could not be adequately visualized in aging cells (**Figure 2.4B**). Kip3p-GFP localization was too faint for detection (**Figure 2.4C**). Results from visualizing GFP-Tub1p with replicative age can be found in Chapter III with the along with the results describing age-associated changes of the mitotic spindle (**Figure 3.9**).

Bud-localized, bud neck-localized, and microtubule-related markers did not exhibit significant changes in organelle morphology with replicative age. Bud and bud neck markers remained similarly localized at all replicative ages. No changes in size, shape, or intensity were observed. Microtubule-related markers were challenging due to their weak fluorescence. It is important to emphasize here, that these findings do not rule out the possibility that these structures change with age. First, a different marker choice may allow visualization of other substructural aspects of an organelle and structure. Second, rare age-associated changes in organelle morphology would not be detected using these screening methods. A screen for infrequent events would require visualization of many more cells. Third, the microtubule-related structures may be altered with age, however, a more sensitive method would be required due to weakly fluorescent or low abundance marker proteins.

Structures that changed in a manner that could possibly be attributed to differences in cell size

Actin and actin-related structures:

Background: Actin localizes to three main structures within the cell: cortical actin patches, actin cables or filaments and the actomyosin ring (Moseley and Goode, 2006). Cortical actin patches are distributed to areas of polarized growth where much secretion and endocytosis occurs. While several cortical actin patches are found in the mother cell, most are distributed to the bud site, new bud, and bud neck. Actin cables are bundles of filamentous actin, whose purposes include providing cytoskeletal support for the cell and establishing directional tracks for polarized growth and organelle

inheritance. The actomyosin ring assembles at the bud neck and its constriction is required for proper cytokinesis. Actin and actin-containing structures likely play a role in aging as the cytoskeleton has to adapt to the larger cell volume of replicatively old cells and the maintenance of polarity is necessary to establish the asymmetry upon which replicative aging is based (Moseley and Goode, 2006).

Markers (**Table 2.4**): Several different proteins marking different actin or actin-related structures were fused to GFP to monitor these cellular substructures with replicative age. Abp140p-GFP was used to visualize filamentous actin, Hof1p-GFP and Myo1p-GFP marked the actomyosin ring, and Sac6p-GFP, Cap1p-GFP, and GFP-Cap2p localized to cortical actin patches. The toxin phalloidin conjugated to Alexa Fluor 488 was used to visualize both actin cables and cortical patches simultaneously (Moseley and Goode, 2006).

Results: Hof1p-GFP, which is reported to localize to the actomyosin ring, actually localized most densely to the bud. Hof1p-GFP localization remained bud-specific through time 24. No budded cells were found at time 48 (**Figure 2.5C**). Myo1p-GFP localized to the actomyosin ring at the bud neck through time 24. At time 48, Myo1p-GFP is localized more diffusely in the cytoplasm (**Figure 2.5D)**.

Actin cables were visualized using Abp140p-GFP, and exhibited varied morphologies with replicative age. In some cells, the filaments became more prominent, and in other cells, Abp140p-GFP seemed to localize either diffusely in the cytoplasm or in foci on the plasma membrane (presumably to cortical actin patches) (**Figures 2.5A,B**).

The cortical actin patches were marked with proteins Sac6p, Cap1p and Cap2p. Examination of Sac6p-GFP containing cells revealed that cortical actin patches increased in number and in intensity with age. Cortical actin patches are primarily localized at areas of polarized growth, and this pattern is seen throughout all timepoints (**Figures 2.6A,B**). Cap1p and Cap2p, actin capping proteins that also localize to cortical actin patches share the same pattern of being localized to regions of polarized growth, however, they do not show any significant changes in the number or size of the cortical actin patches (**Figures 2.7A,B**). This suggests that the changes seen in cortical actin patch morphology with Sac6p-GFP were specific to that marker. Alexa Fluor 488 phalloidin was used to stain fixed and permeabilized cells to visualize both filamentous

actin and cortical actin patches simultaneously. Phalloidin staining supported the results from aging cells containing Abp140p-GFP, Cap1p-GFP, and GFP-Cap2p (data not shown). Actin cables are occasionally more prominent in aging cells; cortical actin patches retain their polarized localization throughout aging, and they did not suggest any increase in cortical actin patch density or size in the aging mother cell.

Cortical actin patches and actin filaments were also visualized at higher resolution using the fluorescent marker protein Sac6p-GFP (**Figure 2.6C**) and the fluorescent Alexa Fluor 488 conjugated to the actin-binding toxin phalloidin (**Figure 2.7C**). Both markers were used to quantify the number of cortical actin patches on the mother cell surface with age. The intensity of Sac6p containing actin patches was also monitored as a function of replicative age. The intensity of phalloidin-containing patches could not be used because it may reflect the degree of permeabilization required for staining and not be proportional to amount of actin present. Phalloidin was used to monitor the actin filaments with age.

The number of cortical actin patches on young (time 0 and 3 hours) and old (time 24 hours) mother cells was quantified manually with both Volocity and Softworx software programs. The average number of Sac6p-GFP marked actin cortical patches increased from 19 in young cells to 42 in 24-hour old cells. The average number of phalloidin marked actin cortical patches increased from 29 in young cells to 48 in old cells. This is likely not biologically significant. As cells age, they increase in size and therefore surface area. The dimensions of each cell was measured and used to calculate the surface area of the cell assuming cells are approximately oblate ellipsoid in shape. The patch densities for Sac6p-GFP-containing cells were 0.2 patches/μm^2 in young cells and 0.2 patches/μm^2 for old cells (**Figure 2.6D**). The patch densities for phalloidin-stained cells were 0.3 patches/μm^2 in young cells and 0.3 patches/μm^2 for old cells (**Figure 2.7D**). There is no significant difference in cortical actin patch density between young and old cells, although Sac6p must not be present at all phalloidin staining actin patches. Interestingly, The abundance of Sac6p-GFP at cortical actin patches increases 2-fold as a function of replicative age.

Phalloidin staining of actin filaments was reduced in old cells compared to young cells (**Figure 2.7C**). This observation may be due to a structural change in the actin filaments, or it may be a result of a difference in the ability of old cells to be permeabilized for staining. The cell wall has been reported to thicken in cells as a function of replicative age, and this is one potential reason for the differences in

phalloidin staining. In the cells where phalloidin staining is evident, young and old cells appear similar.

Cortical actin patch localization remained at sites of polarized growth throughout replicative aging. Cortical actin patch density also remains constant throughout replicative aging. Actin filament staining with phalloidin was reduced in old cells. This could represent a biological change in the actin filament or a change in the old cell's ability to be permeabilized for staining.

Chromosomes and the nucleus:

Background: The nucleus contains all the essential genetic material required for the cell. It is the center for genetic regulation, and the faithful duplication and segregation of the nucleus and its contents are essential for both mother and daughter cell viability (Taddei et al., 2010). Nuclear volume has been shown to scale with cellular volume, and not total genetic material (Jorgensen et al., 2007).

Markers (**Table 2.5**): *HTB1* and *HHF2*, which encode histones 2B and 4 respectively, were used to mark chromosomes (Rando and Winston, 2012). Nuclear pore components Nup1p, Nup49p, Nup82p, Nup188p and Nic96p were used to mark the nuclear envelope (Aitchison and Rout, 2012; Huh et al., 2003a). The nucleoplasmic marker Pus1p was used to observe nuclear contents in general (Hellmuth et al., 1998; Campbell and Lorenz, 2006).

Results: C-terminal GFP fusions of the histones and the nuclear pore components rendered the cells growth defective with an elongated cell morphology. Creating strains that were hemizygous for the tagged version of each of the proteins alleviated the growth and cell morphology defects. Despite the apparent growth defects, similar observations were made when visualizing the nucleus using nuclear pore markers. Finally, all markers reflected the increased nuclear volume at times 24 and 48. Representative images from both fixed- and live-cell screens are shown in **Figures 2.8A-E.**

The nucleoplasmic marker Pus1p, which when N-terminally tagged does not exhibit any growth or cell morphological defect, showed that cells have nuclear segregation problems at more advanced replicative ages. These defects included but are not limited to: multiple nuclei, nuclei segregating within the mother cell perpendicular

to the mother/bud axis, mitotic delay and missegregation of the nucleus into the daughter cell (daughterly phenotype). The frequency of nuclear migration defects increased from time 24 to time 48. Representative images of GFP-Pus1p with replicative age are shown in **Figure 3.10**.

COPI transport vesicles:

Background: COPI vesicles mediate retrograde transport from the Golgi apparatus to the endoplasmic reticulum. The primary purpose of COPI vesicles is to return escaped resident ER proteins back to the ER from the Golgi apparatus. These vesicles are essential to the cell, and allow communication between the organelles of the secretory pathway (Beck et al., 2009).

Markers (**Table 2.6**): Coat proteins were used as markers for COPI vesicles. Sec21p, Glo3p, Sec27p, and Sec28p were used to monitor COPI vesicles (Huh et al., 2003a).

Results: COPI markers revealed that the number of COPI vesicles modestly increase in number with age (**Figures 2.9, 2.10A**). However, it is unclear whether this increase is biologically significant or if it reflects an increase in cell size. The screens also revealed that the localization of COPI markers are highly affected by fixation. In order to maximize the amount of protein localized to COPI vesicles, young and old cells expressing Sec21p-GFP were imaged while living (**Figures 2.10B,C**). While this improved localization and fluorescence at the vesicles, the quantification of vesicles is suboptimal because the COPI vesicles continued to move during image acquisition. Because of this, and because they are so numerous, the number of COPI vesicles could not be accurately quantified. Relative total fluorescence was measured in young and old cells as an approximation for changes in COPI vesicle number. By high-resolution microscopy (**Figure 2.10C**), on average, old cells had 1.2-fold more total Sec21p-GFP fluorescence compared to young cells. When total fluorescence was normalized to cell volume, the difference between old and young cells was abrogated (only 0.7-fold), suggesting that the increase in COPI vesicles is less than proportional to the increase in cell volume with age (**Figure 2.10D**).

As visualized by Sec21p-GFP, COPI transport vesicle numbers appear to increase with replicative age, but this increase does not exceed the increase that would be expected to accommodate a larger cell volume. This finding is supported

biochemically, as Western blot analysis showed Sec21p-GFP levels remained constant with replicative age (**Figure 2.10E**). Of note is the appearance of a lower molecular weight band specifically in the extracts of old time 24-hour cells.

COPII transport vesicles:

Background: COPII vesicles mediate anterograde transport of proteins from the ER to the Golgi for additional carbohydrate post-translational modification. COPII vesicles have coat proteins that confer cargo and target specificity. These vesicles are essential to the cell, and allow communication between the organelles of the secretory pathway (Sato and Nakano, 2007).

Markers (**Table 2.7**): Coat proteins were used as markers for COPII vesicles. Sec23p, Sec24p, Sec13p and Sec31p were used to visualize COPII vesicles (Huh et al., 2003a).

Results: COPII markers revealed that the number of COPII vesicles modestly increase in number with age (**Figures 2.11**). However, it is unclear whether this increase is biologically significant or if it reflects an increase in cell size. The screens also revealed that COPII coat proteins are highly affected by fixation. In an effort to maximize the amount of protein localized to the transport vesicles, young and old cells expressing Sec31p-GFP were imaged while living (**Figures 2.12B,C**). While this improved localization and fluorescence at the vesicles, the quantification is suboptimal because the transport vesicles continued to move during image acquisition. Because of this, and because they are so numerous, the number of transport vesicles could not be accurately quantified. Relative total fluorescence was measured in young and old cells as a crude approximation for changes in transport vesicle number. On average, old cells had 2.1-fold more total Sec31p (COPII) fluorescence compared to young cells. When total fluorescence was normalized to cell volume, the difference between old and young cells decreased to 1.2-fold indicating that the increase in COPII vesicles is slightly greater than expected for the increase in cell volume with age (**Figure 2.12D**).

As visualized by Sec31p-GFP, COPII transport vesicle numbers appear to increase with replicative age, but this increase does not exceed the increase that would be expected to accommodate a larger cell volume. This finding is supported biochemically, as Western blot analysis showed Sec31p-GFP levels remained constant

with replicative age (**Figure 2.12E**). Of note is the appearance of lower molecular weight bands that increased in quantity as a function of replicative age.

Endoplasmic reticulum:

Background: The endoplasmic reticulum (ER) is responsible for folding and modifying proteins that are destined to be exported. In yeast, the ER has been divided into subcompartments based on their localization and morphology. Beyond its role in ensuring only properly folded and modified proteins are exported, the ER membrane is thought to have important interorganellar functions, as it shares contact sites with the majority of organelles, including the plasma membrane, lipid particles, and the mitochondria (Elbaz and Schuldiner, 2011; Toulmay and Prinz, 2011). The ER may play an important role in aging because of its role in protein quality control (Vembar and Brodsky, 2008).

Markers (**Table 2.8**): Ncp1p, Nsg1p, Hmg1p, Hmg2p, Erg4p, Sec61p and Sec63p are all integral ER membrane proteins (Flury et al., 2005; Hampton and Rine, 1994; Zweytick et al., 2000; Osborne et al., 2005). GFP containing the N-terminal ER targeting sequence and the C-terminal ER retention signal HDEL (ss-GFP-HDEL) was used to visualize the ER lumen (Rossanese et al., 2001).

Results: All markers reflected the perinuclear ER's concomitant expansion with the increase in nuclear volume with replicative age. Some older cells appeared to have a modest increase in the amount of ER membrane, however it is unclear whether this is due to the increase in cell volume. Inheritance of cortical ER appeared normal at all timepoints, which suggested that ER stress is not rampant (**Figures 2.13A-D; 2.14A**).

GFP containing the N-terminal ER targeting sequence and the C-terminal ER retention signal HDEL (ss-GFP-HDEL) was used to visualize the ER lumen. Higher resolution microscopy was used in conjunction with ss-GFP-HDEL to compare the volume of the ER in young and old cells, and to examine the structure of ER in three-dimensions. The general structure of the ER remains intact with replicative age, as cortical, tubular, and perinuclear ER appear similar in young and old cells (**Figure 2.14B**). The ER lumen volume was determined by setting a threshold for fluorescent signal, and only age-matched pairs were compared to each other. On average, the ER lumen volume of an old (time 24 hours) cell is 1.4-fold larger than the ER lumen volume

of a young (time 3 hours) cell. Once normalized for cell volume, the ER volume of old cells were actually decreased compared to those of younger cells (**Figure 2.14C**). One serious caveat to this, however, is that the expression of HDEL may be the same regardless of age or size of the cell. If the volume of the ER increases with cell size as a function of age, and the abundance of HDEL remains the same, the fluorescence signal will be effectively diluted in old cells and result in a falsely decreased ER volume with age. It should be noted that cortical ER is inherited into the small bud at all replicative ages, suggesting the absence of ER stress (Babour et al., 2010).

Golgi apparatus:

Background: The Golgi apparatus is the site of additional carbohydrate modification for proteins that are destined to be exported. *Saccharomyces cerevisiae* are unique in that they have punctate Golgi structures instead of the stacks found in other organisms. Proteins are directed from the Golgi to the vacuole, plasma membrane, periplasm or back to the ER (Suda and Nakano, 2011).

Markers (**Table 2.9**): The markers used to visualize the Golgi apparatus with age include Sec7p, Och1p, Ric1p, Rgp1p and Vrg4p (Harris and Waters, 1996; Losev et al., 2006; Siniossoglou et al., 2000).

Results: Och1, Ric1 and Rgp1 were fairly weak markers for the Golgi. Sec7p and Vrg4p both showed modest increases in the number and size of the Golgi as a function of age, however, it is unclear whether this increase exceeds that which would be expected by the age-associated increase in cell volume (**Figures 2.15A,B**).

The early and late Golgi apparatus were also visualized by high-resolution microscopy using Vrg4p-GFp and Sec7p-GFP, respectively (**Figure 2.15C,D**). Both Vrg4p and Sec7p are highly affected by fixation. In an effort to optimize subcellular localization and GFP signal strength, the Golgi in young and old cells were imaged alive. This was not ideal because the Golgi continued to move within the cell during image acquisition. Because of this, and because they are so numerous, the amount of total fluorescence was used as a crude approximation for quantity of Golgi.

The ratio of the average total amount of Vrg4p-GFP fluorescence per old cell (time 24 hours) to young cell (time 3 hours) was 1.4. When total fluorescence was

normalized to cell volume, this ratio was only 0.8 (**Figure 2.15E**). Thus, while there was an increase in Golgi with age, the increase is less than would be expected for the increase in cell size. The ratio of the average total amount of Sec7p-GFP fluorescence per old (time 24 hours) cell to young cell (time 3 hours) was 1.4. When total fluorescence was normalized to cell volume, this ratio became 0.9, suggesting that the increase in Golgi is also proportional to the increase in cell volume with age (**Figure 2.15E**).

Lipid droplets/particles:

Background: The primary function of the lipid droplet is the storage of neutral lipids, such as triacyglycerols and sterol esters. Lipid droplets may also play a role in lipid transfer between membranes and in lipid biosynthesis. Lipid particles, while not essential, are important in providing lipids for membrane biosynthesis. Lipid particle number is responsive to the nutritional state of the cell. We are just now uncovering all the important roles lipids play in every aspect of cellular function, organization, regulation and maintenance (Goodman, 2009; Walther and Farese, 2009). Lipid droplets are known to interact closely with the ER, mitochondria, and peroxisome (Jacquier et al., 2011; Pu et al., 2011).

Markers (**Table 2.10**): Erg6p and Erg7p were used to visualize the lipid particle in aging cells. Both proteins have roles in ergosterol biosynthesis, and localize to lipid particles. Erg7p also localizes to the endoplasmic reticulum, making it the less ideal marker (Goodman, 2009). Nile red is a stain for intracellular lipids also used to visualize lipid particles with replicative age (Greenspan et al., 1985; Wolinski and Kohlwein, 2008).

Results: Erg7p-GFP marked lipid particles were not significantly changed with replicative age (**Figure 2.16C**). Erg6p-GFP marked lipid particles generally increased in number and size with replicative age (**Figures 2.16A,B**). The sizes of these lipid particles varied greatly, but the total fluorescence was increased at time 24 and 48 hours.

The fixed- and live-cell screens suggested that lipid particles as marked by Erg6p-GFP might be increasing as a function of replicative age. Because of this, I used high-resolution microscopy to better quantitate the number and size of lipid particles in cells only stained with Nile Red (**Figure 2.16D**) and in Erg6p-GFP expressing cells

stained with Nile Red (**Figure 2.17A**). Nile Red staining intracellular lipid droplets were more regular in size, and increased in number as a function of replicative age from 13 in young cells to 29 in old cells ($p<0.05$) (**Figure 2.16E**). In contrast, Erg6p-GFP containing structures were irregularly shaped and varied in size, and therefore were difficult to quantitate except by total fluorescence. Compared to young cells, old cells exhibited increased total fluorescence, however this was abrogated when fluorescence was normalized to cell volume (**Figure 2.17B**). Similar to Erg6p-GFP, when total Nile Red fluorescence was compared in young and old cells, the total fluorescence increased as a function of age, but once normalized to cell volume, this increase was also abrogated (**Figure 2.17B**). Interestingly, high-resolution microscopy of both young and old cells also revealed some non-overlapping staining between the two markers, suggesting that all lipid droplets are not equivalent (**Figure 2.17A**). The incomplete colocalization of Nile Red stain and Erg6p-GFP is present independent of replicative age.

Cortical actin patches, nuclear volume, COPI and COPII transport vesicles, ER volume, the Golgi apparatus, and lipid droplets all exhibit age-dependent morphological or numerical changes in their structures that could be explained by changes in cell size. The principles and mechanisms that govern if and how organelles are scaled in relation to cell size are largely unknown (Chan and Marshall, 2010; Levy and Heald, 2012). It is unclear at this time, whether the findings in this section have greater biological significance. Thus, priority has been placed on organelles that exhibit age-associated morphological changes that could not be attributed to cell size. Experiments that assess the function and activity of the organelles and structures in this category are required to determine their significance in replicative aging.

Structures that changed significantly, but are not further characterized in this work

Eisosomes:

Background: Eisosomes were long thought to be very static regions on the plasma membrane that indicated potential sites for endocytosis. However, recent evidence suggests that eisosomes actually organize and demarcate special domains of the plasma membrane that have a specific lipid and protein composition. Yeast cells generally have 50-100 eisosomes distributed across its plasma membrane. Pil1p is not an integral membrane protein, but is thought to be the primary protein that recruits the

other eisosome components. Sur7p is recruited by Pil1p and is an integral membrane protein (Olivera-Couto and Aguilar, 2012).

Markers (**Table 2.11**): Pil1p-GFP and Sur7p-GFP were used to observe eisosomes in cells as they age. Pil1p is a membrane-associated protein, whereas Sur7p is an integral membrane protein (Karotki et al., 2011).

Results: Both markers show that the number of eisosomes increase as the surface area of the cell increases with replicative age, and both markers are localized predominantly in the mother cell (when small-budded). However, one significant difference between eisosomes marked with Pil1p-GFP compared to Sur7p-GFP is that the abundance of Sur7p-GFP at the eisosomes increased as a function of age. Representative images for both markers are shown in **Figures 2.18A-D**.

The number and intensity of Pil1p-GFP and Sur7p-GFP marked eisosomes were quantified following high-resolution microscopy. Eisosomes of old cells contained increased levels of Sur7p-GFP, but not Pil1p-GFP (**Figure 2.18B,D**). The relative average intensities of Pil1p-GFP and Sur7p-GFP foci were compared in young versus old cells using Volocity software. Direct comparisons between young and old cells were only made if they shared a common image field. For Pil1p-GFP, out of 11 matched young and old cell sets, five out of eleven showed an increase average Pil1p-GFP focus intensity with age, and six out of 11 showed a decrease. The average of the old to young focus intensities for the 11 age-matched pairs was 1.0, indicating no change in Pil1p-GFP abundance at the eisosome with age (**Figure 2.18E**). For Sur7p-GFP, ten matched young and old cell pairs were compared. The Sur7p-GFP foci were brighter in the old cells in nine of the ten comparisons. The average of the old to young focus intensities for the ten age-matched pairs was 1.6, suggesting a significant increase in Sur7p-GFP abundance at eisosomes with replicative age (**Figure 2.18E**).

Endosomes:

Background: Endosomes are part of the secretory pathway, connecting the plasma membrane, Golgi apparatus and the vacuole. They play important roles in sorting proteins for recycling back to the plasma membrane or for degradation in the vacuole (Hanson et al., 2009).

Markers (**Table 2.12**): Two endosomal sorting complex required for transport (ESCRT) proteins, Hse1p (ESCRT-0) (Bilodeau et al., 2002) and Snf7p (ESCRT-III) (Babst et al., 2002) were used to mark endosomes, along with the proprotein convertase Kex2p (Fuller et al., 1989) and the endosomal sodium/proton ion exchanger Nhx1p (Brett and Tukaye, 2005).

Results: Endosomes appear as cytoplasmic foci in yeast cells. Hse1p and Nhx1p revealed that the number of endosomes increased with replicative age. This is particularly apparent in the region just cytoplasmic of the vacuolar rim (**Figures 2.19A,B)**. Kex2p-GFP also exhibited a change with replicative age: the signal from GFP in the vacuole became more prominent with advanced age (**Figure 2.19D**). This finding is supported biochemically, as Western blot analysis of Kex2p-GFP expressing young and old cells show clipped GFP in old time 24-hour cells. Detection of free GFP in old cells suggests increased Kex2p-GFP delivery to the vacuole or decreased degradation within the vacuole (Huang and Chang, 2011). Kex2p-GFP levels remained constant with replicative age (**Figure 2.19E**). The ESCRT-III protein Snf7p behaves in a dominant-negative manner when C-terminally tagged, creating a class E vacuolar protein sorting mutant with an unnaturally expanded pre-vacuolar compartment (Teis et al., 2008). Interestingly, while Snf7p-GFP cells have the expected class E compartment, this compartment accumulated significantly with increasing replicative age (**Figure 2.19C**).

Plasma membrane:

Background: The plasma membrane is a lipid bilayer whose main function is to provide a selective permeability barrier for the cell. It harbors many transporters and channels that regulate nutrient, ion and pH homeostasis within the cell (Ziółkowska et al., 2012). Much is being elucidated about the importance and function of the many lipid/protein microdomains found within the plasma membrane. The plasma membrane is a particularly interesting cellular structure for the study of aging, as it may play a role in maintaining the asymmetry required for the mother cell's ability to produce daughter cells with full replicative potential (Takizawa, 2000; Henderson and Gottschling, 2008a).

Markers (**Table 2.13**): The markers used to visualize the plasma membrane include Fet3p (Silva and Askwith, 1995), Hxt2p (Kruckeberg and Ye, 1999), Ylr413wp (Huh et al., 2003a) and Mrh1p (Wu et al., 2000). All four proteins are integral membrane

proteins. Fet3p belongs to the class of multicopper oxidases (Askwith et al., 1994), Hxt2p is a high-affinity glucose transporter (Ozcan and Johnston, 1995), and Ylr413wp and Mrh1p are proteins of unknown function (Wu et al., 2000).

Results: Fet3p and Hxt2p were not ideal marker proteins for the plasma membrane as their expression exhibited high cell-to-cell variability; their expression was also dependent on the nutritional status of the cells. Ylr413wp expression on the plasma membrane was consistent and symmetric between the mother cell and the bud. Visualization of this marker revealed that there is greater GFP signal detected in the vacuole with age, and that while the plasma membrane itself looked similar in young and old cells, there was significant thickening of the cell wall and/or the periplasmic space in replicatively aged cells (**Figure 2.20A**). In contrast, Mrh1p expression on the plasma membrane is asymmetric, and much more highly expressed in the mother cell compared to the bud. Additionally, the abundance of Mrh1p-GFP at the plasma membrane greatly increased as a function of replicative age (**Figure 2.20B**).

Mrh1p-GFP and Ylr413wp-GFP were both visualized using high-resolution microscopy with deconvolution (**Figures 2.20C,D**). Mrh1p and Ylr413wp are plasma membrane proteins, both of unknown function. Mrh1p is an integral plasma membrane protein with homology to Hsp30p (Wu et al., 2000). Mrh1p-GFP asymmetrically localizes to the mother cell in small-budded cells. The relative intensity densities (fluorescent signal per area) of Mrh1p-GFP and Ylr413wp-GFP were compared in young versus old mother cells using Volocity software. Direct comparisons between young and old cells were only made if they shared a common image field. For Mrh1p-GFP, ten age-matched pairs were compared. In all ten pairs, the old cell exhibited greater Mrh1p-GFP abundance. The average of the old to young intensity density for the ten age-matched pairs was 1.8, suggesting a significant increase in Mrh1p-GFP in the plasma membrane with replicative age (**Figure 2.20E**). For Ylr413wp-GFP, out of ten age-matched pairs, only three showed an increase in Ylr413wp-GFP abundance with age. The average of old to young intensity density for the ten age-matched pairs was 1.0, indicating no change in Ylr413wp-GFP abundance at the plasma membrane with age (**Figures 2.20E**).

Significant age-associated changes were observed with visualization of Sur7p-GFP, Mrh1p-GFP, and several endosomal protein markers. Sur7p-GFP and Mrh1p-GFP accumulation at the

plasma membrane with replicative age may represent a subset of integral membrane proteins that are asymmetrically retained in the mother cell, and not turned over (Eldakak et al., 2010). Other members in the Gottschling laboratory are formally testing this hypothesis and its underlying mechanism(s). The age-associated differences in endosomal structures is significant, however additional studies were not carried out due to the difficulty in fixing endosome-related marker proteins, and the weak fluorescence/low abundance of the many protein markers tested.

Cells exhibit general replicative age-associated phenotypes

Several general, marker-independent phenotypes were observed in all strains during replicative aging with the MEP. First, cells markedly increased in size as function of replicative age (**Figure 2.21A)**. This phenotype has been previously described by early studies examining general morphological changes of replicatively old cells (Eglimez, Chen, & Jazwinski, 1990; Mortimer & Johnston, 1959). The increased volume of old mother cells is particularly apparent in some time 24-hour cells and all time 48-hour cells. The second general phenotype of aging cells is that many older mother cells possess buds with abnormal morphologies. Buds are often elongated and larger than normal and many very old mother cells are multi-budded (**Figure 2.21B**). Third, aging cells enlarge at the poles from which budding occurs, in a manner that is proportional to the number of bud scars. Thus, a cell that buds evenly from both poles will be more ellipsoid, and cells that exhibit a pole bias for budding will have a teardrop shape (**Figure 2.21C**). Finally, the distance between the outer cell wall and the plasma membrane increases with age. This could reflect thickening of the cell wall or an increase in periplasmic space. Time 24 and 48 cells that were stained with rhodamine and contain a marker for the plasma membrane highlight this phenotype (**Figure 2.21D**).

Summary of findings from the primary screens and high-resolution microscopy

The fixed- and live-cell primary screens revealed that many cellular structures change modestly as a function of replicative age (**Table 2.14)**. The marker proteins that were not observed to change significantly included the bud-localized protein Ymr295cp-GFP, bud neck-localized proteins, and the weakly fluorescent microtubule-related markers. Structures that exhibited age-associated morphological changes that could be attributed to the increase in cell size include cortical actin patches, nuclear volume, COPI and COPII transport vesicles, Golgi,

endoplasmic reticulum volume, and lipid droplets. Finally, the structures that changed significantly, but are not further characterized in this study are the eisosome protein Sur7p-GFP, plasma membrane protein Mrh1p-GFP, and endosomes. Structures that both exhibited age-associated changes and are further characterized are discussed in Chapter III. These include the nucleolus, vacuole, peroxisomes, and nuclear morphology and segregation.

Some age-associated changes in organelle morphology were subtle and required more quantitative analysis. These markers were subjected to high-resolution microscopy, and the results summarized in **Table 2.14**. Two themes became more apparent by making the cell biological screens quantitative. The first is that many organelles do increase in size, shape or number with replicative age, however many do so in proportion to the increase in cell volume. It is unclear what the biological importance of the scaling is, but here we assume it is adaptive to accommodate a larger cell, and focus on the organelles that changed qualitatively (Chan and Marshall, 2010; Levy and Heald, 2012). The second theme was that some integral membrane plasma membrane proteins, Sur7p and Mrh1p, asymmetrically localized to the mother cell in small-budded cells, and accumulated in abundance with replicative age. This is an area of active research in the Gottschling lab, and while it is a very robust and penetrant phenotype, it will not be further addressed in these studies.

This two-step pan-organellar screen was successful in identifying several organelles that undergo stereotypical changes with replicative age. The remainder of my work will focus on these organelles: the nucleolus, peroxisomes, the nucleus and mitotic apparatus, and vacuoles. Specifically, the phenotypes that will be further explored are nucleolar fragmentation, the increase in number and concomitant decrease in size of the peroxisomes, the number and position of the nucleus and mitotic spindle, and vacuolar fragmentation.

Table 2.1. Bud localized marker protein. The marker used to visualize the bud, and its cellular functions are listed below. The type(s) of microscopy performed on cells expressing each of the marker proteins is indicated. Representative images of the marker proteins can be found in the figures stated in the final column.

Marker Protein or Stain	Marker Function	Type(s) of Microscopy Performed			Image Location
		Fixed	Live	High-res	
Ymr295cp	Protein of unknown function, localized to the cell periphery and bud	X	X		Figure 2.2

Table 2.2. Bud neck localized marker proteins. The markers used to visualize the bud neck, and their cellular functions are listed below.

Marker Protein or Stain	Marker Function	Type(s) of Microscopy Performed			Image Location
		Fixed	Live	High-res	
Cdc10p	Component of the septin ring that is required for cytokinesis, localized to the bud neck	X			Figure 2.3B
Cdc11p	Component of the septin ring that is required for cytokinesis, localized to the bud neck		X	X	Figure 2.3D,E
Cdc12p	Component of the septin ring that is required for cytokinesis, localized to the bud neck	X			Figure 2.3C
Bni4p	Targeting subunit for Glc7p protein phosphatase, localized to the bud neck	X			Figure 2.3A

Table 2.3. Microtubule and microtubule-related marker proteins. The markers used to visualize the microtubules and microtubule-related structures, and their cellular functions are listed below.

Marker Protein or Stain	Marker Function	Type(s) of Microscopy Performed			Image Location
		Fixed	Live	High-res	
Cin8p	Kinesin motor protein involved in mitotic spindle assembly and chromosome segregation	X			Figure 2.4A
Dyn1p	Dynein heavy chain, required for spindle assembly, orientation, and elongation, localized to microtubules and spindle pole bodies	X			Figure 2.4B
Kip3p	Kinesin-related motor protein involved in mitotic spindle positioning	X			Figure 2.4C
Tub1p	Alpha tubulin, localizes to microtubules and spindle pole bodies		X	X	Figure 3.9

Table 2.4. Marker proteins and stain used to visualize actin and actin-related structures. The markers and stain used to visualize actin and actin-related structures, and their cellular functions are listed below.

Marker Protein or Stain	Marker Function	Type(s) of Microscopy Performed			Image Location
		Fixed	Live	High-res	
Abp140p	AdoMet-dependent tRNA methyltransferase and actin binding protein, localizes to cortical actin patches and filamentous actin	X	X		Figures 2.5A,B
Hof1p	SH3 domain-containing protein required for cytokinesis, regulates actomyosin ring dynamics and septin localization, interacts with formins, localizes to bud neck	X			Figure 2.5C
Myo1p	Type II myosin heavy chain, required for cytokinesis and cell separation, localizes to the actomyosin ring at the bud neck	X			Figure 2.5D
Sac6p	Fimbrin, actin-bundling protein, localizes to cortical actin patches	X	X	X	Figure 2.6A-C
Cap1p	Alpha subunit of capping protein heterodimer which binds barbed ends of actin filaments, localized predominantly to cortical actin patches	X	X		Figure 2.7A
Cap2p	Beta subunit of capping protein heterodimer which binds to barbed ends of actin filaments, localized to cortical actin patches	X	X		Figure 2.7B
Phalloidin (Alexa Fluor 488)	Toxin that binds filamentous actin, when conjugated to a fluorescent molecule, can be used to visualize cortical actin patches and filamentous actin	X	X	X	Figure 2.7C

Table 2.5. Markers used to visualize the chromosomal mass and nuclear rim. The markers used to visualize the chromosomal mass and the nuclear rim, and their cellular functions are listed below.

Marker Protein or Stain	Marker Function	Type(s) of Microscopy Performed			Image Location
		Fixed	Live	High-res	
Hhf2p	Histone H4, localized to the nuclear nucleosome	X			Not shown
Htb1p	Histone H2B, localized to the nuclear nucleosome	X			Figure 2.8A
Pus1p	tRNA:pseudouridine synthase, localized to the nucleus		X		Figure 3.10
Nup1p	Nuclear pore complex subunit	X			Figure 2.8D
Nup49p	Nuclear pore complex subunit	X	X		Figure 2.8B,C
Nup82p	Nucleoporin, nuclear pore complex subunit	X			Figure 2.8E
Nup188p	Nuclear pore complex subunit	X			Not shown
Nic96p	Nuclear pore complex subunit	X		X	Not shown

Table 2.6. Markers used to visualize COPI transport vesicles. The markers used to visualize COPI transport vesicles, and their cellular functions are listed below.

Marker Protein or Stain	Marker Function	Type(s) of Microscopy Performed			Image Location
		Fixed	Live	High-res	
Sec21p	Gamma subunit of COPI coatomer, localized to the COPI vesicle coat	X	X	X	Figure 2.10A-C
Sec27p	Beta' subunit of the COPI coatomer, localized to the COPI vesicle coat	X			Figure 2.9A
Sec28p	Epsilon subunit of the COPI coatomer, localized to the COPI vesicle coat	X			Figure 2.9B
Glo3p	ADP-ribosylation factor GTPase activating protein, localized to the COPI vesicle coat	X	X		Figure 2.9C,D

Table 2.7. Markers used to visualize COPII transport vesicles. The markers used to visualize COPII transport vesicles, and their cellular functions are listed below.

Marker Protein or Stain	Marker Function	Type(s) of Microscopy Performed			Image Location
		Fixed	Live	High-res	
Sec23p	GTPase activating protein, component of the COPII coat	X	X		Figure 2.11C,D
Sec24p	Component of the COPII coat, required for cargo selection	X			Figure 2.11B
Sec13p	Component of the Nup84 nuclear pore sub-complex and component of the COPII coat	X			Figure 2.11A
Sec31p	Component of the COPII vesicle coat	X	X	X	Figure 2.12A-C

Table 2.8. Markers used to visualize the endoplasmic reticulum. The markers used to visualize the endoplasmic reticulum, and their cellular functions are listed below.

Marker Protein or Stain	Marker Function	Type(s) of Microscopy Performed			Image Location
		Fixed	Live	High-res	
Erg4p	C-24(28) sterol reductase, catalyzes the final step in ergosterol biosynthesis, integral endoplasmic reticulum protein	X			Figure 2.13A
Ncp1p	NADP-cytochrome P450 reductase, involved in ergosterol biosynthesis, localized to the endoplasmic reticulum	X			Figure 2.13B
Nsg1p	Protein involved in regulation of sterol biosynthesis, involved in the catalysis of the rate-limiting step, localized to the endoplasmic reticulum	X			Not shown
Hmg2p	Involved in the catalysis of the rate-limiting step of ergosterol biosynthesis, localized to the endoplasmic reticulum	X			Not shown
Sec63p	Subunit of Sec63 complex, involved in protein targeting and import into the endoplasmic reticulum	X	X		Figure 2.13D
Sec61p	Subunit of the Sec61 complex, involved in protein import into the endoplasmic reticulum and transport of misfolded proteins out of the ER	X			Not shown
SS-GFP-HDEL	Motif in proteins that are destined for retention in the endoplasmic reticulum	X	X	X	Figure 2.14A,B
Hmg1p	Involved in the catalysis of the rate-limiting step of sterol biosynthesis, localized to the endoplasmic reticulum	X			Figure 2.13C

Table 2.9. Markers used to visualize the Golgi apparatus. The markers used to visualize the Golgi apparatus, and their cellular functions are listed below.

Marker Protein or Stain	Marker Function	Type(s) of Microscopy Performed			Image Location
		Fixed	Live	High-res	
Sec7p	Guanine nucleotide exchange factor (GEF) for ADP ribosylation factors involved in proliferation of the Golgi, localized to Golgi-associated	X	X	X	Figure 2.15A,C
Och1p	Mannosyltransferase of the cis-Golgi	X			Not shown
Ric1p	Involved in retrograde transport to the cis-Golgi network, localized to the Golgi membrane	X			Not shown
Rgp1p	Subunit of a Golgi membrane exchange factor that catalyzes nucleotide exchange on Ypt6p	X			Not shown
Vrg4p	Golgi GDP-mannose transporter, regulates Golgi function and glycosylation	X	X	X	Figure 2.15B,D

Table 2.10. Markers and stain used to visualize lipid particles. The markers and stain used to visualize lipid particles, and their cellular functions are listed below.

Marker Protein or Stain	Marker Function	Type(s) of Microscopy Performed			Image Location
		Fixed	Live	High-res	
Erg6p	Delta(24)-sterol C-methyltransferase, involved in ergosterol biosynthesis, localized to lipid particles	X	X	X	Figure 2.16A,B Figure 2.17A
Erg7p	Lanosterol synthase, involved in ergosterol biosynthesis, localized to the endoplasmic reticulum and lipid particles	X	X		Figure 2.16C
Nile Red	Lipophilic dye for intracellular lipid dropets			X	Figure 2.16D Figure 2.17A

Table 2.11. Markers used to visualize eisosomes. The markers used to visualize the eisosomes, and their cellular functions are listed below.

Marker Protein or Stain	Marker Function	Type(s) of Microscopy Performed			Image Location
		Fixed	Live	High-res	
Pil1p	Primary component of eisosomes		X	X	Figure 2.18A,B
Sur7p	Integral plasma membrane protein, component of eisosomes		X	X	Figure 2.18C,D

Table 2.12. Markers used to visualize endosomes. The markers used to visualize the endosomes, and their cellular functions are listed below.

Marker Protein or Stain	Marker Function	Type(s) of Microscopy Performed			Image Location
		Fixed	Live	High-res	
Snf7p	Subunit of endosomal sorting complex required for transport III (ESCRT-III), involved in sorting of transmembrane proteins into multivesicular bodies, localized to endosomal membranes	X			Figure 2.19C
Kex2p	Subtilisin-like protease, involved in the activation proproteins of the secretory pathway, localized to the trans-Golgi network	X	X		Figure 2.19D
Nhx1p	Na+/H+ and K+/H+ exchanger, required for intracellular sequestration of Na+ and K+ and for vacuolar fusion, localized to the vacuole and late endosome compartments	X	X		Figure 2.19B
Hse1p	Subunit of the endosomal Vps27/Hse1 complex (ESCRT-0), required for sorting membrane proteins for vacuolar degradation, localized to endosomes	X	X		Figure 2.19A

Table 2.13. Markers used to visualize the plasma membrane. The markers used to visualize the plasma membrane, and their cellular functions are listed below.

Marker Protein or Stain	Marker Function	Type(s) of Microscopy Performed			Image Location
		Fixed	Live	High-res	
Fet3p	Ferro-O2-oxidoreductase required for high-affinity iron uptake, integral plasma membrane protein	X			Not shown
Hxt2p	High-affinity glucose transporter, expression depends on glucose availability, integral plasma membrane protein	X			Not shown
Ylr413wp	Protein of unknown function, integral plasma membrane protein	X	X	X	Figure 2.20A,C
Ras2p	GTP-binding protein that regulates nitrogen starvation response, sporulation, and filamentous growth, localized to the plasma membrane	X			Not shown
Mrh1p	Protein of unknown function, similarity to Hsp30 and Yro2, integral plasma membrane protein	X	X	X	Figure 2.20B,D

Table 2.14. Summary of findings from the screen and from high-resolution microscopy. The findings from visualization of all major organelles and cellular substructures is listed below. These include the results from both the screens and from high-resolution microscopy where applicable.

Structure	Summary of the results from the screens and from high-resolution microscopy
Bud	Localizes to the bud at all ages.
Bud neck	Fixation can shift septin proteins away from the bud neck in an age-dependent manner. In live cells, the septin ring is always at bud neck. The bud neck can be widened when large, abnormally shaped buds are present.
Mirrotubule and microtubule-related structures	Most mircotubule-related protein markers were faint. The spindle marked with GFP-Tub1p was abnormal in a small population of old cells. GFP-Tub1p phenotypes are discussed in Ch. 3.
Actin and actin-related structures	Filaments were more prominent in some old cells with age. The protein marker for the actomyosin ring remained localized to the bud neck with age. Cortical actin patch localization remained at areas of polarized growth. Sac6p and phalloidin staining showed increased cortical actin patch abundance and intensity. Cap1p and Cap2p only showed an increase in cortical actin patch abundance with age. High-resolution microscopy showed that the number of cortical actin patches increased with replicative age, but in proportion to the increase in surface area with age. The abundance of Sac6p-GFP at cortical actin patches increased 2-fold with age. Phalloidin staining actin filaments were reduced in old cells.
Chromosomal mass and nuclear rim	These markers showed that the nucleus enlarged when the cell enlarged with replicative age.
COPI transport vesicles	The number of vesicles appeared to be increased in old cells. High-resolution microscopy showed that total Sec21p-GFP fluorescence was increased in old cells, but in proportion to cell volume. Total fluorescence was used as a proxy for vesicles.
COPII tranport vesicles	The number of vesicles appeared to be increased in old cells. High-resolution microscopy showed that total Sec31p-GFP fluoresence was increased in old cells, but in proportion to cell volume. Total fluorescence was used as a proxy for vesicles.
Endoplasmic reticulum	Localization of some ER markers lost at time 24 hours. Perinuclear ER enlarges with age with the enlargement of the nucleus. Possible increase in ER membrane and lumen volume with age. By high-resolution microscopy, the volume of the ER lumen, as measured using SS-GFP-HDEL fluorescence as a threshold, did not increase with replicative age.
Golgi	Total Golgi appears to increase with replicative age. High-resolution microscopy showed that Sec7p-GFP and Vrg4p-GFP fluorescence increased with age, but in proportion to the increase in cell volume.
Lipid droplets	Erg6p-GFP marked lipid particles increased in number with age, whereas Erg7p-GFP marked structures did not. High-resolution microscopy revealed that Nile Red staining lipid particles increased with age. The total amount of Erg6p-GFP also increased with age. Both increased in proportion to the increase in cell volume. Erg6p and Nile Red did not always colocalize.
Eisosomes	High-resolution microscopy revealed that Sur7p-GFP foci increased in intensity 1.6-fold with age, whereas Pil1p-GFP foci did not increase.
Endosomes	Number of endosomes appears to increase with replicative age. Increased GFP signal in vacuoles of old Kex2p-GFP cells.
Plasma membrane	Plasma membrane proteins remain localized to the plasma membrane with age. Mrh1p-GFP abundance at the plasma membrane increases as a function of replicative age. By high-resolution microscopy, the point intensity of Mrh1p-GFP at the plasma membrane increased 1.8-fold with age. Ylr413wp-GFP point intensity remained constant with age.

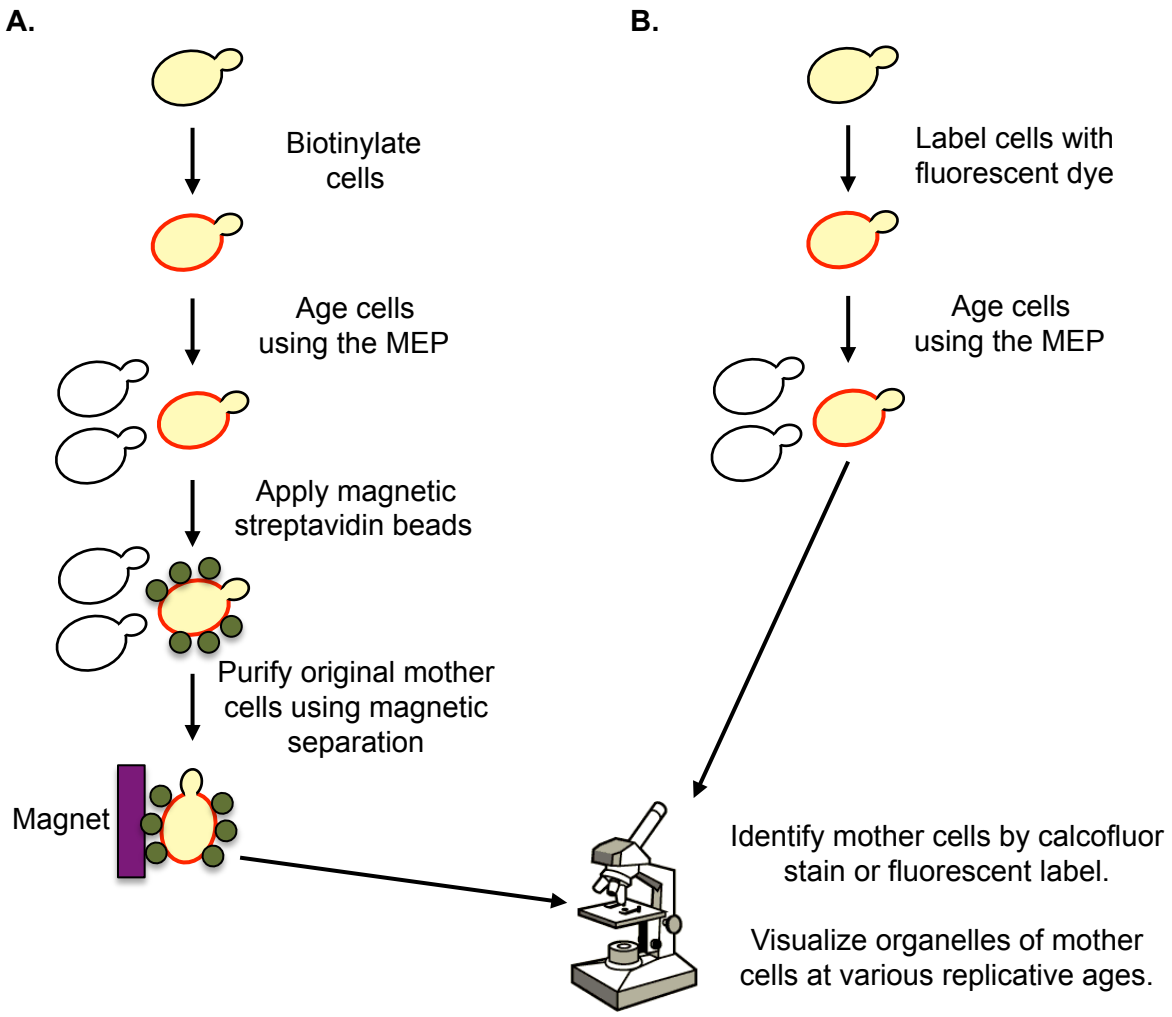

Figure 2.1. Schematic drawing of two methods used to acquire and/or identify replicatively aging mother cells for fluorescence microscopy. (A) Mother cells can be further purified from a mixed population containing arrested daughter cells by magnetic bead separation. Biotin is covalently cross-linked to the cell walls of an initial population of mother cells, which are subsequently cultured in liquid using the MEP. Cells are harvested for purification at timepoints that correspond to various replicative ages. Magnetic microbeads coated with streptavidin are used to bind and recover the original population of aged biotinylated mother cells using magnetic separation columns. This method can be used for either fixed or live cells. Purified cells are stained with calcofluor to allow identification of mother cells and bud scar quantitation (determination of replicative age) with fluorescence microscopy. (B) Mother cells can be identified throughout the aging process following covalent reactions with fluorescent dyes. Fluorescent moieties, such as rhodamine, can be covalently attached to the cell walls of an initial population of mother cells. These cells are subsequently cultured in liquid using the MEP. Cells are harvested at timepoints that correspond to various replicative ages. The original mother cells can be identified by fluorescence microscopy. The replicative age of each cell can be determined as bud scars appear as voids on the cell wall. This method can be used for either fixed or live cells.

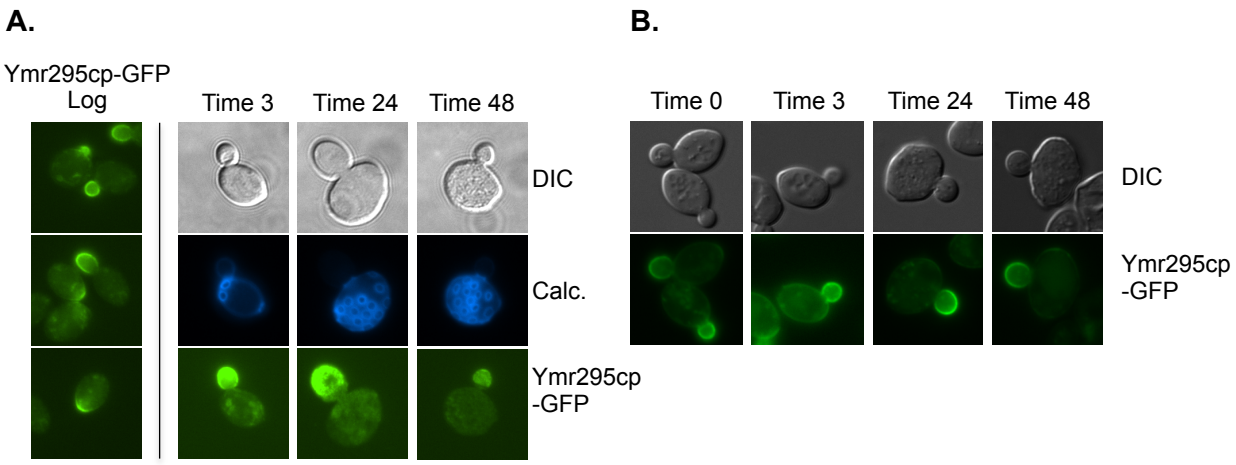

Figure 2.2. The bud-specific marker protein Ymr295cp-GFP is localized to the bud throughout replicative aging. Log-phase cells were used to verify expected subcellular localization of chromosomally tagged marker proteins prior to MEP induction and aging. Fluorescence microscopy was used to identify mother cells, determine the cell's replicative age, and to visualize the marker protein of interest. Cellular substructures were monitored for changes in localization, number, size, position, and intensity at various replicative ages. 10-20 cells were visualized at each timepoint. Representative images for each timepoint are shown in all figures. Timepoints are shown in hours, and approximately correspond to: log = ~1-2 divisions, time 0 hours = ~2-3 divisions, time 3 hours = ~4-7 divisions, time 24 hours = ~16-22 divisions, time 48 hours = 28+ divisions. Time 48 hours corresponds to the median lifespan of the strain. DIC, differential interference contrast. Calc, calcofluor. (A) Ymr295cp-GFP localization to the bud was not observed to change with replicative age in fixed cells. Cells expressing Ymr295cp-GFP were biotinylated, aged using the MEP, harvested at the indicated timepoints, fixed, purified using magnetic bead separation, and visualized using fluorescence microscopy. (B) Ymr295cp-GFP localization to the bud was not observed to change with replicative age in live cells. Cells expressing Ymr295cp-GFP were covalently labeled with rhodamine, aged using the MEP, and visualized using fluorescence microscopy at the indicated timepoints. Cell wall fluorescence represents emission bleed-through of the rhodamine label.

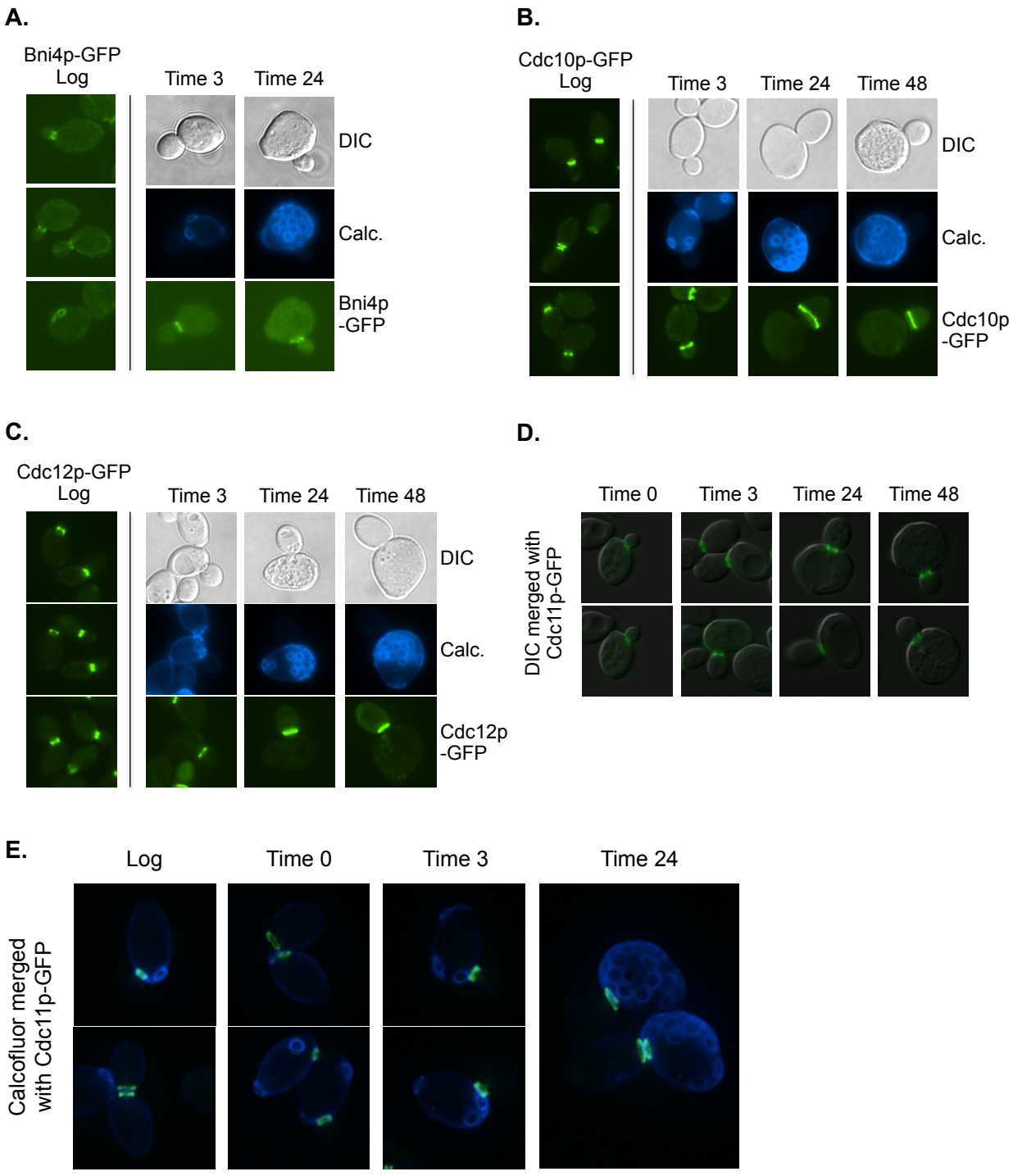

Figure 2.3. The septin ring remains localized at the bud neck throughout replicative aging. Cells expressing chromosomally tagged Bni4p-GFP, Cdc10p-GFP, Cdc12p-GFP, and Cdc11p-GFP were aged and analyzed as described in Figure 2.2. The septin ring as marked by (A) Bni4p-GFP, (B) Cdc10p-GFP, and (C) Cdc12p-GFP, were visualized in fixed and purified mother cells at the indicated timepoints. The shift of the septin ring into the bud is an artifact of fixation with paraformaldehyde diluted in water. (D) The septin ring marked by Cdc11p-GFP was visualized in live rhodamine-labeled mother cells at the indicated timepoints. (E) Cdc11p-GFP expressing cells were aged, harvested at the indicated timepoints, fixed, and subjected to high-resolution microscopy. Images were acquired at 0.25 μm intervals, deconvolved, and shown here as maximum intensity projections.

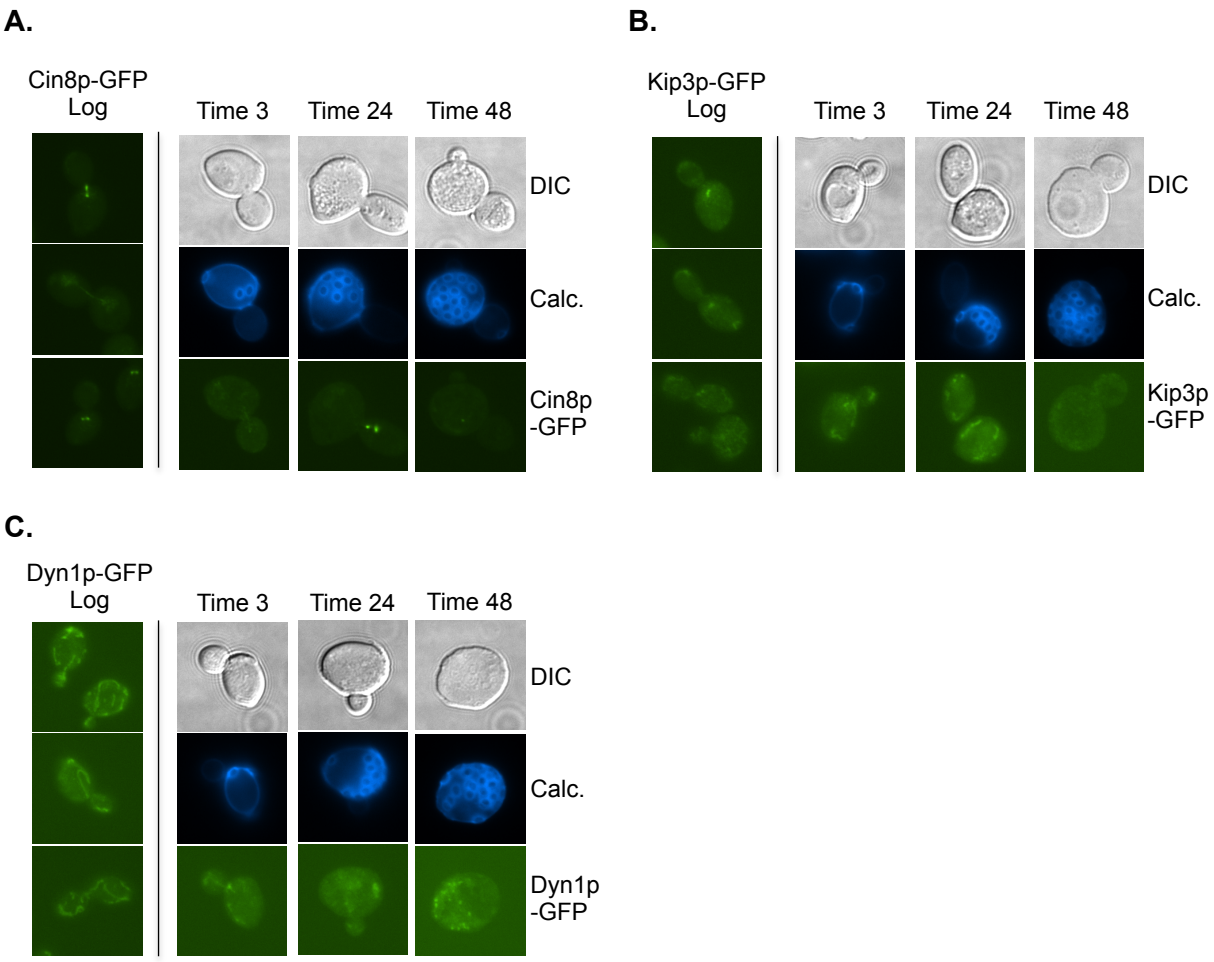

Figure 2.4. Microtubule-related structures were too faint to detect significant changes in aging cells. Cells expressing chromosomally tagged Cin8p-GFP, Kip3p-GFP, and Dyn1p-GFP were aged and analyzed as described in Figure 2.2. (A) Cin8p-GFP, (B) Kip3p-GFP, and (C) Dyn1p-GFP cells were biotinylated, aged with the MEP, fixed, purified, and visualized at the indicated timepoints.

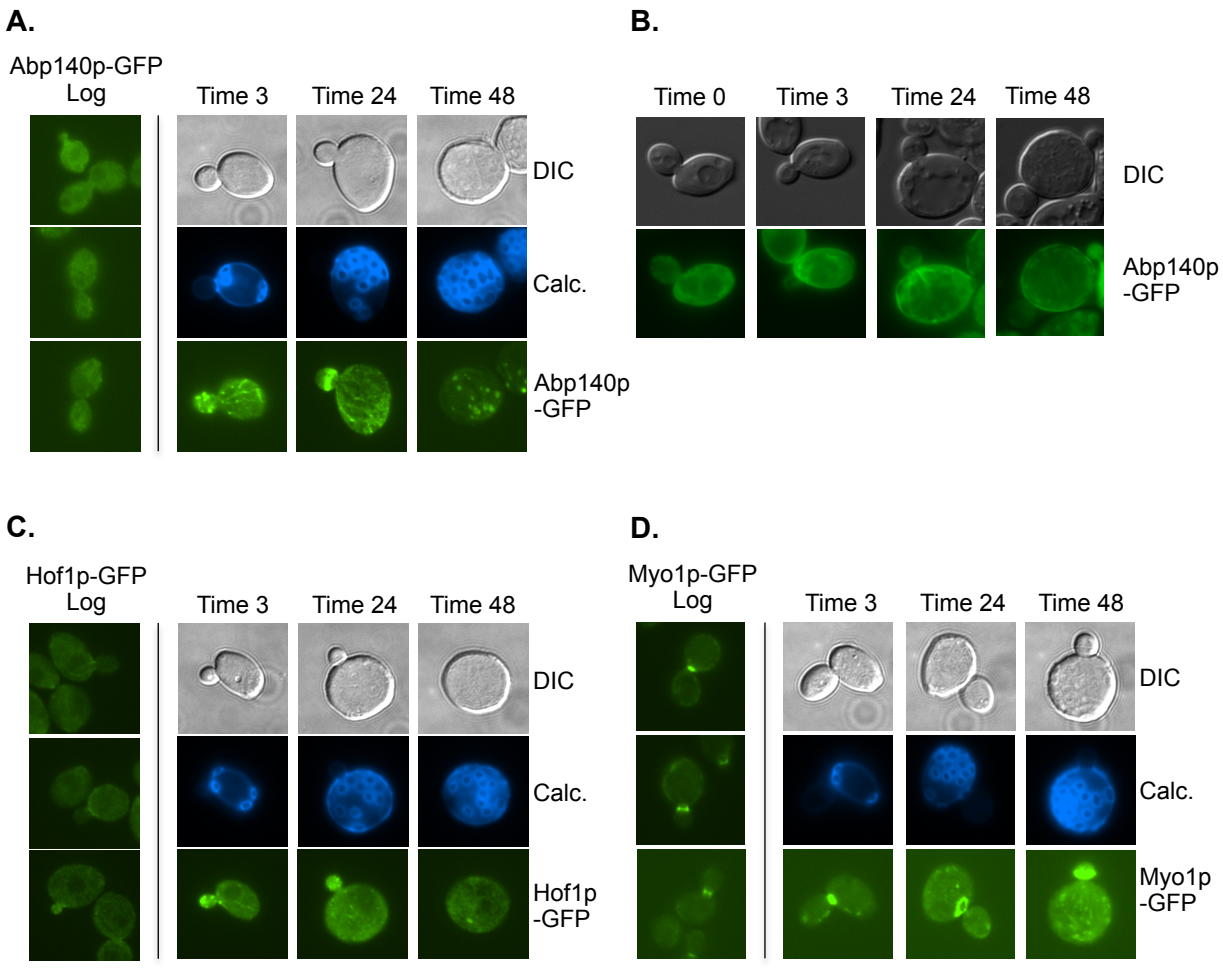

Figure 2.5. Actin structures marked by Abp140p-GFP, Hof1p-GFP, and Myo1p-GFP did not exhibit significant changes in localization or intensity with replicative age. Cells expressing chromosomally tagged Abp140p-GFP, Hof1p-GFP, and Myo1p-GFP were treated as in Figure 2.2. DIC, differential interference contrast. Calc, calcofluor. (A and B) Abp140p-GFP localization to cortical actin patches and filamentous actin was unchanged at the indicated timepoints in (A) purified fixed cells, and (B) rhodamine-labeled live cells. Cortical actin patches are predominantly found in the bud, and actin cables run along the mother-bud axis at all replicative ages. (C) Hof1p-GFP localization to the bud and bud neck was unchanged at all indicated timepoints in purified fixed cells. (D) Myo1p-GFP localized to the actomyosin ring at the bud neck at all timepoints in purified fixed cells. The actomyosin ring as observed with Myo1p-GFP is shifted slightly into the bud at time 48 hours. This shift is an artifact of fixation of cells with paraformaldehyde diluted in water, and is only apparent in older time 24 and 48 hour cells.

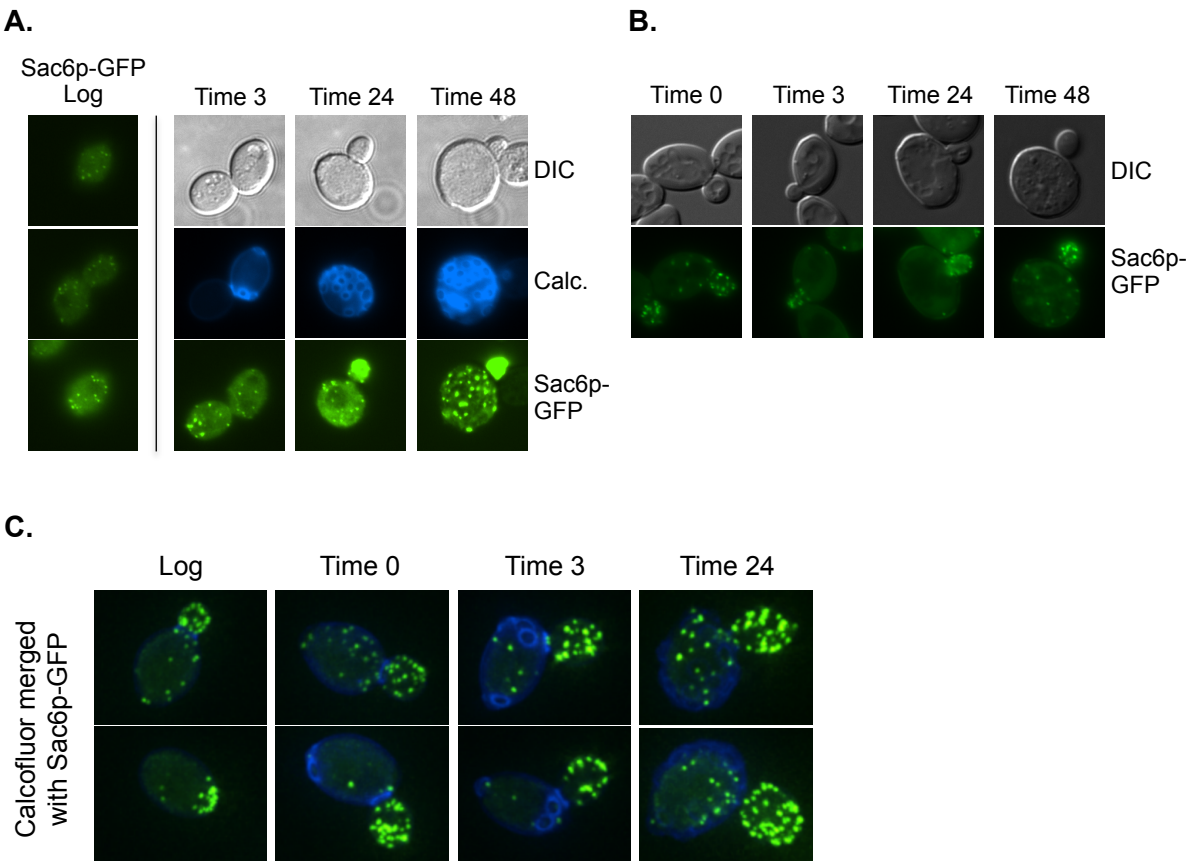

D.

Sac6p-GFP cortical actin patch density (foci/μm^2) Time 0 and 3 hours	Sac6p-GFP cortical actin patch density (foci/μm^2) Time 24 hours	Old/young Cortical actin patch intensity Sac6p-GFP
0.2	0.2	2.0

Figure 2.6. Sac6p-GFP marked cortical actin patches increased in number and intensity with replicative age. Cells expressing chromosomally tagged Sac6p-GFP were aged and analyzed as described in Figure 2.2. (A and B) Sac6p-GFP localized to cortical actin patches in (A) purified fixed cells, and (B) rhodamine-labeled live cells, at all replicative ages. Sac6p-GFP patches appeared increased in both number and intensity at time 24 and 48 hours. (C) Sac6p-GFP cells were biotinylated, aged, fixed, purified, and subjected to high-resolution microscopy. Images were acquired at 0.25 μm intervals, deconvolved, and shown here as maximum intensity projections. The number and intensity of foci, as well as the dimensions of each cell, were quantitated using Volocity software. (D) Quantification of Sac6-GFP foci number and intensity in young (time 0 and 3 hours) and old (time 24 hours) cells with and without normalization to cell surface area.

A.

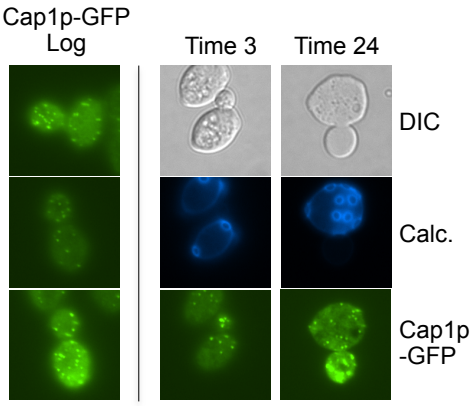

B.

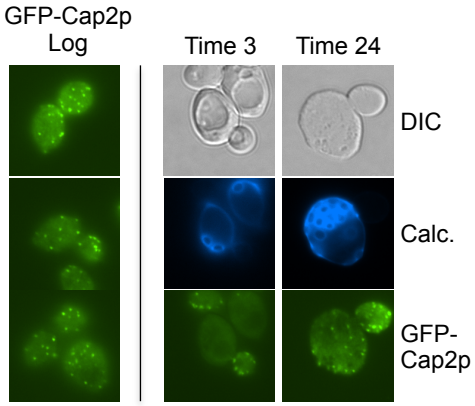

C.

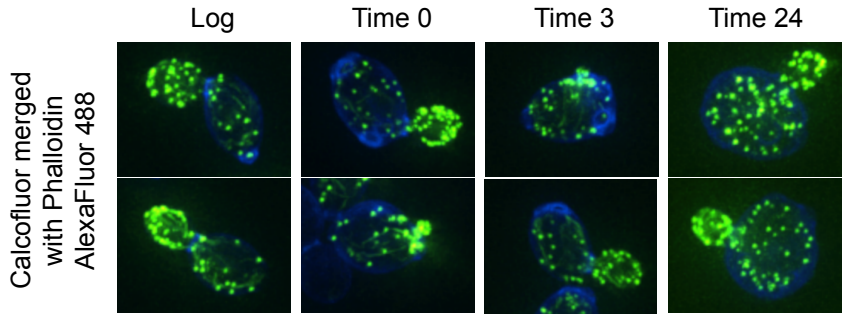

D.

Phalloidin cortical actin patch density (foci/μm^2) Time 0 and 3 hours	Phalloidin cortical actin patch density (foci/μm^2) Time 24 hours
0.3	0.3

Figure 2.7. Cortical actin patches marked by Cap1p-GFP, Cap2p-GFP, and Phalloidin Alexa Fluor 488 increase in number with replicative age. Untagged cells and cells expressing chromosomally tagged Cap1p-GFP and GFP-Cap2p were aged and analyzed as described in Figure 2.2. The number of cortical actin patches in the mother cells increased with replicative age as seen with both (A) Cap1p-GFP and (B) GFP-Cap2p. (C) Untagged cells were aged, harvested at the indicated timepoints, fixed, permeabilized, stained with Phalloidin Alexa Fluor 488, and subjected to high-resolution microscopy. Images were acquired at 0.25 μm intervals, deconvolved, and shown here as maximum intensity projections. The number of foci and the dimensions of the corresponding cell were determined using Volocity software. (D) Quantification of foci number in young (time 0 and 3 hours) and old (time 24 hours) cells with and without normalization to cell surface area.

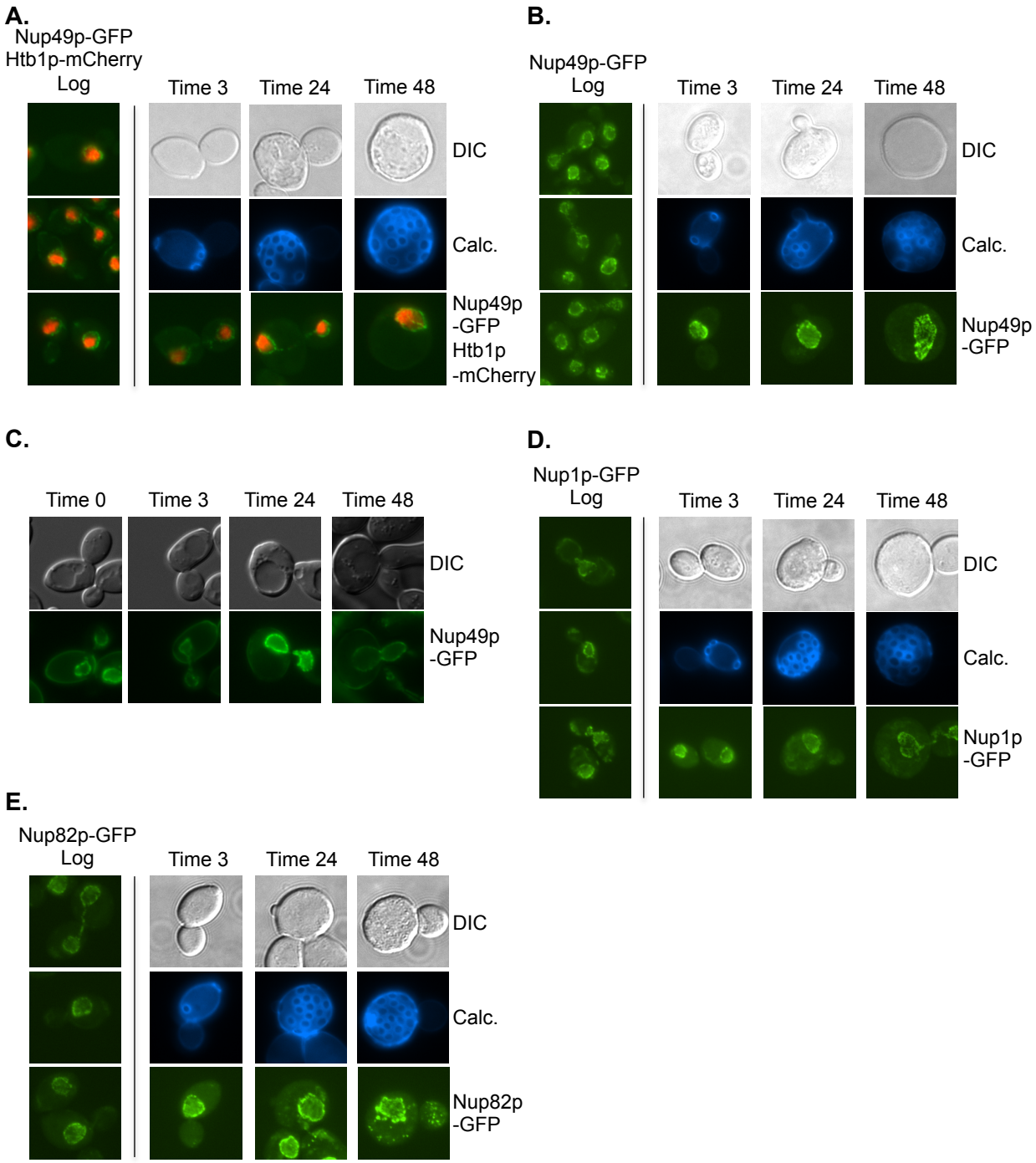

Figure 2.8. The nucleus becomes enlarged in replicatively aged cells. Cells expressing chromosomally tagged Nup49p-GFP and Htb1p-mCherry (hemizygous tags), Nup49p-GFP, Nup1p-GFP, and Nup82p-GFP were aged and analyzed as described in Figure 2.2. The nuclear envelope and chromosomes as marked by (A) Nup49p-GFP and Htb1p-mCherry, was visualized in fixed and purified mother cells at the indicated timepoints. The nuclear envelope as marked by Nup49p-GFP was visualized in (B) fixed and purified mother cells and (C) live rhodamine-labeled cells. The nuclear rim as marked by (D) Nup1p-GFP and (E) Nup82p-GFP was visualized in fixed and purified mother cells. All nuclear markers show increased nuclear size in cells of advanced replicative age (time 24 and 48 hours).

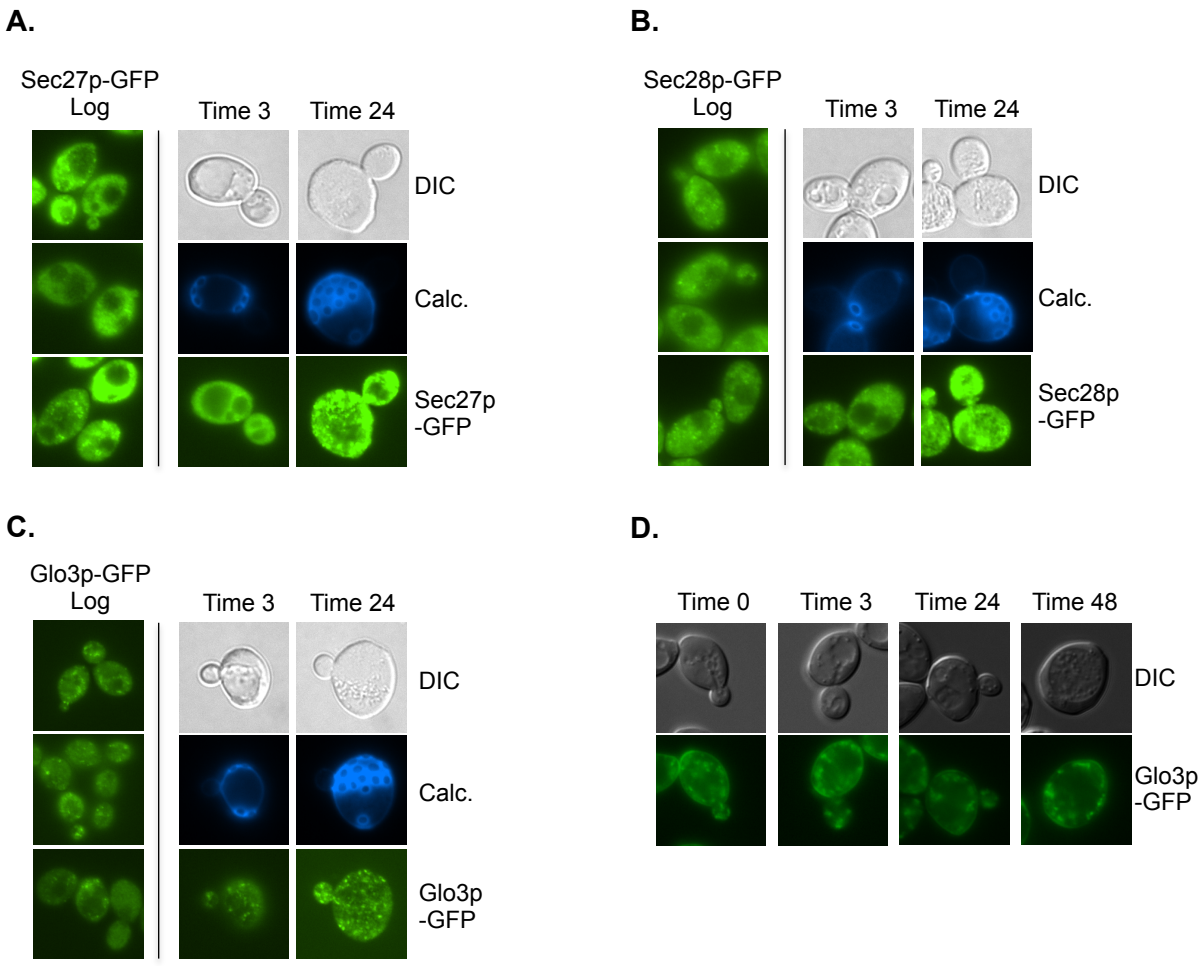

Figure 2.9. Additional COPI transport vesicle markers exhibit an increase in COPI vesicle number with replicative age. Cells expressing chromosomally tagged Sec27p-GFP, Sec28p-GFP, and Glo3p-GFP were aged and analyzed as described in Figure 2.2. COPI transport vesicles as marked by (A) Sec27p-GFP, (B) Sec28p-GFP, and (C) Glo3p-GFP were visualized in fixed and purified cells at the indicated timepoints. (D) Glo3p-GFP expressing cells were labeled with rhodamine, aged, and visualized live at the indicated timepoints. All COPI transport vesicles markers suggest COPI vesicle number increases with replicative age.

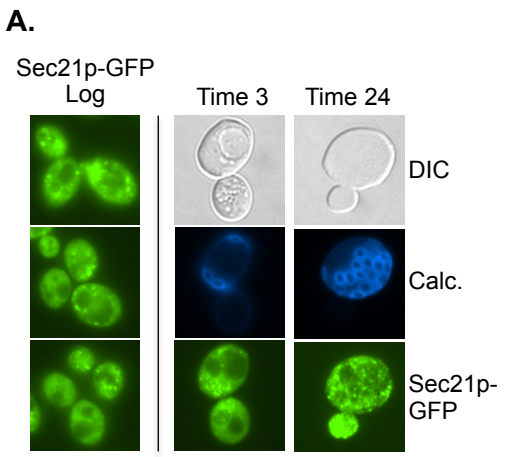

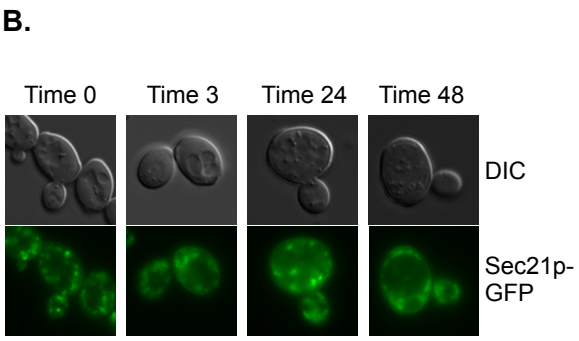

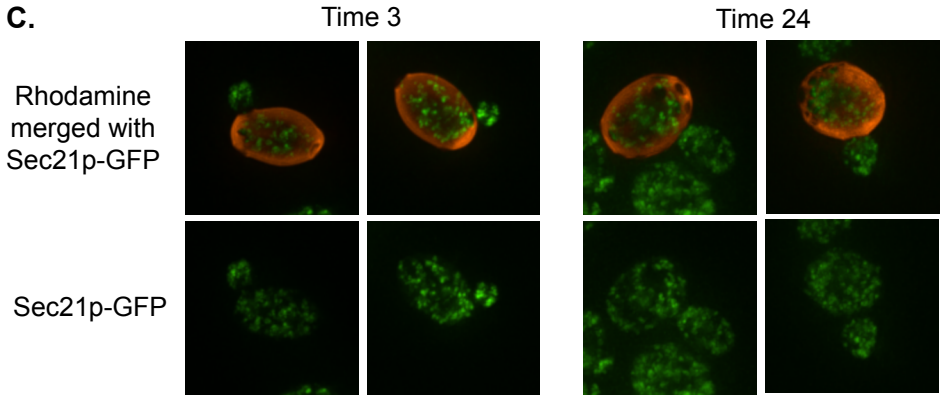

D.

Old/young Total fluorescence Sec21p-GFP	Old/young Cell volume-adjusted
1.2	0.7

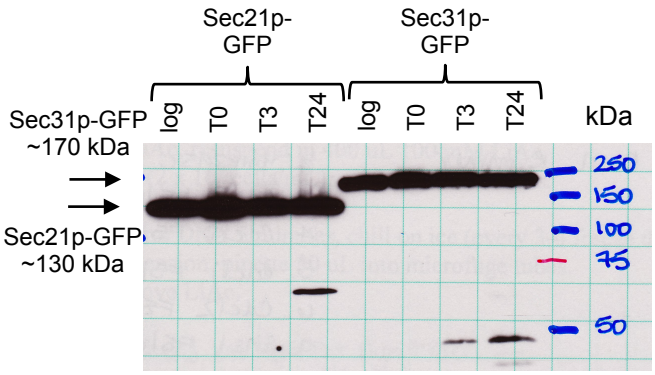

Figure 2.10. Sec21p-GFP marked COPI vesicles increase in number in proportion to the increase in cell volume with replicative age. Cells expressing chromosomally tagged Sec21p-GFP were aged and analyzed as described in Figure 2.2. COPI transport vesicles as marked by Sec21p-GFP were visualized in (A) fixed and purified and (B) live rhodamine-labeled cells at the indicated timepoints. (C) Sec21p-GFP expressing cells were labeled in rhodamine, harvested at time 3 and 24 hours, and subjected to high-resolution microscopy. Images were acquired at 0.25 μm intervals, deconvolved, and shown here as maximum intensity projections. (D) Quantification of total fluorescence in young (time 3 hours) and old (time 24 hours) cells, as well corresponding cell dimensions was accomplished using Volocity software. (E) Total protein was extracted from cells expressing Sec21p-GFP harvested prior to MEP induction, and at times 0, 3, and 24 hours of aging. Equal quantities of cell lysates from each timepoint were compared by Western bot analysis with an anti-GFP antibody.

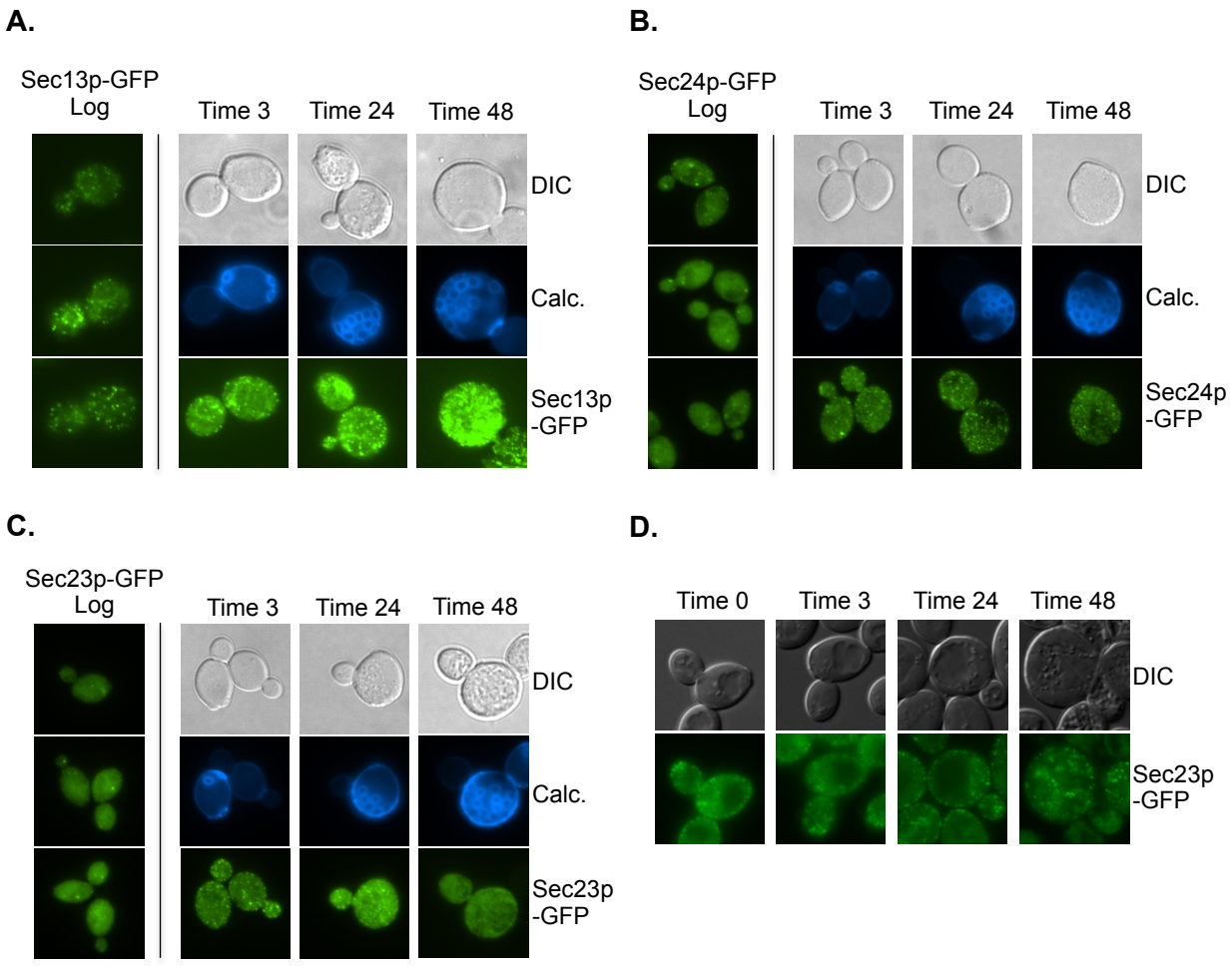

Figure 2.11. Additional COPII transport vesicle markers exhibit an increase in COPII vesicle number with replicative age. Cells expressing chromosomally tagged Sec13p-GFP, Sec23p-GFP, and Sec24p-GFP were aged and analyzed as described in Figure 2.2. COPII transport vesicles as marked by (A) Sec13p-GFP, (B) Sec24p-GFP, and (C) Sec23p-GFP were visualized in fixed and purified cells at the indicated timepoints. (D) Sec23p-GFP expressing cells were labeled with rhodamine, aged, and visualized live at the indicated timepoints. All COPII transport vesicles markers suggest COPII vesicle number increases with replicative age.

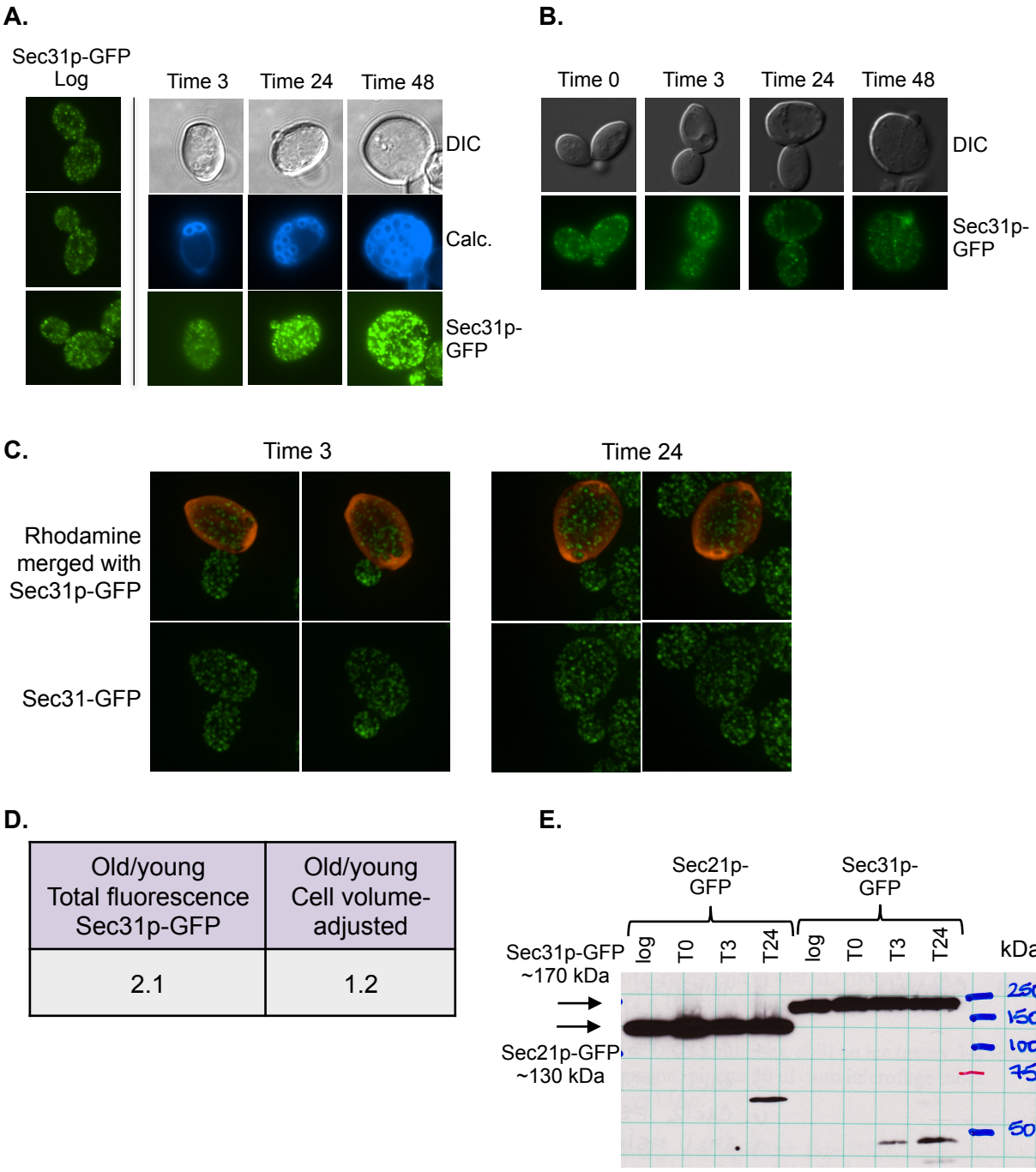

Figure 2.12. Sec31p-GFP marked COPII vesicles increase in number in proportion to the increase in cell volume with replicative age. Cells expressing chromosomally tagged Sec31p-GFP were aged and analyzed as described in Figure 2.2. COPII transport vesicles as marked by Sec31p-GFP were visualized in (A) fixed and purified and (B) live rhodamine-labeled cells at the indicated timepoints. (C) Sec31p-GFP expressing cells were labeled in rhodamine, harvested at time 3 and 24 hours, and subjected to high-resolution microscopy. Images were acquired at 0.25 μm intervals, deconvolved, and shown here as maximum intensity projections. (D) Quantification of total fluorescence in young (time 3 hours) and old (time 24 hours) cells, as well corresponding cell dimensions was accomplished using Volocity software. (E) Total protein was extracted from cells expressing Sec31p-GFP harvested prior to MEP induction, and at times 0, 3, and 24 hours of aging. Equal quantities of cell lysates from each timepoint were compared by Western bot analysis with an anti-GFP antibody.

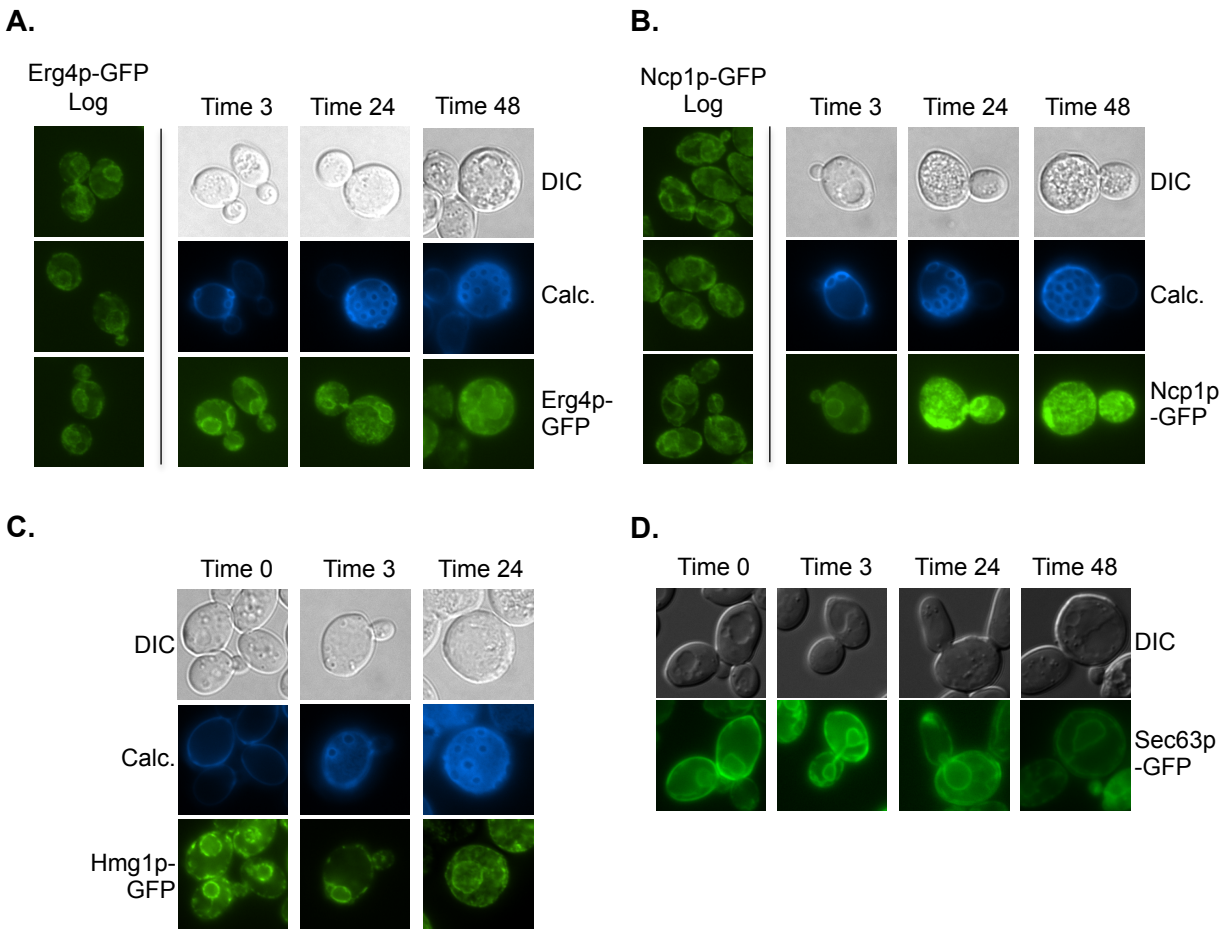

Figure 2.13. Additional endoplasmic reticulum protein markers show an increase in nuclear size with age, but do not reveal any consistent changes in ER morphology. Cells expressing chromosomally tagged Erg4p-GFP, Ncp1p-GFP, Hmg1p-GFP, and Sec63p-GFP were aged and analyzed as described in Figure 2.2. The ER marked by (A) Erg4p-GFP, (B) Ncp1p-GFP, (C) Hmg1p-GFP were visualized in fixed and purified mother cells at the indicated timepoints. (D) Sec63p-GFP expressing cells were labeled with rhodamine, aged, and visualized live at the indicated timepoints. All ER markers suggest that the nucleus increases in size with replicative age, however, no other consistent changes in ER morphology were observed.

A.

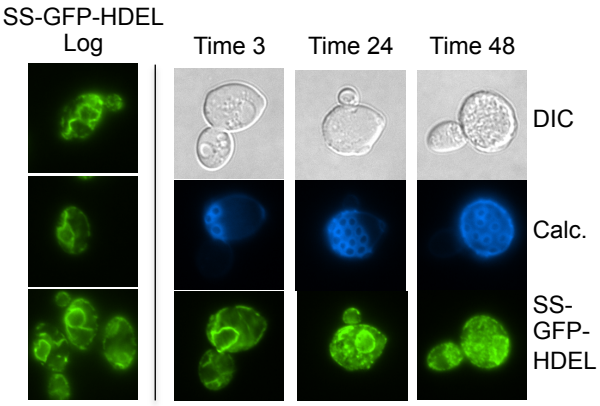

B.

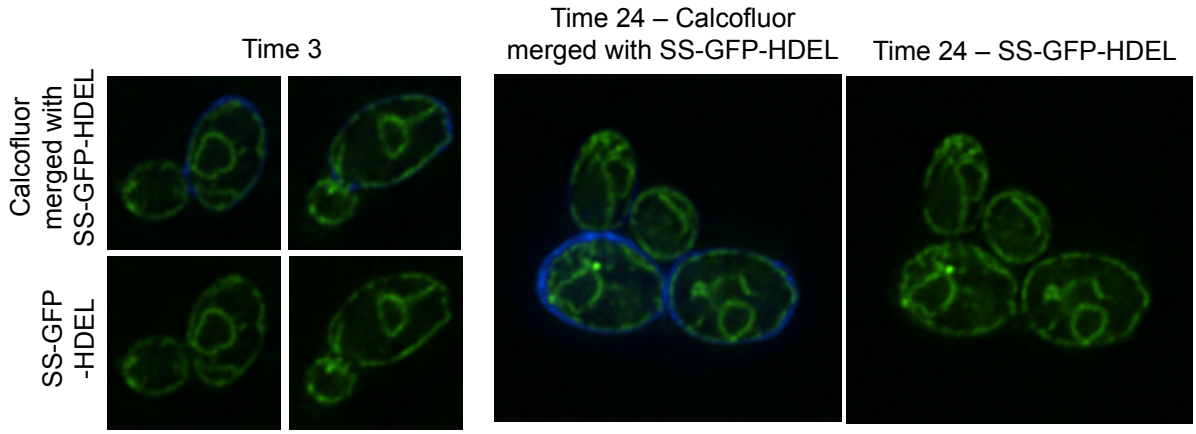

C.

Old/young Total ER volume ss-GFP-HDEL	Old/young Cell volume-adjusted
1.4	0.6

Figure 2.14. No age-associated changes in the endoplasmic reticulum were observed using a lumenal marker to visualize the ER. Cells were transformed with GFP fused to a N-terminal signal sequence and C-terminal ER retention sequence, ss-GFP-HDEL, at an ectopic gene poor site on Chromosome I. Cells expressing this construct were aged and analyzed as described in Figure 2.2. (A) Fixed and purified mother cells were visualized at the indicated timepoints. (B) Cells expressing ss-GFP-HDEL were aged, fixed, purified, and subjected to high-resolution microscopy. Young (time 3 hours) and old (time 24 hours) cells were mixed such that direct comparisons could be made between young and old cells in the same field. Images were acquired at 0.25 μm intervals and deconvolved for quantitation. Images shown here represent a single Z-section. (C) ER volume, as defined by ss-GFP-HDEL signal, as well as corresponding cell dimensions were determined using Volocity software. The ER volume increased with replicative age, but no more than would be expected by the age-associated increase in cell volume.

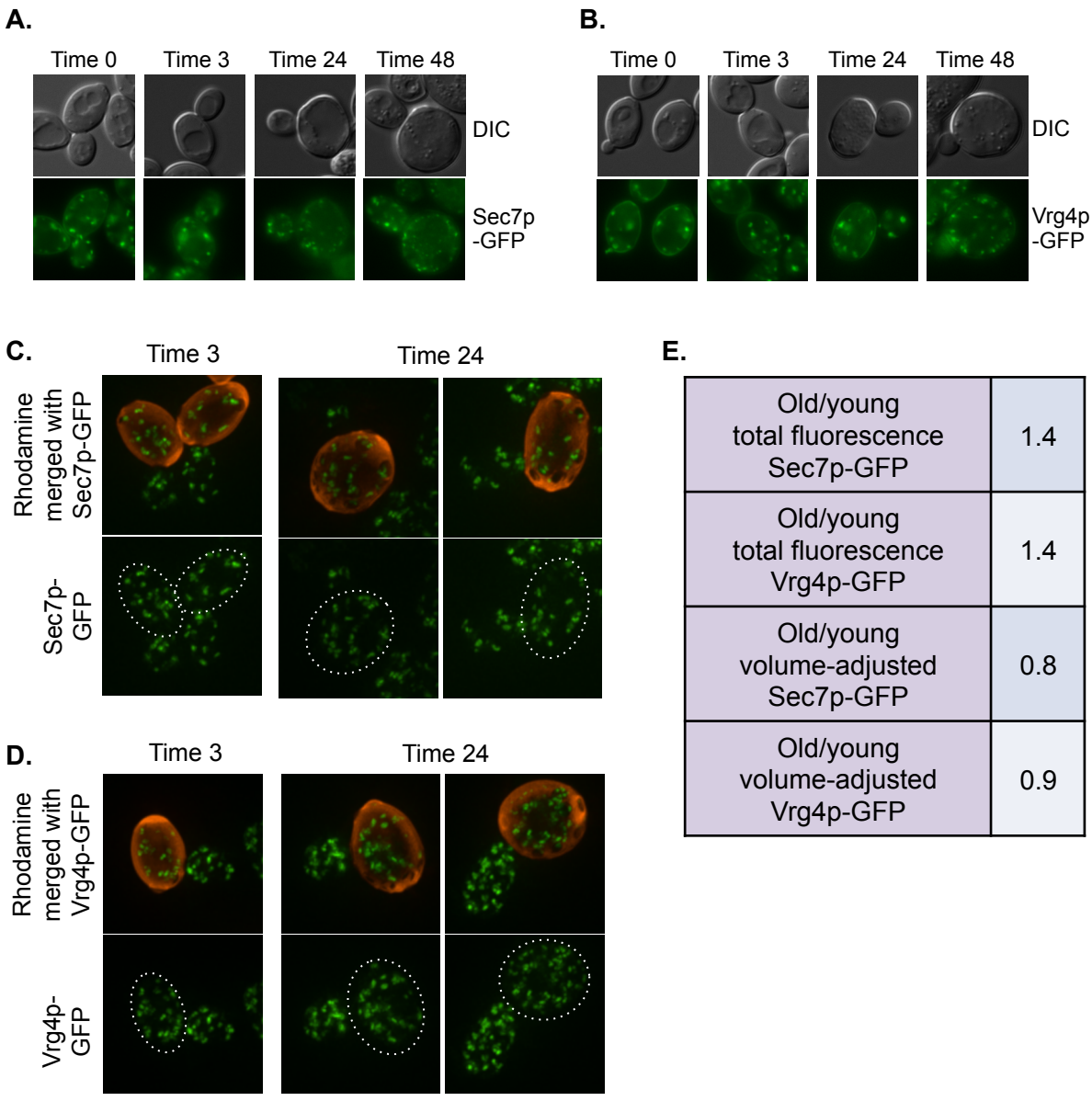

E.

Old/young total fluorescence Sec7p-GFP	1.4
Old/young total fluorescence Vrg4p-GFP	1.4
Old/young volume-adjusted Sec7p-GFP	0.8
Old/young volume-adjusted Vrg4p-GFP	0.9

Figure 2.15. The Golgi apparatus marked by Sec7p-GFP and Vrg4p-GFP increased in proportion to increased cell volume with replicative age. Cells expressing chromosomally tagged Sec7p-GFP and Vrg4p-GFP were aged and analyzed as described in Figure 2.2. The Golgi apparatus as marked by (A) Sec7p-GFP and (B) Vrg4p-GFP were visualized in rhodamine-labeled live using standard wide-field epifluorescence microscopy at the indicated timepoints. Rhodamine-labeled cells expressing (C) Sec7p-GFP and (D) Vrg4p-GFP were also subjected to high-resolution microscopy at times 3 and 24 hours. Images were acquired at 0.25 μm intervals, deconvolved, and shown here as maximum intensity projections. Young and old cells were mixed for microscopy to allow direct comparisons between young and old cells within a single field. Dotted white lines outline the mother cell. (E) Quantification of total fluorescence and corresponding cell dimensions were accomplished using Volocity software. The increase in total Sec7p-GFP and Vrg4p-GFP fluorescence with replicative age was proportional to the increase in cell volume with replicative age.

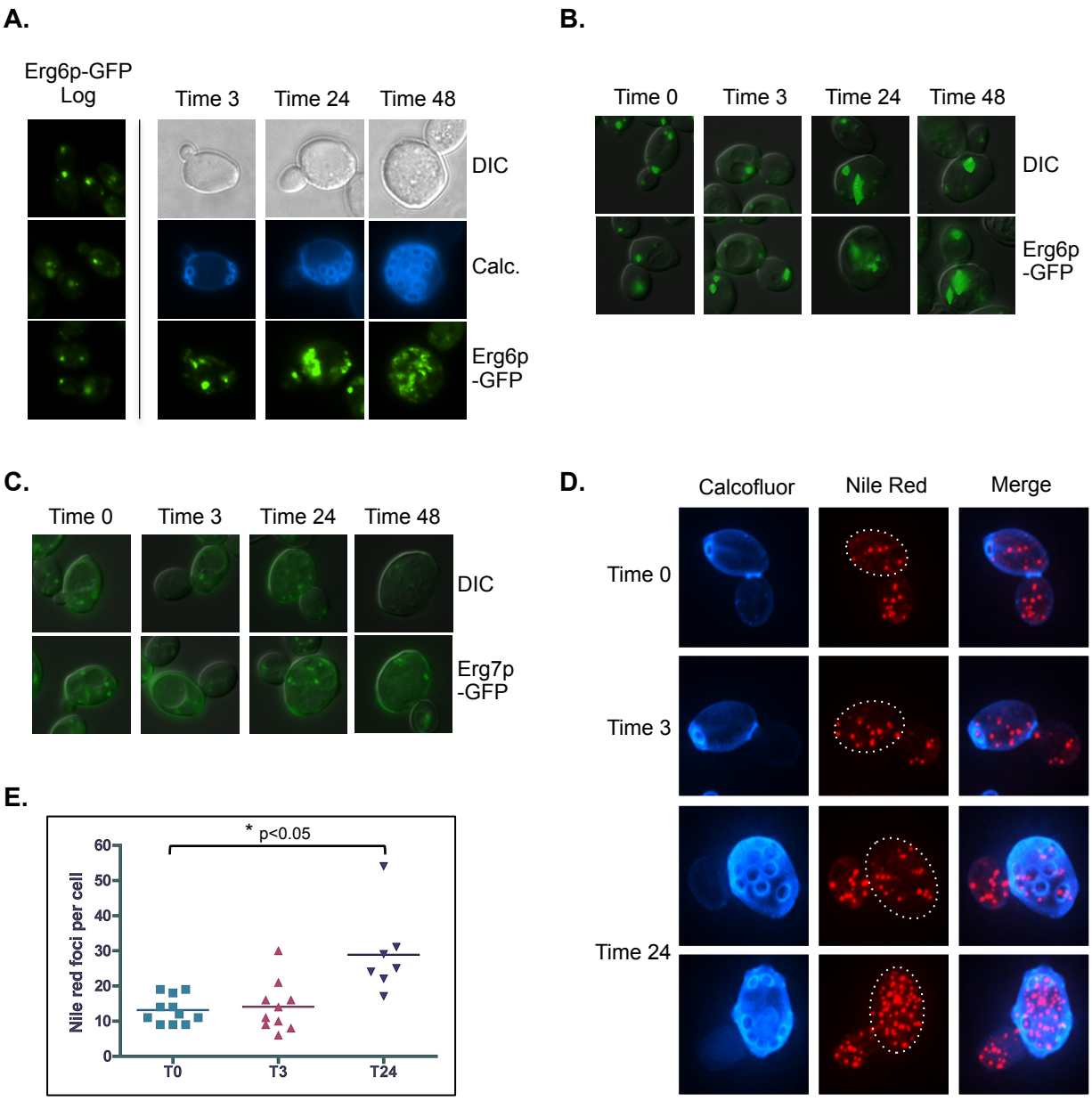

Figure 2.16. Lipid particles increase in size and/or number as a function of replicative age. Cells expressing chromosomally tagged Erg6p-GFP and Erg7p-GFP were aged and analyzed as described in Figure 2.2. Lipid particles marked by Erg6p-GFP and Nile Red increased in size and number, respectively, with replicative age. (A) Lipid particles as marked by Erg6p-GFP were visualized in fixed and purified mother cells at the timepoints indicated. Lipid particles as marked by (B) Erg6p-GFP and (C) Erg7p-GFP were visualized in rhodamine-labeled cells at the timepoints indicated. Structures containing Erg6p-GFP increased with replicative age, whereas structures containing Erg7p-GFP did not exhibit any increase. (D) Untagged cells were aged using the MEP, fixed, stained with the intracellular lipid dye Nile Red, and subjected to high-resolution microscopy at the indicated timepoints. Images were acquired at 0.25 μm intervals, deconvolved, and shown here as maximum intensity projections. Dotted white lines outline the mother cells. (E) Quantification of Nile Red stained lipid particle number was determined using Volocity software. The number of Nile Red containing foci per cell is plotted for each timepoint. An unpaired t-test with Welch's correction showed a significant ($p<0.05$) increase in the number of lipid particles per cell in young cells (time 0 hours) compared to old cells (time 24 hours).

A.

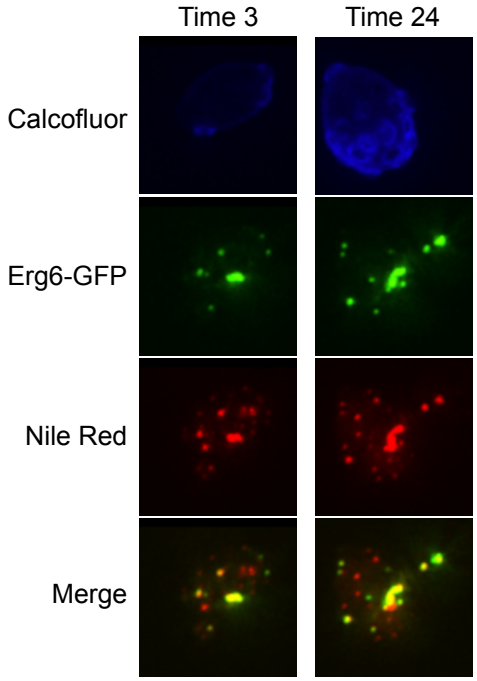

B.

Old/young total fluorescence Nile Red	Old/young total fluorescence Erg6-GFP	Old/young volume-adjusted Nile Red	Old/young volume-adjusted Erg6-GFP
1.9	1.9	1.1	1.2

Figure 2.17. Erg6p-GFP and Nile Red are not always colocalized in young and old cells, however quantities of both increased in proportion to the increase in cell volume with age. (A) Cells expressing chromosomally tagged Erg6p-GFP were biotinylated, aged with the MEP, harvested at time 3 hours and time 24 hours, fixed, and purified by magnetic bead separation. Purified time 3 and time 24 hour old Erg6p-GFP cells were stained with Nile Red and subjected to high-resolution microscopy. Images were acquired at 0.25 μm intervals, deconvolved, and shown here as maximum intensity projections. Structures that colocalize appear yellow in the merged images. (B) Quantification of Erg6p-GFP and Nile Red total fluorescence, as well as corresponding cell dimensions, were accomplished using Volocity software. Erg6p-GFP and Nile Red fluorescence was similarly increased in old cells (time 24 hours) compared to young cells (time 3 hours). This increase, however, was approximately proportional to the age-associated increase in cell volume.

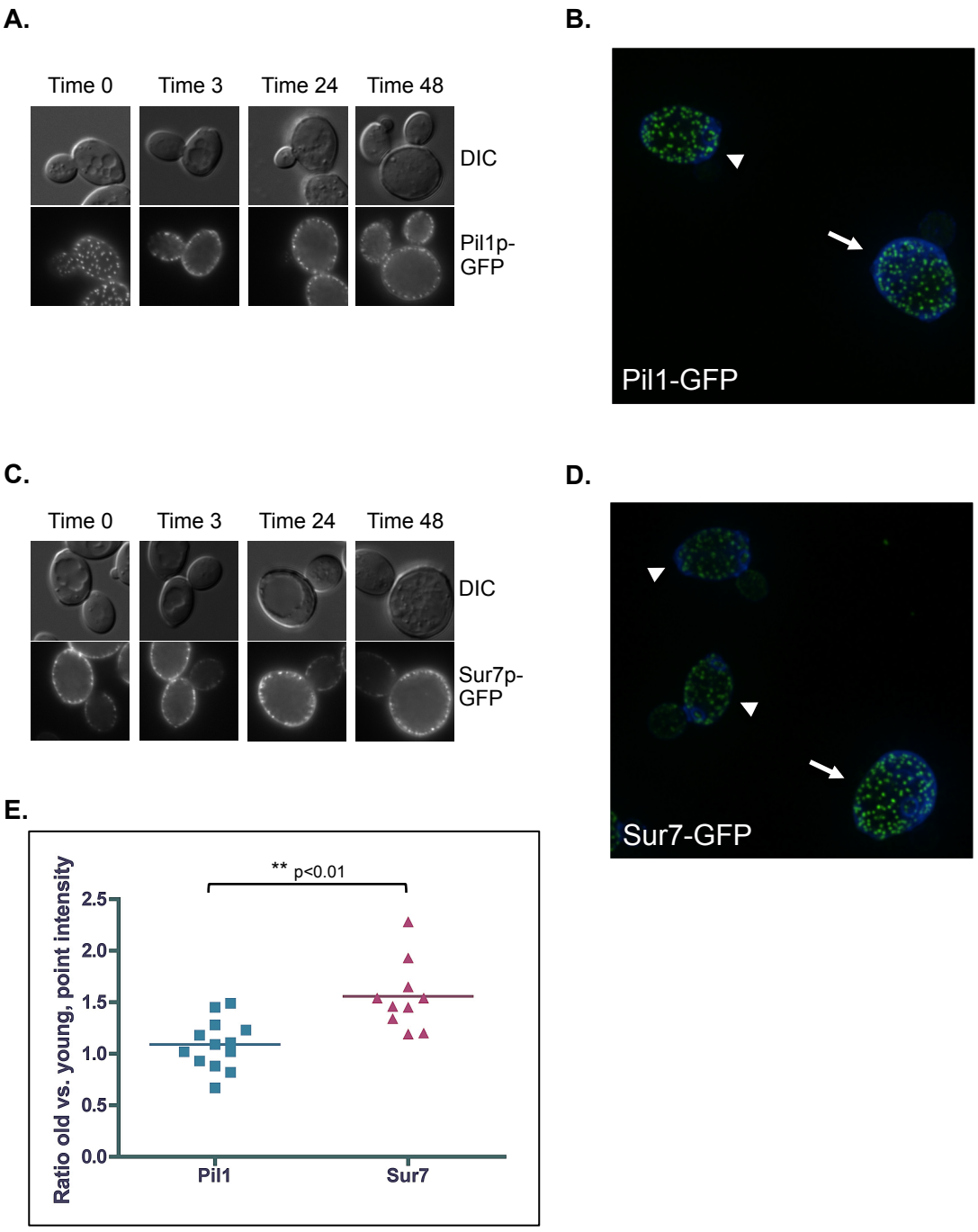

Figure 2.18. Integral membrane eisosome protein Sur7p-GFP increases in abundance as a function of replicative age. Cells expressing chromosomally tagged Pil1p-GFP and Sur7p-GFP were aged and analyzed as described in Figure 2.2. Eisosomes marked by (A) Pil1p-GFP and (C) Sur7p-GFP were visualized in live, rhodamine-labeled mother cells at the indicated timepoints. (B) Pil1p-GFP and (D) Sur7p-GFP expressing cells were aged, fixed, purified, and subjected to high-resolution microscopy. Young (time 3 hours, indicated by white arrowheads) and old (time 24 hours, indicated by white arrows) cells were mixed such that direct comparisons could be made between young and old cells in the same field. Images were acquired at 0.25 μm intervals, deconvolved, and shown here as maximum intensity projections (E) Quantification of Pil1p-GFP and Sur7p-GFP foci intensity in young and old cells was measured using Volocity software. The ratio of old compared to young Pil1p-GFP and Sur7p-GFP foci show a Sur7-specific age-associated increase in abundance with replicative age. An unpaired t-test with Welch's correction showed a very significant ($p<0.001$) difference between old and young intensity ratios between Pil1p-GFP and Sur7p-GFP.

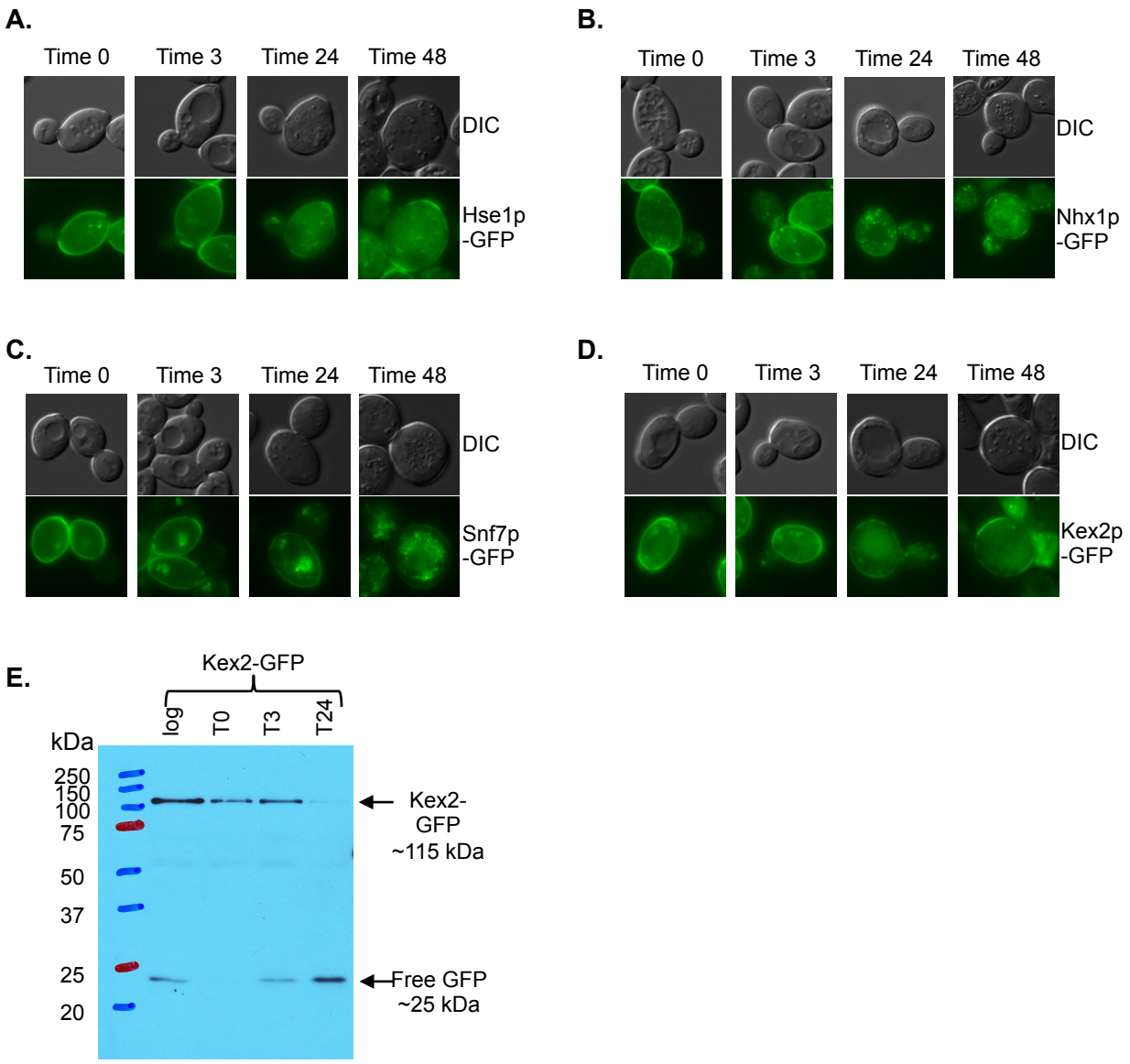

Figure 2.19. Endosome markers reveal multiple differences between young and old cells. Cells expressing chromosomally tagged Hse1p-GFP, Kex2p-GFP, Nhx1p-GFP, and Snf7p-GFP were aged and analyzed as described in Figure 2.2. Cells were labeled with rhodamine, aged, and visualized live at the indicated timepoints. (A) ESCRT-0 containing structures marked by Hse1p-GFP and (B) late endosomes marked by Nhx1p-GFP showed an age-associated increase in structure number. (C) ESCRT-III containing structures marked by Snf7p-GFP (fusion results in a dominant negative loss of function class E mutant blocked in the multivesicular body pathway) increased in number with replicative age. (D) Kex2p-GFP expressing cells showed increased amounts of GFP in the vacuole in older cells (time 24 and 48 hours). (E) Total protein was extracted from cells expressing Kex2p-GFP harvested prior to MEP induction, and at times 0, 3, and 24 hours of aging. Equal quantities of cell lysates from each timepoint were compared by Western bot analysis with an anti-GFP antibody. Increased quantities of free GFP are detected in lysates from old time 24 hour cells.

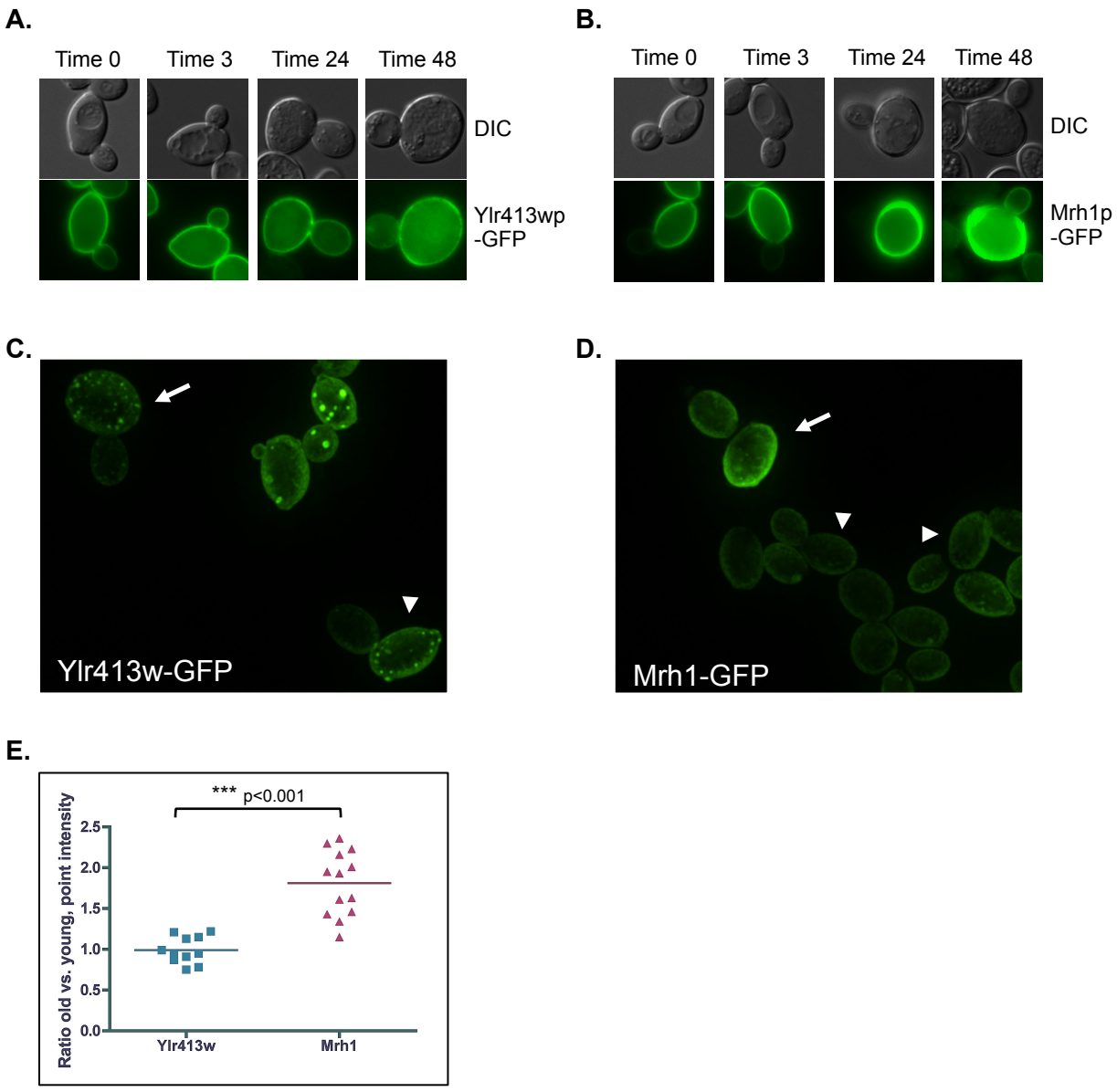

Figure 2.20. The plasma membrane protein Mrh1p-GFP increased in abundance as a function of replicative age. Cells expressing chromosomally tagged Ylr413wp-GFP and Mrh1p-GFP were aged and analyzed as described in Figure 2.2. The plasma membrane marked by (A) Ylr413wp-GFP and (B) Mrh1p-GFP were visualized in live, rhodamine-labeled mother cells at the indicated timepoints. Mrh1p-GFP abundance is increased in old cells (time 24 and 48 hours) compared to young cells (time 0 and 3 hours). (C) Ylr413wp-GFP and (D) Mrh1p-GFP expressing cells were aged, fixed, purified, and subjected to high-resolution microscopy. Young (time 3 hours, indicated by white arrowheads) and old (time 24 hours indicated by white arrows) cells were mixed such that direct comparisons could be made between young and old cells in the same field. Images were acquired at 0.25 μm intervals, deconvolved, and shown here as maximum intensity projections. (E) Quantification of Ylr413wp-GFP and Mrh1p-GFP intensity in young and old cells was measured using Volocity software. The ratio of old compared to young Ylr413wp-GFP and Mrh1p-GFP plasma membrane intensity showed a Mrh1p-specific age-associated increase in abundance with replicative age. An unpaired t-test with Welch's correction showed a very significant ($p<0.001$) difference between old and young intensity ratios between Ylr413wp-GFP and Mrh1p-GFP.

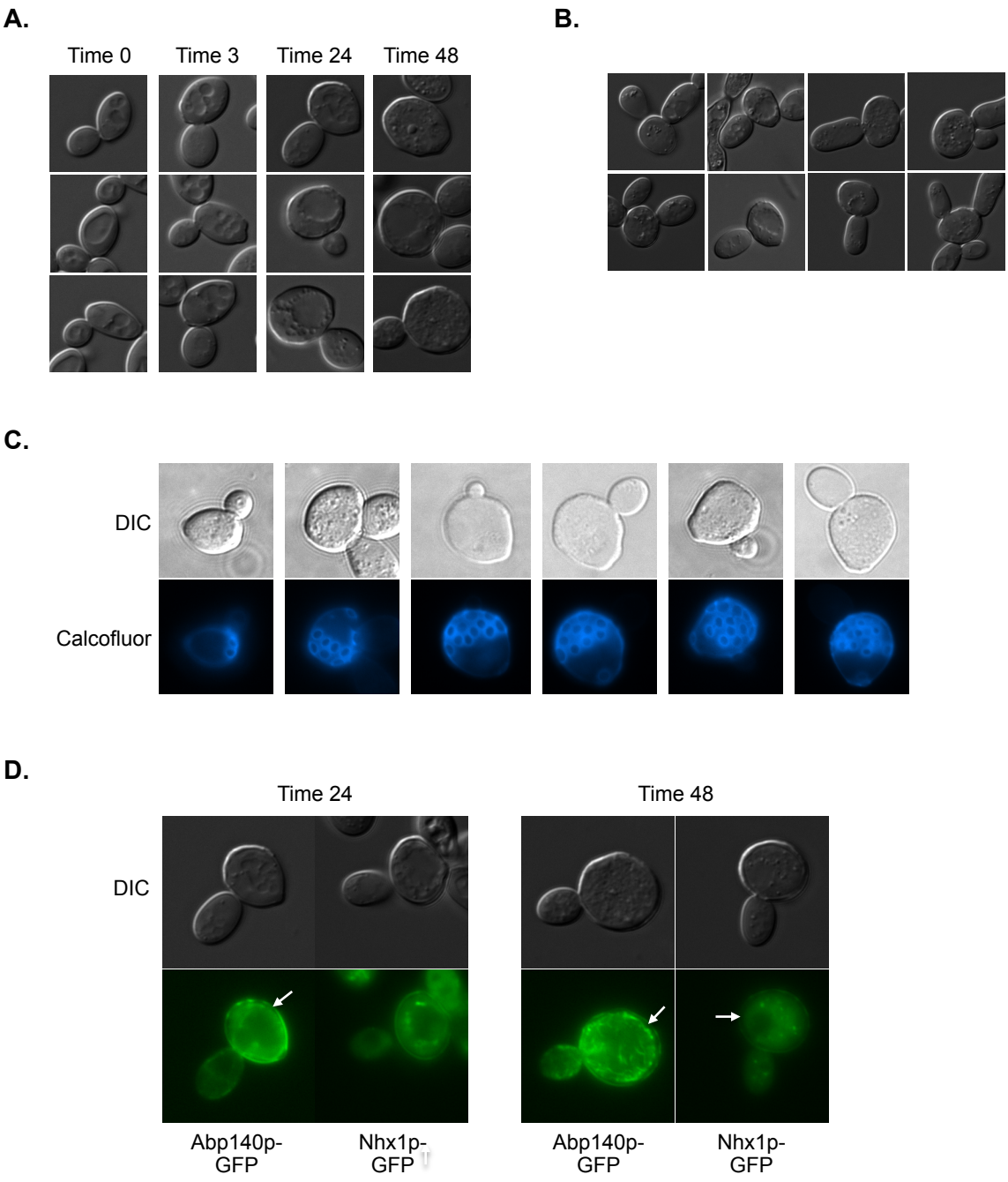

Figure 2.21. General age-associated cell morphological changes were observed in most cells independent of fluorescently tagged marker protein. (A) Cell size increased with replicative age. Cells were aged with the MEP and old cells were imaged at the indicated timepoints. Representative differential interference contrast (DIC) images are shown for each timepoint. (B) Old (time 24 and 48 hours) cells commonly had an abnormally shaped bud. (C) Cells possessing multiple bud scars were often teardrop shaped. The wider pole corresponded to the pole with more bud scars. (D) Old (time 24 and 48 hours) cells possessed a widened space between the rhodamine-labeled outer cell wall and GFP-tagged marker proteins at the plasma membrane, indicated by white arrows.

Chapter III: Age-associated changes in selected organelles and cellular substructures

The organelles that exhibited substantial changes in morphology with replicative age and are characterized further in this body of work are discussed in this chapter. Additional background information, the results from the screens and from high-resolution microscopy, as well as additional characterization of the age-associated change in organelle morphology are presented here.

The nucleolus fragments with advanced replicative age

The yeast nucleolus is a crescent-shaped subcompartment of the nucleus where rDNA transcription, ribosome subunit assembly and ribosome biogenesis occurs (Taddei et al., 2010). In general, the nucleolus is crescent-shaped, and resides within approximately one third of the total volume of the nucleus, but its size and morphology can vary depending on the stage of the cell cycle (Taddei et al., 2010). The nucleolus has been previously reported to fragment with advanced replicative age as a result of the accumulation of extrachromosomal rDNA circles (ERCs), which is discussed in much greater detail in Chapter I (Sinclair, 1997; Sinclair & Guarente, 1997). As such, the nucleolus was an important cellular structure to monitor during the replicative aging process to support the use of the MEP for acquiring replicatively aged cells and to provide evidence that the fixed- and live-cell screens are sensitive for the detection of aging phenotypes.

Nop58p-GFP and Ssf1p-GFP were used to visualize the nucleolus with replicative age (**Table 3.1**). Both proteins localize to the nucleolus, are abundant, and are commonly used to monitor the nucleolus in cell-biological studies (Gautier et al., 1997; Kim and Hirsch, 1998). Wide-field epifluorescence in both live and fixed cells revealed that the nucleolus becomes fragmented with advanced replicative age (**Figure 3.1A-C**). The nucleolus also appeared to be brighter in replicative aged cells, suggesting an increase in Nop58p-GFP and Ssf1p-GFP marker proteins with age. This is at least partially due to the oscillations of nuclear and nucleolar protein abundance observed during the cell cycle (Ball et al., 2011), and may indicate changes in cell cycle kinetics in old cells compared to young cells. The aging nucleolus as marked with Nop58p-GFP was also subjected to higher resolution three-dimensional microscopy to determine if the frequency of nucleolar fragmentation was underestimated due to visualization using a simple epifluorescence microscope. High-resolution microscopy showed that the percent of cells containing a fragmented nucleolus are: 0% (n=9) prior to labeling, 0%

(n=6) at the time of MEP induction, 0% (n=10) at time 3 hours, 17% (n=12) at time 24 hours, and 40% (n=10) at time 48 hours. Representative images are shown in **Figure 3.1D**. The proportion of cells with fragmented nuclei increased between time 24 and 48 hours, suggesting that ERCs accumulate as a function of replicative age (**Figure 3.1E**). The degree of fragmentation varied, but does not correlate with the replicative age of the cell. The nucleoli that remained unfragmented, even in old mother cells, often retained their crescent shape and still inhabited approximately one third of the nuclear volume. High-resolution microscopy did not detect additional events of nucleolar fragmentation compared to standard epifluorescence microscopy.

Peroxisomes exhibit both quantitative and qualitative changes in old mother cells

Peroxisomes are highly dynamic organelles found in most eukaryotic cells. In *Saccharomyces cerevisiae*, the peroxisome is the sole organelle capable of beta-oxidation of fatty acids. In addition to fatty acid metabolism, the peroxisome is responsible for the metabolism of atypical carbon and nitrogen sources and detoxifying the cell of these potentially reactive compounds, such as hydrogen peroxide and glyoxylate (Alberts et al., 2002).

Peroxisome abundance and size is highly regulated, and largely depends on the nutritional state of the cell (Fagarasanu et al., 2007). Young yeast cells growing exponentially in ample glucose will contain 2-5 peroxisomes per cell, and this number is maintained by the balance of organelle fission, distribution to daughter cells, and turnover (Fagarasanu et al., 2007). C-terminal fusions of fluorescent proteins to peroxins reveal cytoplasmic punctate structures that vary in size. Changes in peroxisome shape, size or number usually reflect a change in cellular metabolism or disruption of normal peroxisomal dynamics (Fagarasanu et al., 2007).

Peroxisomes are initially formed *de novo* by the heterotypic fusion of vesicles originating from the endoplasmic reticulum (Van der Zand et al., 2012). Each type of vesicle contains one half of the translocon required to import peroxisomal matrix proteins containing either PTS1 or PTS2 (peroxisome targeting sequence type 1 or 2) (Van der Zand et al., 2012). Once formed and matured, it is thought that peroxisomes increase in number by elongation followed by growth and division – fission (Fagarasanu et al., 2007). The Pex11 family of proteins is responsible for peroxisome elongation; deletion of this family results in a few enlarged peroxisomes, and overexpression of this family results in over-proliferation and many small peroxisomes (Erdmann and Blobel, 1995; Marshall et al., 1995). Peroxisome fission occurs by two different mechanisms (Fagarasanu et al., 2007). Under typical growth conditions,

peroxisome fission requires the dynamin-related protein Vps1. Under peroxisome-inducing conditions, i.e. growth on oleate, peroxisome fission requires another dynamin-related protein, Dnm1. Dnm1-mediated division is dependent on Fis1, and this fission machinery is the same as that required for mitochondrial fission.

Peroxisomes reduce their numbers by degradative turnover by the vacuole (pexophagy) and by segregation to the daughter cell (Manjithaya et al., 2010). Differences in peroxisome abundance and morphology with age could reflect changes in the cell's perceived nutritional status or metabolism, organelle biogenesis, turnover, or fission as a function of replicative age.

The peroxisomes undergo both qualitative and quantitative changes with increasing replicative age (originally observed by Adam Hughes). All markers used to visualize peroxisomes in this study are listed in **Table 3.2**. As cells become older, peroxisomes increase in number, however, the increase is largely in smaller-sized Pex11p-GFP-containing structures (**Figure 3.2A,B**). Young cells generally have several peroxisomes, usually one larger structure and a couple to a few smaller ones. Older cells with have upwards of 20-30 peroxisomes, and the majority of those are small in size (**Figure 3.2D**). The increase in peroxisome number is most dramatic between time 3 and 24 hours. This phenotype does become more penetrant at time 48 hours (data not shown). The expansion of peroxisome number exceeds that which would be expected from the age-associated increase in cell size. This phenotype could suggest an increase in organelle biogenesis, peroxisome fission, or a change in peroxisome turnover or degradation.

Replicatively aged cells exhibit an increase in the total number of Pex11p-GFP containing punctate structures, presumed to be peroxisomes, compared to young cells (**Figures 3.2C**). These additional structures also tended to be smaller in size, suggesting they may not be mature, functioning peroxisomes, but rather immature import-incompetent pre-peroxisomes or degradative intermediates (**Figure 3.2D**). Additional peroxisome membrane and matrix markers were utilized to better determine the nature of age-associated Pex11p-GFP containing structures. Pex25p, like Pex11p, is a member of the Pex11 family of proteins, is a peripheral peroxisomal membrane protein, and is required for the regulation of peroxisome size and number (Rottensteiner and Stein, 2003). Pex25p-GFP phenocopies Pex11p-GFP in aging cells (**Figure 3.2B**); the number of Pex25p-GFP containing structures increase as a function of replicative age, and these structures were also smaller in size. Furthermore, Pex25-GFP foci colocalized with Pex11p-mCherry containing structures (**Figure 3.2B**). This suggests that the age-related phenotype seen with Pex11p-GFP is not marker-specific.

Pex14p is a peroxisomal integral membrane protein necessary for the import of all peroxisomal matrix proteins. Pex14p interacts with Pex5p and Pex7p, the receptors for PTS1 (peroxisome targeting sequence) and PTS2 containing matrix proteins, respectively (Azevedo and Schliebs, 2006). Pex14p-GFP containing structures also become more numerous with replicative age (data not shown). Pex14p-GFP also colocalizes with Pex11p-mCherry at all replicative ages, suggesting that the structures seen at time 24 and 48 hours, albeit smaller, contain peroxisomal membrane (data not shown).

To determine if the peroxisomes observed at later replicative ages are import-competent, mCherry-SKL (the PTS1 import tripeptide) was expressed from the strong GPD/TDH3 promoter from an ectopic site in Chromosome I in a strain also expressing Pex11p-GFP from its endogenous promoter (Appendix C) (Gould et al., 1989). The majority of Pex11p-GFP containing peroxisomes at all timepoints also contained mCherry-PTS1, suggesting that even the small-sized peroxisomes detected at advanced replicative age are import-competent (**Figure 3.3**).

To summarize the findings from localizing Pex11p, Pex25p, Pex14p and mCherry-PTS1 in aging cells, the more numerous and smaller peroxisomes seen in older mother cells contain both peripheral and integral peroxisome membrane proteins, and are capable are importing proteins containing the PTS1 tripeptide SKL. Together these results suggest that the age-associated peroxisomes are mature, and may reflect an increase in peroxisome biogenesis, a disruption of whole-organelle degradation (pexophagy) where the intermediates of turnover persist within the cell, and/or a lack of segregation to daughter cells.

Biochemical and genetic approaches were taken to determine if the age-associated increase in peroxisome number could be attributed to increased organelle biogenesis. First, metabolism-induced peroxisome biogenesis is associated with phosphorylation of Pex11p and/or an increase in Pex25 protein expression (Smith et al., 2002). Whole-cell extracts from young and old Pex11p-GFP and Pex25p-GFP containing cells were subjected to polyacrylamide-gel electrophoresis and subsequent Western blot analysis with an antibody specific for the GFP epitope tag. These analyses showed that there was no age-associated species that could correspond to phosphorylated Pex11p-GFP (**Figure 3.4A**). However, multiple slowly migrating bands were detected in an age-dependent manner. These species could represent covalent oligomerization of Pex11p-GFP or other post-translational modification of Pex11p-GFP, such as polyubiquitination. Consistent with an absence of nutrition-induced peroxisome biogenesis, no increase in Pex25p-GFP abundance with replicative age was detected (**Figure 3.4A)**. Interestingly, the abundance of Pex11p-GFP and Pex25p-GFP

remained approximately constant throughout replicative aging. Furthermore, Western blot analysis of Pex14p-GFP (**Figure 3.4B**) revealed that Pex14p-GFP abundance decreased with age. Together, these results suggest that the total amount of peroxisome membrane does not increase despite the significant increase in abundance.

A second approach to determine if the age-associated increase in peroxisome number is attributable to nutrition-stimulated organelle biogenesis was to characterize the effect of fission on the peroxisome phenotype. As described above, the Fis1- and Dnm1-dependent mechanism is thought to mediate nutrient-related peroxisome fission (Kuravi et al., 2006). Accordingly, the number of peroxisomes was quantified in aging cells in the absence of one of the dynamin-related proteins, Dnm1p or Vps1p. Deletion of *DNM1* had no effect on the age-associated increase in peroxisome number and concomitant decrease in size (**Figure 3.5A,B**). One caveat is that deletion of *DNM1* also results in the loss of mitochondrial fission, which could have significant bystander effects on age-related processes. Deletion of *VPS1* resulted in the single large peroxisome in young cells. The number of peroxisomes is still increased as a function of replicative age, however it was difficult to determine if the phenotype was consistent with that seen in wild-type due to the drastic baseline decrease in peroxisome number and increase in size (**Figure 3.5C,D**). These results suggest that Dnm1 is expendable for the age-associated peroxisome increase, and that the role of peroxisome fission machineries in aging remains unclear.

An alternative explanation that could address the increase in smaller-sized peroxisomes is an increase in peroxisome turnover, and that the structures seen in older cells are actually intermediates of pexophagy. Previous studies have shown that increased pexophagy can be detected using cell biological, biochemical and genetic techniques. First, increased pexophagy is often reflected by an increase in GFP in the vacuole of a strain expressing a peroxisome protein-GFP fusion, detectable using microscopy. Second, increased pexophagy is also reflected by the presence of clipped GFP by Western blot (Reggiori and Monastyrska, 2005). Examination of aging cells expressing Pex14p-GFP did not reveal any age-dependent increase in GFP signal in the vacuole (data not shown). Furthermore, Western-blot analysis of whole-cell extracts from young and old Pex14p-GFP expressing cells did not reveal an increase in clipped GFP (**Figure 3.4B**). In the case that there is a modest increase in pexophagy with age – enough to increase the number of peroxin-containing structures but not sufficient to overwhelm degradative processes – the number of peroxisomes with age was quantified in the absence of Pep4p, the protease required for the maturation of all vacuolar proteinases. In this genetic background, vacuolar degradation is blocked and if pexophagy increases in an age-dependent

manner, there should be an exacerbation of the peroxisome phenotype (Hutchins et al., 1999). However, the number of peroxisomes in old cells was not increased in *pep4Δ* cells compared to wild-type cells (**Figure 3.6)**. Together, these findings indicate that delivery of peroxisomes to the vacuole is not increased as function of replicative age.

Finally, it has been previously shown that mitochondrial dysfunction can be correlated with increased peroxisome abundance (Motley et al., 2008). Cells lose mitochondrial membrane potential and the mitochondria fragment with replicative age so it is possible that age-associated peroxisome phenotype is a direct consequence of age-associated mitochondrial dysfunction (Hughes & Gottschling, 2012). To test this, Pex11p-GFP-containing foci were quantified in the presence of a suppressor of the aging mitochondrial phenotype, overexpression of *VMA1* (Hughes & Gottschling, 2012). If the peroxisome phenotype is downstream of mitochondrial dysfunction, then *VMA1*-overexpression should suppress both phenotypes. Cells overexpressing *VMA1* contained significantly fewer peroxisomes at time 24 hours compared to cells expressing an empty vector. However, *VMA1*-overexpression did not reduce the number of peroxisomes to young-cell levels, and small-sized peroxisomes were still observed (**Figure 3.7A,B**). The effect of *VMA1*-overexpression is further explored in later sections. Additionally, Pex11p-GFP cells treated with concanamycin A, an agent that abolishes vacuolar acidity and induces mitochondrial dysfunction, induced an increase in peroxisome number but not to the levels seen in old cells (**Figure 3.7C,D**) (Drose et al., 1993). Together, these results suggest the peroxisome phenotype cannot be fully explained by changes in vacuolar acidity and mitochondrial dysfunction.

Genetic manipulation did not conclusively indicate a mechanism that could be responsible for the quantitative and qualitative changes observed in peroxisomes with replicative age. There is no evidence that the increase of peroxisomes with age occurs in a manner similar to nutrient-stimulated peroxisome proliferation. The role of fission remains unclear, as deletion of either dynamin-related protein alone did not suppress the phenotype. Degradation pathways do not seem to play a major role because peroxisomes appear unchanged when vacuole protein degradation is inhibited. The possibility that peroxisome segregation from the mother to the daughter cell may be dampened in replicatively old cells cannot be ruled out. Finally, age-associated loss of vacuolar acidity and mitochondrial dysfunction are not likely to be directly upstream of peroxisome proliferation, as suppression of loss of vacuolar acidity and mitochondrial fragmentation/dysfunction did not reduce the number peroxisomes in time 24 hour cells to young cell levels. The basis of increased peroxisome abundance and decreased peroxisome size with age remain unknown.

Vacuole fragmentation occurs later during the aging process

The yeast vacuole is a highly dynamic organelle, undergoing constant fission and fusion (Li and Kane, 2009). The vacuole typically comprises approximately 10-20% of the cell's volume, but can grow to be much larger under certain conditions. The dynamin-related protein Vps1p, the same protein that mediates peroxisome fission under normal growth conditions, is required for both vacuolar fusion and fission (Peters et al., 2004). Vacuolar fusion is homotypic and requires the presence, but not necessarily the function, of the V_0 domain of the vacuolar H^+-ATPase (V-ATPase). Homotypic fusion typically occurs in a cell-cycle dependent manner, but is also induced under conditions of hypotonic stress and when the cell becomes deficient in phosphotidylinositol (3,5)-bisphosphate. Vacuolar fission also occurs during the cell cycle to facilitate Myo2p-dependent vacuole inheritance into the daughter cell. Fission events require acidification of the vacuole, and are induced by low cellular pH and hypertonic stress (Li and Kane, 2009). Dnm1p, another dynamin-related protein also responsible for mitochondrial and peroxisome fission, is hypothesized to participate in membrane scission during vacuolar fission, as is true in fission yeast *Schizosaccharomyces pombe* (Rothlisberger et al., 2009; Armstrong, 2010).

The yeast vacuole shares many of the same functions as the lysosome in higher organisms. The vacuole has two primary features: the vacuolar H^+-ATPase and a large collection of amino acid, ion and metal transporters (Li and Kane, 2009). These features allow the vacuole to have several important functions. First, the vacuole is a degradative organelle containing many non-specific proteases. Proteins are targeted to the vacuole from many different pathways, including from endosomes, directly from the cytoplasm, from macro- and micro-autophagosomes, and from the Golgi. Second, the vacuole is a storage organelle for non-acidic amino acids, ions (including protons) and metals. Thus, the vacuole also plays a significant role in maintaining nutrient and ion homeostasis within the cell. Finally, the vacuole has some capacity to detoxify the cell by sequestering otherwise harmful molecules (Li and Kane, 2009).

The vacuole has recently been shown to have a causative role early in the aging process (Hughes & Gottschling, 2012). The role of vacuolar acidity and replicative lifespan was addressed in the introduction. Briefly, the vacuole quickly loses acidity during the first few divisions. This drop in acidity leads to the loss of mitochondrial membrane potential and a fragmented/aggregated mitochondrial morphology. Age-associated decline in vacuolar acidity,

however, is less complete than that seen in mutants that prevent acidification of the vacuole (Hughes & Gottschling, 2012). In addition to causing changes in mitochondria, decreased vacuolar acidity can alter the targeting and recycling of proteins. For instance, a previous study showed that Kex2p-GFP, a protein that typically localizes to the Golgi and to late endosomes, is targeted to the vacuole in the absence of vacuolar acidity (Huang and Chang, 2011). This was apparent from a marked increase in GFP fluorescence within the vacuolar lumen and by detection of clipped GFP by Western blot analysis.

Kex2p-GFP coincidentally was one of the markers in the primary screen. As described in the first section, old cells expressing Kex2p-GFP exhibited increased GFP fluorescence in the vacuole compared to young cells (**Figure 2.19D**). Western blot analysis on extracts from young and old cells expressing Kex2p-GFP also revealed free, clipped GFP only in old cells (**Figure 2.119E**). Together, these results further support the decline in vacuolar acidity, and suggest that the degree of acidity loss further increases between time 3- and 24-hour cells. Suppression of vacuolar acidity loss results in lifespan extension. Changes in vacuolar morphology would likely have or reflect significant effects on the course of replicative aging.

Vph1p-GFP was used to monitor vacuolar morphology with replicative age (**Table 3.3**). Vph1p is one of subunits of the V0 domain of the vacuolar H^+-ATPase, and is localized to the vacuolar rim (Manolson et al., 1992; Huh et al., 2003a). During replicative aging, the vacuole undergoes a very stereotypical series of morphological changes. Cells begin with several medium-sized vacuoles. After a few divisions, the vacuoles of some cells begin to enlarge. At time 24 hours, some cells have huge vacuoles that comprise the majority if the cellular volume, and is readily apparent upon differential interference contrast (DIC) microscopy. Other time 24-hour cells, however, exhibited highly fragmented vacuoles. Finally, at time 48 hours, nearly all cells have fragmented vacuoles, ranging in their degree of fragmentation (**Figure 3.8)**.

Mitotic defects are more prevalent in replicatively aged cells

Successful mitotic events are the basis of replicative aging. The mitotic apparatus, as addressed here, consists of replicated chromosomes, their kinetochores, the microtubule spindle, and spindle pole bodies. The mitotic apparatus is very dynamic and many cellular events must be coordinated for successful cell division. Failure to execute mitosis perfectly can result in chromosome instability and aneuploidy (Tanaka, 2008; Cheeseman and Desai, 2008). Severe mis-executions of mitosis may represent terminal events for the mother cell, daughter

cell or both. With age being one of the most potent risk factors for cancer, the connection between mitotic defects and replicative age should be carefully examined.

Saccharomyces cerevisiae undergo closed mitoses, where the nuclear envelope remains intact throughout the entire process (Taddei et al., 2010). This characteristic allows inferences to be made regarding the localization of DNA by visualizing the nucleoplasm, nuclear envelope, spindle pole bodies, kinetochores or spindle microtubules. The spindle pole bodies (SPBs) are the microtubule organizing centers for the cell, and equivalent to centrioles in higher organisms. SPBs are anchored in the nuclear envelope and their number and localization varies greatly with the stage of the cell cycle (Jaspersen and Winey, 2004). The cell starts with a single SPB that duplicates at the beginning of G_1. Once duplicated, the SPBs are capable of nucleating interpolar and kinetochore microtubules. The bipolar spindle is formed when the SPBs separate (Jaspersen and Winey, 2004).

Kinetochore microtubules emanating from the SPB at each pole interact with the kinetochores located at the centromeres of each chromosome. The primary role of the kinetochore is to mediate attachment of the chromosome to microtubules for the purposes of segregation, and to signal the spindle assembly checkpoint (mitotic checkpoint) if attachment is not bi-oriented and amphitelic. Separation of the sister chromatids is mediated by kinetochore microtubule dynamics (Pearson and Bloom, 2004; Moore et al., 2009; Pereira and Yamashita, 2011).

Proper spindle positioning at the bud neck and orientation along the mother/bud axis are required for segregation of the chromosomes. Spindle positioning begins with the Myo2p-dependent transport of plus-ended astral microtubules into the bud; this process also requires the proteins Kar9p and Bim1p. Finer spindle orientation is aided by astral microtubule shortening, and microtubule interactions with bud neck proteins. Later, during anaphase, dynein is activated at the bud cortex and uses its minus-end directed motor activity to pull the daughter-bound SPB through the bud neck. Failure of the spindle to orient properly results in activation of the spindle position checkpoint (Pearson and Bloom, 2004; Moore et al., 2009; Pereira and Yamashita, 2011).

Spindle pole body segregation is asymmetric in budding yeast with the original/older SPB fated for the daughter cell and the newly duplicated SPB retained in the mother cell (Vallen et al., 1992). SPB asymmetry is established by the asymmetric localization of Clb4p-Cdc28p at the original (mother-bound) SPB, which phosphorylates and inactivates Kar9p. Therefore, active Kar9p is only found at the daughter-bound SPB and regulates the microtubule plus-end

interactions required for transport into the bud. Mutants in any of these components result in spindle abnormalities (Liakopoulos et al., 2003; Grava et al., 2006).

The FEAR (Cdc14p early anaphase release) and MEN (mitotic exit network) are two pathways that occur at early and late anaphase, respectively, that promote the progression and completion of mitosis (Dumitrescu and Saunders, 2002). Components of both pathways are important in the regulation of spindle dynamics and proper nuclear segregation. Mutants of certain members of either pathway can result in spindle mis-positioning, cell-cycle arrest, and segregation errors (Ross and Cohen-Fix, 2004; Hotz et al., 2012; Chan and Amon, 2010; Valerio-Santiago and Monje-Casas, 2011; Falk et al., 2011; Dumitrescu and Saunders, 2002).

In the initial screens, the mitotic spindle was visualized using spindle pole body (Spc42p-GFP, Spc72p-GFP, Nud1p-GFP), tubulin (GFP-Tub1p), and kinetochore (Mtw1p-GFP, Nuf2p-GFP) markers (**Table, 3.4**, **Figure 3.9**) (Huh et al., 2003a). Cursory examination of the mitotic spindle using microtubule, spindle pole body, and kinetochore marker proteins revealed a mitotic defect in approximately 10% of replicatively old mother cells (**Figure 3.9**). The most common phenotype observed with microtubule, SPB and kinetochore markers was the daughterly phenotype where the mitotic apparatus appeared to translocate into the daughter cell in its entirety (**Figures 3.11A**) (Ross and Cohen-Fix, 2004). The consequence of the daughterly phenotype is most likely death for the mother cell and perhaps death for the daughter cell as well. The mitotic apparatus is likely to be functional as all three classes of marker proteins exhibited the same phenotype at the same frequency.

The nucleoplasmic marker GFP-Pus1p was also utilized to look for mitotic defects for two major reasons (**Table 3.4**). First, GFP-Pus1p was the optimal marker for characterizing nuclear morphology and size with age because C-terminal fusions of the histones and nuclear pore components resulted in growth defect (Hellmuth et al., 1998). Second, GFP-Pus1p marks both nucleolar and non-nucleolar nucleoplasm. The nucleolus is a late-segregating region of the nucleus and is often a much better indicator of mitotic delay compared to just visualizing the chromosomal mass (Torres-Rosell and Machín, 2004; Witkin et al., 2012). For instance, if a problem arises after the chromosomal masses have segregated but prior to cytokinesis, SPB, kinetochore and microtubule markers will falsely detect a normal cell division. Only nucleolar and nucleoplasmic markers are appropriate for detecting late delays in mitosis.

Visualization of GFP-Pus1p with age revealed that cells had nuclear segregation problems at more advanced replicative ages. These defects included but were not limited to: multiple nuclei, nuclei segregating within the mother cell perpendicular to the mother/bud axis, mitotic delay and missegregation of the nucleus into the daughter cell (daughterly phenotype).

The frequency of nuclear migration defects increased from time 24 to time 48 hours. Representative images are shown in **Figure 3.10**.

Few mother cells were visualized during the primary fixed- and live-cell screens. The low frequency of the mitotic spindle abnormalities necessitated examination of a much larger population of old mother cells. To achieve the power necessary to show that old mother cells were significantly more prone to mitotic defect, old cells were acquired by serial purification in the absence of the MEP (**Appendix A**). This method was preferred for several reasons: 1) contaminating cells in the old mother purification will be young cells instead of the grossly mitotically aberrant dumb-bells, 2) the purity is markedly higher making imaging large numbers of old mother cells much easier, and 3) MEP components could be eliminated as a potential cause for the abnormalities, as *cdc20* and *ubc9* mutants both exhibit extensive mitotic defects.

Cells containing either Spc42p-GFP (SPB marker) or GFP-Tub1p (spindle microtubule marker) were serially purified live following growth at low densities in the absence of MEP induction. Young and old cells were imaged using three-dimensional wide-field fluorescence microscopy and manually scored for both mitotic and budding abnormalities. Analysis of young (n = 500 cells) and old (n = 550) mother cells expressing the SPB marker Spc42p-GFP revealed SPB abnormalities in 0.8% and 8.4% of cells, respectively. SPB defects included aberrancies in SPB number, distribution and position, and representative images are shown in **Figure 3.11B**. These same cells were scored for budding. Abnormal bud morphologies were detected in 1.6% and 16.2% of young and old cells, respectively. Similar analysis of the GFP-Tub1p expressing cells found that 0.4% of young cells (n = 460) and 7.1% of old cells (n = 789) harbored an abnormal spindle. These results are summarized in **Figure 3.11B**.

Additionally, the fluorescence intensity of the spindle was much brighter in cells that appeared to be experiencing mitotic difficulties (data not shown). This would suggest an increase in α-tubulin in these spindles, however, in yeast, the number of kinetochore microtubules should be the same as the number of chromosomes. An increase in the amount of α-tubulin in replicatively old cells is supported by Western-blot analysis. Untagged wild-type and GFP-Tub1p expressing MEP cells were aged, and harvested for purification prior to biotin-labeling and at time 0, 3 and 24 hours following MEP induction. Extracts from these populations were assayed by PAGE and Western blot analysis with both anti-GFP and anti-tubulin antibodies. In both cases, the quantity of tubulin increased with replicative age (**Figure 3.12**). Equivalent amounts of total protein confirmed by Ponceau S staining were analyzed in these experiments. Tubulin is not an appropriate control for Western blot analysis in aging cells.

Summary of age-associated phenotypes to be characterized further in this work

Four age-associated phenotypes were described here: 1) the fragmentation of the nucleolus, 2) the increase in peroxisome number and decrease in peroxisome size, 3) the fragmentation of the vacuole, and 4) missegregation of the mitotic spindle and other mitotic abnormalities (**Table 3.5**). These phenotypes all occur within a similar timeframe. Of significance, the defects observed using mitotic apparatus and the nucleoplasmic marker GFP-Pus1p potentially represent the terminal event for the cell. Although the penetrance varies, the phenotypes are all first observed at time 24 hours, and increased in incidence by time 48 hours. Because of the similar timing, it is unclear if any of the morphological changes are related. To better understand the relationships among these age-dependent phenotypes, strains expressing marker proteins for two different organelles in various combinations were visualized and scored for both phenotypes with replicative age.

Table 3.1. The marker proteins used to visualize the nucleolus. The markers used to visualize the nucleolus, and the cellular function of those proteins, are listed below. The type(s) of microscopy performed on cells expressing each of the marker proteins is indicated. Representative images of the marker proteins can be found in the figures stated in the final column.

Marker Protein or Stain	Marker Function	Type(s) of Microscopy Performed			Image Location
		Fixed	Live	High-res	
Ssf1p	Component of the 66S pre-ribosomal particle, localized to the nucleolus	X			Figure 3.1C
Nop58p	Involved in pre-rRNA processing, 18S rRNA synthesis and snoRNA synthesis, localized to the nucleolus	X	X	X	Figure 3.1A,B,D

Table 3.2. The marker proteins used to visualize peroxisomes. The markers used to visualize peroxisomes, and the cellular function of those proteins, are listed below.

Marker Protein or Stain	Marker Function	Type(s) of Microscopy Performed			Image Location
		Fixed	Live	High-res	
Pex11p	Peroxisomal membrane protein required for peroxisome proliferation	X	X	X	Figures 3.2A,B Figure 3.3 Figures 3.5-7
Pex25p	Peripheral peroxisomal membrane protein required for the regulation of peroxisome size.			X	Figure 3.2B
Pex14p	Peroxisomal membrane protein required for peroxisomal protein import. Interacts with Pex5p (PTS1), Pex7p (PTS2), and Pex13p (membrane receptor).		X	X	Not shown
PTS1-mCherry	PTS1 is the peroxisomal targeting sequence 1 required for import into the peroxisome following interaction with Pex5p.			X	Figure 3.3

Table 3.3. The marker protein used to visualize the vacuole. The marker used to visualize the vacuole, and the cellular function of the protein, is listed below.

Marker Protein or Stain	Marker Function	Type(s) of Microscopy Performed			Image Location
		Fixed	Live	High-res	
Vph1p	Vph1p is a subunit of the V0 domain of the V-ATPase, localized to the vacuolar rim		X		Figure 3.8

Table 3.4. The marker proteins used to visualize the mitotic apparatus and the nucleoplasm. The markers used to visualize the mitotic apparatus and the nucleoplasm, and the cellular function of those proteins, are listed below.

Marker Protein or Stain	Marker Function	Type(s) of Microscopy Performed			Image Location
		Fixed	Live	High-res	
Mtw1p	Component of the MIND kinetochore complex	X			Figure 3.9
Nuf2p	Component of the kinetochore-associated Ndc80 complex	X			Figure 3.9
Spc42p	Component of the spindle pole body, central plaque	X	X	X	Figure 3.9 Figure 3.11
Spc72p	Component of the cytoplasmic Tub4 complex, binds spindle pole bodies and links them to microtubues	X			Figure 3.9
Nud1p	Component of the spindle pole body, outer plaque, required for mitotic exit	X			Figure 3.9
Tub1p	Alpha tubulin, localizes to microtubules and spindle pole bodies		X	X	Figure 3.9
Pus1p	tRNA:pseudouridine synthase, localized to the nucleus		X		Figure 3.10

Table 3.5. Summary of findings from the screen and from high-resolution microscopy. The findings from visualization of all major organelles and cellular substructures is listed below. These include the results from both the screens and from high-resolution microscopy where applicable.

Structure	Summary of the results from the screens and from high-resolution microscopy
Nucleolus	The nucleolus fragments with replicative age. Fragmentation is first observed at time 24 hours, and the fraction of cells with fragmented nucleoli increases between time 24 and 48 hours. The nucleolus increases in size when the nucleus increases in size.
Peroxisomes	Peroxisomes increase in number and decrease in size with replicative age. This phenotype was observed when visualization membrane associated proteins Pex11p and Pex25p, the integral membrane protein Pex14p, and the imported PTS1-mCherry. This phenotype is not affected by deletion of *DNM1* or *PEP4*. Deletion of *VPS1* decreases peroxisome number in both young and old cells. *VMA1* overexpression decreases peroxisome numbers at time 24 hours, and treatment with ConA increase peroxisome number, but not to the same degree that is observed in aging cells.
Vacuole	The vacuole fragments with replicative age. This is first observed at time 24 hours. Nearly all cells contain fragmented vacuoles at time 48 hours.
Mitotic apparatus and the nucleoplasm	The spindle pole body and kinetochore markers exhibited a daughterly phenotype in fewer than 10% of cells at time 24 hours. Upon examination of a very large population of cells in the absence of the MEP, the percent of time 24 hour cells with some defect with the mitotic spindle was approximately 8%. Visualization of the nucleus using a nucleoplasmic marker revealed that mitosis was abnormal and/or delayed in many cells at time 24 and 48 hours.

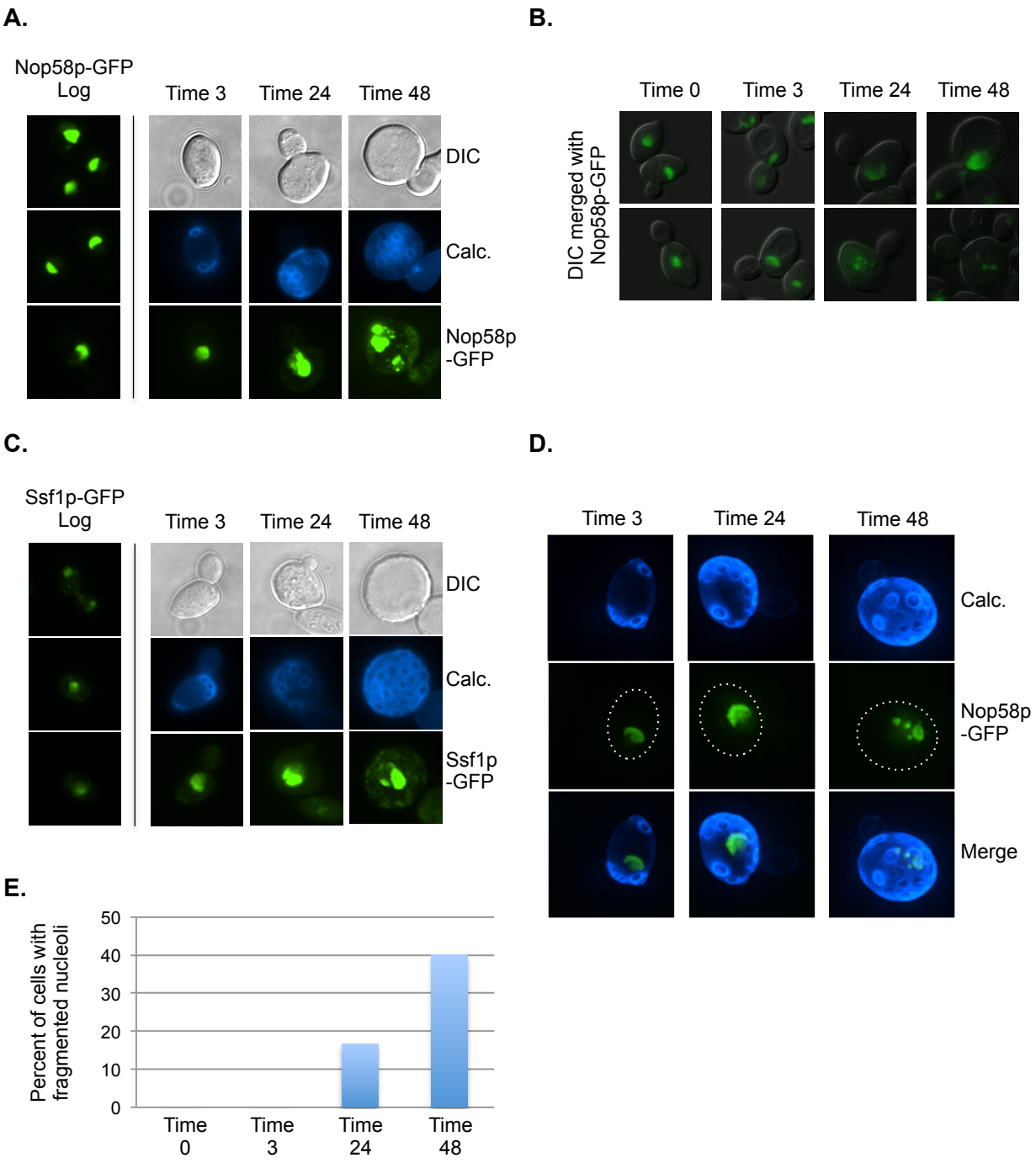

Figure 3.1. The nucleolus fragments with replicative age. Cells expressing chromosomally tagged Nop58p-GFP and Ssf1p-GFP were aged and analyzed as described in Figure 2.2. The nucleolus as marked by (A) Nop58p-GFP and (C) Ssf1p-GFP were visualized in fixed and purified mother cells harvested at the indicated timepoints. Nucleolar fragmentation was observed in cells at later timepoints (time 24 and 48 hours). (B) Nop58p-GFP expressing cells were labeled with rhodamine, aged, and visualized at the indicated timepoints. Nucleolar fragmentation was also observed in live cells at later timepoints (time 24 and 48 hours). (D) Nop58p-GFP expressing cells were biotinylated, aged with the MEP, fixed, purified, and subjected to high-resolution microscopy at the indicated timepoints. Images were acquired at 0.25 μm intervals, deconvolved, and shown here as maximum intensity projections. Dotted white lines outline the mother cells. (E) The percent of cells with a fragmented nucleolus increased as a function of replicative age. The graph represents data from one of many independent experiments.

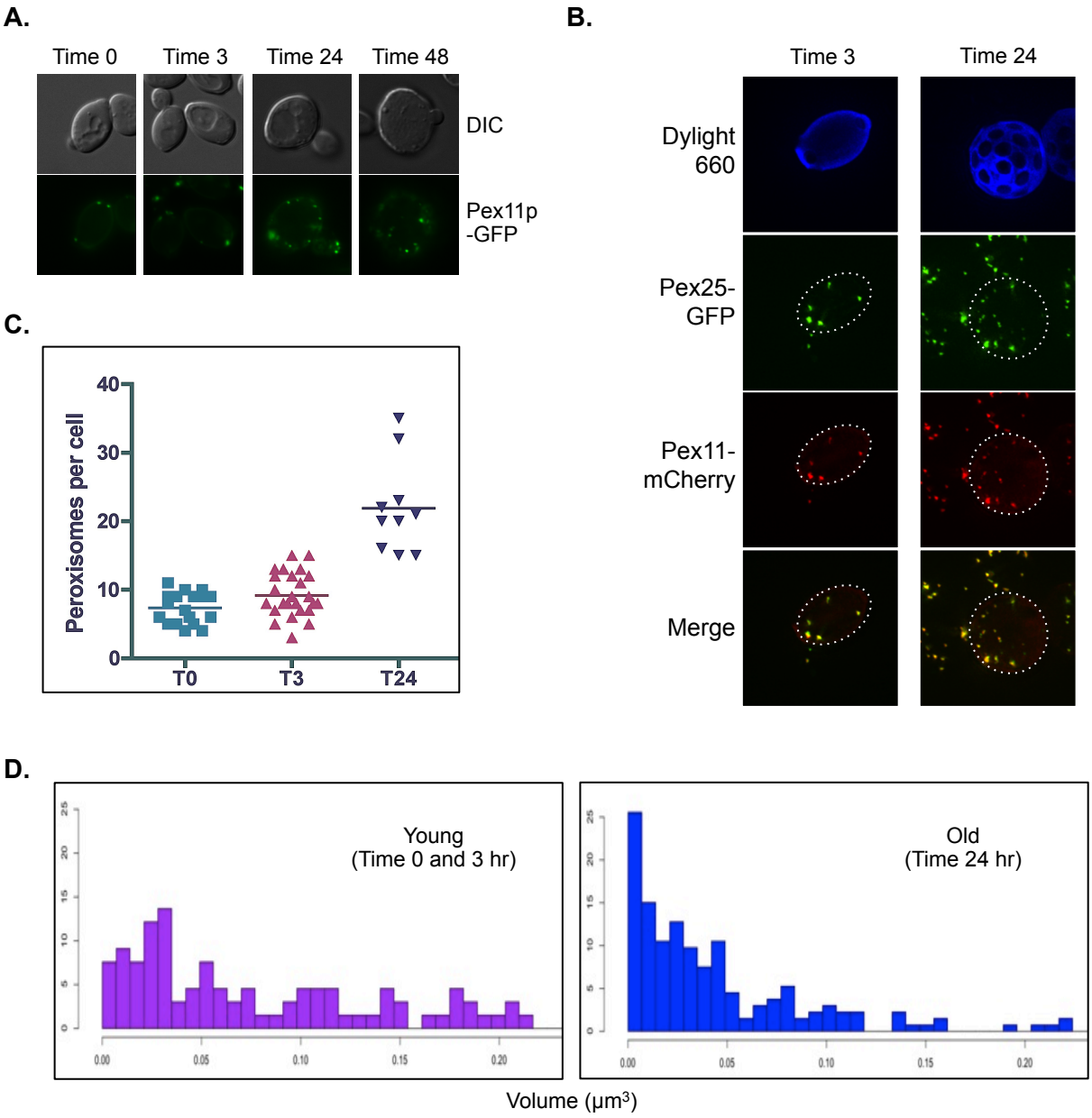

Figure 3.2. The number and size distribution of peroxisomes is altered with replicative age. Cells expressing chromosomally tagged Pex11p-GFP, Pex11p-mCherry, and Pex25p-GFP were aged and analyzed as described in Figure 2.2. (A) Pex11p-GFP containing foci increased in number and decreased in size as a function of replicative age. Cells expressing the peroxisomal marker protein Pex11p-GFP was aged and visualized in rhodamine-labeled cells at the indicated timepoints. (B) Cells expressing peroxisomal marker proteins Pex25p-GFP and Pex11p-mCherry were labeled with Dylight 660, aged using the MEP, fixed, and subjected to high-resolution microscopy at young (time 3 hours) and old (time 24 hours) timepoints. Images were acquired at 0.25 μm intervals, deconvolved, and shown here as maximum intensity projections. Dotted white lines outline the mother cells. (C) The number of Pex11p-mCherry foci per cell is plotted for the indicated timepoints, and shows an increase in peroxisome number with replicative age. (D) Peroxisomes in old cells tend to be smaller than those in young cells. Histograms showing the volume distribution of peroxisomes marked by Pex11p-mCherry in young (time 0 and 3 hours) cells compared to old (time 24 hours) cells.

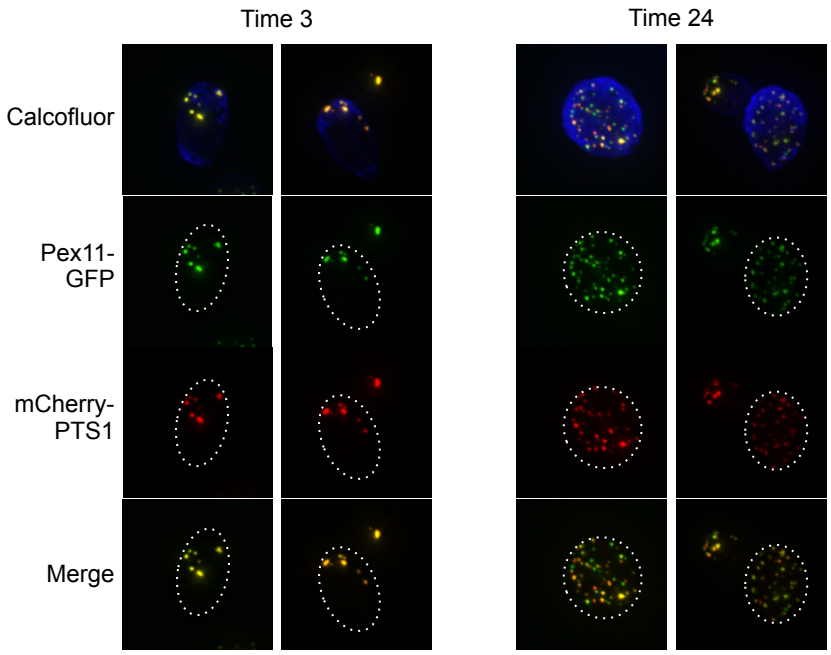

Figure 3.3. Peroxisomes in young and old cells contain imported peroxisome matrix marker mCherry-PTS1. A construct containing mCherry fused to the peroxisome targeting sequence 1 (PTS1) and expressed from the *TDH3* promoter was integrated into a gene-poor region of Chromosome 1 in Pex11p-GFP expressing cells. Cells expressing both Pex11p-GFP and mCherry-PTS1 were aged and analyzed as described in Figure 2.2. Briefly, Pex11p-GFp mCherry-PTS1 cells were biotinylated, aged using the MEP, fixed, purified, and subjected to high-resolution microscopy at times 3 and 24 hours following MEP induction. Images were acquired at 0.25 μm intervals, deconvolved, and shown here as maximum intensity projections. Dotted white lines outline the mother cells. The colocalization of Pex11p-GFP and mCherry-PTS1 is much more complete in young cells compared to old cells, however, most Pex11p-GFP foci in old cells also contain some mCherry-PTS1.

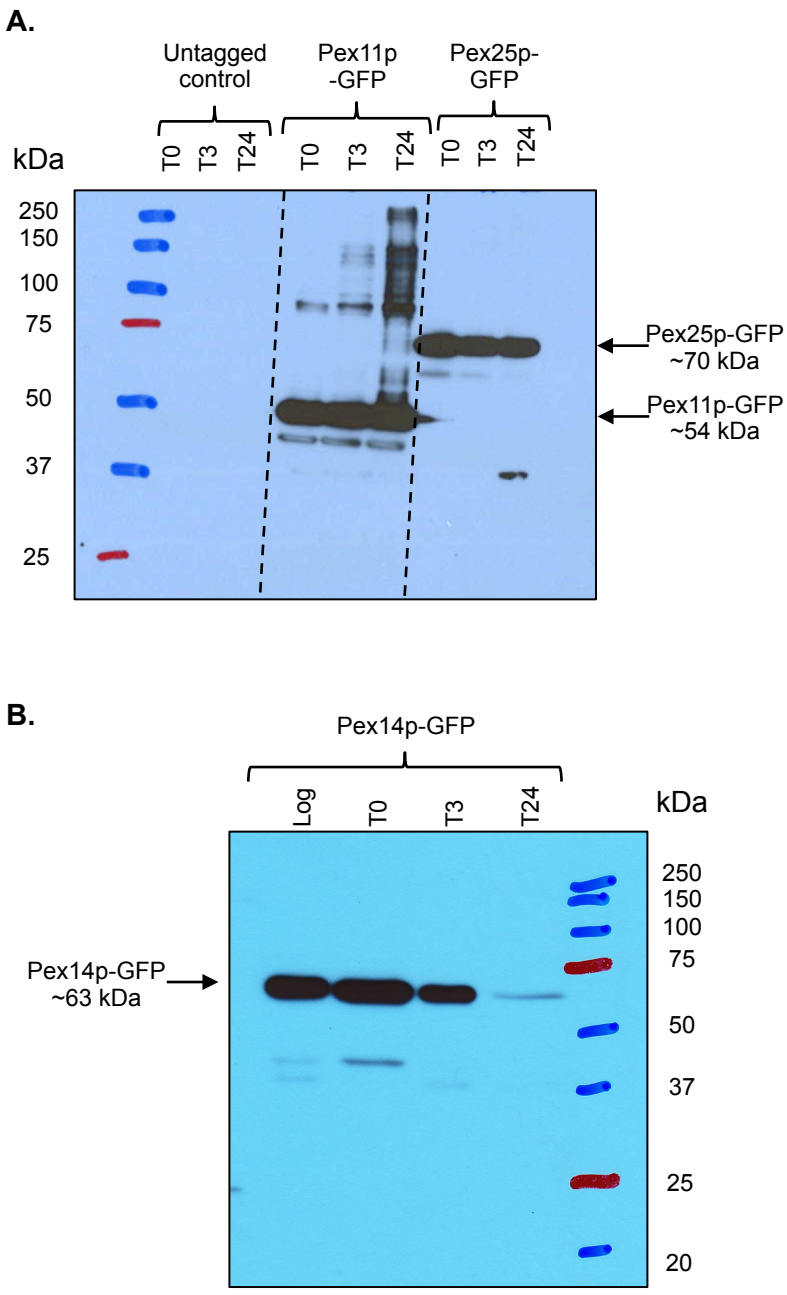

Figure 3.4. Quantity and migration characteristics of peroxisomal proteins. (A) Pex11p-GFP migration is altered in time 24 hour old cells, whereas no differences are detected in Pex25p-GFP quantity or migration with age. Total protein was extracted from cells expressing Pex11p-GFP or Pex25p-GFP at time 0, 3, and 24 hours of MEP aging. Equal amounts of total protein from each timepoint were loaded and compared by Western blot analysis with an anti-GFP antibody. (B) Pex14p-GFP quantities are decreased in time 24 hour old cells. Total protein was extracted from cells expressing Pex14p-GFP prior to aging, and at time 0, 3, and 24 hours of MEP aging. Equal amounts of total protein from each timepoint were loaded and compared by Western blot analysis with an anti-GFP antibody.

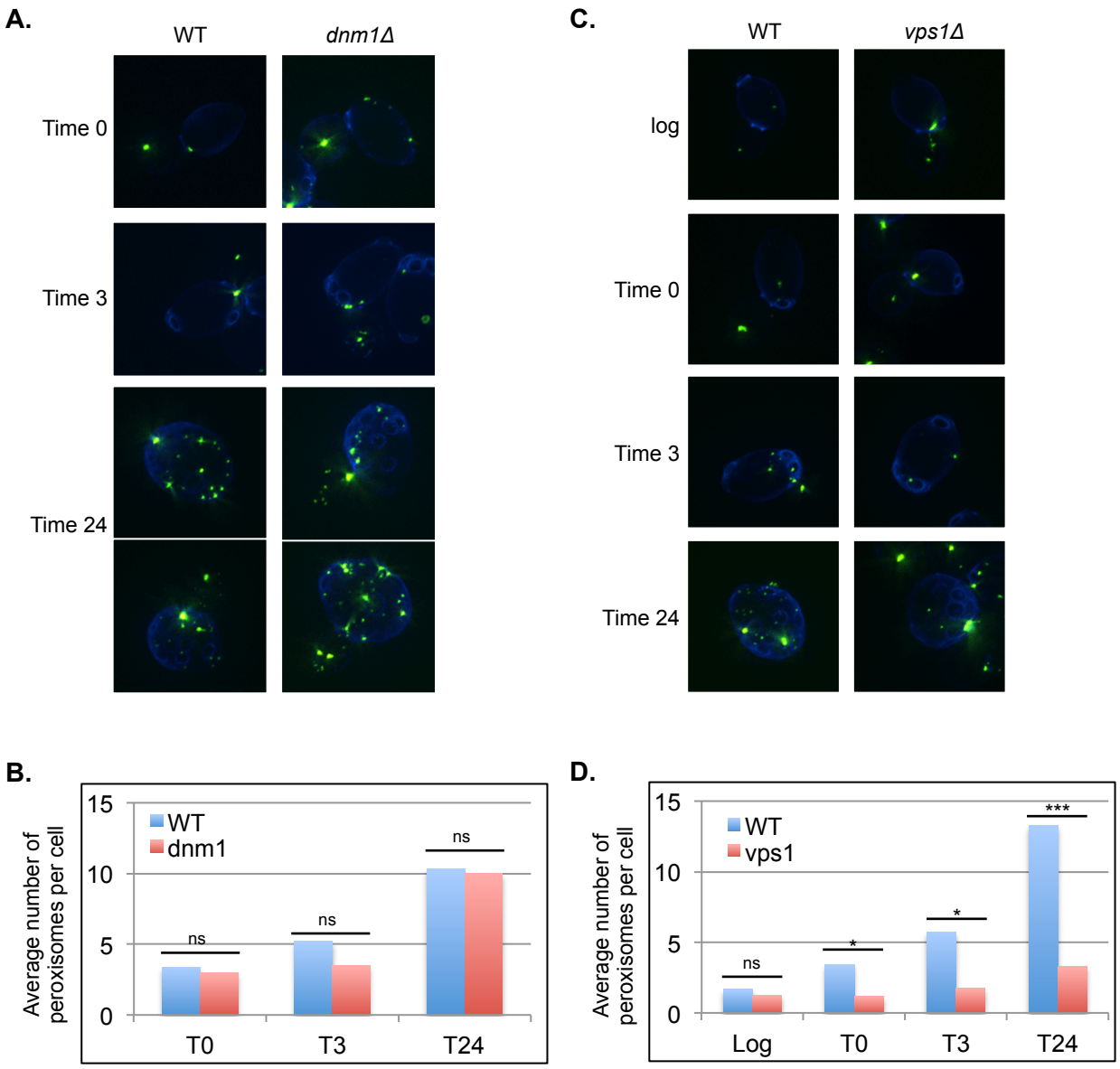

Figure 3.5. The effect of deleting the dynamin-related proteins responsible for peroxisome fission. Pex11p-GFP cells and Pex11p-GFP cells lacking *dnm1* or lacking *vps1* were aged and analyzed as described in Figure 2.2. Cells were biotinylated, aged with the MEP, fixed, purified, and subjected to high-resolution microscopy at the indicated timepoints. Images were acquired at 0.25 μm intervals, deconvolved, and shown here as maximum intensity projections. (A and B) Deletion of *dnm1* had no effect on the age-associated increase in peroxisome number. (A) Representative images of peroxisomes in wildtype and *dnm1Δ* cells at each timepoint. (B) The average number of peroxisomes per cell in wildtype cells compared to *dnm1Δ* cells did not differ at any timepoint. (C and D) Deletion of *vps1* significantly reduced the number of peroxisomes in young and aging cells, however, the number of peroxisomes still increased with age in *vps1Δ* cells. (C) Representative images of peroxisomes in wildtype and *vps1Δ* cells at each timepoint. (D) The average number of peroxisomes in wildtype cells compared to *vps1Δ* cells at the indicated timepoints.

* P<0.05. ** P<0.01, *** P<0.001, ns=not statistically significant (p>0.05) by unpaired t-test with Welch's correction, comparing wildtype to mutant at a single timepoint.

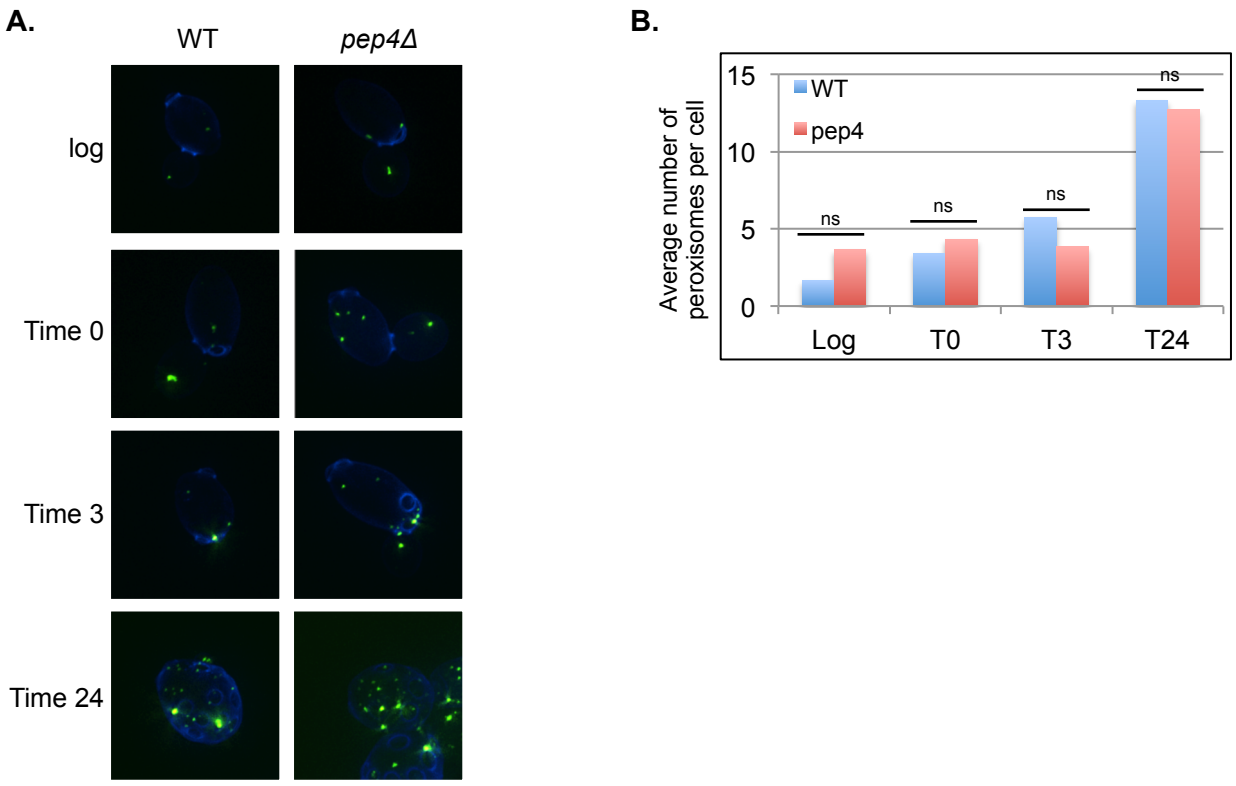

Figure 3.6. Deletion of *pep4* had no effect on the age-associated increase in peroxisome number. Pex11p-GFP cells and Pex11p-GFP cells lacking *pep4* were aged and analyzed as described in Figure 2.2. Cells were biotinylated, aged with the MEP, fixed, purified, and subjected to high-resolution microscopy at the indicated timepoints. Images were acquired at 0.25 μm intervals, deconvolved, and shown here as maximum intensity projections. (A and B) Deletion of *pep4* had no effect on the age-associated increase in peroxisome number. (A) Representative images of peroxisomes in wildtype and *pep4Δ* cells at each timepoint. (B) The average number of peroxisomes per cell in wildtype and *pep4Δ* cells did not differ at any timepoint.

ns=not statistically significant ($p>0.05$) by unpaired t-test with Welch's correction, comparing wildtype to mutant at a single timepoint.

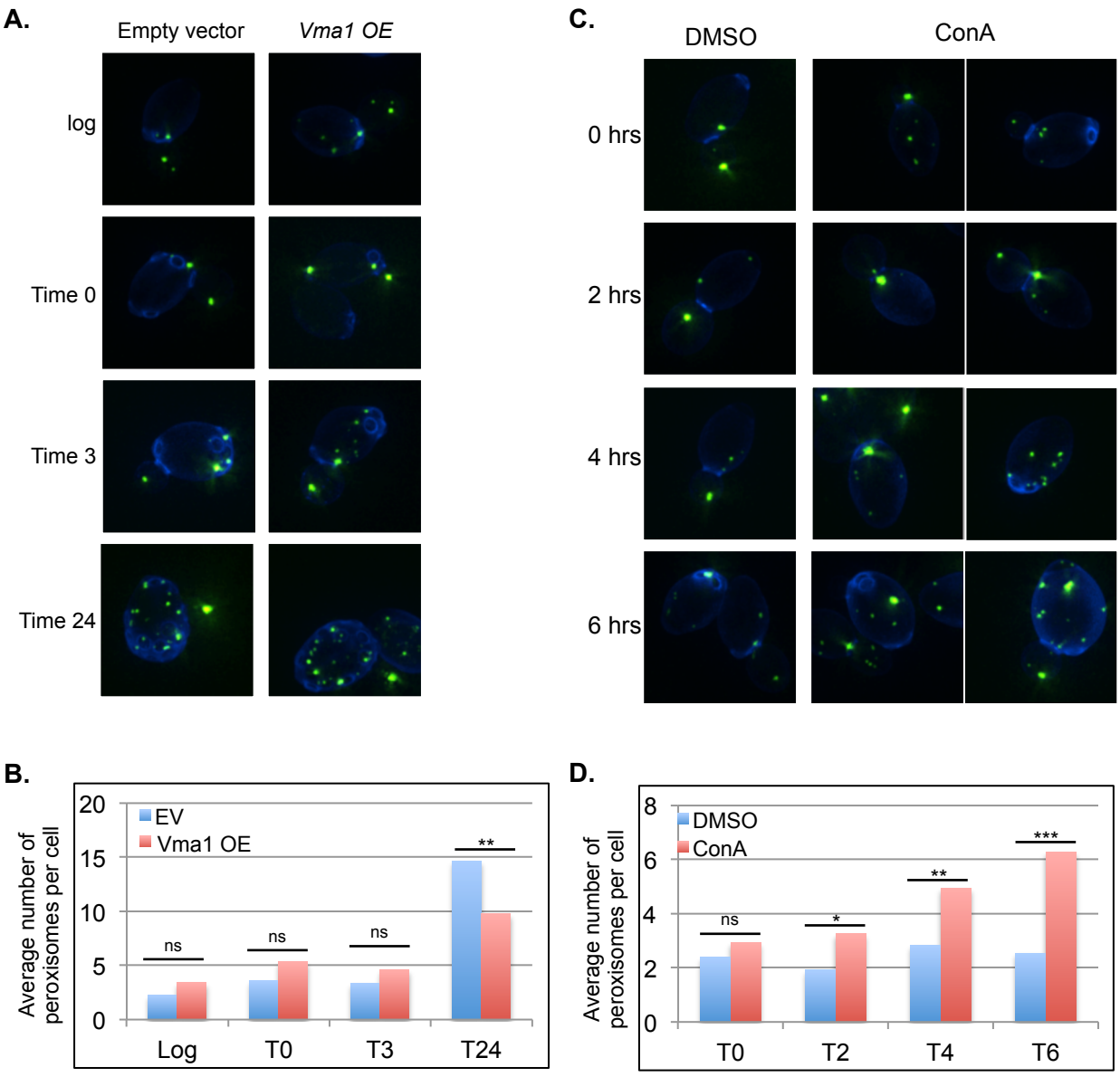

Figure 3.7. The effect of vacuolar acidity on the age-associated increase in peroxisome number. (A and B) Increasing vacuolar acidity by *VMA1* overexpression decreased peroxisome number at time 24 hours. Pex11p-GFP cells transformed with empty vector and Pex11p-GFP cells transformed with a *VMA1* over-expression construct at an ectopic site on Chromosome I were aged and analyzed as described in Figure 2.2. Cells were biotinylated, aged with the MEP, fixed, purified, and subjected to high-resolution microscopy at the indicated timepoints. Images were acquired at 0.25 μm intervals, deconvolved, and shown here as maximum intensity projections. (A) Representative images of peroxisomes in cells expressing empty vector and cells overexpressing *VMA1*. (B) The average number of peroxisomes per cell in cells expressing empty vector and cells overexpressing *VMA1* at the indicated timepoints. *VMA1* overexpression significantly decreased the number of peroxisomes per cell at time 24 hours. (C and D) Treatment of cells with vacuolar H^+-ATPase inhibitor concanamycin A abolishes vacuolar acidity. Pex11p-GFP expressing cells were either mock treated with DMSO or with 500 nM concanamycin A. Cells were harvested, fixed, and subjected to high-resolution microscopy after 0, 2, 4,and 6 hours of treatment. Images were acquired at 0.25 μm intervals, deconvolved, and shown here as maximum intensity projections. (C) Representative images of peroxisomes in cells treated with DMSO and cells treated with concanamycin A. (D) The average number of peroxisomes per cell in DMSO- and concanamycin-treated cells after 0, 2, 4, and 6 hours of treatment.
* P<0.05. ** P<0.01, *** P<0.001, ns=not statistically significant (p>0.05) by unpaired t-test with Welch's correction, comparing wildtype to mutant at a single timepoint.

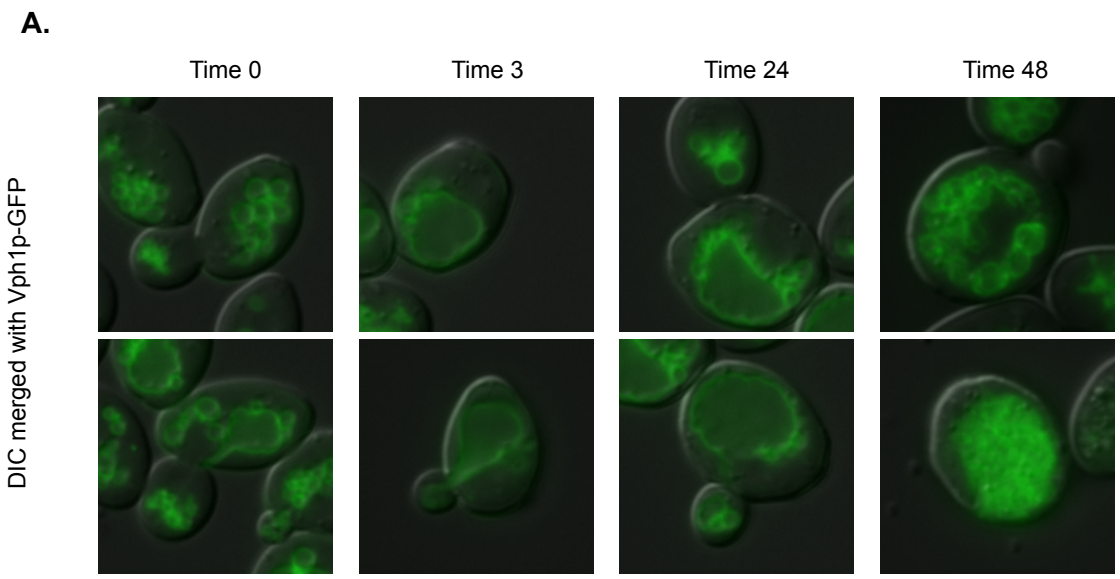

Figure 3.8. Replicative age-induced vacuolar fragmentation. Cells expressing chromosomally tagged Vph1p-GFP were aged and analyzed as described in Figure 2.2. The vacuole as marked by the vacuolar rim marker Vph1p-GFP was visualized in rhodamine-labeled aging cells at the indicated timepoints. The vacuole was often enlarged at time 3 and 24 hours, however, many time 48 hour cells possessed vacuoles that were fragmented to varying degrees.

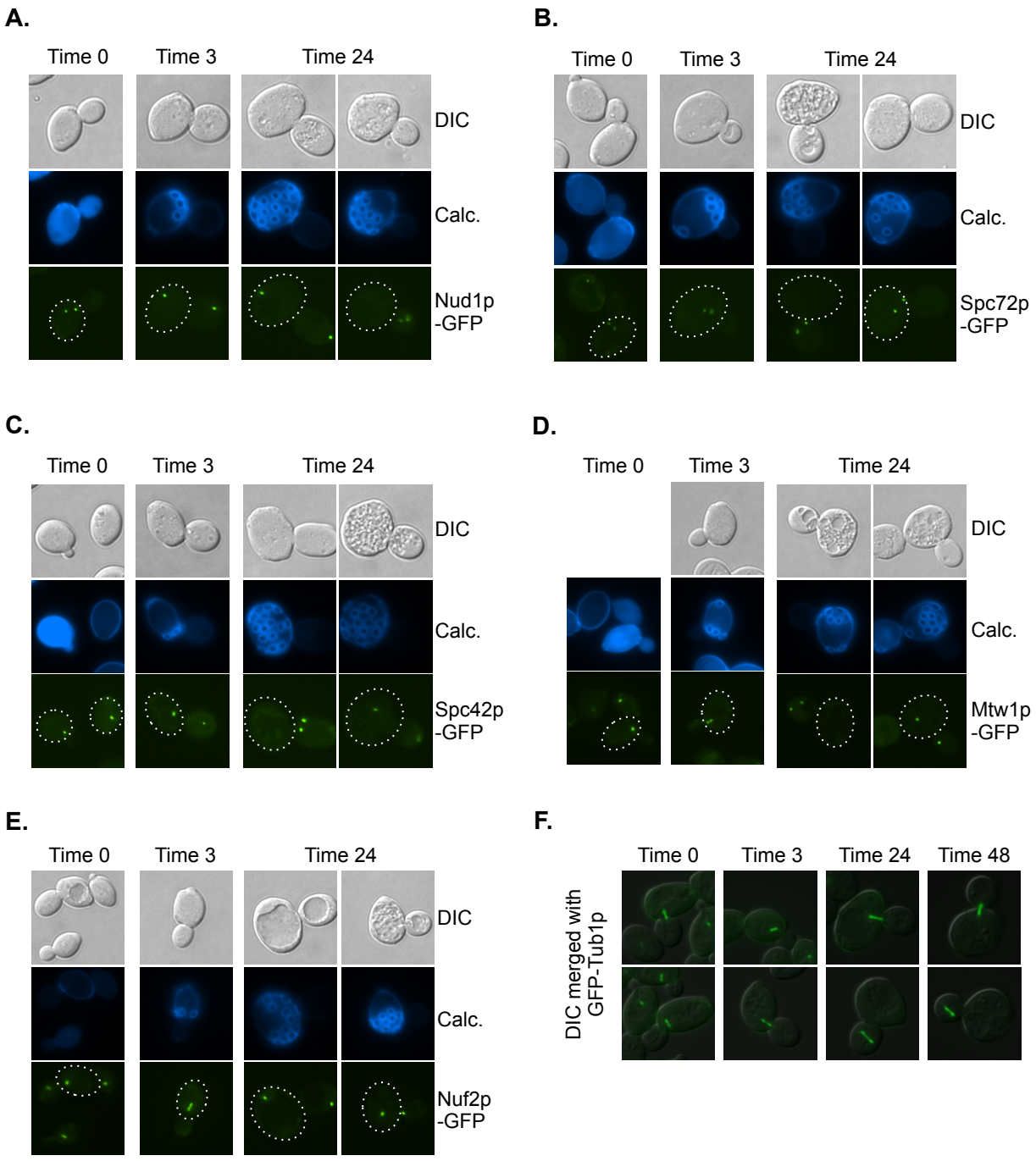

Figure 3.9. Missegregation of nuclear contents was observed in a subset of replicatively aged cells. Cells expressing chromosomally tagged spindle pole body markers Nud1p-GFP, Spc72p-GFP, and Spc42p-GFP, kinetochore markers Mtw1p-GFP and Nuf2p-GFP, and ectopic N-terminally tagged Tub1 were aged and analyzed as described in Figure 2.2. Dotted white lines outline the mother cell. The spindle poles marked by (A) Nud1p-GFP, (B) Spc72p-GFP, and (C) Spc42p-GFP were visualized in fixed and purified mother cells at the indicated timepoints. The kinetochores marked by (D) Mtw1p-GFP and (E) Nuf2p-GFP were visualized in fixed and purified mother cells at the indicated timepoints. (F) The microtubule spindle marked by GFP-Tub1p was visualized in rhodamine-labeled live cells at the indicated timepoints. These components of the mitotic apparatus: the spindle pole bodies, kinetochores, and microtubule spindle all suggest nuclear missegregation occurs in a subset of old cells.

A.

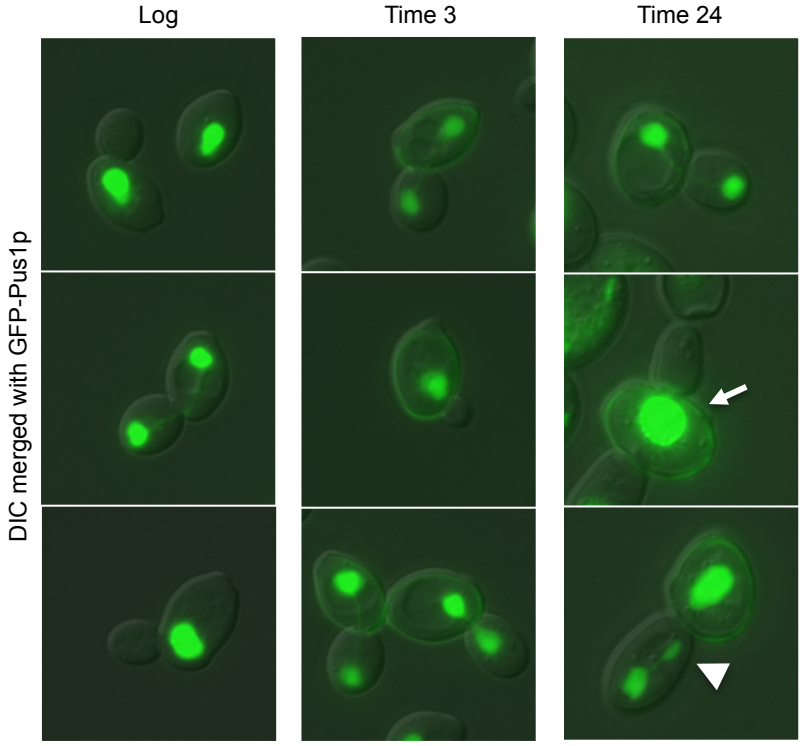

Figure 3.10. The diffusible nucleoplasmic marker GFP-Pus1p revealed an age-dependent increase in the frequency of nuclear or mitotic abnormalities. Cells expressing Pus1p fused to GFP at its N-terminus from its endogenous locus were aged and analyzed as described in Figure 2.2. GFP-Pus1p cells were labeled with rhodamine, aged using the MEP, and visualized at the indicated timepoints. A subset of cells at more advanced replicative ages (i.e. time 24 hour cells) exhibited nuclear or mitotic abnormalities. Old cells often contained a large nucleus in the mother cell despite possessing a large bud (white arrow) or exhibited evidence of an abnormal or delayed mitosis (white arrowhead).

A.

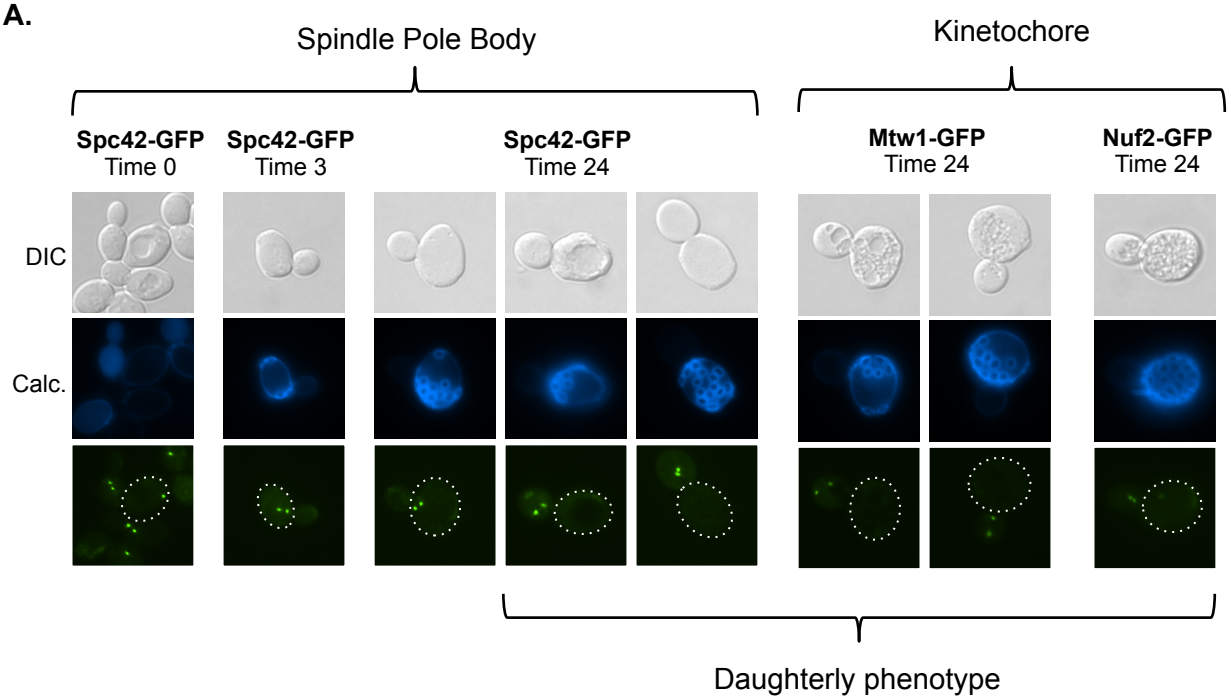

B.

	Total abnormal	Aberrant SPB number	Daughterly phenotype	Elongated in mother	Aberrant SPB position	Abnormal bud mophology
Spc42p-GFP Time 3	7/500 1.4%	4/500 0.8%	0/500 0%	0/500 0%	3/500 0.6%	8/500 1.6%
Spc42p-GFP Time 24	71/550 12.9%	43/550 7.8%	2/550 0.4%	8/550 1.5%	18/550 3.3%	89/550 16.2%

Spc42-GFP merged with DIC Time 24

Figure 3.11. Various mitotic abnormalities occur in old cells. (A) Cells expressing the spindle pole body marker Spc42p-GFP or kinetochore markers Mtw1p-GFP and Nuf2p-GFP, were biotinylated, aged with the MEP, fixed, purified using magnetic bead separation, and visualized at the indicated timepoints. A subset of old time 24 hour cells exhibited a daughterly phenotype where both spindle pole bodies or both sets of kinetochores are localized in the bud. Dotted white lines outline the mother cell. (B) Old cells exhibit various types of spindle pole body and bud morphology abnormalities. Cells expressing Spc42p-GFP were biotinylated, cultured without MEP induction, and purified live by magnetic bead separation at time 3 hours for young cells, and at time 12 and 24 hours for old cells. Time 3 and time 24 hour cells were subjected to high-resolution microscopy and scored for spindle pole body position, number, and segregation. Abnormal bud morphologies were also noted. Cells were categorized as exhibiting a daughterly phenotype, spindle elongation in the mother cell, having other abnormalities in SPB number, or otherwise having aberrant spindle pole body position. Representative images of each category are shown below the table.

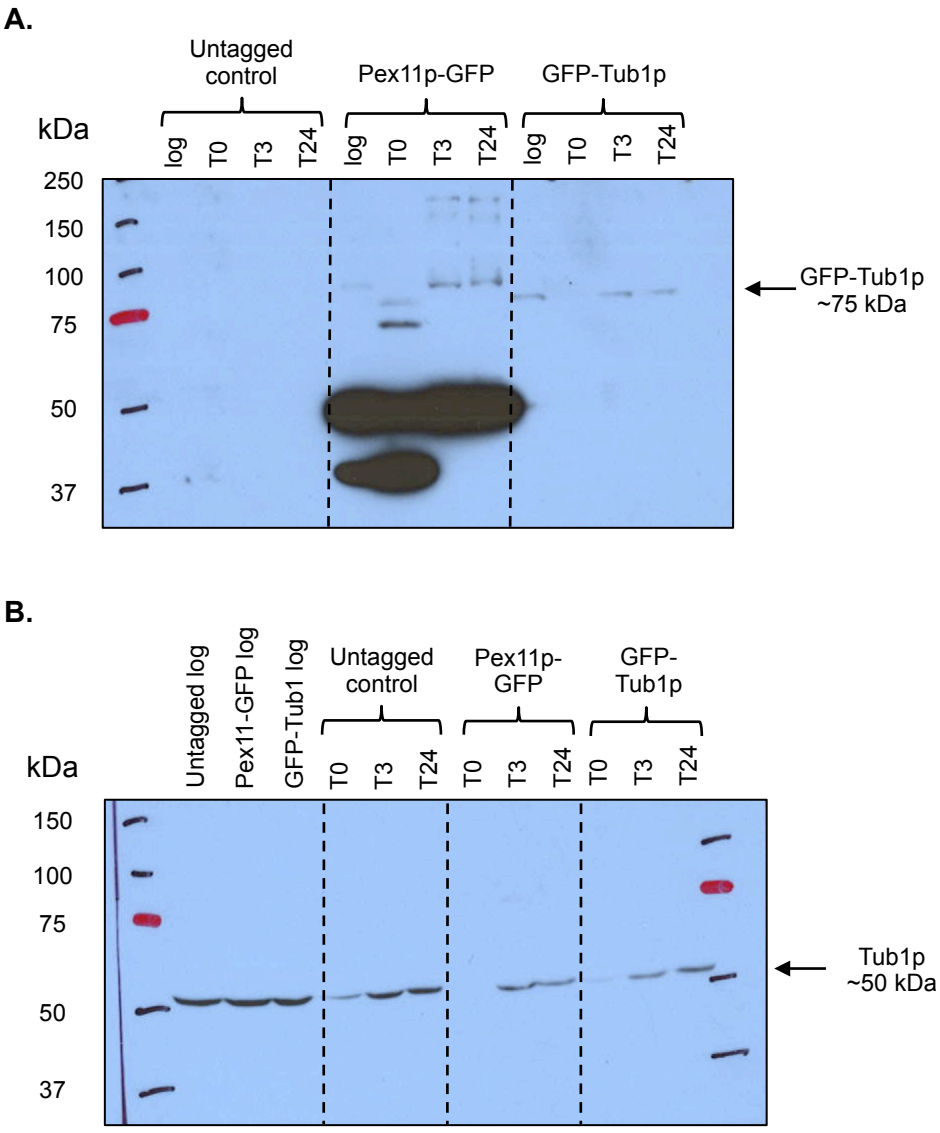

Figure 3.12. The quantity of tubulin increased with replicative age. Untagged, Pex11p-GFP, and GFP-Tub1p cells were biotinylated, aged using the MEP, harvested at the indicated timepoints, fixed with RNALater, and purified using magnetic bead separation. Total protein was extracted from cells. Equal quantities of cell lysate were loaded and examined by Western blot analysis using an (A) anti-GFP antibody and using an (B) anti-tubulin antibody.

Chapter IV: Chronology and correlation of selected age-associated phenotypes

A similar approach to the live-cell screen (**Figure 2.1B**) was utilized in strains containing multiple organelle markers in order to 1) determine the chronology of the phenotypes during aging, with the idea that early phenotypes may represent causative events and later phenotypes might reflect downstream effects or terminal events for the cell, 2) determine if certain phenotypes are related, and 3) determine if any of the phenotypes are mediated by the few known pathways involved in replicative aging (topic of Chapter V).

The primary fixed- and live-cell screens in addition with the more detailed characterization of each of the organelles with replicative age showed that the most robust age-associated phenotypes are nucleolar fragmentation, mitotic defects, increased peroxisome number, decreased peroxisome size, and vacuolar fragmentation. Determination of the chronology of these phenotypes will provide insight into which morphological changes could represent causative changes and which are more likely downstream consequences of the aging process. To better resolve the timeline of events, I also introduced a marker for the mitochondria (Tom70p-GFP), as mitochondrial fragmentation is one of the earliest occurring and most penetrant age-associated phenotypes (Scheckhuber et al., 2007; Huh et al., 2003a). Mitochondria begin as mostly tubular structures in exponentially growing cells. After several divisions, fragmentation begins to occur. Nearly all cells at time 24 hours exhibit fragmented mitochondria and often contain aggregates (**Figure 4.1**) (Hughes & Gottschling, 2012).

To ascertain the relative timing and relationships between the various phenotypes, MEP strains were constructed that contain marker proteins for two different organelles using GFP and mCherry fluorescent protein fusions. These double-tagged strains were constructed in many combinations to best deduce the relative timing of the most robust age-associated events (Appendix G). Double-tagged cells were aged using the MEP and approximately 10-20 cells (fewer if imaged using Deltavision) at each timepoint (log-phase prior to labeling, and at 0, 3, 24 and 48 hours after MEP induction) were scored for morphology of both markers. Time 48 hours corresponds to our strain's median replicative lifespan (Lindstrom and Gottschling, 2009a). Analysis of double-tagged strains with replicative age not only provided additional information regarding the timing of each individual organelle and the relative timing of each pair of organelles, it also revealed novel relationships between certain phenotypes.

Results for each of the double-tagged strains are described below, including the method used to obtain and identify aged mother cells. Information compiled from all the experiments will be described at the end of this section.

Peroxisomes (Pex11p) and Mitochondria (Tom70p)

Both Tom70p-GFP/Pex11p-mCherry and Pex11p-GFP/Tom70p-mCherry strains were scored for changes in age-associated morphology. Cells were biotinylated, aged using the MEP, fixed, purified and imaged using three-dimensional microscopy with deconvolution. In the Tom70p-GFP/Pex11p-mCherry strain, the percent of cells exhibiting mitochondrial fragmentation at log, time 0, 3, 24, and 48 was 0% (n=17), 12.5% (n=16), 4.2% (n=24), 100% (n=9) and 100% (n=4), respectively. The increase in fragmentation between 0 and 24 hours is statistically significant ($p<0.05$). The timing and severity of the mitochondrial fragmentation was similar in the Pex11-GFP/Tom70-mCherry background. The percent of cells exhibiting fragmented mitochondria are 0% (n=17) for log-phase cells, 5.6% (n=18) at time 0 hours, 3.8% (n=26) at 3 hours, 100% (n=10) at 24 hours, and 100% (n=5) at 48 hours. The increase in fragmentation between 3 and 24 hours is statistically significant ($p<0.05$). The average number of peroxisomes in the Tom70p-GFP/Pex11p-mCherry expressing strain is 7 (n=17) before biotinylating, 10 (n=16) at time 0 hours, 11 (n=24) at 3 hours, 27 (n=9) at 24 hours, and 27 (n=4) at 48 hours. The increase between time 0 and time 24 is statistically significant ($p<0.0001$). For the Pex11p-GFP/Tom70p-mCherry strain, the average number of peroxisomes prior to labeling was 6 (n=17), 7 (n=18) at time 0 hours, 9 (n=26) at 3 hours, 22 (n=10) at 24 hours, and 28 (n=5) at 48 hours. The increase between time 0 and 24 hours is statistically significant ($p<0.05$). These findings are summarized graphically in **Figure 4.2**. Both mitochondrial and peroxisomal phenotypes occurred at similar times and to a similar degree in both strains. Because mitochondrial fragmentation was entirely penetrant at time 24 and 48 hours, all cells exhibiting the peroxisome phenotype also had fragmented mitochondria (**Figure 4.2C**). However, the opposite is not true. A subset of old mother cells were found to have fragmented mitochondria but few peroxisomes, suggesting that the peroxisome phenotype cannot cause mitochondrial fragmentation. That mitochondrial fragmentation could cause peroxisome number expansion, with some phenotypic lag, cannot be eliminated.

Peroxisomes (Pex11p) and Vacuoles (Vph1p)

Cells expressing Pex11p-GFP and Vph1p-mCherry were biotinylated, aged using the MEP, purified live in media, and examined using simple epifluorescence microscopy. Ten cells were

scored at each timepoint. The average number of peroxisomes prior to labeling was 5, 5 at time 0 hours, 5 at 3 hours, 17 at 24 hours, and 27 at 48 hours. The increase in peroxisome number between time 0 and 24 hours and the increase between 24 and 48 hours are statistically significant ($p<0.05$). The timing and degree of increase is similar to other experiments. Mother cells were also scored for fragmentation at the same timepoints. The percent of cells with fragmented vacuoles prior to biotinylation, at time 0, 3, 24, and 48 hours after MEP induction was 0%, 0%, 0%, 20%, and 100%, respectively. The increase in the incidence of vacuole fragmentation is not statistically significant until time 48 hours ($p<0.05$). These findings are summarized graphically in **Figure 4.3**. At time 24 hours, all cells with fragmented vacuoles also have more than 20 peroxisomes. At time 48 hours, all cells with more than 20 peroxisomes also have fragmented vacuoles (**Figure 4.3C**). This suggests that the age-associated peroxisome increase and the age-associated fragmentation of the vacuole may be independent phenotypes.

Nucleus (Pus1) and Nucleolus (Nop58)

GFP-Pus1p and Nop58p-mCherry expressing cells were labeled with Dylight 350, aged with the MEP, and scored for nuclear morphology and localization and nucleolar fragmentation using simple epifluorescence microscopy. No nuclear abnormalities or fragmented nucleoli were detected prior to labeling or at time 0 or 3 hours (n=28, 20, and 20, respectively). At time 24 hours, 10% of cells showed a severe nuclear abnormality and 30% of cells had a large nucleus (n=20). Examining the nucleolus of the same cells, 25% had a fragmented nucleolus. All cells with a fragmented nucleolus also had an enlarged nucleus. At time 48 hours, 35% of cells showed a severe nuclear abnormality and 25% of cells had a large nucleus (n=20). Examining the nucleolus in those same cells, 65% contained a fragmented nucleolus. Of all the cells with a fragmented nucleolus, only one cell did not also have an enlarged or abnormal nucleus. Both nuclear and nucleolar abnormalities exhibit statistically significant increases between time 0 and 24 hours ($p<0.05$). The increase in the frequency of nuclear abnormalities from time 24 to time 48 hours is also significant ($p<0.05$). These findings are summarized in **Figure 4.4**. Together, these results suggest a correlation between nuclear enlargement and abnormality with nucleolar fragmentation.

Nucleus (Pus1) and Mitochondria (Tom70)

Cells expressing GFP-Pus1p and Tom70p-mCherry were biotinylated, aged using the MEP, purified live in media, and examined using simple epifluorescence microscopy. Cells were scored for nuclear abnormality prior to labeling and at times 0, 3, 24 and 48 hours after MEP

induction. The nucleus was abnormal in 0% (n=20), 0% (n=20), 4.5% (n=22), 22.7% (n=22) and 53.8% (n=26) of cells at each timepoint, respectively. The mitochondria was fragmented in 0% of cells prior to labeling, 0% of cells at time 0 hours, 31.8% of cells at time 3, and 100% of cells at time 24 and 48 hours. Because of the extreme penetrance of the mitochondrial phenotype at advanced replicative ages, the only conclusion that can be made is that an abnormal nucleus is not required for mitochondrial fragmentation. These findings are summarized in **Figure 4.5**.

Nucleus (Pus1) and Vacuole (Vph1)

Cells expressing GFP-Pus1p and Vph1p-mCherry were biotinylated, aged using the MEP, purified live in media, and examined using simple epifluorescence microscopy. Cells were scored for nuclear abnormality prior to labeling and at times 0, 3, 24 and 48 hours after MEP induction. The nucleus was abnormal in 0% (n=20), 0% (n=20), 0% (n=20), 18.2% (n=22) and 51.6% (n=31) of cells at each timepoint, respectively. The vacuole was fragmented in 0% of cells prior to labeling, 0% of cells at time 0 hours, 10% of cells at time 3, 22.7% of cells at time 24, and 74.2% of cells at time 48. No cells at time 24 hours shared both phenotypes, suggesting that the two phenotypes occur independently. These findings are summarized in **Figure 4.6**.

Nucleolus (Nop58) and Mitochondria (Tom70)

Nop58p-GFP and Tom70p-mCherry cells were biotinylated, aged with the MEP, fixed, purified and imaged using three-dimensional microscopy with deconvolution. The nucleolus and mitochondria both fragmented with approximately the same kinetics as was observed before. Timepoints were taken prior to biotinylation and 0, 3, 24 and 48 hours after MEP induction. 0% (n=35), 0% (n=23), 6.3% (n=32), 62.5% (n=8) and 60% (n=10) of cells were observed to have a fragmented nucleolus, respectively. The mitochondria were also scored in each of those cells. The percent of cells containing fragmented mitochondria are as follows: 5.7% prior to labeling, 0% at MEP induction, 37.5% at time 3 hours, 100% at time 24 hours and 100% at time 48 hours. These findings are summarized graphically in **Figure 4.7**. Both mitochondrial and nucleolar phenotypes occurred at similar times and to a similar degree in both strains. Because mitochondrial fragmentation was entirely penetrant at time 24 and 48 hours, all cells exhibiting a fragmented nucleolus also had fragmented mitochondria. However, the opposite is not true. A subset of old mother cells were found to have fragmented mitochondria but an unfragmented nucleolus, suggesting that the nucleolar fragmentation cannot induce mitochondrial fragmentation.

Nucleolus (Nop58) and Vacuole (Vph1)

Nop58p-GFP and Vph1p-mCherry cells were biotinylated, aged with the MEP, purified live in media and imaged using simple wide-field epifluorescence microscopy. The nucleolus and the vacuole fragmented with similar kinetics as previously described. No cells prior to labeling and at time 0 and 3 hours after MEP induction had a fragmented nucleolus or fragmented vacuoles. At time 24 hours, 45% of cells had a fragmented nucleolus and 40% had fragmented vacuoles (n=20). At time 48 hours, 69% of cell had a fragmented nucleolus and 92% had fragmented vacuoles. However, the phenotypes were only partially overlapping at either timepoint, suggesting that nucleolar fragmentation and vacuolar fragmentation are unlikely to be interrelated. These findings are summarized graphically in **Figure 4.8**.

Mitochondria (Tom70) and Vacuole (Vph1)

Visualization of Tom70p-GFP and Vph1p-mCherry in the same strain with replicative age revealed that fragmentation of these two organelles is likely to be related. Cells were biotinylated, aged with the MEP, purified live in media and imaged using simple epifluorescence microscopy. The mitochondria and vacuoles were normal in all cells prior to labeling and at MEP induction (n=10 for both). At time 3 hours, 10% of cells exhibited fragmented mitochondria whereas the vacuoles remained normal (n=10). At time 24 hours, 90% of cells contained fragmented mitochondria, and 40% of cell contained fragmented vacuoles (n=10). Finally, at time 48 hours, 100% of cells contained both fragmented mitochondria and fragmented vacuoles (n=10). Fragmented vacuoles were never observed in the absence of mitochondrial fragmentation, suggesting that mitochondrial fragmentation occurred first, and may cause the vacuoles to fragment. These findings are summarized in **Figure 4.9**.

Spindle Pole Body (Spc42) and Nucleolus (Nop58)

Cells expressing the spindle pole body marker Spc42p-GFP, a proxy for nuclear and DNA segregation, and expressing the nucleolar marker Nop58p-mCherry were labeled with Dylight 350, aged with the MEP, and visualized using simple epifluorescence microscopy. Cells were scored for SPB abnormalities in position and/or number and for nucleolar fragmentation prior to labeling and times 0, 3, 24 and 48 hours. Prior to labeling (n=43) and at MEP induction (n=42), 0% of cells were found to be abnormal. At time 3, 24 and 48 hours, 4.7% (n=42), 26.8% (n=41) and 36.4% (n=22) exhibited abnormal SPBs, respectively. 0%, 48.8% and 72.7% of these same cells contained a fragmented nucleolus. These findings are summarized in **Figure 4.10**.

Abnormal SPB position and/or number is likely to occur independently of nucleolar fragmentation because only a subset of each population contain both phenotypes.

Spindle (Tub1) and Spindle Pole Body (Spc42)

GFP-Tub1p and Spc42p-mCherry mark two major components of the mitotic spindle. Cells were labeled with Dylight 350, aged with the MEP, and visualized using wide-field epifluorescence microscopy. The spindle pole bodies are functional throughout replicative aging as they are always associated with the microtubule spindle. In other words, abnormalities detected by visualizing the microtubule spindle are always apparent by localizing the spindle pole bodies, and vice versa. No abnormalities were detected until time 24 hours (n=20 prior to labeling, n=19 at time 0, and n=20 at time3). At time 24, 40% of cells showed some defect of the mitotic spindle (n=20). This number increased to 60% at time 48 hours (n=20). These findings are summarized in **Figure 4.11**.

Summary of the relative chronology and relationships between age-associated phenotypes

These results, when taken all together, and organized by each individual marker reveal an approximate timeline of events during the aging process. Mitochondrial fragmentation precedes the other age-associated phenotypes. Nearly 100% of cells at time 24 have fragmented mitochondria (**Figure 4.12A**). In contrast, vacuolar and nucleolar fragmentation occur later (**Figure 4.12B,C**). Vacuolar fragmentation is also penetrant with nearly all cells exhibiting fragmented vacuoles by time 48 hours. The kinetics of nucleolar fragmentation in the aging population takes on a slower trajectory. The latest events seem to be abnormal localization and morphology of the nucleus. Mitotic defects occur at a lower frequency at time 24 hours compared to the other phenotypes, and become more common at time 48 hours. The occurrence of peroxisome number expansion is more difficult to place in the timeline because the phenotype is incremental and not binary in nature. Depending on the criteria for phenotype, the timing of the peroxisome phenotype is most similar to the timing of the mitochondrial fraction (>10 peroxisomes) or most similar to the nucleolar and vacuolar fragmentation (>20 peroxisomes) in that not all cells exhibit the phenotype at time 24 hours and most cells exhibit the phenotype at time 48 hours. The compilation of all the data sorted by organelle is found in **Figure 4.12**.

In the double-tagged experiments, the proportion of cells that exhibited two phenotypes compared to the proportion of cells that exhibited only one phenotype indicates if and how the

two phenotypes might be related. The most striking example is the relationship between mitochondrial and vacuolar fragmentation. Vacuolar fragmentation is never observed in the absence of mitochondrial fragmentation, suggesting that the mitochondrial phenotype always precedes the vacuolar phenotype and may cause or be required for vacuolar fragmentation. The other two phenotypes that indicate interrelatedness are enlargement of the nucleus and nucleolar fragmentation. Most cells with an enlarged nucleus also possess a fragmented nucleolus. This may suggest a response by the cell to increase its nuclear volume to accommodate an expanding nucleolus. Analysis of the double-tagged strains provided vital information about the relative timing of the age-associated phenotypes and was also able to provide some insight into which organellar changes might be biologically related. However, these experiments were not ideal for understanding how potentially connected phenotypes might be mechanistically related in the context of replicative aging. To address how the various aging pathways might affect different subsets of organelles, I examined each of the age-associated phenotypes discussed in this section in conditions and in mutants known to modulate lifespan.

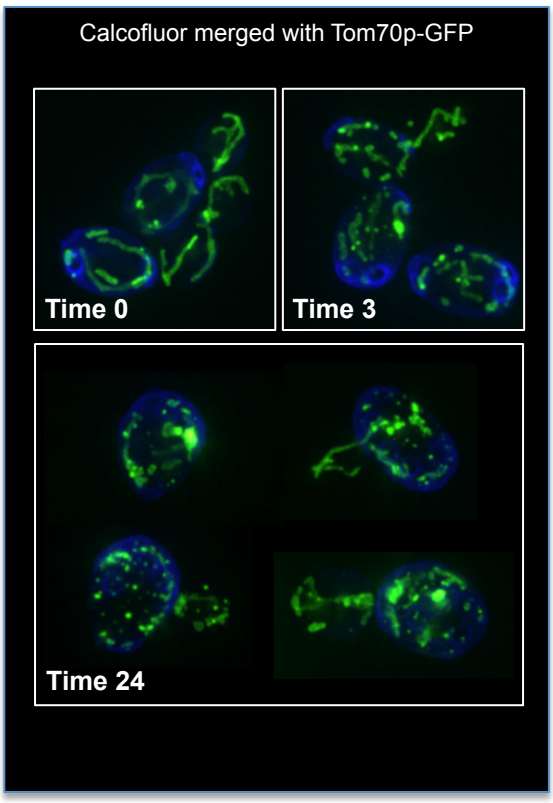

Figure 4.1. Age-induced mitochondrial fragmentation. Cells expressing chromosomally tagged Tom70p-GFP were biotinylated, aged using the MEP, fixed, purified, and subjected to high-resolution microscopy at times 0, 3, and 24 hours. Images were acquired at 0.25 μm intervals, deconvolved, and shown here as maximum intensity projections. Mitochondria are mostly tubular at time 0, begin to fragment between time 3 and 24 hours, and nearly all time 24 hour cells contain fragmented mitochondria.

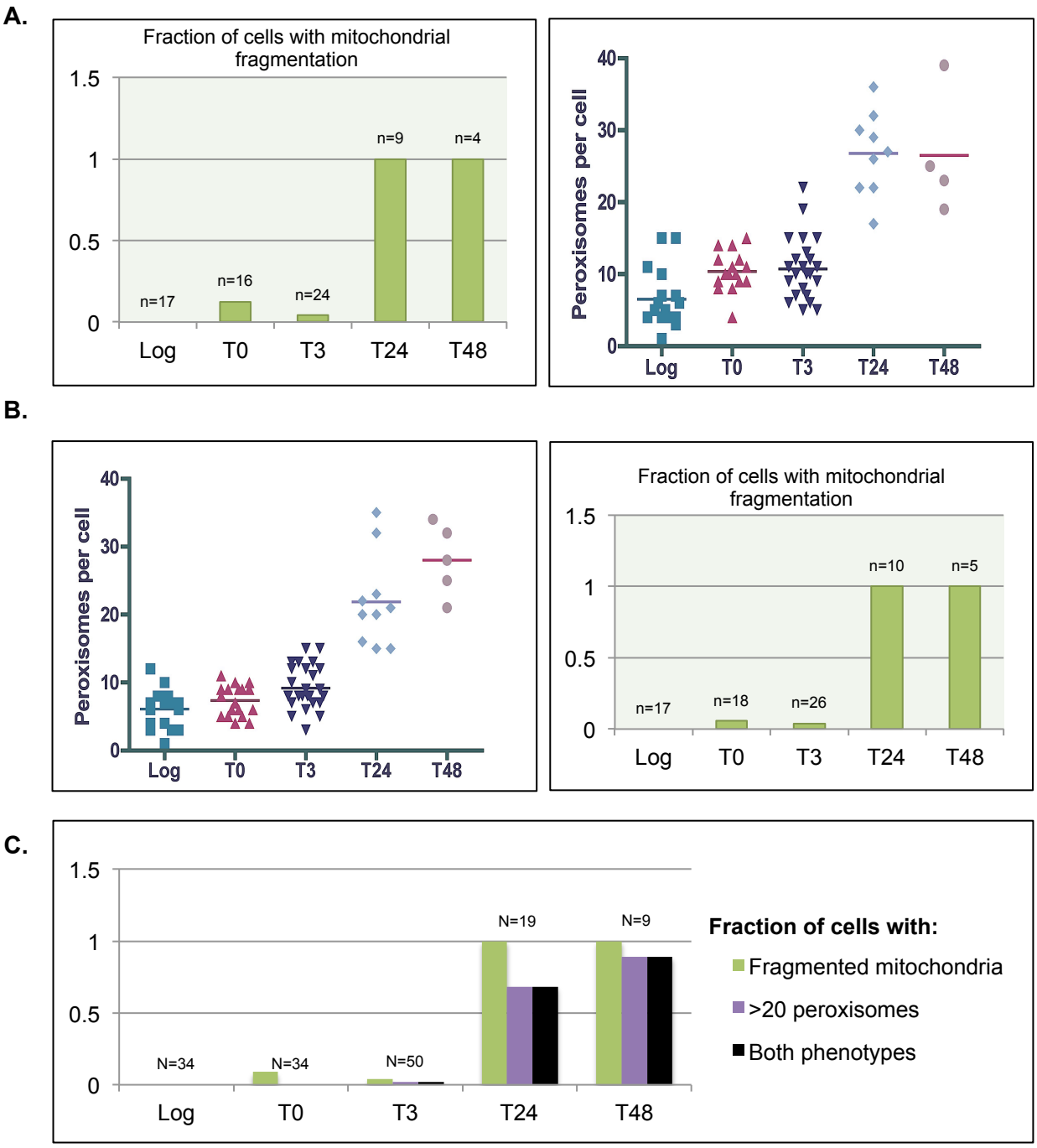

Figure 4.2. Mitochondria fragmentation and the increased peroxisome numbers are both prevalent at time 24 hours, however mitochondrial fragmentation is much more penetrant. Cells expressing both (A) Tom70p-GFP and Pex11p-mCherry or (B) Pex11p-GFP and Tom70p-mCherry, were biotinylated, aged, harvested at the indicated timepoints, and purified live using magnetic bead separation. Cells were visualized live and scored for mitochondrial fragmentation and number of peroxisomes. The number of cells scored is indicated above each bar graph or by the number of dots on the dot plot. Mitochondrial fragmentation was present in nearly every cell by time 24 hours. The increase in peroxisome number is also apparent at time 24 hours, however, is not found in every cell. The proportion of cells with increased peroxisome number increases from time 24 to 48 hours. (C) Graph of the fraction of cells with mitochondrial fragmentation, greater than 20 peroxisomes and the fraction of cells that contain both phenotypes at each timepoint. At time 24 and 48 hours, all cells that contain more than 20 peroxisomes also have fragmented mitochondria.

A.

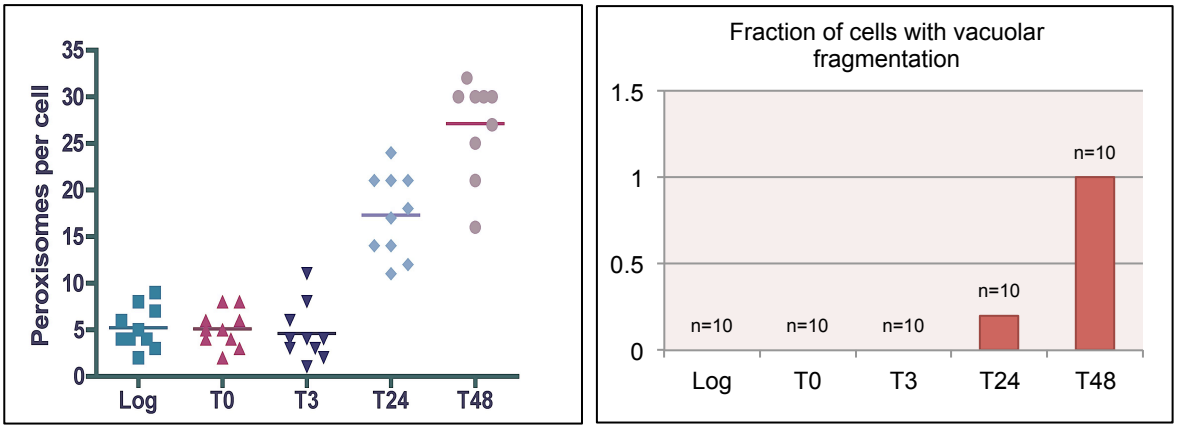

B.

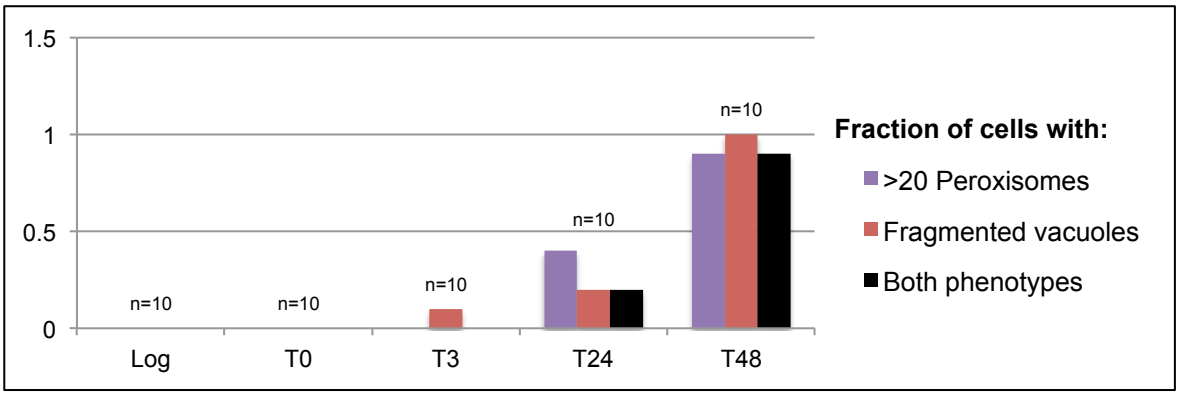

Figure 4.3. The onset of increased peroxisome number is earlier than vacuolar fragmentation. (A) Cells expressing both Pex11p-GFP and Vph1p-mCherry were biotinylated, aged, harvested at the indicated timepoints, and purified live using magnetic bead separation. Cells were visualized live and scored for peroxisome number and changes in vacuolar morphology. The number of cells scored is indicated above each bar graph or by the number of dots on the dot plot. The increase in peroxisome number is apparent at time 24 hours, however, is not found in every cell. The proportion of cells with increased peroxisome number increases from time 24 to 48 hours. Few cells at time 3 and 24 hours have fragmented vacuoles, however, nearly all cells have fragmented vacuoles by time 48 hours. (B) Graph of the fraction of cells with greater than 20 peroxisomes, fragmented vacuoles, and the fraction of cells that contain both phenotypes at each timepoint. At time 24 hours, all cells with fragmented vacuoles also have more than 20 peroxisomes. At time 48 hours, all cells with more than 20 peroxisomes also have fragmented vacuoles.

A.

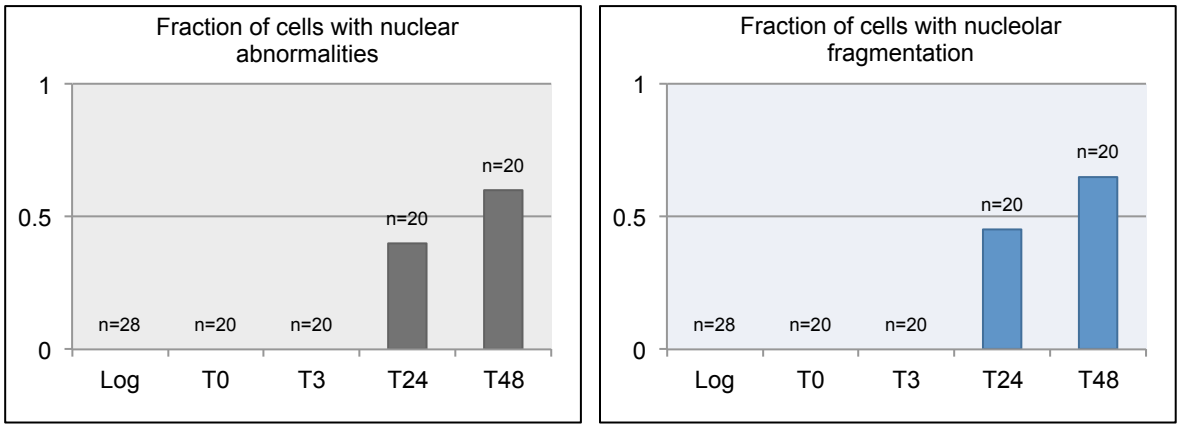

B.

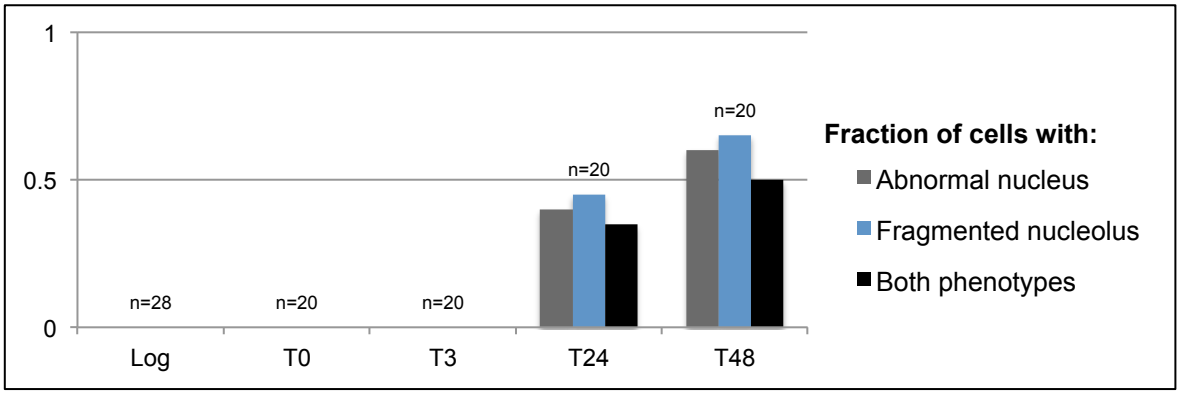

Figure 4.4. The onset and penetrance of nuclear abnormalities and nucleolar fragmentation is similar. (A) Cells expressing both GFP-Pus1p and Nop58p-mCherry were biotinylated, aged, harvested at the indicated timepoints, and purified live using magnetic bead separation. Cells were visualized live and scored for abnormal nuclear morphology or mitosis and fragmentation of the nucleolus. The number of cells scored is indicated above each column on the bar graph. Nuclear abnormalities and nucleolar fragmentation are both detected in approximately 40% of cells at time 24 hours, and increases to approximately 60% at time 48 hours. (B) Graph of the fraction of cells with an abnormal nucleus, a fragmented nucleolus, and the fraction cells that contain both phenotypes at each timepoint. At time 24 and 48 hours, the fraction of cells with both phenotypes is less than either phenotype alone.

A.

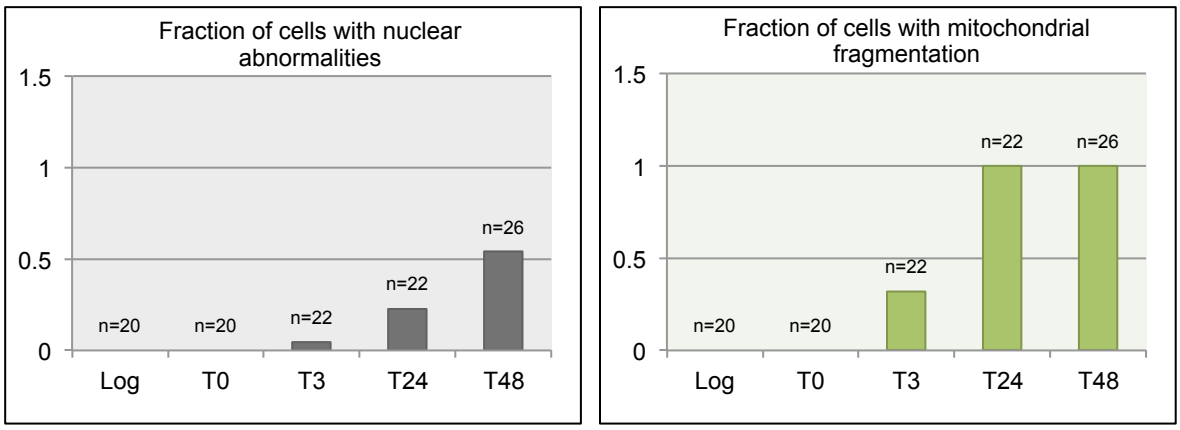

B.

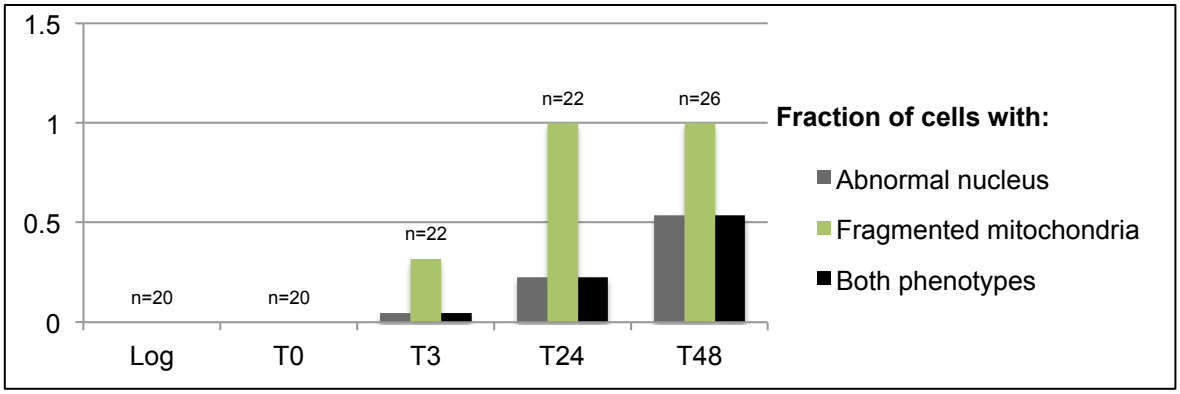

Figure 4.5. Mitochondrial fragmentation is an early and very penetrant phenotype, whereas nuclear abnormalities occur later, and is not present in every cell even at time 48 hours. (A) Cells expressing both GFP-Pus1p and Tom70p-mCherry were biotinylated, aged, harvested at the indicated timepoints, and purified live using magnetic bead separation. Cells were visualized live and scored for abnormal nuclear morphology or mitosis and mitochondrial fragmentation. The number of cells scored is indicated above each column on the bar graph. (B) Graph of the fraction of cells with an abnormal nucleus, fragmented mitochondria, and the fraction of cells that contain both phenotypes at each timepoint. All cells that have an abnormal nucleus also have fragmented mitochondria.

A.

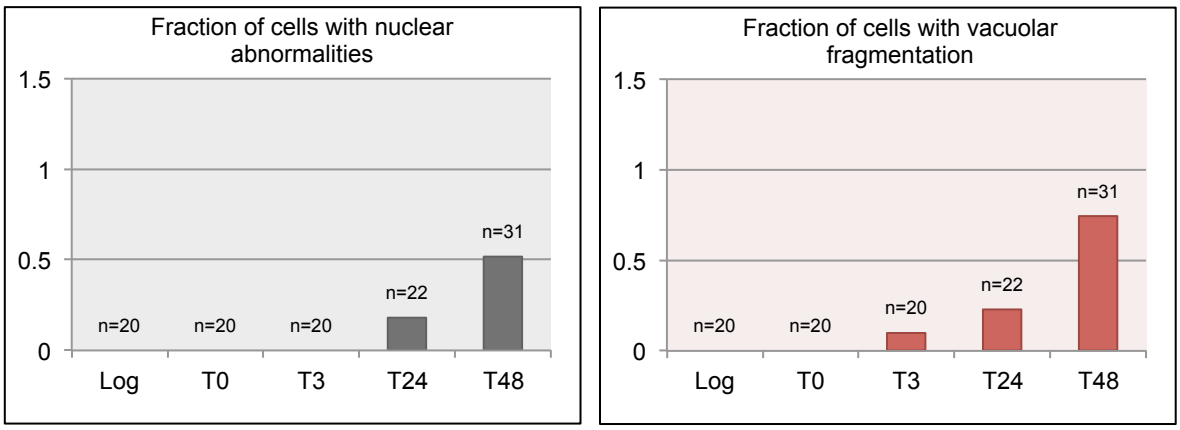

B.

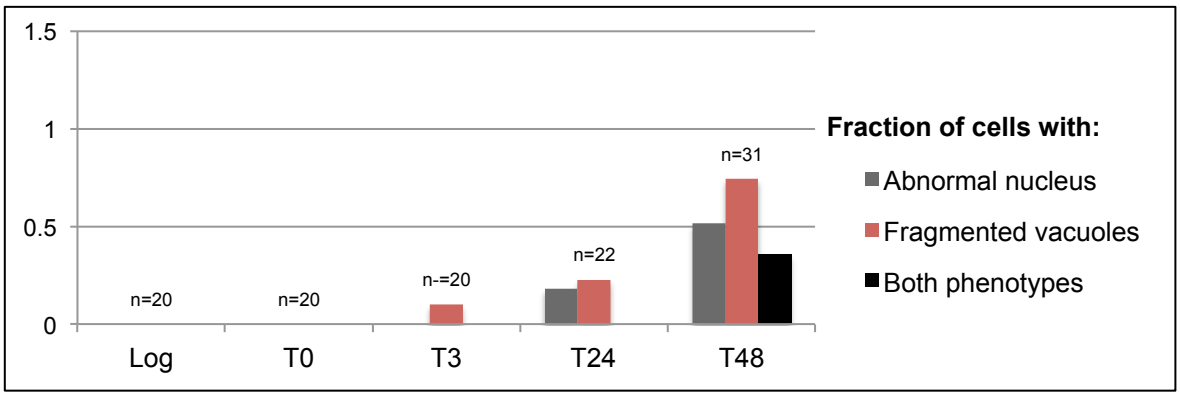

Figure 4.6. Nuclear abnormalities and vacuolar fragmentation affect a similar number of cells at time 24 hours, and affect a greater number of cells at time 48 hours. (A) Cells expressing both GFP-Pus1p and Vph1p-mCherry were biotinylated, aged, harvested at the indicated timepoints, and purified live using magnetic bead separation. Cells were visualized live and scored for abnormal nuclear morphology or mitosis and vacuolar fragmentation. The number of cells scored is indicated above each column on the bar graph. (B) Graph of the fraction of cells with an abnormal nucleus, fragmented vacuoles, and the fraction of cells that contain both phenotypes at each timepoint. The fraction of cells that contain both phenotypes is less than the fraction of cells with either phenotype alone.

A.

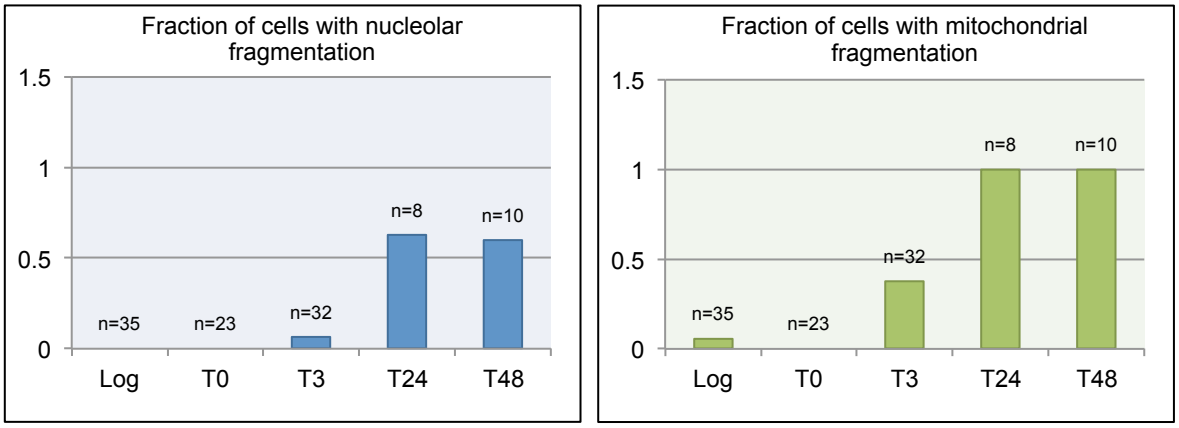

B.

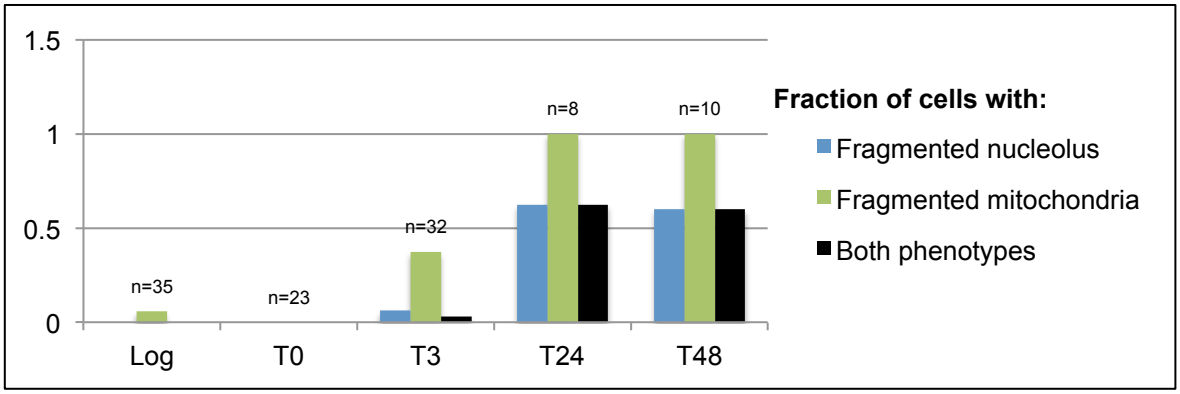

Figure 4.7. Mitochondrial fragmentation is an early and very penetrant phenotype, whereas nucleolar fragmentation occurs later, and is not present in every cell, even at time 48 hours. (A) Cells expressing both Nop58p-GFP and Tom70p-mCherry were biotinylated, aged, harvested at the indicated timepoints, and purified live using magnetic bead separation. Cells were visualized live and scored for nucleolar fragmentation and mitochondrial fragmentation. The number of cells scored is indicated above each column on the bar graph. (B) Graph of the fraction of cells with a fragmented nucleolus, fragmented mitochondria, and the fraction of cells that contain both phenotypes at each timepoint. All cells that have a fragmented nucleolus also have fragmented mitochondria.

A.

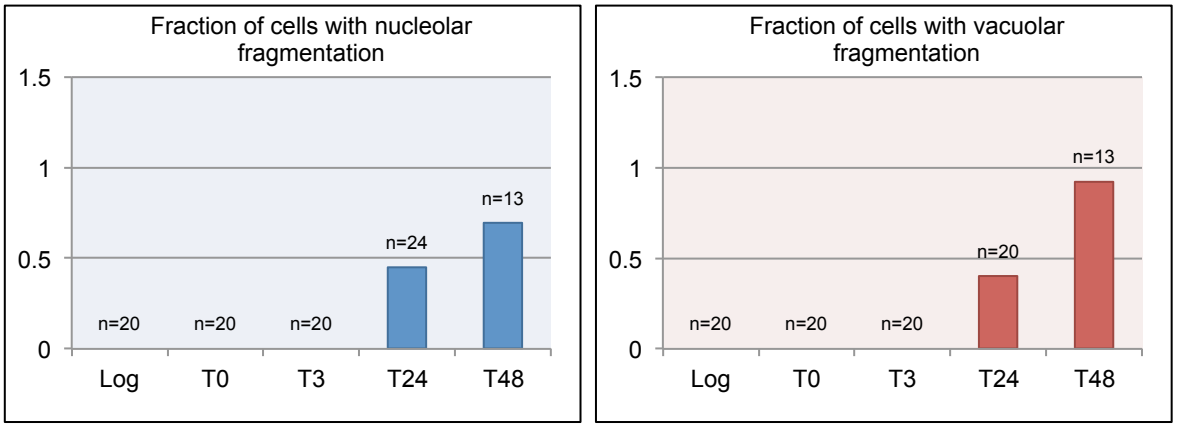

B.

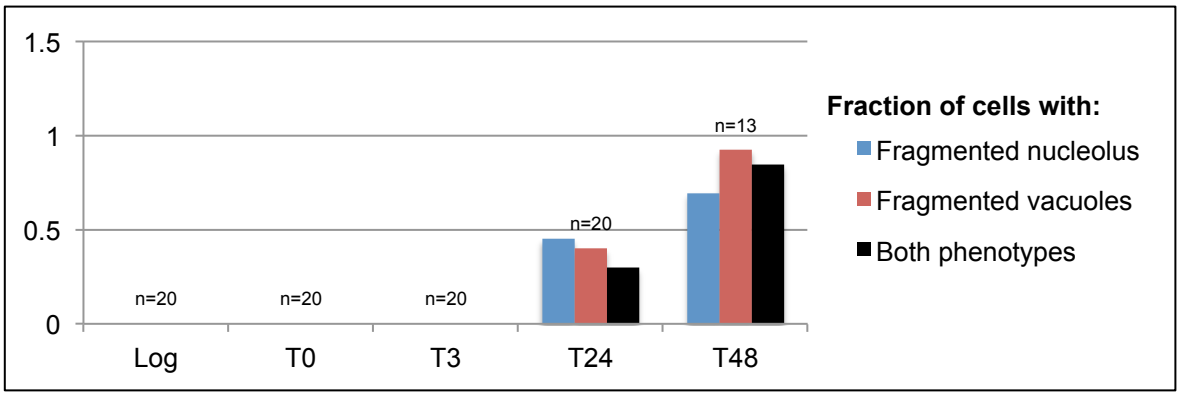

Figure 4.8. Fragmentation of the nucleolus and vacuoles occur in a subset of cells at time 24 hours, and becomes more prevalent at time 48 hours. (A) Cells expressing both Nop58p-GFP and Vph1p-mCherry were biotinylated, aged, harvested at the indicated timepoints, and purified live using magnetic bead separation. Cells were visualized live and scored for nucleolar fragmentation and vacuolar fragmentation. The number of cells scored is indicated above each column on the bar graph. (B) Graph of the fraction of cells with a fragmented nucleolus, fragmented vacuoles, and the fraction of cells that contain both phenotypes at each timepoint.

A.

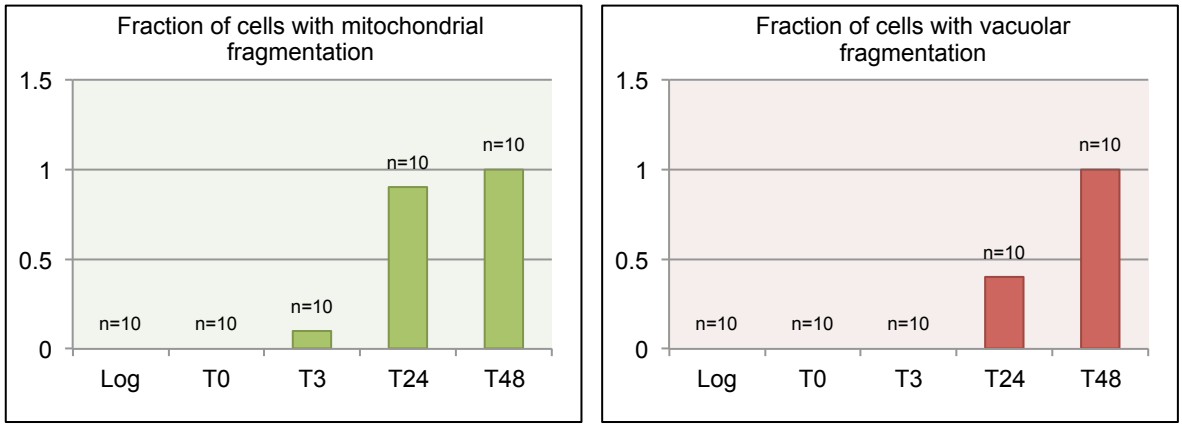

B.

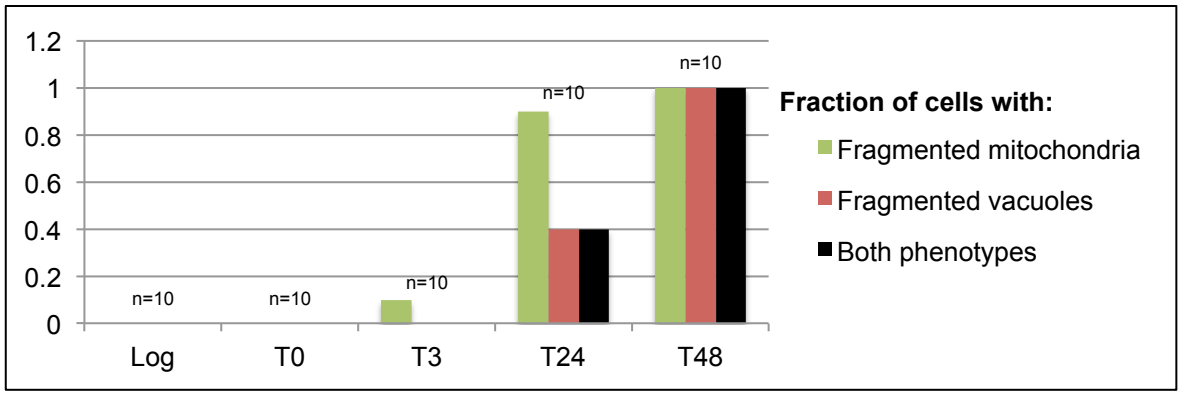

Figure 4.9. Mitochondrial fragmentation is an early and very penetrant phenotype, whereas vacuolar fragmentation occurs later, and is not present in every cell until time 48 hours. (A) Cells expressing both Tom70p-GFP and Vph1p-mCherry were biotinylated, aged, harvested at the indicated timepoints, and purified live using magnetic bead separation. Cells were visualized live and scored for mitochondrial fragmentation and vacuolar fragmentation. The number of cells scored is indicated above each column on the bar graph. (B) Graph of the fraction of cells with a fragmented mitochondria, fragmented vacuoles, and the fraction of cells that contain both phenotypes at each timepoint. All cells that have a fragmented vacuole also have fragmented mitochondria.

A.

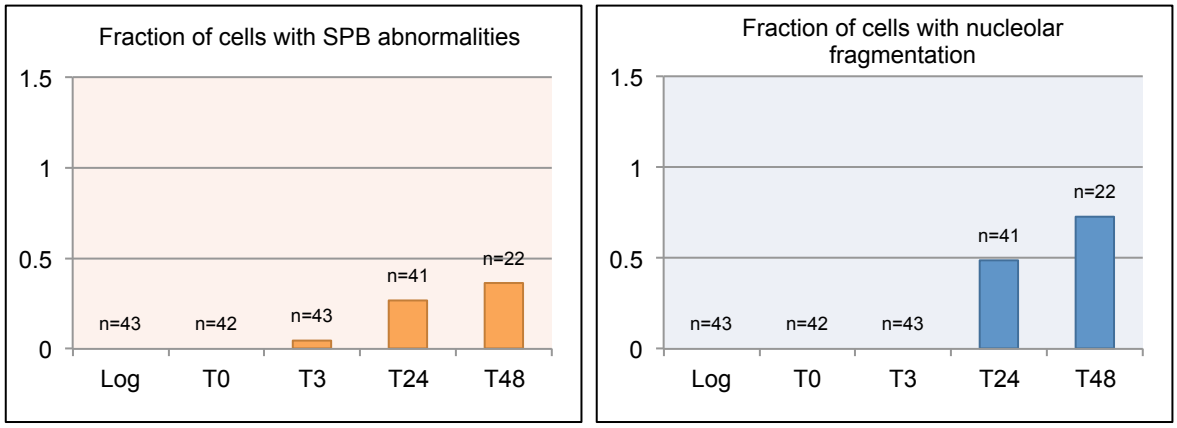

B.

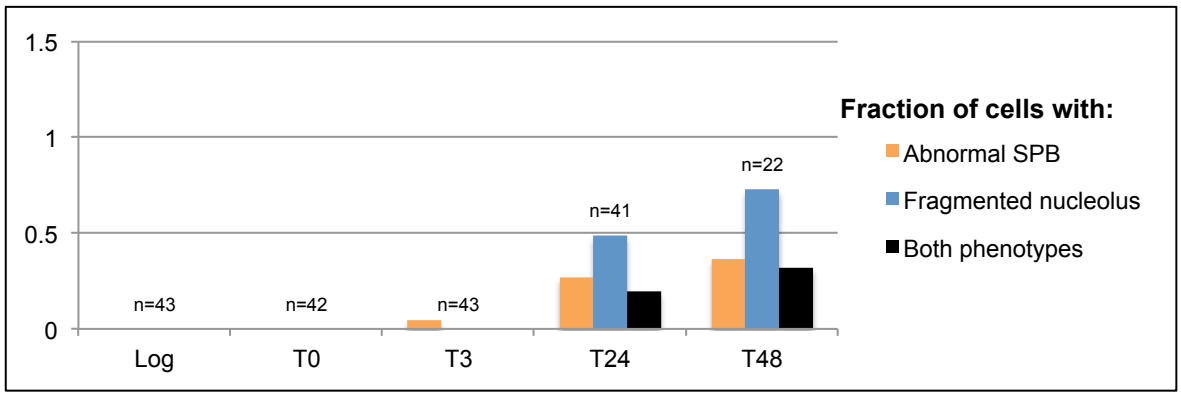

Figure 4.10. Spindle pole body abnormalities and nucleolar fragmentation occur in a subset of cells at time 24 hours, and becomes more prevalent at time 48 hours. (A) Cells expressing both Spc42p-GFP and Nop58p-mCherry were biotinylated, aged, harvested at the indicated timepoints, and purified live using magnetic bead separation. Cells were visualized live and scored for spindle pole body (SPB) abnormalities, such as missegregation and abnormal SPB number, and nucleolar fragmentation. The number of cells scored is indicated above each column on the bar graph. (B) Graph of the fraction of cells with spindle pole body position or number abnormalities, a fragmented nucleolus, and the fraction of cells that contain both phenotypes at each timepoint. The fraction of cells with both phenotypes is less than the fraction of cells with either phenotype alone.

A.

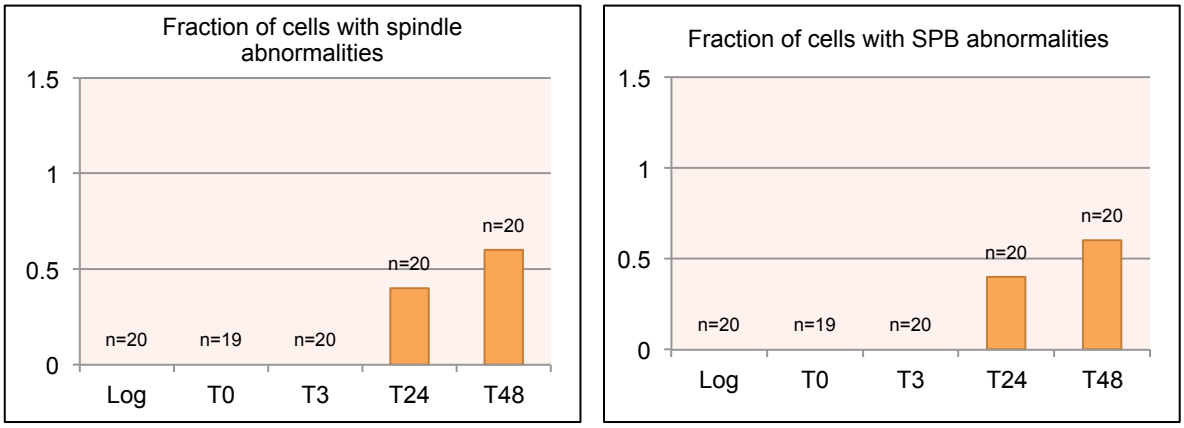

B.

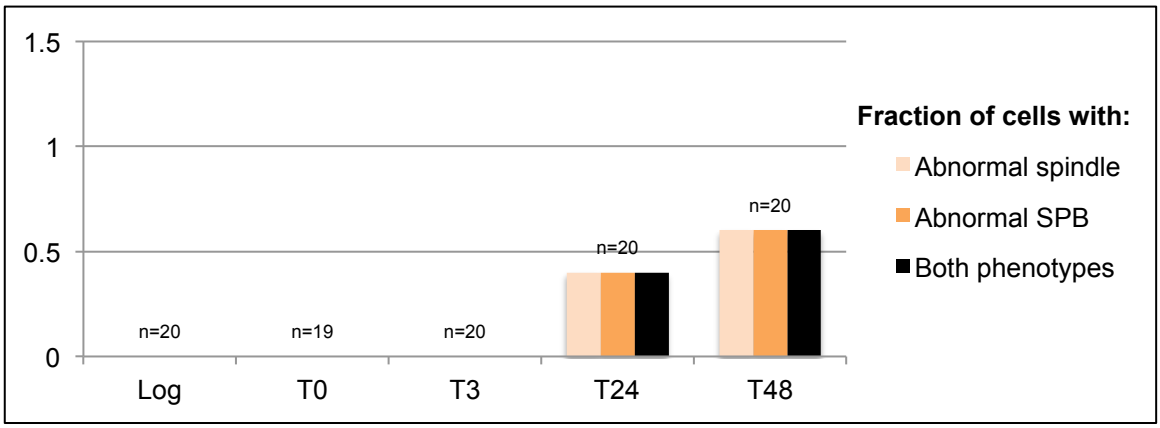

Figure 4.11. Abnormal spindle pole body position or number is always accompanied by an abnormal mitotic microtubule spindle. (A) Cells expressing both GFP-Tub1p and Spc42p-mCherry were biotinylated, aged, harvested at the indicated timepoints, and purified live using magnetic bead separation. Cells were visualized live and scored for spindle pole body (SPB) abnormalities, such as missegregation and abnormal SPB number, and microtubule spindle abnormalities. The number of cells scored is indicated above each column on the bar graph. (B) Graph of the fraction of cells with spindle pole body position or number abnormalities, spindle abnormalities, and the fraction of cells that contain both phenotypes at each timepoint. All cells that have spindle pole body abnormality also have a spindle abnormality.

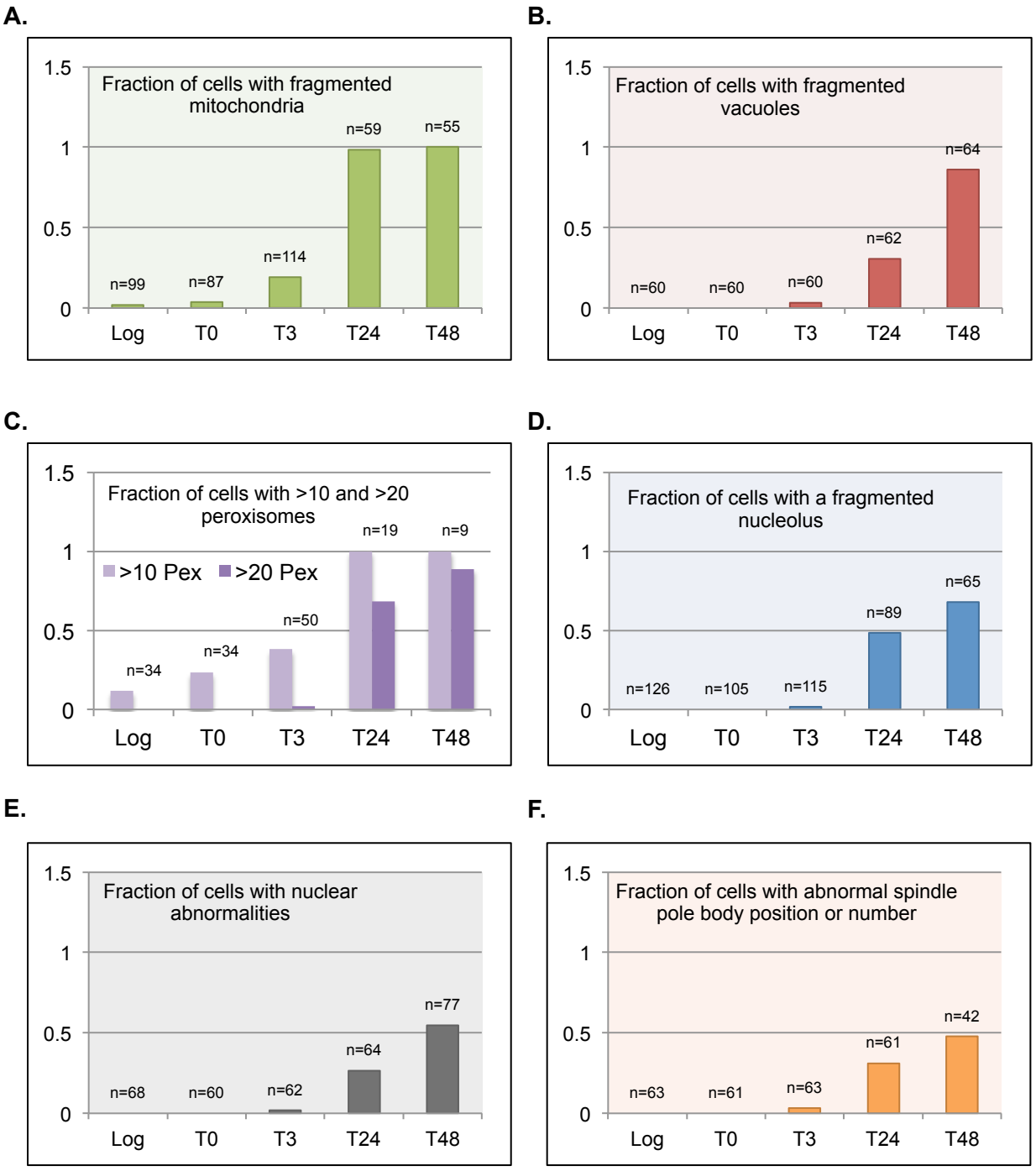

Figure 4.12. Compiled data for each age-associated phenotypes. Data for each organelle from all independent experiments are added and compiled here. (A) Fraction of cells with mitochondrial fragmentation from four independent experiments. (B) Fraction of cells with vacuolar fragmentation from four independent experiments. (C) Fraction of cells with >10 or >20 peroxisomes from two independent experiments (high-resolution). (D) Fraction of cells with nucleolar fragmentation from four independent experiments. (E) Fraction of cells with nuclear abnormalities from three independent experiments. (F) Fraction of cells with abnormal spindle pole body position or number from two independent experiments.

Chapter V: The effects of lifespan-extending conditions on selected age-associated phenotypes

Several pathways have been previously described to modulate replicative aging. By determining how these pathways affect the age-associated changes in organelle morphology (and likely function), I can 1) gain insight into which aging pathways are important for which organelles, 2) uncover evidence of new aging pathways, and 3) determine which organelles are of premier importance as the phenotypes suppressed by the most extreme lifespan extenders may be involved in pathways critical for healthy replication.

To answer these questions, replicatively aging cells were scored for mitochondrial, nucleolar and vacuolar fragmentation, quantitative and qualitative changes in peroxisomes and evidence of nuclear abnormalities and mitotic defects, in one growth condition and multiple mutant backgrounds that confer extended replicative lifespan. These regulators of lifespan were discussed in detail in the introduction, and therefore will only be briefly reviewed here.

Caloric restriction is an evolutionarily conserved method for lifespan extension as various forms of caloric restriction has proven effective to extend the lifespans of higher eukaryotic model organisms, from the worm to the mouse (Steinkraus et al., 2008). In yeast, caloric restriction has been shown to effectively extend lifespan at both 0.5% and 0.05% glucose concentrations. For these experiments, rich media containing 0.5% glucose was used because it did not greatly affect cell growth rates. The mechanism by which caloric restriction extends lifespan has been the topic of great study, and several mutants have been characterized to act as mimetics of caloric restriction. Deletion of the nutrient-signaling G-protein alpha subunit gpa2 is one such mimetic, and the age-associated phenotypes were also characterized in cells lacking gpa2. Both 0.5% caloric restriction and deletion of *GPA2* have been shown to suppress the age-related decline in vacuolar acidity and mitochondrial fragmentation (Steinkraus et al., 2008).

An overexpression screen for genes that suppress the age-associated mitochondrial fragmentation yielded several candidates, including *VMA1*, the gene that encodes subunit A of the V1 portion of the vacuolar H^+-ATPase (Hughes & Gottschling, 2012). *VMA1* overexpression suppresses mitochondrial fragmentation by suppressing the decline in vacuolar acidity that occurs early in the replicative aging process. Furthermore, overexpressing *VMA1* extends lifespan (Hughes & Gottschling, 2012). For these reasons, the various organellar changes were scored in a strain constitutively overexpressing *VMA1* from a chromosomal locus, and compared to a strain expressing an empty vector from the same locus.

Extrachromosomal rDNA circles (ERCs) have been implicated as an aging factor because their accumulation has been correlated with advanced replicative age (D. Sinclair & Guarente, 1997). Deletion of the replication fork block protein Fob1 has been shown to delay the accumulation of ERCs with replicative age by decreasing the frequency of double strand breaks within the rDNA array, and cells lacking Fob1 experience a modestly extended lifespan (Defossez et al., 1999). Nucleolar fragmentation has been correlated with ERC accumulation, and therefore deletion of *FOB1* should delay or suppress nucleolar fragmentation in replicatively old cells (Sinclair et al., 1997) . Furthermore, other phenotypes that are also suppressed by deletion of *FOB1* may indicate that they too are related to ERC accumulation. While ERCs may play a role in limiting lifespan, they only represent one contributing pathway for replicative aging as caloric restriction further extends lifespan in *fob1*Δ mutants.

The last major pathway that is known to significantly extend lifespan is overexpression of the proteasome (Kruegel et al., 2011). The proteasome is responsible for degrading ubiquitylated proteins in the cytoplasm and nucleus (Saeki and Tanaka, 2012). Deletion of *UBR2*, the negative regulator of Rpn4, the master transcription factor for genes encoding proteasome components, extends replicative lifespan (Kruegel et al., 2011). The proteasome pathway is believed to be independent of both caloric restriction and ERC-related pathways because deleting *UBR2* further extends lifespan in caloric restriction mimetic mutants and in *fob1Δsir2Δ* cells. One proposed mechanism of how increasing proteasome activity might promote cellular survival is by clearing damaged or misfolded proteins that would otherwise accumulate and be toxic to the cell. The effect of increasing proteasome activity on other age-related phenotypes is unknown, and will be explored here.

Double-tagged strains (Appendix G) were used to determine the effect of caloric restriction and various mutant backgrounds on organelle morphology. This allowed the mitochondria, vacuole, peroxisomes, nucleolus, and the mitotic apparatus to be visualized with age multiple times and in several different genetic contexts, confirming reproducibility in all results. This section is organized first by the condition or mutant that is known to extend lifespan, and then by organelle. Results shown consist of pooled data from many experiments.

Cells were labeled with Dylight 350, aged using the MEP and visualized live immediately after harvesting the timepoint. Strains containing peroxisome markers were also labeled with biotin, aged using the MEP, fixed, purified, and visualized using three-dimensional fluorescence microscopy with deconvolution to allow more accurate quantification of peroxisome number.

Cells were scored prior to labeling (log), at the time of MEP induction (time 0 hours), and at times 3, 24, and 48 hours.

The effects of calorie restriction (0.5% glucose) on age-associate phenotypes

Mitochondria: The mitochondria, marked by Tom70-GFP or Tom70-mCherry were visualized in four independent experiments. Calorie restriction suppressed mitochondrial fragmentation at time 24 and time 48 (**Figures 5.1A, B**). The proportion of cells with fragmented mitochondria increased between time 24 and 48 hours even under calorie restriction, suggesting that calorie restriction only delays the mitochondrial phenotype.

Vacuoles: Cells aged under calorie restriction were scored for vacuolar fragmentation in four different experiments. Interestingly, calorie restriction generally increased the frequency of vacuolar fragmentation at time 24, but suppressed fragmentation at time 48 compared to wildtype (**Figure 5.1C**).

Peroxisomes: Peroxisome number was estimated using simple wide-field microscopy as well as more precisely quantitated using three-dimensional microscopy with deconvolution. Calorie restriction did not significantly alter the number of peroxisomes in either young or old cells (**Figure 5.2A**).

Nucleolus: The state of the nucleolus was investigated in aging cells with and without calorie restriction on five separate occasions. Calorie restriction has no effect on the percentage of cells with fragmented nucleoli at any timepoint (**Figure 5.2B**).

Nucleus and mitotic apparatus: Calorie restriction increased the frequency of nuclear abnormalities in aging cells as observed with the nucleoplasmic marker GFP-Pus1 (**Figures 5.2C**).

Summary: Calorie restriction delayed mitochondrial fragmentation, slightly reduced peroxisome number, but did not suppress nucleolar or vacuolar fragmentation. Calorie restriction had a negative effect on the nucleus. These findings suggest that the fragmentation of the nucleolus is mediated by another independent pathway important in the aging process.

The effects of *gpa2Δ,* a genetic mimetic of calorie restriction, on age-associated phenotypes

Mitochondria: The mitochondria, marked by Tom70-GFP or Tom70-mCherry were visualized in *gpa2*Δ cells. The absence of Gpa2 suppressed mitochondrial fragmentation at time 24 hours and at time 48 hours, when compared to wildtype (**Figures 5.3A,B**). However, compared to the suppression observed in calorie restriction and with *VMA1* overexpression, deletion of *GPA2* is a weaker suppressor. Mitochondrial fragmentation still increased between time 24 and 48 hours in *gpa2*Δ cells, suggesting that like the other suppressors, it acts by delaying mitochondrial fragmentation, and not by preventing it altogether.

Vacuole: Cells were scored for vacuolar fragmentation in the presence and absence of Gpa2. Deletion of *GPA2* did not affect the frequency of vacuolar fragmentation at either time 24 or 48 hours (**Figure 5.3C**).

Peroxisomes: Deletion of *GPA2* did not significantly affect the average number of peroxisomes per cell at any timepoint when compared to wildtype (**Figure 5.4A**).

Nucleolus: *GPA2* deletion did not consistently increase or decrease the percentage of cells containing a fragmented nucleolus compared to wildtype (**Figure 5.4B**).

Nucleus and mitotic apparatus: Deletion of *GPA2* did not have an effect on the frequency of cells exhibiting nuclear abnormalities at any timepoint when compared to wildtype (**Figures 5.4C**).

Summary: The effects of deleting *GPA2* were similar to the effects of calorie restriction, but not to the same degree. Like calorie restriction, fewer *gpa2Δ* cells contained fragmented mitochondria with advanced replicative age, but the suppressive effects of eliminating Gpa2 were less dramatic when compared to the suppressive effects of calorie restriction. Also in common with calorie restriction, the absence of Gpa2 did not have an effect on nucleolar fragmentation. These results support the use of *gpa2Δ* as a calorie restriction mimetic, and substantiate the idea that calorie restriction also acts on pathways independent of Gpa2.

How increasing vacuolar acidity by *VMA1* overexpression affects organelle morphology

Mitochondria: Overexpression of *VMA1* suppressed mitochondrial fragmentation at time 24, and suppressed severe mitochondrial fragmentation at time 24 and 48 hours (**Figure 5.5A, B**). The proportion of cells with fragmented mitochondria increased between time 24 and 48 hours even under suppressing conditions, suggesting that *VMA1* overexpression only delays the mitochondrial phenotype.

Vacuole: Vacuolar fragmentation in cells overexpressing *VMA1* were compared to empty-vector expressing cells at multiple replicative ages. *VMA1* overexpression suppressed vacuolar fragmentation at time 24 and 48 hours (**Figure 5.5C**).

Peroxisomes: *VMA1* overexpression decreased the average number of peroxisomes in each cell at times 24 and 48 hours (**Figure 5.6A**). However, it is important to note that overexpressing *VMA1* did not change the general distribution of peroxisome number with replicative age.

Nucleolus: *VMA1* overexpression resulted in inconsistent findings, causing reduction of nucleolar fragmentation at time 24 hours, and a significant increase at time 48 hours (**Figure 5.6B**). These findings are inconsistent with previous experiments not shown.

Nucleus and mitotic apparatus: *VMA1* overexpression did not have a consistent effect on the frequency of nuclear abnormalities (**Figure 5.6C**).

Summary: The effects of *VMA1* overexpression were similar to the effects of calorie restriction, but to a much greater degree. Overexpressing *VMA1* greatly decreased the population of cells with fragmented mitochondria and vacuoles at times 24 and 48 hours. These results indicate that the lifespan extension and phenotype suppression obtained by overexpression *VMA1* may be achieved by a mechanism similar to caloric restriction.

The effect of suppressing ERC formation in a *fob1Δ* background on age-associated phenotypes

Mitochondria: The absence of Fob1 slightly increases the frequency of age-associated mitochondrial fragmentation compared to wildtype (**Figure 5.7A, B**).

Vacuole: Vacuolar fragmentation was scored in aging *fob1Δ* and wildtype cells. At time 48 hours, *fob1Δ* increased the fraction of cells exhibiting vacuolar fragmentation when compared to wildtype (**Figure 5.7C**).

Peroxisomes: Deletion of *FOB1* did not significantly affect the average number of peroxisomes per cell at any timepoint when compared to wildtype (**Figure 5.8A**).

Nucleolus: The absence of Fob1 suppressed the age-associated increase in nucleolar fragmentation. This effect was most evident at time 48, and supports the relationship between ERC accumulation with replicative age and nucleolar fragmentation (**Figure 5.8B**).

Nucleus and mitotic apparatus: The nuclei of *fob1Δ* cells tend to be more normal than wildtype cells at advanced replicative age. Deletion of *FOB1* suppresses age-associated abnormalities in nuclear morphology at time 24 and 48 hours (**Figure 5.8C**).

Summary: The absence of Fob1 had minor exacerbating effects on the mitochondria, vacuole, and peroxisomes during the aging process. Deletion of *FOB1*, however, suppressed nucleolar fragmentation and reduced the number of nuclear abnormalities in old cells. These findings support the idea that replicative aging, accumulation of ERCs and nucleolar fragmentation are all interrelated, and suggests that the rDNA and/or ERCs may be problematic for old cells when they try to divide. Consistent with this, *fob1Δ* cells exhibit an age-dependent decrease in budding and bud morphology defects (data not shown). That the mitochondria, vacuoles and peroxisomes are not significantly affected by *FOB1* deletion provides evidence that these organelles change with age by an ERC-independent mechanism.

The effects of the lifespan extending *ubr2Δ* on selected organelle morphologies with replicative age

Mitochondria: Compared to wildtype, mitochondrial fragmentation was increased at time 3 hours and at time 24 hours. Notably, when looking at the incidence of severe fragmentation, the presence of very small foci, time 24 *ubr2Δ* cells were much more likely to contain severely fragmented mitochondria compared to wildtype (**Figures 5.9A, B**). This result was unexpected because severely fragmented mitochondria was hypothesized to indicate advanced replicative age, but is observed to occur earlier in longer-lived *ubr2Δ* cells.

Vacuole: More replicatively old cells (time 24 and 48 hours) contained fragmented vacuoles in *ubr2Δ* cells compared to wildtype cells (**Figure 5.9C**). This is consistent with the idea that mitochondrial fragmentation precedes and is related to vacuolar fragmentation, and more *ubr2Δ* cells have fragmented mitochondria and vacuoles compared to wildtype.

Peroxisomes: Deletion of *UBR2* did not significantly affect the average number of peroxisomes per cell at any timepoint when compared to wildtype (**Figure 5.10A**).

Nucleolus: *UBR2* deletion resulted in the suppression of age-associated nucleolar fragmentation (**Figure 5.10B**). In addition to the nucleolus remaining intact, old *ubr2Δ* cells were observed to have smaller nuclei and nucleoli compared to wildtype.

Nucleus and mitotic apparatus: The absence of Ubr2 strongly suppressed nuclear abnormalities at time 24 and 48 hours (**Figure 5.10C**). Additionally, the nucleus was observed to be smaller in very old *ubr2Δ* cells when compared to wildtype cells of similar replicative age.

Summary: Deleting *UBR2* provided the most information about the age-associated phenotypes and the pathways that might regulate each of them. *ubr2Δ* cells contained more severely fragmented mitochondria and vacuoles compared to wildtype. Conversely, eliminating Ubr2 suppressed both nuclear and nucleolar phenotypes, and suppressed the age-associated increase in budding and bud morphology defects (data not shown). No difference in peroxisome number was observed between *ubr2Δ* and

wildtype cells. These results suggest that the mitochondrial and vacuolar fragmentation are likely linked and are caused by a mechanism distinct from the nucleus, nucleolus and peroxisomes.

How each of the lifespan-extending conditions affects the age-associated changes for all five organelles (mitochondria, vacuoles, peroxisomes, nucleolus, and nucleus) are summarized in **Table 5.1**.

Table 5.1. The effects of lifespan-extending conditions on selected age-associated phenotypes.

Phenotype	Lifespan-extending condition				
	Caloric restriction 0.5% glucose	*gpa2Δ*	*VMA1 OE*	*fob1Δ*	*ubr2Δ*
Mitochondrial fragmentation	↓	↓	↓	Slight ↑ of severe	↑
Vacuolar fragmentation	↓	No change	↓	Slight ↑	↑
Increase in peroxisome abundance	Slight ↓ Low n	No change	Slight ↓	No change	Slight ↑
Nucleolar fragmentation	No change	No change	↑ T24 and T48 opposite	↓	↓
Increase in frequency of nuclear abnormalities	No change	No change	No change	↓	↓

A.

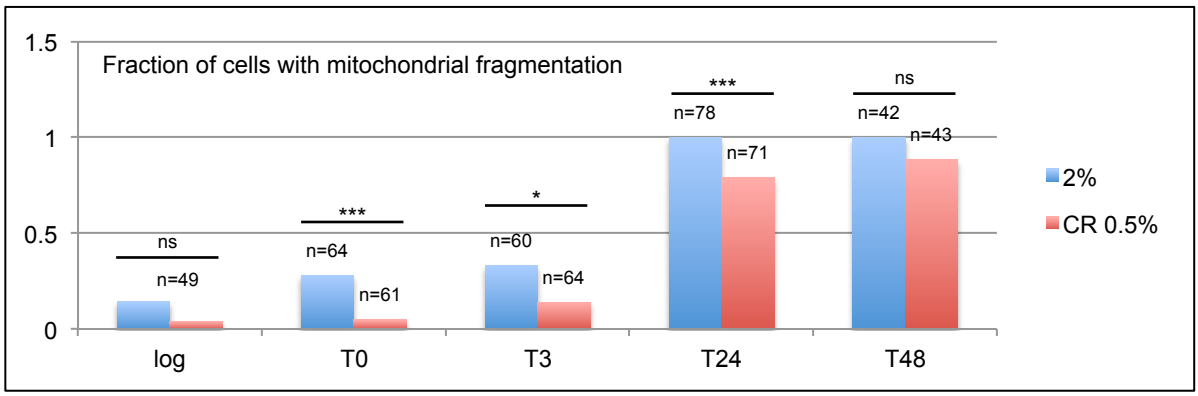

B.

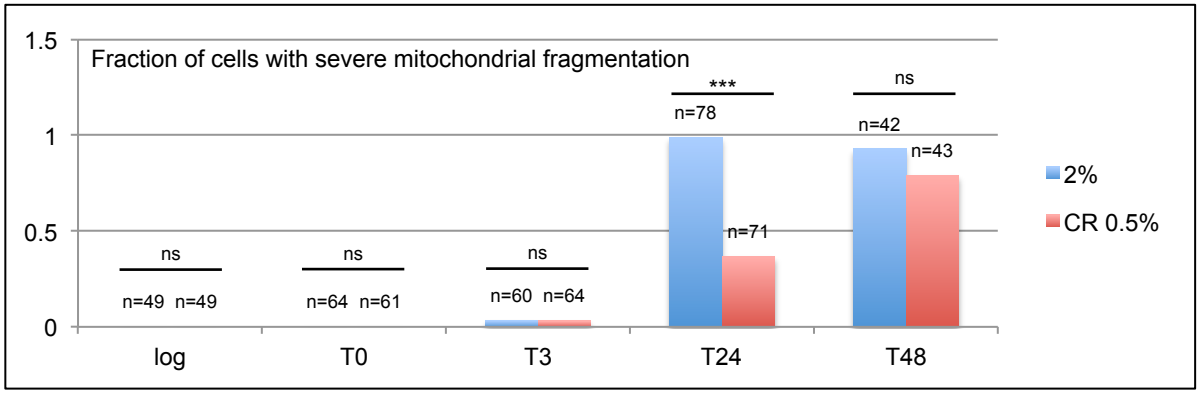

C.

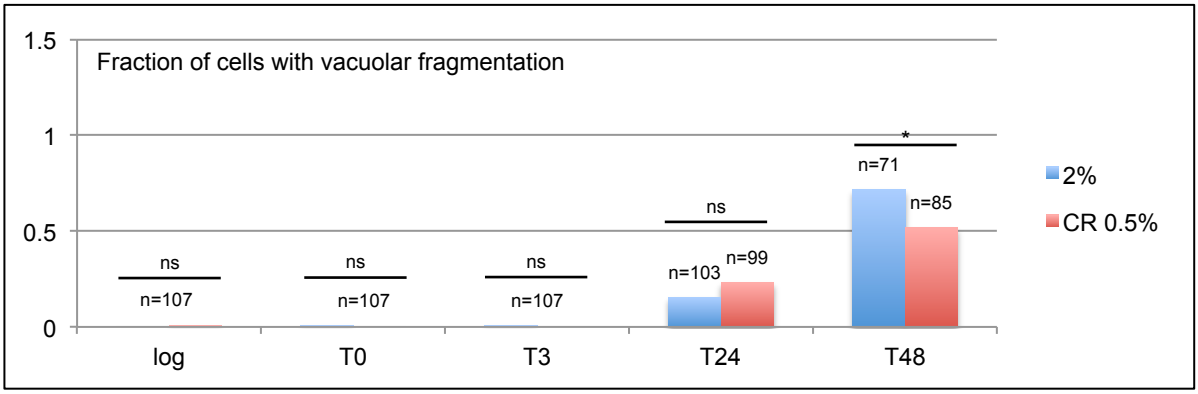

Figure 5.1. Caloric restriction represses total and severe mitochondrial fragmentation and represses vacuolar fragmentation. Cells expressing fluorescently tagged (A and B) Tom70p or (C) Vph1p were cultured in either YEPD containing 2% glucose or 0.5% glucose (calorie restriction, CR), labeled with Dylight 350, aged with the MEP (in 2% or 0.5% (CR)), and scored for (A) any mitochondrial fragmentation, (B) severe mitochondrial fragmentation, presence of very small fragments, and (C) vacuole fragmentation at the indicated timepoints. Data represents multiple independent experiments. The total number of cells scored is indicated above the corresponding columns on the graph. (A) Caloric restriction suppresses total mitochondrial fragmentation at times 0, 3, and 24 hours. (B) Caloric restriction suppresses severe mitochondrial fragmentation at time 24 hours. (C) Caloric restriction suppresses vacuolar fragmentation at time 48 hours. * P<0.05. ** P<0.01, *** P<0.001, ns=not statistically significant (p>0.05) by Fisher's exact test, comparing cells grown in 2% glucose to those grown under caloric restriction (0.5% glucose) at a single timepoint.

A.

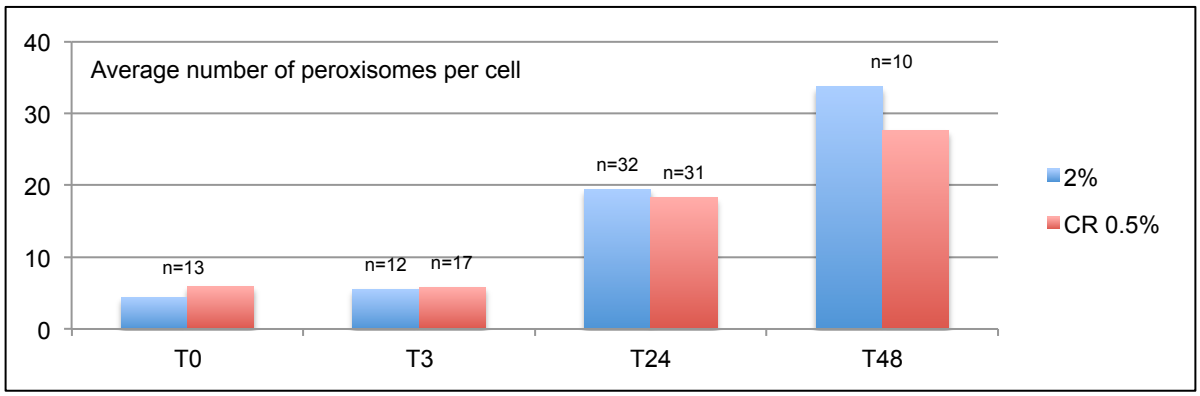

B.

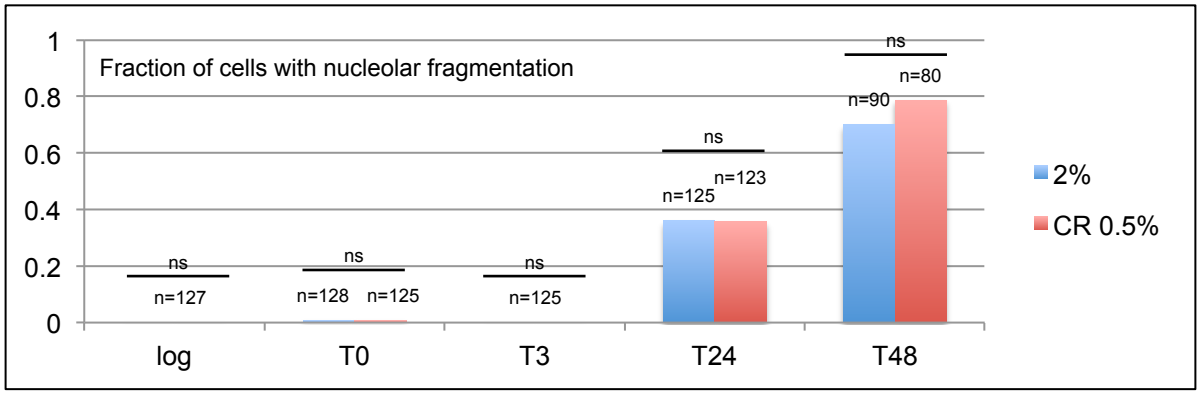

C.

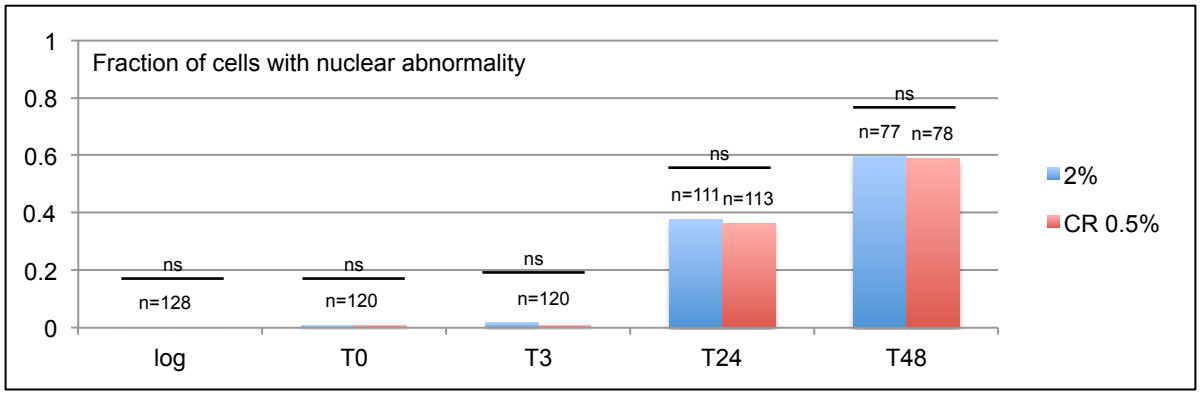

Figure 5.2. Caloric restriction has little effect on peroxisome number and no effect on the frequency of nucleolar fragmentation and nuclear abnormalities. Cells expressing fluorescently tagged (A) Pex11p, (B) Nop58p, and (C) Pus1p were cultured in either YEPD containing 2% glucose or 0.5% glucose (calorie restriction, CR), labeled with Dylight 350, aged with the MEP (in 2% or 0.5% (CR)), and scored for (A) peroxisome number, (B) nucleolar fragmentation, and (C) abnormal nuclear morphology, number, or segregation at the indicated timepoints. Data represents multiple independent experiments. The total number of cells scored is indicated above the corresponding columns on the graph. (A) Caloric restriction modestly reduces the number of peroxisomes at time 48 hours. (B and C) Caloric restriction does not affect age-associated nucleolar fragmentation or the incidence of nuclear abnormalities. * P<0.05. ** P<0.01, *** P<0.001, ns=not statistically significant (p>0.05) by Fisher's exact test, comparing cells grown in 2% glucose to those grown under caloric restriction (0.5% glucose) at a single timepoint.

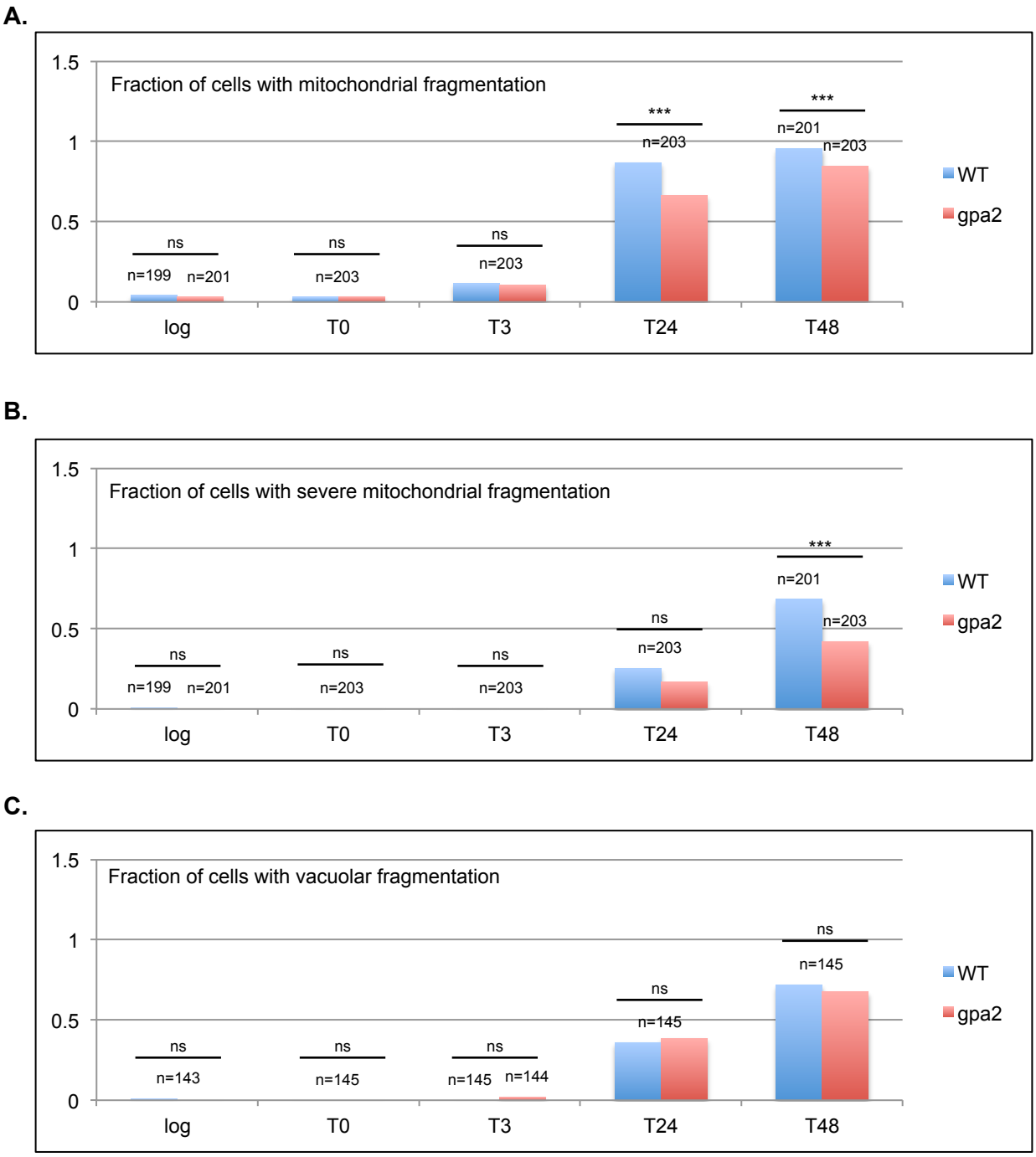

Figure 5.3. The caloric restriction mimetic, *gpa2Δ*, suppresses mitochondrial fragmentation but does not suppress vacuolar fragmentation. Cells with and without *gpa2*, and expressing fluorescently tagged (A and B) Tom70p or (C) Vph1p were labeled with Dylight 350, aged with the MEP, and scored for (A) any mitochondrial fragmentation, (B) severe mitochondrial fragmentation, presence of very small fragments, and (C) vacuole fragmentation at the indicated timepoints. Data represents multiple independent experiments. The total number of cells scored is indicated above the corresponding columns on the graph. (A) *gpa2Δ* suppresses total mitochondrial fragmentation at times 24 and 48 hours. (B) *gpa2Δ* suppresses severe mitochondrial fragmentation at time 48 hours. (C) *gpa2Δ* does not affect age-associated vacuolar fragmentation. * P<0.05. ** P<0.01, *** P<0.001, ns=not statistically significant (p>0.05) by Fisher's exact test, comparing wildtype cells to *gpa2Δ* cells at a single timepoint.

A.

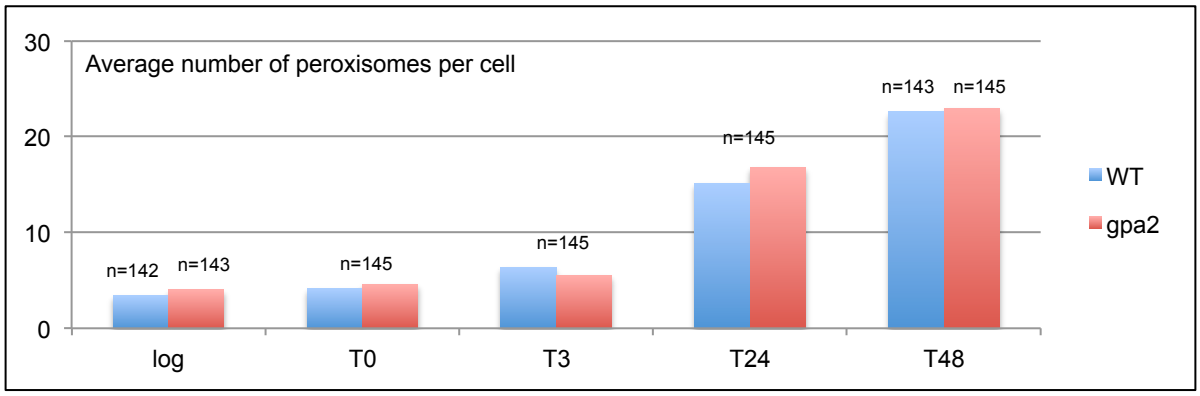

B.

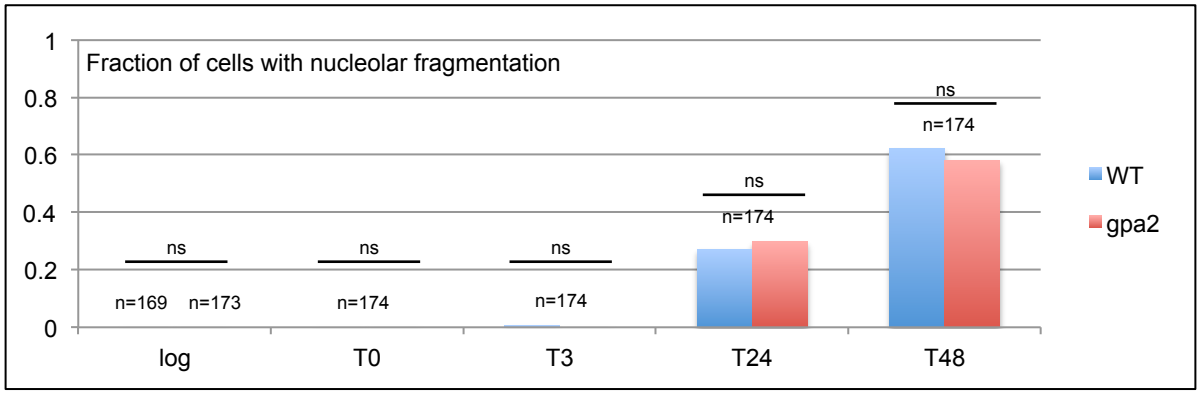

C.

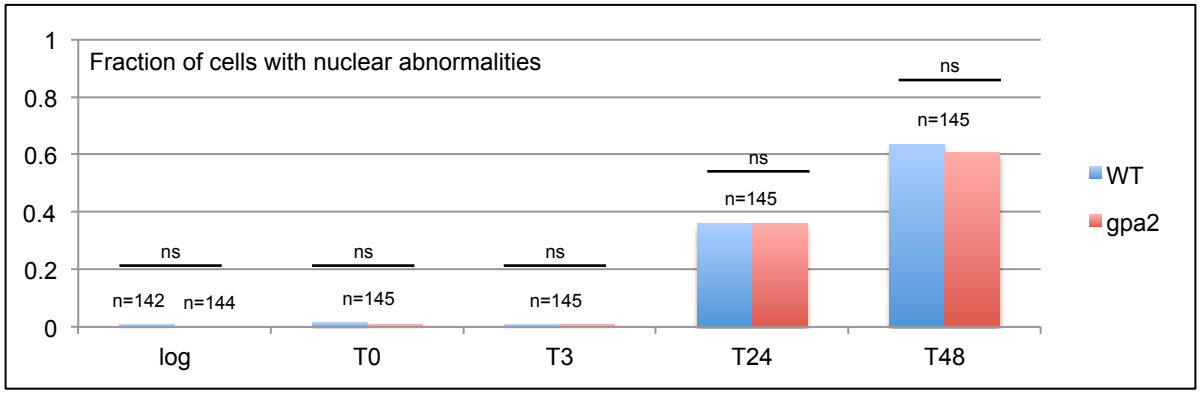

Figure 5.4. The caloric restriction mimetic, *gpa2Δ*, does not significantly affect peroxisome number, nucleolar fragmentation or the frequency of nuclear abnormalities. Cells with and without *gpa2*, and expressing fluorescently tagged (A) Pex11p, (B) Nop58p or (C) Pus1p were labeled with Dylight 350, aged with the MEP, and scored for (A) peroxisome number, (B) nucleolar fragmentation, and (C) abnormal nuclear morphology, number, or segregation at the indicated timepoints. Data represents multiple independent experiments. The total number of cells scored is indicated above the corresponding columns on the graph. *gpa2Δ* does not affect age-associated changes in (A) peroxisome number, (B) nucleolar fragmentation, or (C) the frequency of nuclear abnormalities. * P<0.05. ** P<0.01, *** P<0.001, ns=not statistically significant (p>0.05) by Fisher's exact test, comparing wildtype cells to *gpa2Δ* cells at a single timepoint.

A.

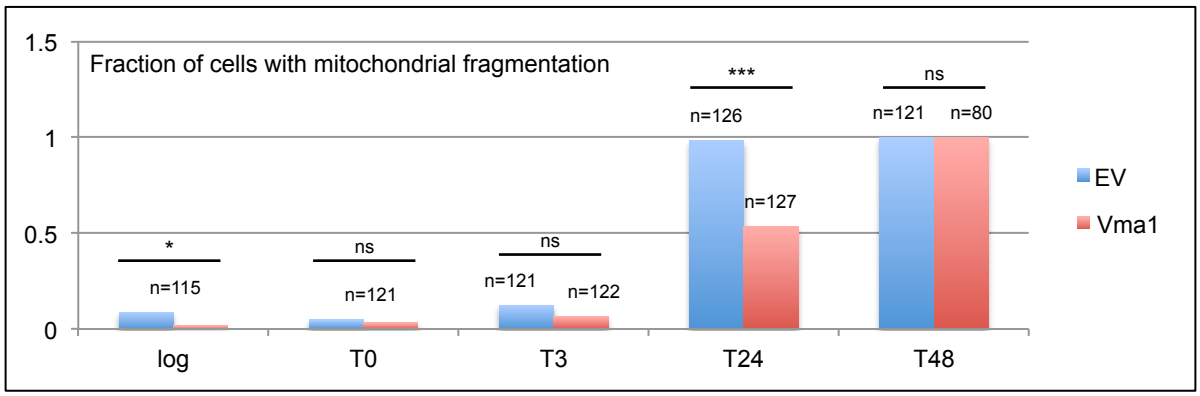

B.

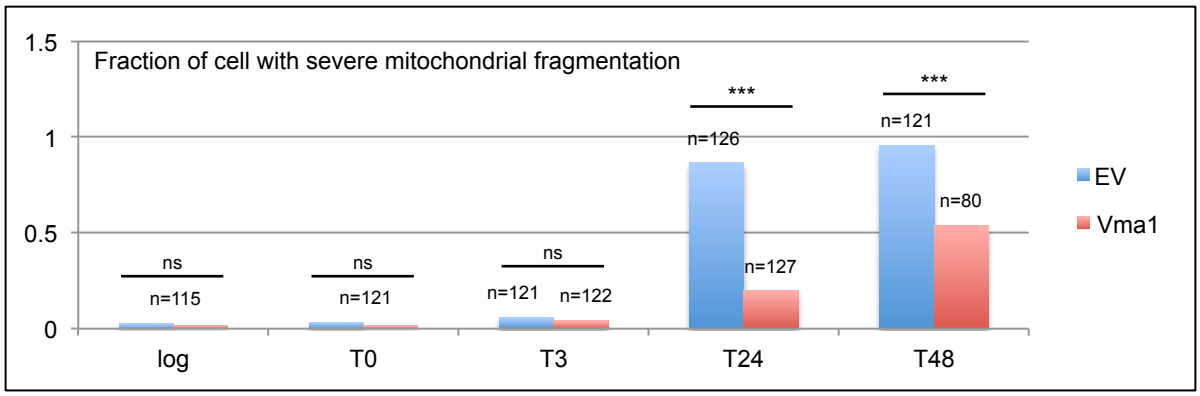

C.

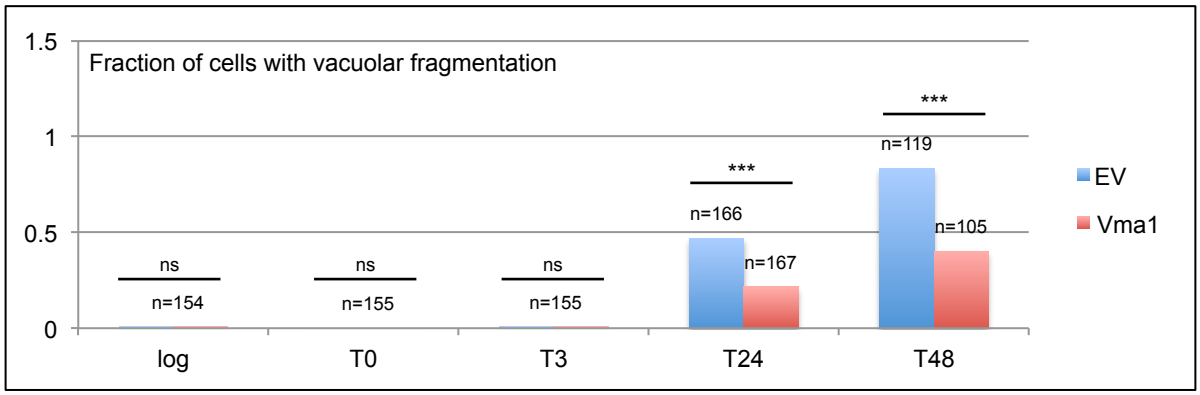

Figure 5.5. Increasing vacuolar acidity by *VMA1* overexpression suppressed mitochondrial and vacuolar fragmentation. Cells expressing either empty vector or overexpressing *VMA1*, and expressing fluorescently tagged (A and B) Tom70p or (C) Vph1p were labeled with Dylight 350, aged with the MEP, and scored for (A) any mitochondrial fragmentation, (B) severe mitochondrial fragmentation, presence of very small fragments, and (C) vacuole fragmentation at the indicated timepoints. Data represents multiple independent experiments. The total number of cells scored is indicated above the corresponding columns on the graph. (A) *VMA1* overexpression suppresses total mitochondrial fragmentation in log-phase cells and at time 24 hours. (B) *VMA1* overexpression suppresses severe mitochondrial fragmentation at times 24 and 48 hours. (C) *VMA1* overexpression suppresses vacuolar fragmentation at times 24 and 48 hours. * P<0.05. ** P<0.01, *** P<0.001, ns=not statistically significant (p>0.05) by Fisher's exact test, comparing empty vector cells to *VMA1* overexpressing cells at a single timepoint.

A.

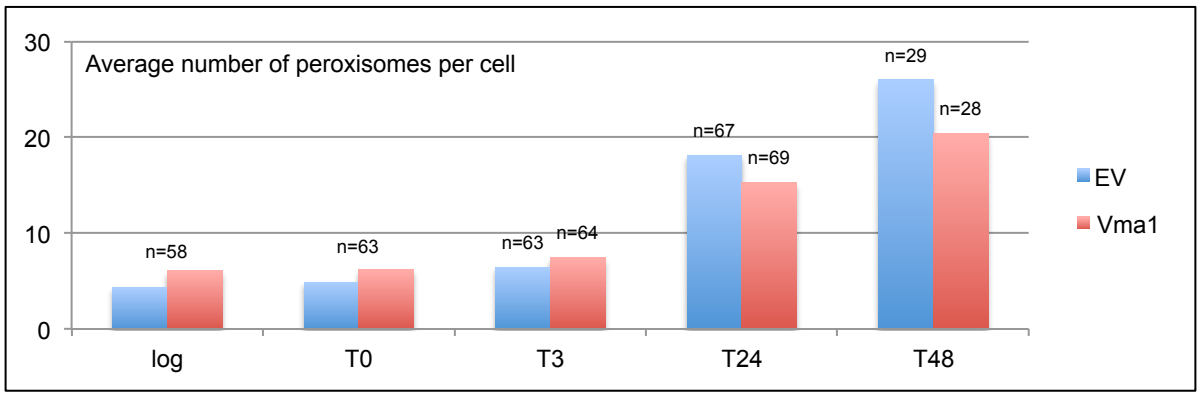

B.

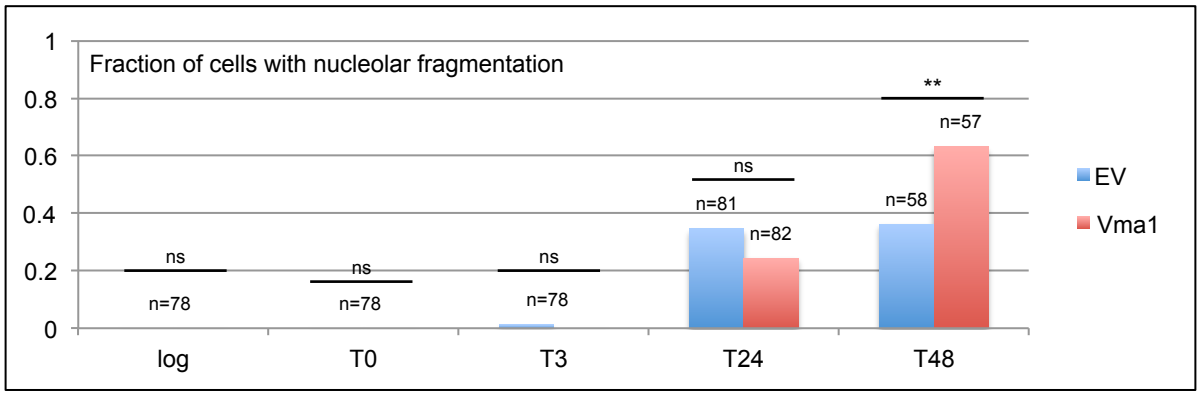

C.

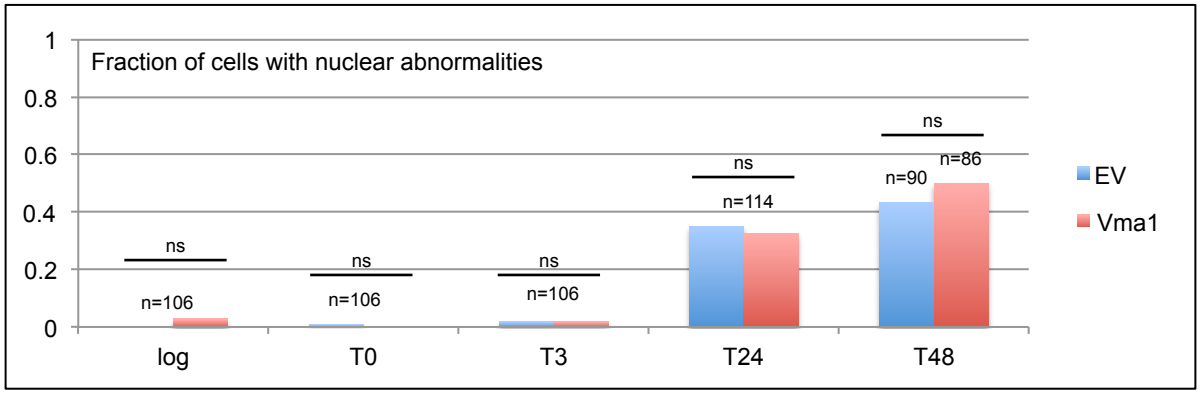

Figure 5.6. Increasing vacuolar acidity by *VMA1* overexpression reduces peroxisome number and does not have a consistent effect on nucleolar fragmentation or nuclear abnormalities. Cells expressing either empty vector or overexpressing *VMA1*, and expressing fluorescently tagged (A) Pex11p, (B) Nop58p, or (C) Pus1p were labeled with Dylight 350, aged with the MEP, and scored for (A) peroxisome number, (B) nucleolar fragmentation, and (C) abnormal nuclear morphology, number, or segregation at the indicated timepoints. Data represents multiple independent experiments. The total number of cells scored is indicated above the corresponding columns on the graph. (A) *VMA1* overexpression reduces peroxisome number at times 24 and 48 hours. (B) *VMA1* overexpression has no consistent effect on nucleolar fragmentation. (C) *VMA1* overexpression has no significant effect on vacuolar fragmentation. * P<0.05. ** P<0.01, *** P<0.001, ns=not statistically significant (p>0.05) by Fisher's exact test, comparing empty vector cells to *VMA1* overexpressing cells at a single timepoint.

A.

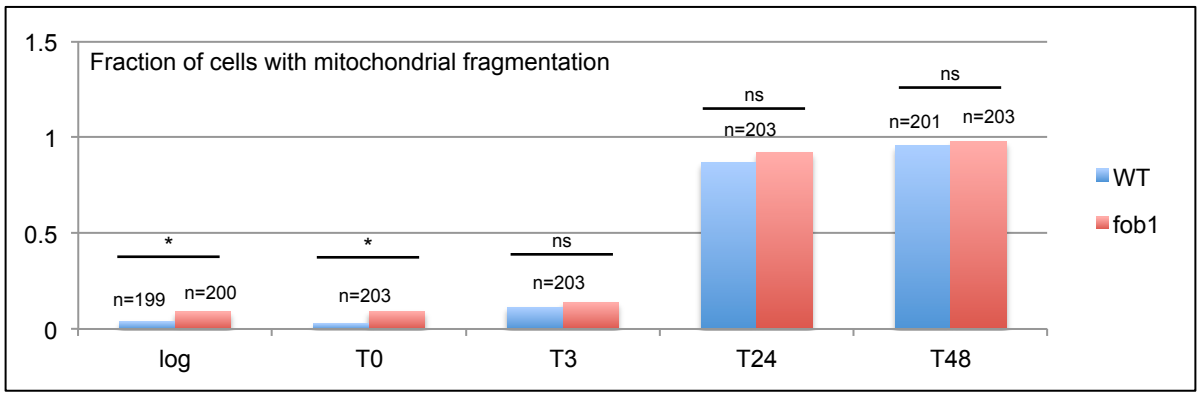

B.

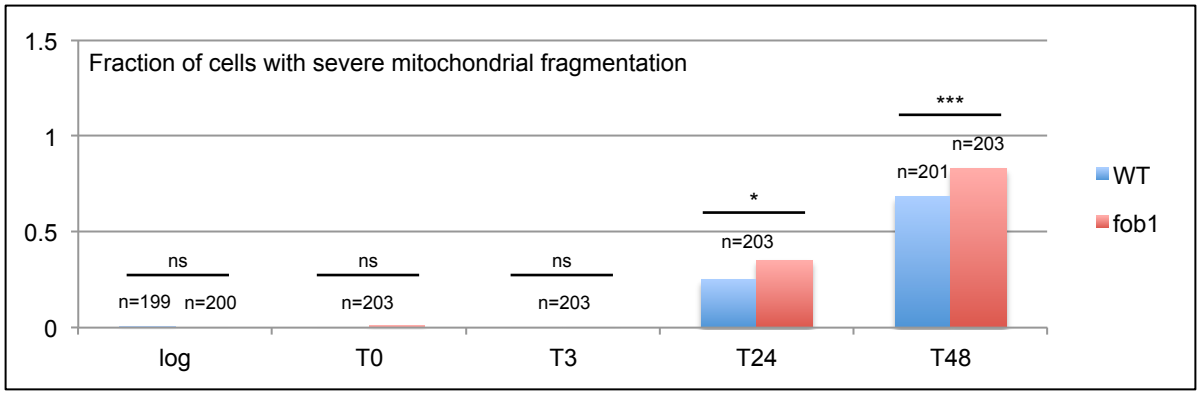

C.

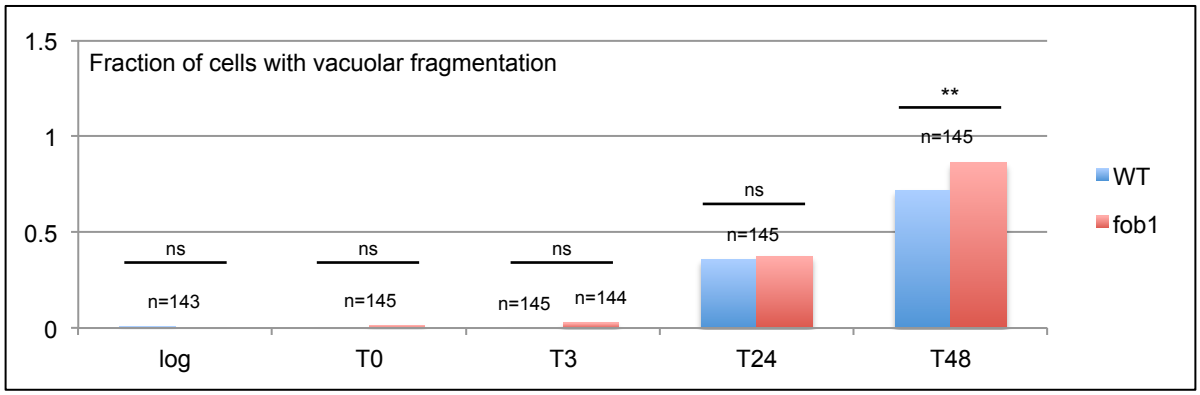

Figure 5.7. Reduction of ERCs by deletion of *fob1* increases severe mitochondrial fragmentation and vacuolar fragmentation. Cells with and without *fob1*, and expressing fluorescently tagged (A and B) Tom70p or (C) Vph1p were labeled with Dylight 350, aged with the MEP, and scored for (A) any mitochondrial fragmentation, (B) severe mitochondrial fragmentation, presence of very small fragments, and (C) vacuole fragmentation at the indicated timepoints. Data represents multiple independent experiments. The total number of cells scored is indicated above the corresponding columns on the graph. (A) *fob1Δ* increases total mitochondrial fragmentation in log-phase cells and at time 0 hours. (B) *fob1Δ* increases severe mitochondrial fragmentation at times 24 and 48 hours. (C) *fob1Δ* increases vacuolar fragmentation at time 48 hours. * P<0.05. ** P<0.01, *** P<0.001, ns=not statistically significant (p>0.05) by Fisher's exact test, comparing wildtype cells to *fob1Δ* cells at a single timepoint.

A.

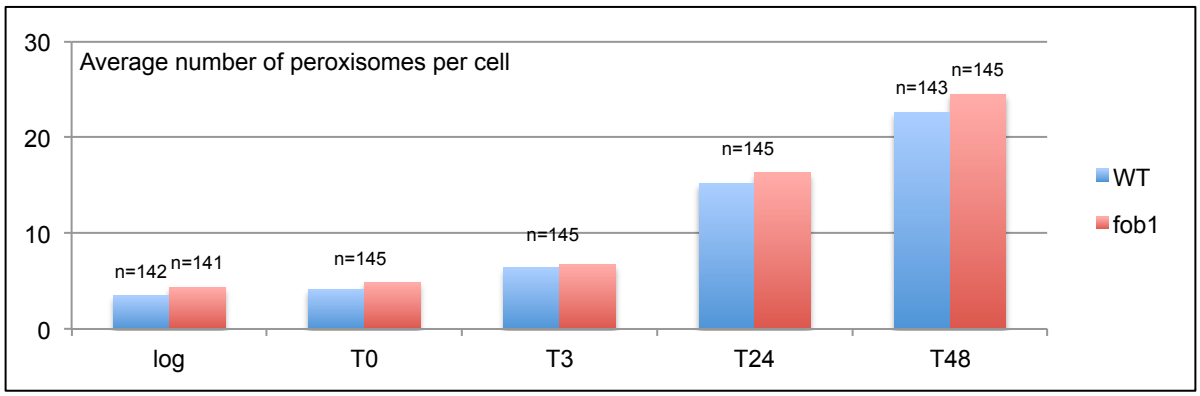

B.

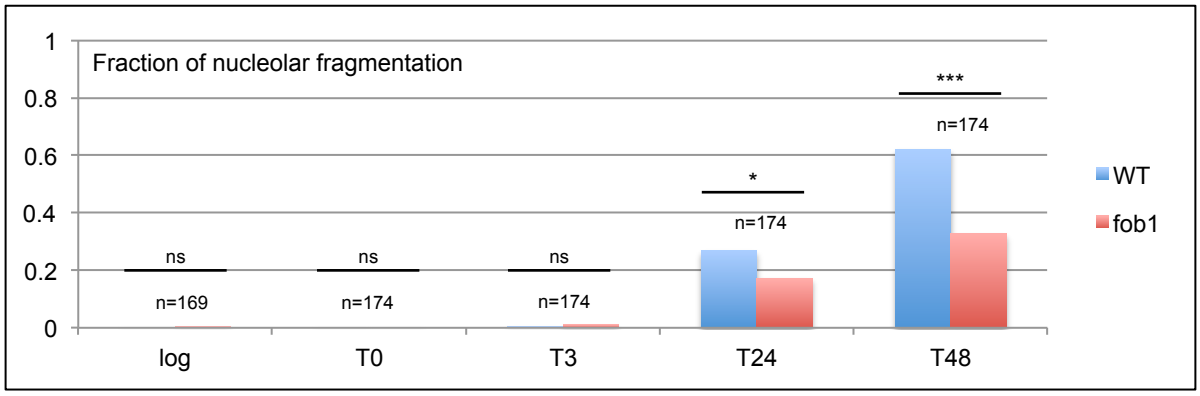

C.

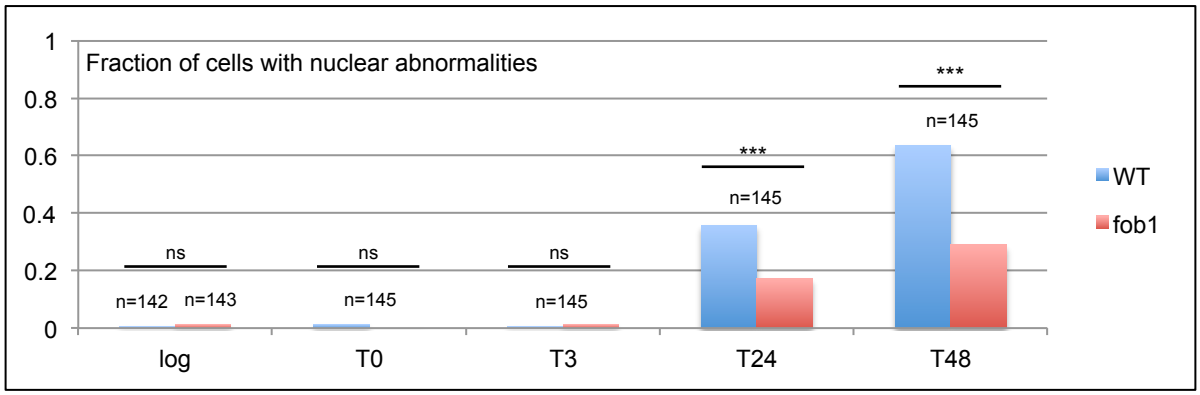

Figure 5.8. Reduction of ERCs by deletion of *fob1* modestly increases peroxisome number, but suppresses nucleolar fragmentation and the incidence of nuclear abnormalities. Cells with and without *fob1*, and expressing fluorescently tagged (A) Pex11p, (B) Nop58p or (C) Pus1p were labeled with Dylight 350, aged with the MEP, and scored for (A) peroxisome number, (B) nucleolar fragmentation, and (C) abnormal nuclear morphology, number, or segregation at the indicated timepoints. Data represents multiple independent experiments. The total number of cells scored is indicated above the corresponding columns on the graph. (A) *fob1Δ* modestly enhances age-associated increases in peroxisome number. *fob1Δ* suppresses age-associated (B) nucleolar fragmentation and (C) nuclear abnormalities at times 24 and 48 hours. * P<0.05. ** P<0.01, *** P<0.001, ns=not statistically significant (p>0.05) by Fisher's exact test, comparing wildtype cells to *fob1Δ* cells at a single timepoint.

A.

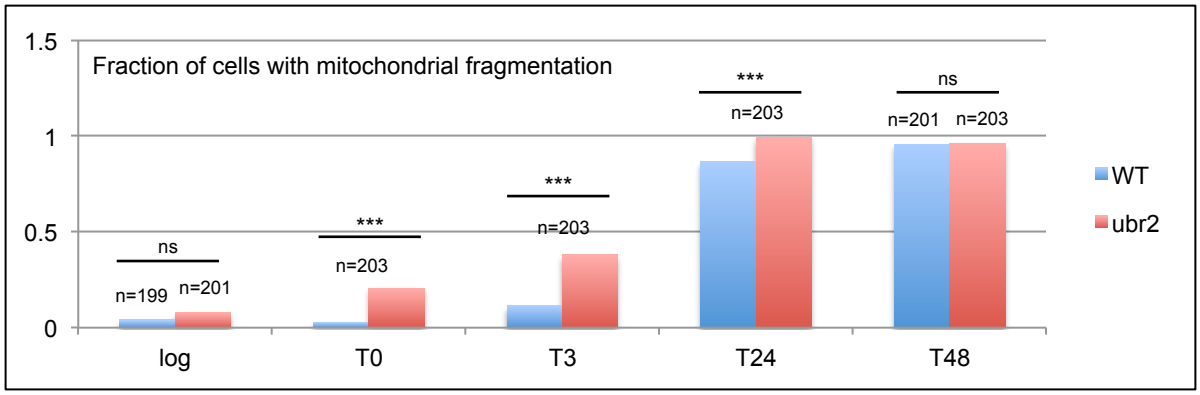

B.

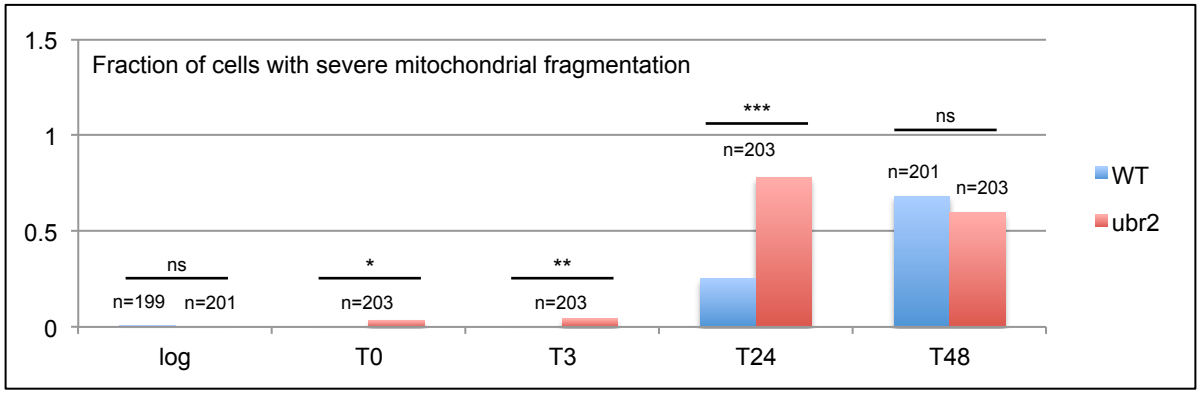

C.

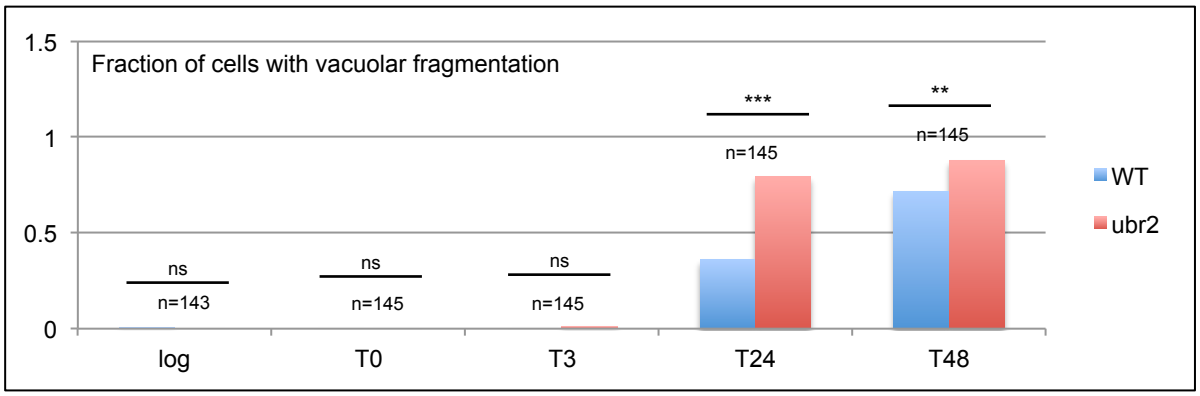

Figure 5.9. Deletion of *ubr2* significantly increases age-associated mitochondrial and vacuolar fragmentation. Cells with and without *ubr2*, and expressing fluorescently tagged (A and B) Tom70p or (C) Vph1p were labeled with Dylight 350, aged with the MEP, and scored for (A) any mitochondrial fragmentation, (B) severe mitochondrial fragmentation, presence of very small fragments, and (C) vacuole fragmentation at the indicated timepoints. Data represents multiple independent experiments. The total number of cells scored is indicated above the corresponding columns on the graph. *ubr2Δ* increases (A) total and (B) severe mitochondrial fragmentation times 0, 3, and 24 hours. (C) *urb2Δ* increases vacuolar fragmentation at times 24 and 48 hours. * P<0.05. ** P<0.01, *** P<0.001, ns=not statistically significant (p>0.05) by Fisher's exact test, comparing wildtype cells to *ubr2Δ* cells at a single timepoint.

A.

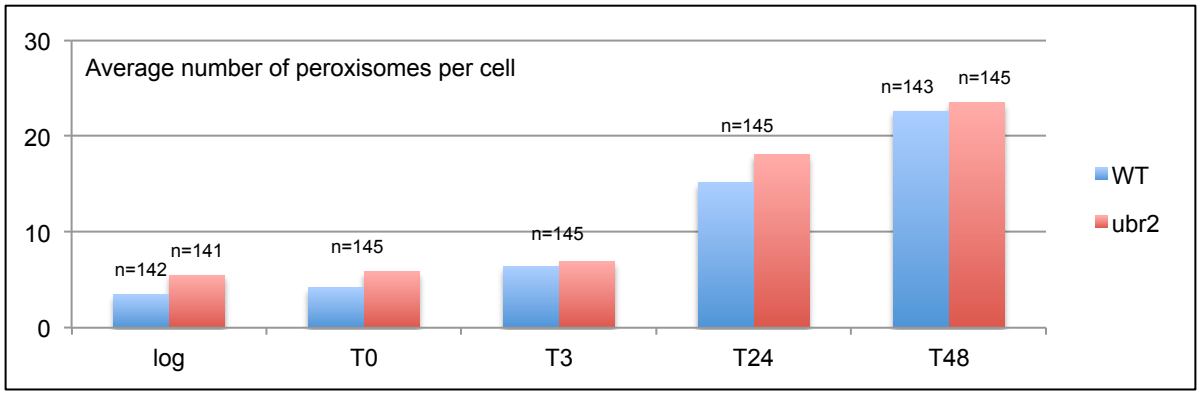

B.

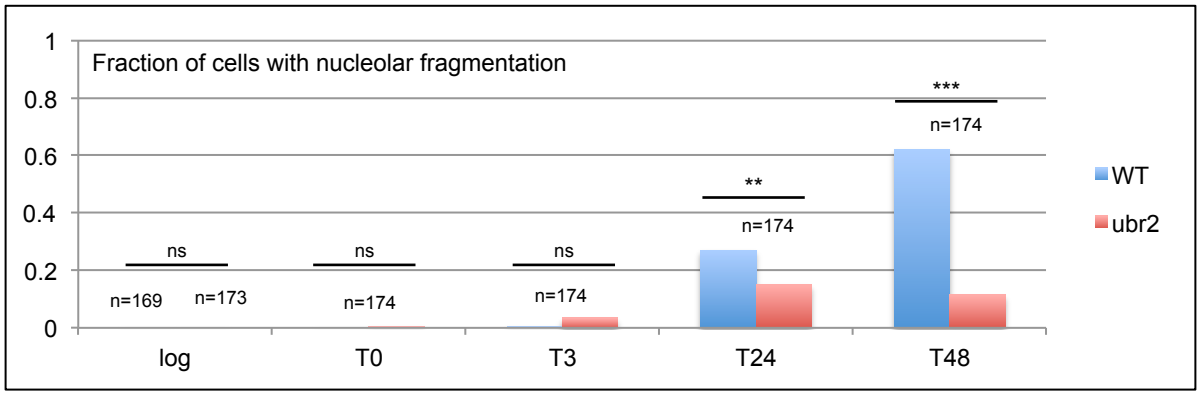

C.

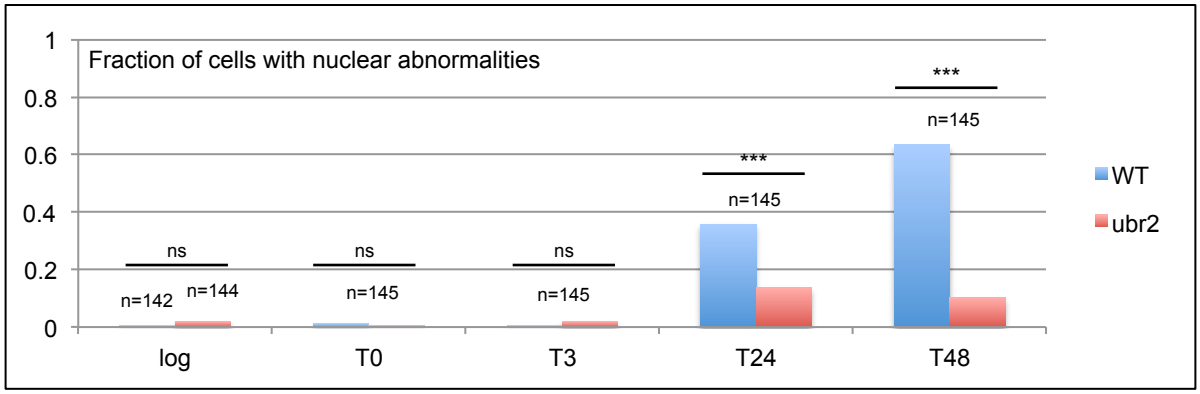

Figure 5.10. Deletion of *ubr2* modestly increases peroxisome number and significantly suppresses nucleolar fragmentation and the frequency of nuclear abnormalities. Cells with and without *ubr2*, and expressing fluorescently tagged (A) Pex11p, (B) Nop58p or (C) Pus1p were labeled with Dylight 350, aged with the MEP, and scored for (A) peroxisome number, (B) nucleolar fragmentation, and (C) abnormal nuclear morphology, number, or segregation at the indicated timepoints. Data represents multiple independent experiments. The total number of cells scored is indicated above the corresponding columns on the graph. (A) *ubr2Δ* modestly enhances age-associated increases in peroxisome number. *ubr2Δ* suppresses age-associated (B) nucleolar fragmentation and (C) nuclear abnormalities at times 24 and 48 hours. * P<0.05. ** P<0.01, *** P<0.001, ns=not statistically significant (p>0.05) by Fisher's exact test, comparing wildtype cells to *ubr2Δ* cells at a single timepoint.

Chapter VI: Summary of findings for age-associated changes in organelle morphology with replicative age

In order to identify organelles that may be involved with cellular processes that become defective with age, fluorescently tagged marker proteins representing over 20 different cellular structures and substructures were used to screen for changes in organelle morphology that occurred as a result of replicative age. Interestingly, many structures in replicatively old cells exhibited qualitative and/or quantitative differences when compared to young cells. The results of the screen are discussed in detail in **Chapter II**, and are summarized in **Table 2.14.** The four age-associated changes in organelle morphology that were further characterized included the fragmentation of the nucleolus, the increase in peroxisome number and decrease in peroxisome size, the fragmentation of the vacuole, and the missegregation of the mitotic spindle and other mitotic abnormalities (Topic of **Chapter III**, and summarized in **Table 3.5**). These changes were further characterized in order to differentiate between early and late phenotypes that may represent either causative or terminal events, respectively. The relative timing of each phenotype and their association with each other was determined by observing aging cells that contained two fluorescently tagged structures, and described in **Chapter IV**. Finally, each of the age-associated phenotypes were characterized under known lifespan-extending conditions to determine if currently known pathways that extend replicative lifespan play a role in any of the phenotypes. The effects of environmental and genetic caloric restriction, increased vacuolar acidity, suppression of ERCs, and increased proteasome activity were determined for each of the age-associated phenotypes (**Chapter V**).

The results for this section of the thesis were organized into chapters II, III, IV, and V. A separate summary of findings is found at the end of each of these chapters.

Limitations of the screen for age-associated changes in organelle morphology and challenges in the interpretation of results

This cell biological screen for replicative age-associated changes in organelle morphology is novel in its undertaking and in its breadth. Accordingly, there were challenges faced during this screen that were anticipated and obstacles that were unexpected. The goal of the screen was to take an unbiased cell biological approach to identify novel age-associated changes in organelle morphology with the premise that changes in morphology would reflect altered

organelle function. In order to accomplish this, ~80 marker proteins corresponding to over 20 different cellular structures were fluorescently tagged and observed at various replicative ages.

Were the markers chosen representative of their corresponding structures?

The choice of the marker proteins used to represent each structure of interest was the first major decision point of the screen. The marker proteins were not chosen arbitrarily incorporating some bias into the screen. Instead, well-established marker proteins were selected based on their previous use by other laboratories to characterize morphological changes in specific cellular structures. Whenever possible, multiple marker proteins were used for each structure to prevent identification of marker-specific changes. The choice in marker brings up several interesting aspects intrinsic to the design of this screen. First, despite our best efforts, the possibility that significant age-associated phenotypes were overlooked cannot be ruled out. The ability to detect changes in organelle morphology is dependent on the substructure localization, abundance, and function of the marker chosen. For example, mitochondrial morphology differs significantly in very old mother cells when visualized with an outer membrane marker protein compared to an inner membrane marker protein (Hughes and Gottschling, unpublished data). Second, many structures were difficult to characterize due to the lack of availability of high-abundance proteins within the structure or due to transient localization of marker proteins, as was the case with dynein and the secretory vesicles. Finally, the consequence of introducing fluorescent fusion proteins on the function, stability, and regulation of both the marker protein and the organelle is not known. While many of the fusion proteins used in the screen have been previously used in young cells, the effect of either the fluorescent tag or the fusion protein in old cells is unclear as replicatively old cells likely differ in their ability to tolerate marker proteins.

Although these are universal caveats for any cell biological screen, they are important to consider, particularly in the context of replicative aging because how cellular physiology differs in old cells has not yet been completely explored. Two approaches can be taken to compensate for these considerations. First is the addition of alternative, non-genetic methods for visualizing cellular structures. This was done for several structures in the screen including using Nile Red to stain lipid particles and Phalloidin to stain actin, however similar methods can be applied to other organelles. A second approach would be to expand the scope of the primary screen to include a global analysis of the all proteins with replicative age, as was done in young cells by the O'Shea lab (Huh et al., 2003a). This would reduce the bias introduced by marker protein selection, and would allow the identification of significant marker-specific

changes with replicative age, as well as identify themes in the types of changes that occur as a function of replicative age.

Do the changes in organelle morphology reflect changes in organelle function?

The ultimate goal of the cell biological screen was to identify organelles that demonstrated altered morphology with replicative age in order to gain insight into the cellular pathways important in the aging process. The success of this approach relies on the premise that changes in organelle morphology reflect a change in organelle function. This approach is supported by many examples in the literature in young yeast cells, and has been shown to be a fruitful approach in identifying and characterizing novel aging mechanisms as with the loss of vacuolar acidity and mitochondrial dysfunction and fragmentation (Hughes and Gottschling, 2012). An alternative approach that could be used in lieu of or in conjunction with the approach described in this work is to use assays to test cellular function directly in young and old cells. This approach would eliminate the dependence on organelle morphology and the localization of specific marker proteins as the inherent behavior of these marker proteins might be drastically different in replicatively old cells, i.e. levels of transcription and translation. One example of how this might be done is described in **Appendix B** with the use of FM4-64 (Invitrogen) to simultaneously identify changes in endosomal and vacuolar morphology and monitor the efficacy and efficiency of the endocytic process.

What are the limitations specific to this screen?

Because of the number of the markers to be screened, and because of the time-consuming and tedious nature of isolating and identifying replicatively old cells, particularly for high-resolution microscopy, the number of cells that could reasonably be monitored in a given experiment was necessarily small. In the initial screens, approximately 10-20 cells were visualized at each timepoint. Phenotypes that occur at an incidence of less than 10% of cells were less likely to be detected, and the variation from experiment to experiment would be expected to be large for events that occur infrequently. Given the hypothesis that the aging process may be inherently stochastic, the identification of cell biological changes resulting from stochastic events poses a substantial challenge. In addition, the screen was designed such that cells were visualized at only five timepoints: exponentially growing cells prior to labeling (log, ~1-2 divisions), at the time of MEP induction (time 0 hours, ~2-3 divisions), and at time 3 hours (~4-7 divisions), 24 hours (~16-22 divisions), and 48 hours (28+ divisions, median lifespan of MEP strain) following MEP induction. These timepoints proved to be problematic in interpreting data, particularly from the

chronological experiments in which the onset and incidence of the phenotypes were compared to each other (**Chapter IV**). Because the data represented the distribution of phenotypes in a small population of aging cells, it was difficult to make conclusions regarding the kinetics of each of the phenotypes. In addition, it was not possible to determine if a highly penetrant, early-onset phenotype such as mitochondrial fragmentation was associated with a less penetrant, late-onset phenotype such as mitotic dysfunction.

One recently developed method that could be used to overcome these obstacles is the use of live microscopy combined with microfluidics with or without the enrichment of mother cells (Xie et al., 2012; Lee et al., 2012). The microfluidics device is used to trap the mother cells while the newly formed daughters are swept away. This approach is powerful in that it allows a population of mother cells to be monitored throughout the entire aging process. Because it is possible to obtain lifespan data for each mother cell, the onset of age-associated phenotypes can be retrospectively related to the timing of senescence. Furthermore, multiple organelles can be simultaneously observed throughout the aging process, and live microscopy combined with microfluidics would allow greater definition of the timing between the onset of two different phenotypes. Finally, this approach allows a facile way to alter the environmental conditions at any time during the aging process and removes the need to isolate or purify old cells, increasing the throughout of the experiment.

The number of organelles that changed morphology with replicative age was greater than anticipated

At the outset of the screen, I had expected to identify one or two highly penetrant age-associated phenotypes with the idea that there would be few early changes in cellular function that would result in altered organelle morphology. I had hypothesized that these phenotypes would represent initiating events of the aging process and that there would be additional organelle changes, however these would be detected in much older mother cells with low incidence and represent stochastic terminal events. Instead, the primary screen yielded changes in the majority of visualized structures.

Several of these phenotypes could be attributed to the change in cell size that occurs as a function of replicative age. The phenomenon of organelle scaling suggests that the size or number of organelles increases proportionately to the increase in cell size (Chan and Marshall, 2010; Levy and Heald, 2012). This is thought to occur in order to accommodate increased demands on these organelles. Some well-characterized aspects of organelle scaling held true

in the context of age-associated increases in cell size. For example, yeast nuclear volume scales proportionately compared to cell volume. This was true for the nuclei in larger replicatively aged cells regardless of whether nuclear pore markers or perinuclear endoplasmic reticulum markers were used to determine nuclear volume. In addition, the abundance of punctate structures such as cortical actin patches and Golgi increased proportionately to the age-related increase in cell surface area and volume, respectively. However, organelle scaling did not apply to all organelles as is evidenced by the disproportionate change in peroxisome number and size with replicative age. It is important to consider, however, that organelle scaling was characterized in young cells using large-cell mutants and the concepts defined in these studies may not apply to replicatively old cells. In addition to their large size, old mother cells likely differ in their physical structure and in their cellular physiology. Finally, the organelles of old cells need to accommodate not only their increased size, but also to age-related changing cellular demands.

How does increased proteasome activity affect age-associated phenotypes?

Increased proteasome activity by deletion of *UBR2* extends replicative lifespan independent of both caloric restriction and ERC-related pathways (Kruegel et al., 2011). The absence of Ubr2 is thought to increase proteasome activity by inhibiting Rpn4 turnover, which in turn increases the co-transcriptionally regulated proteasome components (Kruegel et al., 2011). The mechanism by which increased proteasome activity is thought to promote cellular survival is by eliminating damaged and misfolded proteins that accumulate and cause cellular dysfunction with replicative age. This proposed mechanism also suggests that the elimination of damaged proteins by the ubiquitin proteasome system is one of the primary limiting factors for lifespan, however it does not identify the targets of proteasomal degradation that confer lifespan extension.

The age-associated phenotypes subjected to further characterization in this work included mitochondrial fragmentation, vacuolar fragmentation, nucleolar fragmentation, the increase in peroxisome number and decrease in peroxisome size, and mitotic dysfunction. These five phenotypes were observed in aging cells in the context of increased proteasome activity in an *ubr2Δ* background with unexpected results.

Increased mitochondrial and vacuolar fragmentation in ubr2Δ cells

Deletion of *UBR2* resulted in increased mitochondrial fragmentation, and perhaps in an associated way, increased vacuolar fragmentation as well. This provided further support that

these two phenotypes are linked and that mitochondrial fragmentation appears to be required for vacuolar fragmentation. In addition, the deletion of *UBR2* conversely decreased the number of cells that possessed a fragmented nucleolus and suppressed the number of older mother cells exhibiting mitotic abnormalities, such as aberrant bud morphology or delayed mitosis as evidenced by visualization of a nucleoplasmic marker or spindle markers. This finding in turn supports the hypothesis that these two phenotypes are also associated as suggested by the double tagging experiments described in **Chapter IV**. Interestingly, increasing proteasome activity did not have an effect on the age-associated increase in peroxisome number or the decrease in size.

The fragmentation of the mitochondria was initially thought to be a maladaptive event in the aging process associated with loss of mitochondrial membrane potential and reduced lifespan (Hughes and Gottschling, 2012). The fact that a lifespan-extending condition would increase mitochondrial fragmentation suggests a couple different possibilities – that the mitochondrial fragmentation observed in *ubr2Δ* cells is somehow different from the fragmentation seen in replicatively aging cells or that the fragmentation of the mitochondria is actually an adaptive mechanism to preserve lifespan. The role of the proteasome in the regulation of mitochondrial morphology and dynamics (fission and fusion) has been a topic of active investigation. The yeast outer membrane mitofusin Fzo1 is regulated by ubiquitylation and its turnover thought to be responsible for modulating mitochondrial fusion (Westermann, 2010). Most recently Fzo1 was found to affect mitochondrial fusion differently depending on the specific lysine residue ubiquitylated, and that degradation by the proteasome inhibits mitochondrial fusion (Anton et al., 2013). The conclusion of Anton et al. is consistent with the finding of increased mitochondrial fragmentation in the context of increased proteasome activity as fission continues despite inhibition of fusion.

However, because *ubr2Δ* cells are long-lived and because loss of mitochondrial membrane potential associated with mitochondrial fragmentation shortens lifespan, it would be hypothesized that mitochondrial membrane potential would remain intact in *ubr2Δ* cells despite the finding of fragmented mitochondria (Kruegel et al., 2011; Hughes and Gottschling, 2012). If this is true, it would support the former of the possibilities – the nature of the fragmented mitochondria is different in *ubr2Δ* cells compared to aging wildtype cells. Further characterization of the mechanism of how increasing proteasome activity by deleting *ubr2* affects the mitochondria will provide additional insight into the relationship between mitochondrial morphology, function, and dynamics and replicative lifespan.

In addition to increasing the incidence of mitochondrial fragmentation in younger mother cells compared to wildtype, increasing proteasome activity by deleting *ubr2* also increases vacuolar fragmentation in aging cells at earlier timepoints. However, the mitochondrial fragmentation appeared to be required for vacuolar fragmentation in both wildtype and *ubr2Δ* cells. The vacuole is already known to be related to the mitochondria as loss of vacuolar acidity results in loss of mitochondrial membrane potential and mitochondrial fragmentation at an early replicative age (Hughes and Gottschling, 2012). This association has been shown to occur through the loss of the amino acid storage function of the vacuole during replicative aging (Hughes and Gottschling, 2012). If the nature of the mitochondrial fragmentation in *ubr2Δ* cells is indeed different in wildtype replicative aging cells compared to *ubr2Δ* cells as proposed above, it suggests that the subsequent vacuolar fragmentation may be a physical response to the mitochondrial fragmentation and not necessarily a functional consequence. The mitochondria and vacuole share several proteins, and perhaps there are protein-protein interactions that drive the fragmentation of the vacuole after the mitochondria has already fragmented. Again, determining whether the mitochondrial fragmentation in wildtype compared to *ubr2Δ* aging cells will provide insight into the mechanism of vacuolar fragmentation and its relationship with the mitochondrial phenotype.

Suppression of nucleolar fragmentation and age-associated mitotic abnormalities in ubr2Δ cells

Deletion of *UBR2* also suppressed both the fragmentation of the nucleolus and the incidence of mitotic dysfunction with replicative age, suggesting that these two phenotypes may also be associated. Because nucleolar fragmentation is caused by ERC accumulation, the suppression of nucleolar fragmentation in *ubr2Δ* cells suggests that increasing proteasome activity decreases age-associated ERC accumulation. One possible mechanism is that increasing proteasome activity allows for more efficient turnover of the replication factors, which are hypothesized to be sequestered by large quantities of ERCs and result in reduced replication potential (Steinkraus et al., 2008). Another possible mechanism is that ERCs are being directly degraded in a proteasome dependent manner and no longer inhibiting normal cell cycle.

Could ubr2Δ be exerting its effects through a non-proteolytic mechanism?

Finally, it is possible that while deleting *ubr2* does increase proteasome activity, it is actually a non-proteolytic function of the proteasome that is important for these age-associated phenotypes. The proteasome consists of many subunits, several if which are known to functions outside degradation (Finley et al., 2012). One candidate proteasome subunit whose

activity may have an effect on organelle morphology is Rpn11. Rpn11 is a lid subunit that contains deubiquitinating activity at its N-terminus and lid-stabilizing activity at its C-terminus. The C-terminus of Rpn11 has also been shown to be important for cell cycle progression and for normal mitochondrial morphology (Finley et al., 2012; Esposito et al., 2011; Rinaldi and Hofmann, 2008; Rinaldi et al., 1998; Joshi et al., 2011; Hofmann et al., 2009). Cells with expressing Rpn11 with a truncated C-terminus, *rpn11-m1*, exhibit several phenotypes that are reminiscent of the age-associated phenotypes described in this work. *rpn11-m1* cells contain highly fragmented mitochondria and an increased number of peroxisomes under oleate inducing conditions, both thought to be regulated through Fis1 via Rpn11's non-proteolytic function (Hofmann et al., 2009). *rpn11-m1* cells also exhibit a cell cycle defect resulting in the nucleus and nucleolus arresting in the bud neck and large, elongated buds. As with the abnormal budded cells observed with replicative age, *rpn11-m1* cells appear similar to mutants of the FEAR pathway (Esposito et al., 2011). Surprisingly, in the study by Esposito et al., overexpression of the FEAR pathway component Cdc14 suppresses both the mitochondrial fragmentation and the cell cycle defects.

If the age-associated changes in organelle morphology were regulated through the non-proteolytic activity of Rpn11, it would suggest that Rpn11 becomes limiting or defective with replicative age and deletion of *UBR2* suppresses these phenotypes by increasing Rpn11 expression. If this were true, it would also suggest that the FEAR pathway plays a role in at least the mitochondrial and cell cycle phenotypes, and perhaps the age-associated phenotypes could also be suppressed by overexpression of FEAR pathway components. Alternatively, deletion of *UBR2* may suppress age-associated phenotypes by increasing the turnover of FEAR pathways components and promoting progression of the cell cycle. The next step in exploring this line of reasoning would be to determine Rpn11 levels in replicatively old wildtype and *ubr2Δ* cells. Also, it would be interesting to determine if the fragmented mitochondria in *rpn11-m1* cells have intact or disrupted mitochondrial membrane potential.

The exact mechanism of how deletion of *UBR2* extends lifespan has not been completely elucidated. It appears as if increasing proteasome activity extends lifespan however whether there are specific of general age-specific targets for proteasomal degradation remains unclear. However, the importance of this pathway in the aging process is demonstrated by the fact that it alters multiple phenotypes in unexpected and yet unexplained ways.

Does the peroxisome phenotype represent an independent mechanism of aging?

The increase in peroxisome number and the concomitant decrease in peroxisome size with replicative age were first identified by Adam Hughes in the Gottschling lab by visualizing peroxisomes marked with the peripheral peroxisomal membrane protein Pex11p-GFP (Rottensteiner and Stein, 2003). This observation was confirmed through the screen and with high-resolution microscopy, which showed that the increase in peroxisome number is greater than would be expected given the age-associated increase in cell size. The increase in peroxisome number and the general decrease in peroxisome size with age was not a marker-specific protein as evidenced by colocalization with another peripheral membrane associated protein, an integral membrane protein, and an importable fluorescent protein containing a peroxisomal targeting sequence. Several hypotheses to explain this increase were generated and included increased biogenesis, increased pexophagy, increased fission, and decreased segregation to the bud. Also, it was hypothesized that the peroxisome phenotype may be related to the mitochondrial phenotype as peroxisomes and mitochondria share many proteins, including the dynamin-related protein (DRP) Dnm1, involved in mitochondrial and peroxisomal fission (Kuravi et al., 2006). As described in the results section, the mitochondrial fragmentation appears to be a more penetrant and earlier onset phenotype compared to the increase in peroxisomes with age.

Dnm1 is expendable for the age-associated peroxisomal phenotype as deletion of *DNM1* did not affect peroxisome number or size in old mother cells. This is interesting as Dnm1 is thought to be the major fission DRP in the context of ongoing mitochondrial dysfunction (Motley et al., 2008). The role of the other DRP responsible for peroxisome fission, Vps1, could not be determined as deletion of *VPS1* resulted in 1-3 large peroxisomes that did increase in number with replicative age, however it was not possible to determine whether there was no suppression or partial suppression of the phenotype. Because Dnm1 and Vps1 are the DRPs known to regulate peroxisome fission, it will be important to examine the effects of the double mutant on the age-associated peroxisome phenotype.

The peroxisome phenotype may be partially related to the loss of vacuolar acidity, mitochondrial fragmentation, and the loss of mitochondrial membrane potential as overexpression of *VMA1* resulted in a small decrease in peroxisome number but no apparent change in size distribution. Conversely, treatment with concanamycin A, which abolishes vacuolar acidity and induces mitochondrial dysfunction, only resulted in a modest increase in peroxisome number in young cells compared to the more dramatic phenotype in untreated replicatively aged cells. These findings suggest if there is a relationship between the

peroxisomes and vacuolar and mitochondrial dysfunction, it is only a partial association as altering vacuolar acidity could neither induce nor suppress the peroxisome phenotype in young or old cells, respectively.

It was also hypothesized that the increase in peroxisome number and the decrease in peroxisome size with age might be a response to changes in perceived nutritional status. Typically, nutrient-induced peroxisome fission occurs through phosphorylation of Pex11, however total protein from young and old yeast cells did not contain a phosphorylated species of Pex11. The possibility that the small peroxisomes in old cells were immature organelles was eliminated as they were import-competent. Finally, the peroxisomes in replicatively old cells did not represent degradation products as deletion of the protease *pep4* did alter the phenotype and clipped GFP could not be detected in the vacuole or by Western blot in cells expressing Pex14-GFP.

So then what is the mechanism of increased peroxisome number and decreased peroxisome size with replicative age? It is possible that the increase is secondary to decreased segregation to the bud, as this was never formally quantified. However, in several images, the buds of old cells not only contained peroxisomes, but also contained more peroxisomes than expected suggesting either increased transport or loss of asymmetry. Another possibility is that like the hypothesis with the vacuolar fragmentation, the peroxisomes being more numerous and smaller in size may be secondary to the fragmentation of the mitochondria. This is less likely, however, as there were old cells that exhibited the peroxisome phenotype and did not have fragmented mitochondria. This is supported by the finding that none of the lifespan extending conditions had any suppressing or inducing effect on the age-associated increase in peroxisomes. More experiments need to be done to determine the mechanism of this phenotype, as many of the possibilities have already been eliminated. If in fact none of the pathways known to regulate lifespan have any effect on peroxisome number or size, it may truly represent an independent pathway of aging.

Mitotic defects

The mitotic defects described in the further characterization of the phenotypes from the screen likely represent a terminal event as this phenotype occurs late and it is often unlikely that subsequent cell cycles are possible. Some old mother cells are seen with the entire spindle in the daughter cell and the spindle no longer oriented along the mother-bud axis. That there is some problem with mitosis is suggested by the nucleus not being in its predicted position or

being its predicted size given the stage of the cell cycle. Interestingly, this phenotype is partially suppressed by deletion of *FOB1* and dramatically suppressed by deletion of *UBR2*.

A recent study from the Kennedy and Kaeberlein labs demonstrated that cells that senesced in a budded state tended to have had shorter replicative lifespans compared to cells that arrested in an unbudded state, which had a longer lifespan (Delaney et al., 2013). Consistent with my findings that deletion of *FOB1* suppressed mitotic abnormalities in old cells, they found that deletion of *FOB1* resulted in a tendency for cells to have longer lifespans and arrest in an unbudded state. They proposed that the mechanism for this phenomenon is through the stochastic acquisition of DNA mutations as DNA repair mutants have a tendency to arrest in a budded state, similar to the short-lived mother cells. As mentioned above, that deletion of *FOB1* partially suppresses this phenotype suggests that there is some role of ERCs in the interference of the cell cycle in replicatively old cells. On possible explanation for this is that ERCs are sequestering important replication, DNA repair, or other cell cycle factors that result in cell cycle delay or arrest in old cells. It is very interesting that deletion of *UBR2* has a similar but much more dramatic affect compared to deletion of *FOB1*. The mechanism of how *ubr2* suppresses cell cycle abnormalities in replicatively old cells should provide insight into how ERCs are affecting mitosis and limiting replicative lifespan.

Conclusion

The cell biological screen for age-associated changes in organelle morphology is an unprecedented effort to use cell biological tools to identify cellular pathways that become altered with replicative age. This screen resulted in the finding that many structures change with replicative age strongly suggesting a stochastic contribution to the aging process as was discussed at length in the introduction for this section. However, given the wide range of age-associated phenotypes and approximation of their onset, it will be important to more accurately describe the order of age-associated events to determine which phenotypes representative causative changes and which may represent stochastic consequences. The initiating event may very well be the loss of vacuolar acidity that results in a decreased ability of the cell to store amino acids, which then eventually leads to loss of mitochondrial membrane potential and mitochondrial fragmentation (Hughes and Gottschling, 2012). The mitochondrial fragmentation is a very well-developed and robust age-associated phenotype and was thus used for comparison with the major findings from the screen – vacuolar fragmentation, increased peroxisome abundance, fragmentation of the nucleolus, and mitotic and budding abnormalities.

Observation of two organelles within the same aging cell with both wildtype and lifespan extending backgrounds demonstrated a strict association between mitochondrial fragmentation first, followed by vacuolar fragmentation. Although not absolute, nucleolar fragmentation and mitotic abnormality phenotypes were often coexistent in aging cells. In lifespan-extending conditions, the mitochondrial and vacuolar phenotypes were always induced or suppressed together, and similarly, the nucleolar and nuclear phenotypes were always induced or suppressed together.

The effect of deletion of *UBR2* on each of the age-associated phenotypes was most surprising, as it resulted in a dramatic increase in mitochondrial and vacuolar fragmentation with age. This finding combined with the previously characterized association between the vacuole and the mitochondria suggest a different mechanism regulating these similar phenotypes. Furthermore, that deletion of *UBR2* dramatically suppressed the nucleolar and nuclear phenotypes suggest a role of the proteasome in either preventing the accumulation of ERCs or enhancing the cell's ability to complete the cell cycle effectively, even in advanced replicative age. Finally, that the peroxisome phenotype does not appear to fit in any of the patterns or categories described above suggests that it might represent a novel aging pathway.

This screen and its subsequent characterization was successful in that it uncovered new phenotypes that may represent novel pathways important in aging, and that can be further dissected to gain additional insight into the mechanisms that underlie the aging process. There is evidence that increasing proteasome activity is affecting the aging mother cell in very specific ways. It therefore stands to reason that the cell biological manifestations of these effects are an indication of the important targets of degradation necessary for increased lifespan. The next step will be to dissect the mechanisms behind each of the findings described in this work with the ultimate goal of better understanding how aging is initiated, regulated, and what cellular pathways are important for the aging process. Finally, the finding that there is cell-biological evidence that DNA replication and cell cycle progression may be compromised with replicative age supports the long-standing hypothesis that there are age-induced defects in DNA repair, which is discussed in the following section.

Section Two: Age-Induced Defects in DNA Repair

Chapter VII: Introduction to replicative aging and DNA repair

Genetic instability and DNA repair in aging

Genetic instability has been implicated as a cause of aging and is a hallmark of one of the most common age-associated diseases, cancer (Hanahan and Weinberg, 2000). Genetic instability is generally defined as a state in which a cell can no longer maintain its genomic integrity, resulting in any number of manifestations, including increased mutations, loss of heterozygosity, aneuploidy, and epigenetic instability (Beckman and Loeb, 2005). Evidence that genetic instability is associated with aging and age-related diseases, such as cancer, come from human syndromes caused by RecQ family helicase mutations. The RecQ family helicases are proposed to function in DNA repair processes, and defects in certain members of this protein family are associated with cancer predisposition and premature aging (Hickson, 2003). The mechanism of how cells acquire genetic instability with age continues to be debated. The acquisition of genetic changes are predicted to occur by two distinct means: 1) the linear accumulation of mutations due to a constant mutation rate throughout the lifespan of a cell, or 2) an increase in mutation rate due to an age-induced defect in genome maintenance. However, the spontaneous mutation rate measured in young human cells is not high enough to account for the high mutational burden observed in models of aging, suggesting that a mutator effect is involved in the aging process (Beckman and Loeb, 2005). Mutator effects have been widely studied, particularly in the context of cancer. The increased mutation rates are believed to result from compromised DNA repair and provide evidence of a direct association between DNA repair and genetic instability (Kolodner et al., 2002).

The relationships between DNA repair, genetic instability and aging have been much more difficult to elucidate. Studies using yeast pedigree analysis has suggested that loss of heterozygosity occurs at a much higher frequency in the progeny of mother cells with advanced replicative age, thereby establishing a correlation between one aspect of genetic instability and aging (McMurray and Gottschling, 2003). Recent developments in DNA double-strand break (DSB) repair in other model organisms have provided evidence that alterations in DNA repair are associated with age. In Drosophila, many pathways can resolve DSBs, however, *in vivo* comparisons between DSB repair in young and old flies suggested that DSBs were increasingly

repaired by homologous recombination as a function of age (Preston et al., 2006). Furthermore, *in vitro* studies using cell extracts from neonatal and adult rat neurons showed an age-dependent deficiency in the cell's ability to perform non-homologous end joining, another pathway for DSB resolution (Vyjayanti and Rao, 2006). These studies establish a correlation between DNA repair, genetic instability, and aging, and provide the evidentiary support necessary to investigate whether changes in DNA repair are mechanistically involved in the acquisition of a genetically unstable state and the aging process.

***Saccharomyces cerevisiae* as a model for studying DNA repair in aging cells**

Budding yeast *Saccharomyces cerevisiae* is a simple unicellular eukaryotic organism that has an integral role in our ability to understand and characterize fundamental concepts in cellular biology. Yeast is the ideal organism for studying the relationships among DNA repair, genetic instability, and aging for several reasons. First, pathways in DNA metabolism, such as DNA repair, are highly evolutionarily conserved. Many of the DNA repair proteins characterized in yeast have human homologues that play important roles in human disease. For example, mismatch repair genes were intensely studied in yeast, and later mutants in the human homologues of these genes were found to lead to colorectal cancer (Verma et al., 1999). Second, *S. cerevisiae* continues to be a widely used model organism because of its genetic tractability. Its genome is completely sequenced and almost entirely annotated. Furthermore, yeast genetic networks for DNA repair and metabolism have been extensively studied (Zhao et al., 2005; Pan et al., 2006; Loeillet et al., 2005). These efforts have generated a wide variety of specific assays to study particular aspects of genetic instability. Third, *S. cerevisiae* is an excellent biological system for the study of aging. Yeast divide asymmetrically, and the have a limited replicative lifespan (Mortimer & Johnston, 1959). Replicative lifespan is defined as the total number of daughter cells that can be produced by a single mother cell, and is analogous to the replicative behavior of human stem cell populations (Jazwinski, 2005; Mortimer & Johnston, 1959). These advantages of using budding yeast as a model organism provide a simple system to better understand the roles of DNA repair and genetic instability in aging and age-associated diseases. Aging studies in higher eukaryotes have proven to be less feasible due to their greater complexities and longer lifespans. The median lifespan of ~50 hours for yeast provides an impressive technical advantage over longer-lived model organisms. Also, the Mother Enrichment Program developed in the Gottschling lab allows for the growth and enrichment of aged mother cells in bulk culture, providing enough cells to assay for rare genetic events.

DNA damage signatures

In yeast, the repair pathway of lesions produced by specific DNA-damaging agents are known, thus the DNA damage signatures of treated old cells can be used to identify defects in DNA repair pathways that occur with age (Gasch and Werner-Washburne, 2002; Gasch et al., 2001). Evidence for a phenomenon that both influences DNA repair and becomes altered as a function of age can be found in *S. cerevisiae* and Drosophila. Pedigree analysis in yeast showed recombination events and loss of heterozygosity occurred more frequently in older cells (McMurray and Gottschling, 2003). Furthermore, the preferred double strand break repair pathway changes as Drosophila age, supporting further investigation into how DNA repair status may change as a function of age (Preston et al., 2006). Age-related deficiencies in particular DNA repair pathways can be identified by their response to chemical challenges that induce specific types of DNA damage. For example, treatment of cells with hydrogen peroxide causes an increase in oxidative DNA damage, such as 7,8-dihydro-8-oxoguanine (8-oxoG). These lesions are mutatgenic, and recognized and repaired by the base excision repair pathway (David et al., 2007). If the base excision repair pathway becomes deficient during aging, the oxidative lesions will remain unrepaired and accumulate, leading to an age-dependent lethality in hydrogen peroxide treated cells. Conversely, age-dependent resistance to a particular DNA damaging agent may indicate upregulation of protective DNA repair pathways.

Synthetic-lethal genetic interactions

Synthetic-lethal genetic interactions occur when a combination of mutant alleles of two genes result in lethality when neither allele alone is sufficient to affect viability, suggesting a genetic or functional relationship between the two genes. Lethality is not strictly constrained by the nature of the allele, and synthetic-lethal interactions can occur between partial loss of function alleles. In fact, synthetic-lethal interactions can be generated by modulating protein levels. Genome-wide analyses by several laboratories have recently produced an entire network of genetic and biochemical interactions in yeast. Particular emphasis has been placed on pathways involved in DNA integrity, such as DNA replication, repair and checkpoint signaling (Zhao et al., 2005; Pan et al., 2006; Loeillet et al., 2005). These interactions have been characterized across the entire yeast genome, creating an effective network of genes that interact either within the same pathway or in distinct but complementing pathways.

Two approaches to identify age-dependent defects in DNA repair

Defects in DNA repair have been implicated in driving the accumulation of DNA damage that leads to aging and age-associated diseases, such as cancer. I used two different approaches to determine to what extent DNA repair becomes deficient due to the aging process, and which aspects become defective as a function of age. First, I attempted a screen for DNA repair genes, that when repressed, result in a synthetic lethal interaction with replicative age. Second, I subjected aging cells to various DNA-damaging agents to identify types of lesions that could no longer be efficiently repaired in old cells.

Chapter VIII: Age-induced changes in DNA repair

Two approaches to identify changes in DNA repair with replicative age

Identification of the DNA repair pathway or pathways that decline as a function of age will provide greater understanding of how genome integrity is compromised during aging. To address this, I took two independent approaches to identify changes in DNA repair that occur during the aging process. The first approach is based on the idea that genetic interactions may undergo age-associated changes, and how these interactions change will identify pathways that have become compromised due to age. The second approach uses information based on changes in the aging cell's ability to tolerate and respond to various classes of DNA-damaging agents to identify defects in DNA repair.

Approach One: Age-dependent synthetic lethal interactions

Brief introduction to the approach

Synthetically lethal interactions occur when two genes function in parallel and compensatory pathways (Hartman et al., 2001). The null allele of either gene does not result in lethality, but the double null alleles results in an inviable phenotype (**Figure 8.1**). Because much of the yeast DNA repair and metabolism interactions network is known, a screen for age-dependent synthetic lethality could yield the identity of defective pathways in aging. Placement of known genes in various DNA repair pathways under a tetracycline-repressible promoter, allows expression of these genes to be repressed in a controlled manner (**Figure 8.2**) (Bellí et al., 1998).

Specific DNA repair pathways are hypothesized to become deficient during the aging process, effectively rendering the aged cell null for those gene functions. Therefore, age-associated repression of known DNA repair pathway genes should cause synthetic lethality only in aged cells, and will also provide information regarding the identity of the unknown defective pathway. A schematic and explanation of the logic behind using synthetic lethal interactions to identify age-dependent defects in DNA repair is found in **Figure 8.3**. Repression of genes that interact with a DNA repair pathway that becomes defective as a function of age will result in a synthetic-lethal phenotype in old cells, but not young cell.

To systematically determine the effect of repressing DNA repair genes in old cells, I generated a set of strains containing the components required for the Mother Enrichment Program (MEP), the components for tetracycline-inducible gene repression, and individual DNA

repair genes under the control of the tetracycline-repressible *tetO$_2$* promoter. Genes of interest were prioritized based on their connectivity in the genetic interactions network in order to maximize the probability that the repressed gene will interact with a DNA repair pathway that has become defective with age.

RAD52 expression can be conditionally repressed

Conditional repression of *RAD52* by doxycycline (a stable analog of tetracycline) was demonstrated both phenotypically and biochemically prior to experimentation. Rad52 is important for DNA double-strand break repair, and has synthetic lethal interactions with over 100 genes (www.yeastgenome.org). Because of its role in DNA double-strand break repair, cells without Rad52 are lethally sensitive to DNA damaging agents that induce double-strand breaks, such as methyl methanesulfonate (MMS) (Fry et al., 2005).

Cells containing the *tetO$_2$pr-RAD52* exhibited growth similar to wildtype under non-repressing conditions by spot test on solid media with and without 0.08% MMS (**Figure 8.4)**. Cells expressing *tetO$_2$pr-RAD52* exhibited growth similar to *rad52Δ* cells under repressing conditions (20 μg/mL doxycycline) on solid media with and without 0.08% MMS (**Figure 8.4**). This suggests that *RAD52* expression can be repressed to near-null levels based on phenotypic testing.

Western blot analysis was used to biochemically confirm loss of Rad52 and to determine the kinetics of Rad52 repression. Loss of detectable Rad52 protein occurred rapidly, within 2-3 hours following repression with doxycycline (**Figure 8.5**).

Rad52 repression causes lethality in a subset of old cells

Cells were grown exponentially, aged in culture using the MEP, and either treated or not treated with doxycycline (20 μg/mL doxycycline final concentration) at time 3, 27, 50, and 72 hours for 6 hours prior to filtration and plating with glass filters onto solid YEPD containing 20 μg/mL doxycycline. The viability of Rad52 repressed cells was compared to unrepressed cells at each timepoint. The experiment was done in biological duplicate and plated in duplicate. The viability of repressed cells compared to unrepressed cells were 100%, 81%, 75%, and 71% at time 3, 27, 50, and 72 hours, respectively (**Figure 8.6**). These findings suggest that a subpopulation of aging cells were sensitive to Rad52 repression.

No other genes tested could be repressed

I attempted to repress many other DNA repair genes in a similar manner, including *APN1*, *DNL4*, *MAD3*, *MSH1, OGG1*, *PMS1, RAD6*, *RAD1, RAD9, RAD18*, *RAD27*, *RAD54*, *REV3*, and *SGS1*, however these genes could never be repressed to levels sufficient to elicit a null-like phenotype.

Approach Two: Tolerance of aging cells to various DNA-damaging agents

Brief introduction to the approach

In yeast, specific DNA-damaging agents and/or loss of certain DNA repair mechanisms result in a stereotypical pattern of lesions, known as the DNA damage (Fry et al., 2005; Gasch et al., 2001; Gasch and Werner-Washburne, 2002). Age-associated changes in DNA repair efficiency can be identified by comparing the response of young and old cells to well-characterized DNA-damaging agents. For example, treatment of cells with oxidizing agents, such as hydrogen peroxide, induces mutagenic 8-oxoG lesions in DNA (David et al., 2007). Base excision repair pathways are required to address these lesions and to prevent toxicity to the cell. Age-dependent sensitivity to hydrogen peroxide would suggest an acquired defect in base excision.

To identify changes in DNA repair pathways with age, I determined the tolerance of young and old cells to various well-characterized chemical challenges. (**Table 8.1**). Exponentially growing cells were aged in culture using the MEP, and subjected to transient treatment with either DNA-damaging agent or mock-treatment with 1XPBS for 6 hours. Cells were then filtered, washed, and plated onto solid YEPD media. The colony viability of treated cells was compared to untreated cells at approximately times 3, 24, 48, and 72 hours of aging.

Young and old cells were equally tolerant to challenge with cisplatin and MMS

Cells at various replicative ages were assayed for ability to form colonies following transient exposure to 300 μM cisplatin (*cis*-diamminedichloroplatinum (II) or CDDP). Cisplatin is a DNA cross-linking agent that predominantly induces 1,2-intrastrand d(GpG) adducts that require nucleotide excision repair mechanisms for removal (Fry et al., 2005). The viability of treated cells compared to untreated cells were 27%, 35%, 45%, and 30% at time 3, 27, 51, and 72 hours, respectively (**Figure 8.7**).

Cells were also assayed for colony-forming ability following transient exposure to 0.08% methyl methanesulfonate (MMS). MMS is a DNA alkylating agent that methylates deoxyguanine and deoxyadenine. These lesions cause replication forks to stall and require

homologous recombination pathways for repair (Fry et al., 2005). The viability of treated cells compared to untreated cells were 12%, 39%, 20%, and 23% at time 3, 27, 51, and 72 hours of aging, respectively (**Figure 8.7**).

Taken together, these results suggest that nucleotide excision and homologous recombination repair pathway are not dramatically altered as a function of replicative age.

Age-dependent resistance to hydrogen peroxide

Hydrogen peroxide (H_2O_2) is a non-specific chemical agent often used to induce oxidative stress and damage in cells. While not solely a genotoxic agent, H_2O_2 is often used to test cellular response to increased oxidative DNA base damage. H_2O_2 typically induces 8-oxoguanine damage to DNA that requires base excision repair for removal (David et al., 2007). Interestingly, treatment of cells at various replicative ages with 0.5 mM H_2O_2 resulted in a biphasic curve with increased sensitivity in the first 24 hours, and increased resistance in the last 48 hours (**Figure 8.8**).

To determine if this age-dependent pattern of sensitivity and resistance to H_2O_2 is stereotypical for all oxidizing agents, cells were also assayed for viability following treatment with diamide, menadione sodium bisulfite (MSB), and *tert*-butyl hydroperoxide (*t*-BuOOH or *t*-BHP). Diamide is a thiol-oxidizing agent, MSB is a vitamin K class compound that has been reported to increase oxidative radicals, and *t*-BHP is most similar to H_2O_2 in generating reactive oxygen species (Jamieson, 1992, 1998). *t*-BuOOH is often used to study the effects of lipid peroxidation (Jamieson, 1992, 1998; Bokov et al., 2004).

Transient treatment of aging cells with 1 mM diamide did not elicit any differences in response in young cells compared to old cells (**Figure 8.9A**). However, treatment with both MSB and *t*-BuOOH resulted in an age-dependent changes in viability. Treatment with 0.1 mM MSB also resulted in a biphasic curve with increasing sensitivity during the first 48 hours and increased resistance acquired in the last 24 hours (**Figure 8.9B**). Finally, *tert*-butyl hydroperoxide (22mM) treated cells exhibited extreme sensitivity with replicative age (**Figure 8.9C**).

The biphasic nature of the curves resulting from H_2O_2, MSB, and even *t*-BuOOH treatment prompted further investigation. For each experiment, cells were grown to saturation overnight, used to seed dilute cultures, and were allowed to achieve exponential growth for several hours prior to MEP induction and aging. However, the expression of over a thousand genes changes when cells grown to saturation are allowed to undergo exponential growth (Martinez et al., 2004). I wondered whether the first phase of these biphasic curves could be

explained by continued exponential growth as opposed to replicative age. To test this, cells were assayed for viability after H_2O_2 treatment following various periods of log-phase growth. Cells were grown exponentially for 6, 12, 18, 24, 48, 72, and 98 hours, prior to MEP induction for 3 hours and treatment with H_2O_2 for 6 hours. The relative viability of treated compared to untreated cells was determined for every timepoint, and definitively demonstrate that H_2O_2 sensitivity is dependent on time spent in log-phase growth (**Figure 8.10**).

This finding suggests that many of the treatments actually reveal age-dependent resistance of the cells. The effect of exponential growth on H_2O_2 sensitivity appears to stabilize after approximately 24 hours following removal from saturating conditions. Thus, treatment of aging cells with H_2O_2, diamide, MSB, and *t*-BuOOH was repeated, but on cells that were exponentially grown for 24 hours prior to induction of the MEP. Upon retesting, cells exhibit age-dependent resistance to H_2O_2 (**Figure 8.11A**), diamide (**Figure 8.11B**), and MSB (**Figure 8.11C**). Treatment with *t*-BuOOH was inconclusive because the concentration of chemical used caused universal lethality.

The effect of time in log-phase growth on age-associated phenotypes has broader experimental and more importantly, biological implications on cellular lifespan and aging studies. These implications will be further considered in the discussion section and in **Appendix E**.

Table 8.1. DNA-damaging agents, treatment concentrations, and the nature of the drug. All drugs were manufactured by Sigma-Aldrich.

Agent	Treatment concentration	Type of damage induced and repair pathways required
Methyl methanesulfonate	0.08%	Alkylating agent, requires DNA double-strand break repair
Cisplatin	300 μM	DNA cross-linking agent, requires nucleotide excision repair
Hydrogen peroxide	0.5 mM	Oxidizing agent, induces 8-oxoguanine lesions, abasic sites, requires base excision repair
Menadione sodium bisulfite	0.1 mM	Oxidizing agent
Diamide	1 mM	Thiol-oxidizing agent
Ter-butyl hydroperoxide	22 mM	Oxidizing agent, often used for lipid peroxidation

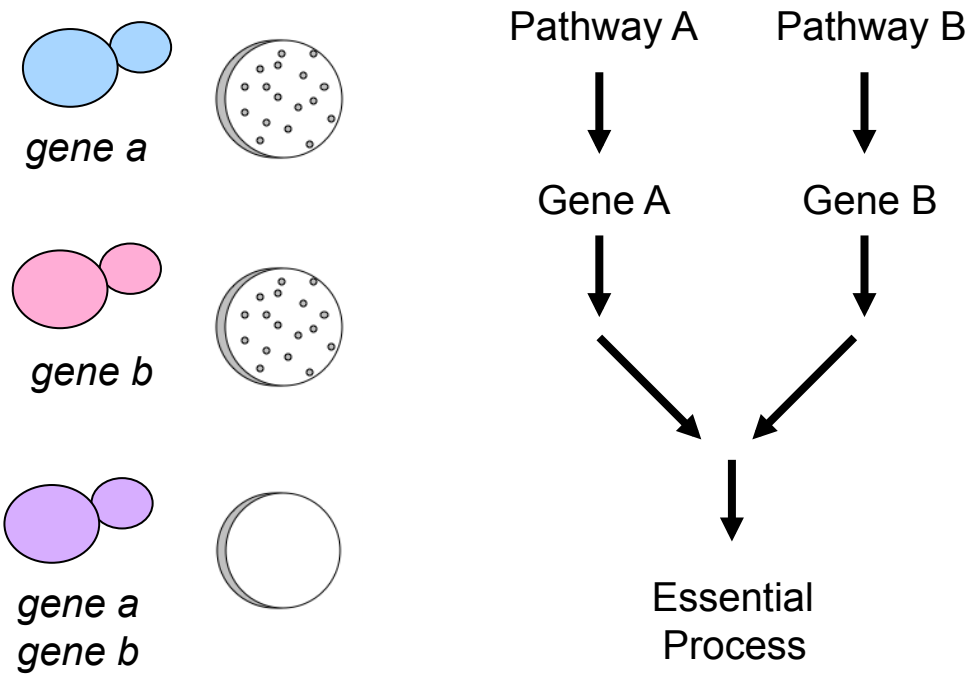

Figure 8.1. Schematic of synthetic-lethal genetic interactions. Synthetic-lethal genetic interactions occur when a combination of mutant alleles of two genes result in lethality when neither allele alone is sufficient to affect viability, suggesting a genetic or functional relationship between the two genes. Synthetic-lethal interactions often occur between two genes that each function in separate, but parallel and compensatory pathways that are required for an essential cellular function. Lethality is not strictly constrained by the nature of the allele, and synthetic-lethal interactions can occur between partial loss of function alleles.

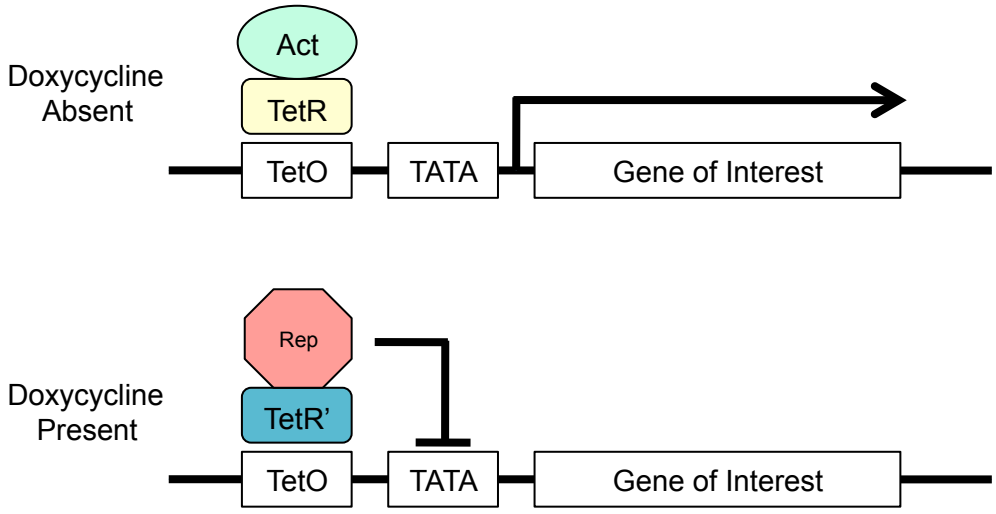

Figure 8.2. Schematic of tetracycline inducible gene repression system. The tetracycline-inducible repression machinery consists of three parts: the tetracycline-responsive promoter (*tetO*$_2$), an activator (VP16-tetR), and a repressor (SSN6-tetR'). The promoter is the bacterial Tn10 transposon-derived tetracycline-responsive *tetO* promoter. The activator is a fusion protein consisting of the *tetO* recognition domain of tetR fused to a strong transcriptional activator VP16. The repressor is comprised of the yeast transcriptional repressor SSN6 fused to a mutated version of tetR that is responsive to tetracycline (tetR'). In the absence of doxycycline, a stable analog of tetracycline, the activator tetR fusion protein binds the *tetO* promoter and allows transcription of the gene of interest. In the presence of doxycycline, the repressor tetR' fusion protein binds the *tetO* promoter and prevents transcription.

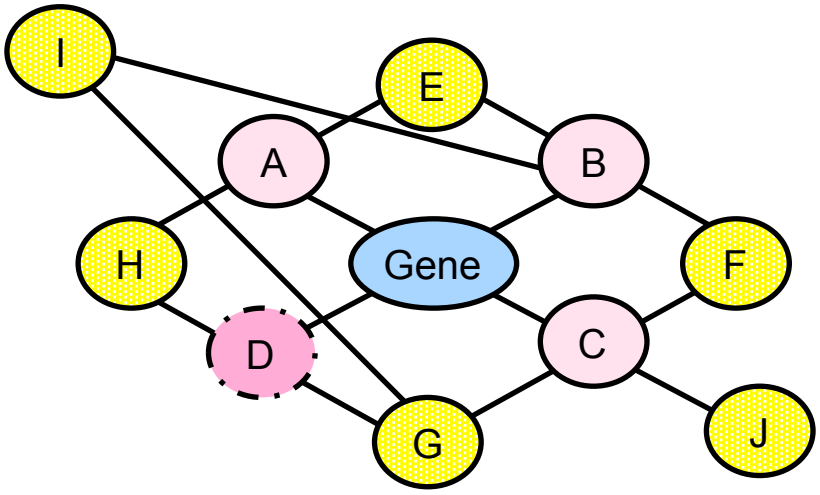

Figure 8.3. How age-dependent synthetic-lethal interactions can be used to identify genes or pathways that have become defective with age. Much of the yeast DNA repair and metabolism genetic interaction network is known. For simplification, a theoretical schematic of the Rad52 interactome is shown. If Rad52 repression produces an age-dependent synthetic-lethal interaction, one of Rad52's direct interactors, A, B, C, or D must have become defective with age. Identification of whether the defect is in A, B, C or D can be accomplished by synthetic lethality analysis of genes E, F, G, H, I and J. For example, if repression of I does not produce a synthetic-lethal phenotype with age, then A and B must not become defective with age. If repression of F also does not produce a synthetic-lethal phenotype in old cells, it can be inferred that D interacts with the unknown defective pathway. This can then be further tested by determining age-dependent conditional lethality with the repression of H.

A.

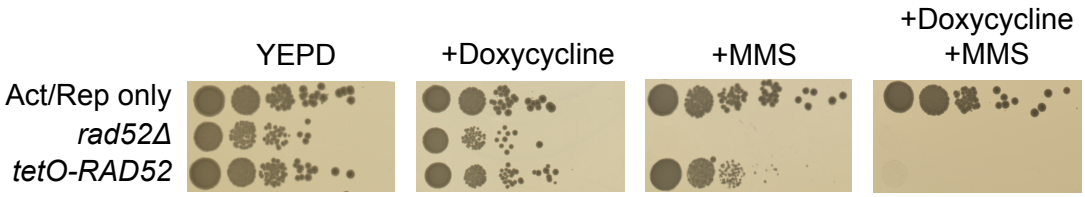

B.

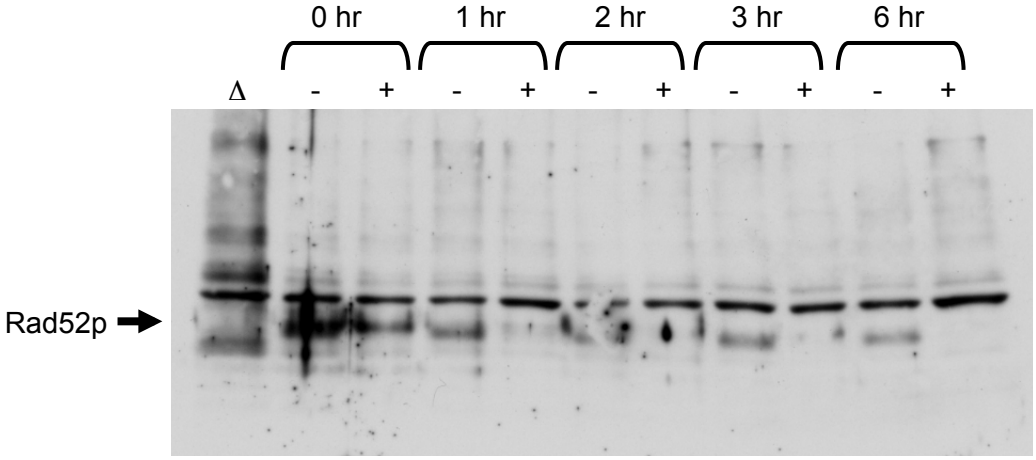

Figure 8.4. Rad52p is eliminated in the presence of doxycycline. (A) Phenotypic demonstration of doxycycline-induced *RAD52* repression. The act/rep only strain only contains the activator and repressor components of the tetracycline-inducible gene repression machinery, and serves as a Rad52p-expressing control. The *rad52Δ* strain serves as a control for cells completely deficient for Rad52p. The *tetO-RAD52* strain contains the activator, repressor, and the tetracycline-responsive allele of *RAD52*. Strains were spotted at 10-fold dilutions on rich YEPD, YEPD containing 20 μg/mL doxycycline, YEPD containing 0.08% MMS, and YEPD containing both doxycycline and MMS. From left to right, Panel 1: The *tetO-RAD52* strain exhibits normal growth on YEPD, similar to act/rep only. *rad52Δ* cells are growth defective. Panel 2: *tetO-RAD52* growth is similar to *rad52Δ* under repression conditions (+doxycycline). Panel 3: *tetO-RAD52* growth is similar to act/rep only on MMS. Cells lacking *RAD52* are sensitive to MMS. Panel 4: *tetO-RAD52* growth is similar to *rad52Δ* under repression conditions on media containing doxycycline and MMS. (B) Western blot analysis showing Rad52p is not detected in cells after 6 hours growth under repression conditions (+doxycycline). Total protein was extracted from exponentially dividing *rad52Δ* cells and from *tetO-RAD52* cells at 0, 1, 2, 3, and 6 hours growth under non-repression (-) or repression (+) conditions. Presence of Rad52p was determined by Western blot analysis with an anti-Rad52 antibody.

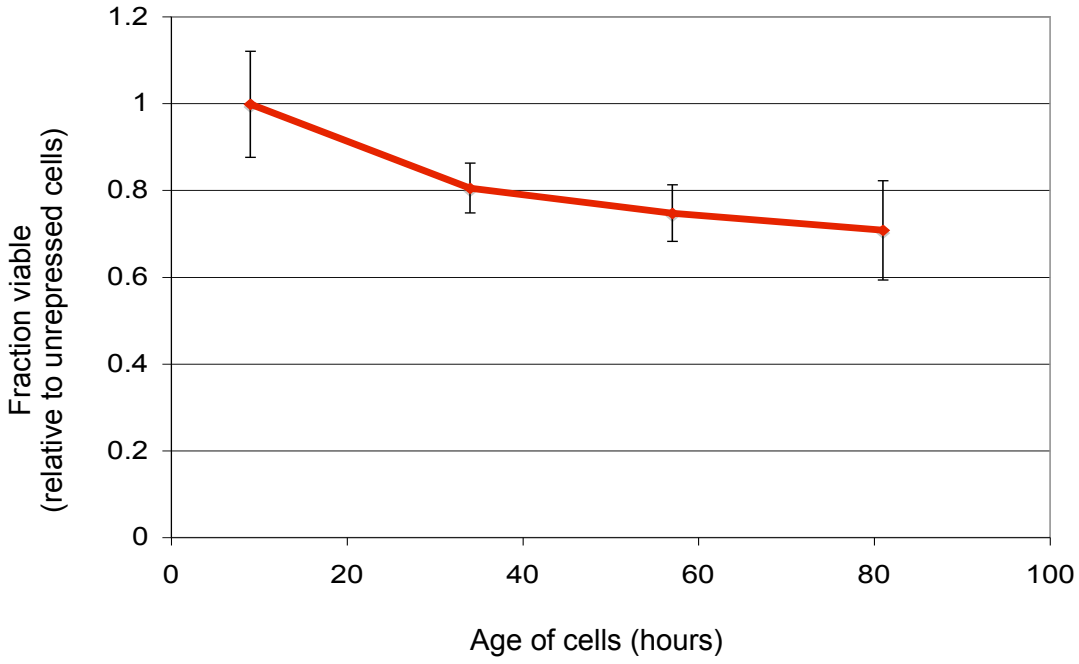

Figure 8.5. Cells become increasingly sensitive to Rad52p deficiency with replicative age. *tetO-RAD52* cells were aged using the MEP. Cells were removed at times 3, 27, 50, and 72 hours following MEP induction, and grown for 6 hours under non-repression and repression (+doxycycline) conditions. The viability of unrepressed and repressed cells was determined by colony viability assay. Experiments were done in triplicate; the average relative viability of repressed to unrepressed cells is shown here. Error bars represent one standard deviation.

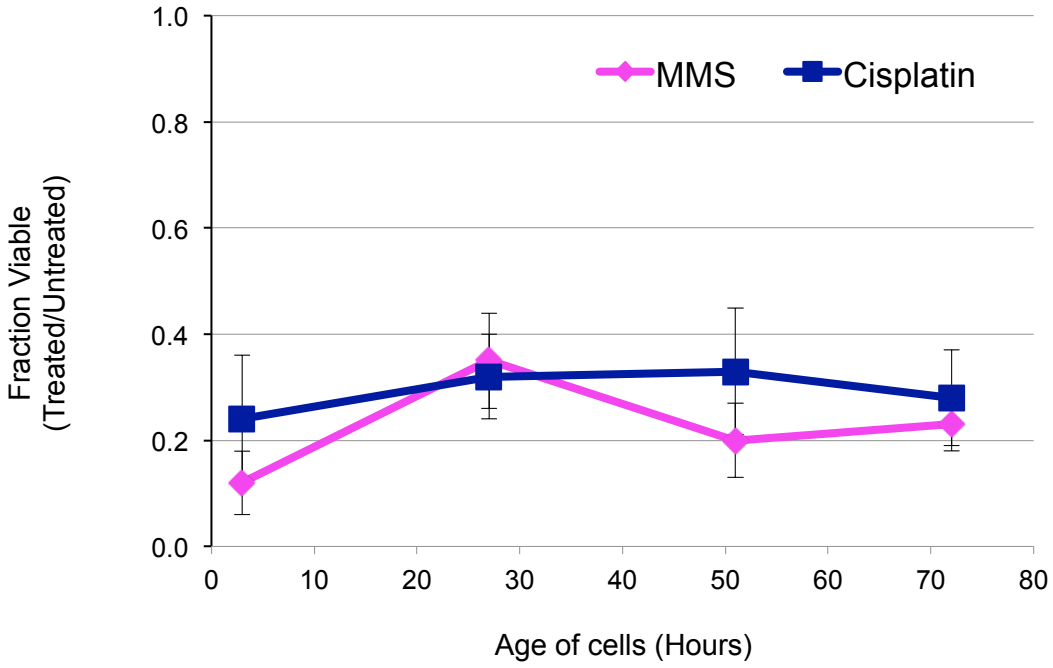

Figure 8.6. Cells do not exhibit any age-dependent changes in viability following treatment with MMS or cisplatin. UCC5185 diploid cells were aged using the MEP. Cells were removed at times 0, 24, 48, and 72 hours following induction of the MEP and either mock treated with 1X PBS or treated with 0.08% MMS or 300 μM cisplatin for 6 hours. Cells were collected and washed by filtration and plated by placement of the filter on solid YEPD media. The viability of untreated and treated cells was determined by colony viability assay. Experiments were done in triplicate; the average relative viability of treated to untreated cells is shown here. Error bars represent one standard deviation.

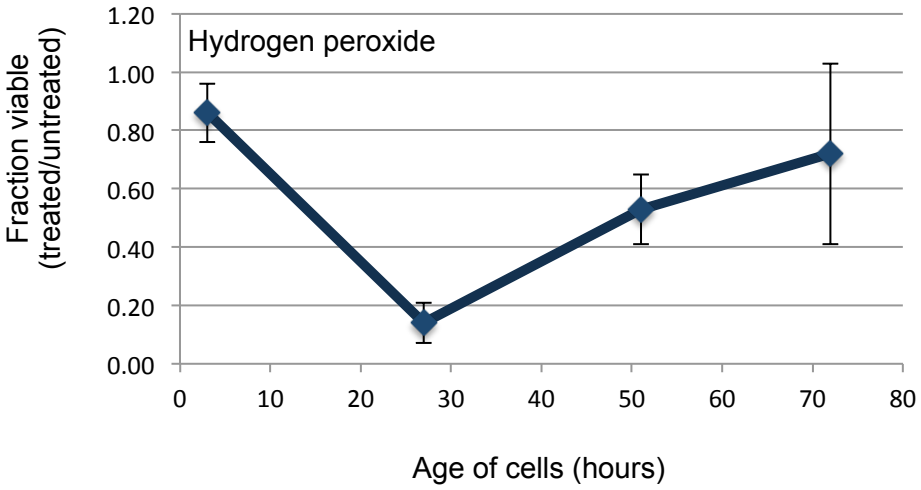

Figure 8.7. Aging cells exhibit a biphasic response to hydrogen peroxide treatment. UCC5185 diploid cells were aged using the MEP. Cells were removed at times 0, 24, 48, and 72 hours following induction of the MEP and either mock treated with 1X PBS or treated with 0.5 mM hydrogen peroxide (H_2O_2) for 6 hours. Cells were collected and washed by filtration and plated by placement of the filter on solid YEPD media. The viability of untreated and treated cells was determined by colony viability assay. Experiments were done in triplicate; the average relative viability of treated to untreated cells is shown here. Error bars represent one standard deviation. Aging cells exhibit sensitivity to hydrogen peroxide between times 0 and 24 hours, and acquire resistance to hydrogen peroxide at later timepoints (hours 48 and 72).

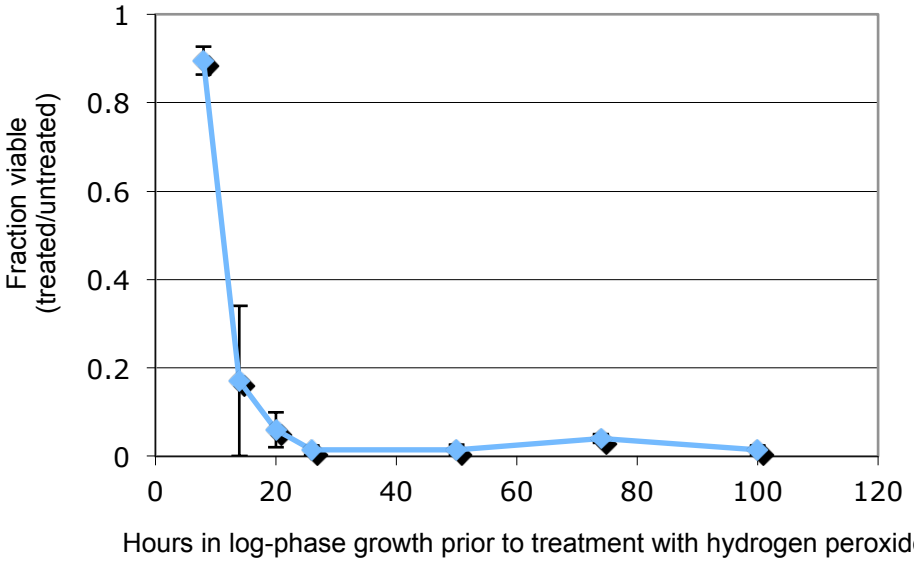

Figure 8.8. Effect of log-phase growth on hydrogen peroxide treated cells. UCC5185 diploid cells were grown at low density in rich medium. Cells were removed at times 0, 6, 12, 18, 24, 48, 72, and 96 hours following dilution from saturation. Cells were either mock treated with 1X PBS or treated with 0.5 mM hydrogen peroxide (H_2O_2) for 6 hours. Cells were collected and washed by filtration and plated by placement of the filter on solid YEPD media. The viability of untreated and treated cells was determined by colony viability assay. Experiments were done in triplicate; the average relative viability of treated to untreated cells is shown here. Error bars represent one standard deviation. Aging cells exhibit increasing sensitivity to hydrogen peroxide during the first 24 hours of exponential growth.

A.

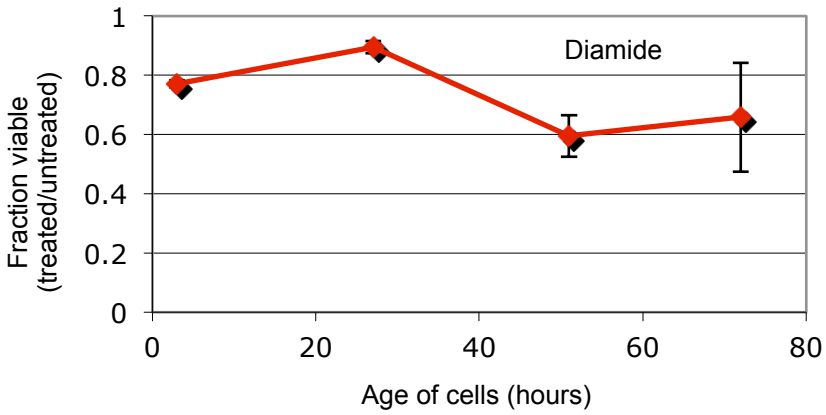

B.

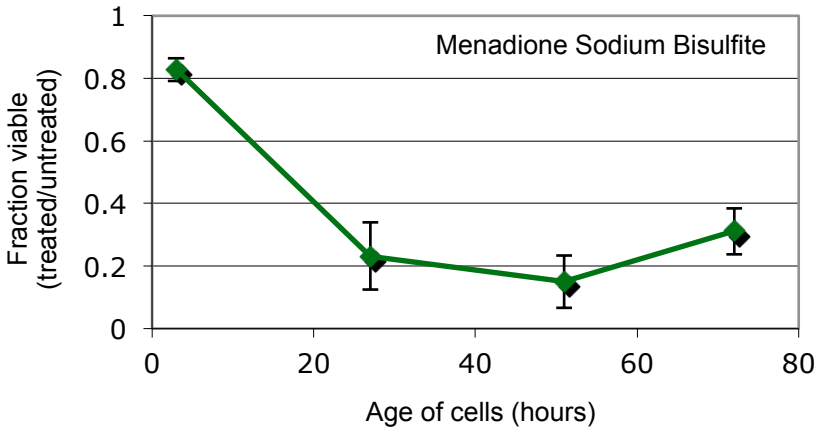

C.

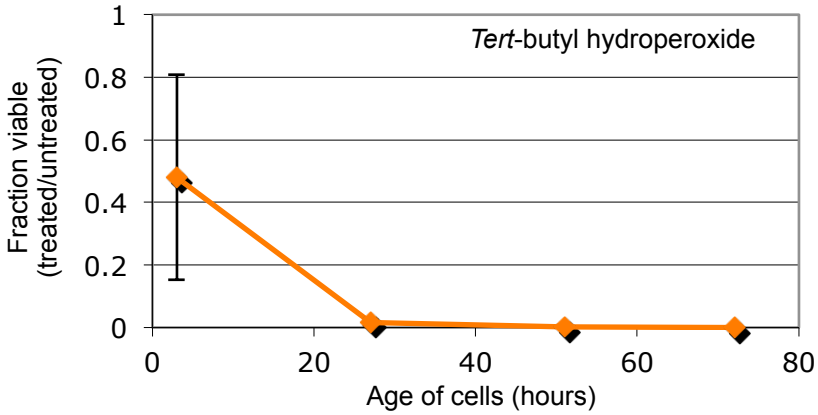

Figure 8.9. The effect of other oxidizing agents on replicatively aging cells. UCC5185 diploid cells were aged using the MEP. Cells were removed at times 0, 24, 48, and 72 hours following induction of the MEP and either mock treated with 1X PBS or treated with (A) 1 mm diamide, (B) 0.1 mM menadione sodium bisulfite, or (C) 22 mM tert-butyl hydroperoxide for 6 hours. Cells were collected and washed by filtration and plated by placement of the filter on solid YEPD media. The viability of untreated and treated cells was determined by colony viability assay. Experiments were done in triplicate; the average relative viability of treated to untreated cells is shown here. Error bars represent one standard deviation. (A) Aging cells exhibited modest sensitivity to diamide. (B) Cells exhibited initial sensitivity followed by modest resistance to menadione with replicative age (C) Cells exhibited age-dependent sensitivity to *tert*-butyl hydroperoxide.

A.

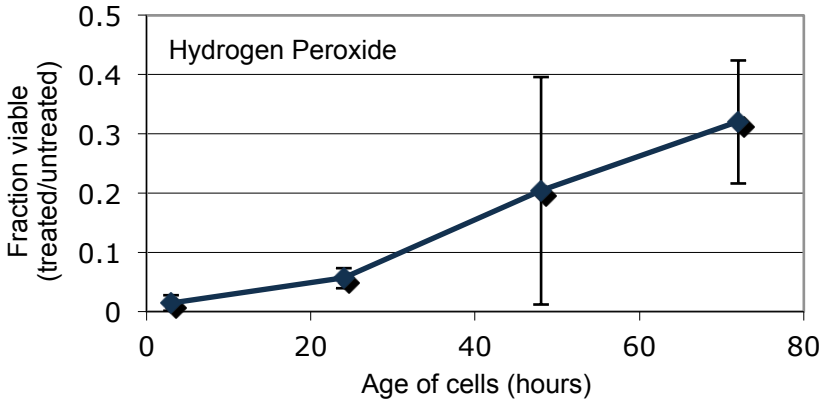

B.

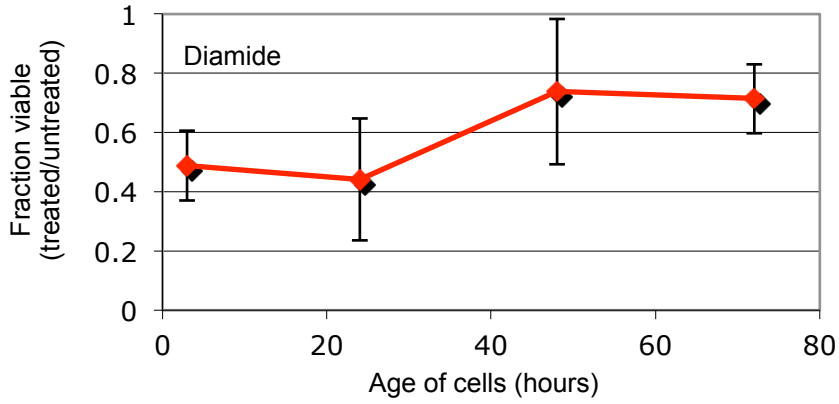

C.

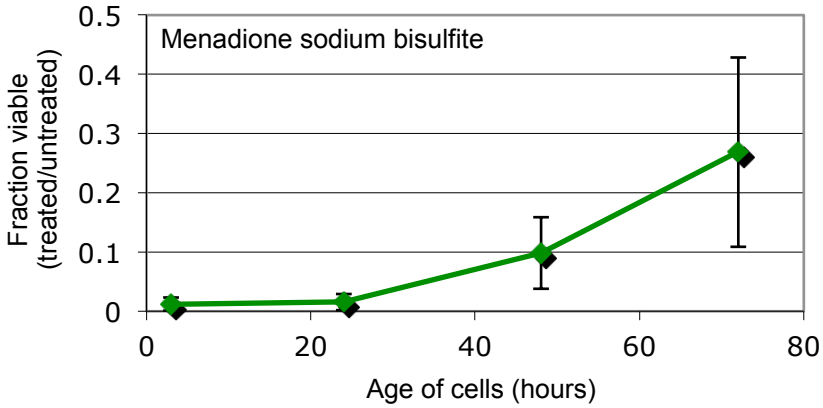

Figure 8.10. Pre-growth of cells at low density prior to MEP induction affects their age-dependent response to treatment with oxidizing agents. UCC5185 diploid cells were grown exponentially for 24 hours prior to MEP induction. Cells were removed at times 0, 24, 48, and 72 hours following induction of the MEP and either mock treated with 1X PBS or treated with (A) 0.5 mM hydrogen peroxide, (B) 1 mM diamide, or (C) 0.1 mM menadione sodium bisulfite for 6 hours. Cells were collected and washed by filtration and plated by placement of the filter on solid YEPD media. The viability of untreated and treated cells was determined by colony viability assay. Experiments were done in triplicate; the average relative viability of treated to untreated cells is shown here. Error bars represent one standard deviation. (A) Cells exhibit age-dependent resistance to hydrogen peroxide. (B) Aging cells may become more resistant to diamide. (C) Cells acquired resistance to menadione sodium bisulfite as a function of replicative age.

Chapter IX: Summary of findings and discussion for age-induced changes in DNA repair

The identification of DNA repair pathways that become dysfunctional with replicative age will provide insight into the mechanisms that underlie age-associated genome instability, such as that seen in cancer. To this end, I attempted two screens to identify pathways or processes that are changing as a function of replicative age. The first relies on conditional repression of important DNA repair genes and detection of age-dependent synthetic-lethal phenotypes. The second is based on finding age-dependent sensitivities to DNA-damaging agents that would indicate defects in certain DNA repair pathways.

Age-dependent synthetic-lethal interactions

Adequate doxycycline-induced repression was only achieved for *RAD52*. Interestingly, the conditional absence of Rad52 did result in a modest loss of population viability in replicatively aged cells.

Age-dependent changes in cell response to DNA-damaging agents

The tolerance of cells to several DNA-damaging agents, such as MMS and cisplatin were unchanged with age. Intriguingly, aging cells exhibited a biphasic response to oxidizing agents, that were later revealed to be a combination of lingering effects from being in saturation and actual age-dependent resistance to the chemical insult.

Complications facing a screen for age-dependent synthetic-lethal interactions

Adequate repression of any other DNA repair gene aside from *RAD52* was not achieved. There are two major factors that may have contributed to repression failure. First, in order for gene expression to occur in the absence of doxycycline, an activator recognizing the *tetO* promoter must be present. In this case, the activator was a fusion protein of a *tetO* recognition domain to the robust herpes simplex virus transcriptional activator, VP16. The strength of VP16 often results in unintentional overexpression of the genes under the *tetO* promoter under non-repressing conditions (Bellí et al., 1998). This increase in expression and concomitant increase in protein levels impede subsequent attempts at repression. Second, the stability of the gene product must be considered. According to a large-scale study of protein turnover, the half-life of Rad52 is 27 minutes, whereas other DNA-repair proteins, such as Rad27 and Rad9 are so stable, their half-lives were not measurable (Belle et al., 2006). Repression of genes that

encode extremely stable proteins will not likely be accomplished by transcriptional repression alone.

The success of a screen for age-dependent synthetic-lethal interactions requires that pathways affected by age are completely defective. While this may occur during the terminal divisions of the cell, it is more likely that age-affected pathways deteriorate with age and exhibit partial loss of function phenotypes. It is this concept that prompted me to include the Rad52 repression results in this work. That repression of such an important double-strand break repair protein causes an age-dependent loss of viability suggests that a significant subset of old cells are acquiring DNA-double strand breaks that are not or cannot be repaired by non-homologous end joining.

Obstacles for a chemical screen to identify defective pathways

The use of drug treatments to identify pathways that are altered due to replicative age did provide important information about the cellular processes that are affected by aging, albeit in an unexpected way. There were several obstacles that were encountered that hampered the identification of DNA repair pathways that become defective with age. First, the assay for viability following drug challenge was inherently tedious and noisy. Although centrifugation steps were eliminated by the filtration and wash process, only a limited number of cells could be placed on each filter to improve the accuracy of counting colony-forming units. This contributed to the experimental variability due to small volume transfers and low numbers per plate. Second, the effect of many classes of drugs on aging cells could not be tested due to the transient nature of drug treatments. Many drugs, such as the ribonucleotide reductase inhibitor hydroxyurea, only induced cell-cycle arrest such that normal growth resumed once cells were filtered out of the drug and plated. Concentrations of hydroxyurea that resulted in toxicity of a subpopulation of cells were not soluble.

The technology available in the laboratory to simultaneously detect mother cells and assess their viability has greatly improved since this drug screen was performed. Currently, we have methods that would allow aging, identification of mother cell populations, chemical treatment, and viability assessment all in bulk culture. Using such an approach would greatly diminish the noise that was inherent to the previous drug screen, and be high-throughput enough to permit a more comprehensive drug screen beyond DNA-damaging agents.

Why do cells become resistant to oxidizing agents with age?

Hydrogen peroxide was an obvious candidate to test because of its role in inducing oxidative damage to both DNA and the rest of the cell. Based on the reactive oxygen species theory of aging, cellular deterioration occurs due to the accumulation of oxidative damage to important macromolecules (Harman, 1956). This is supported by the age-associated increase in oxidatively damaged proteins and by the fact that altering neutralizing pathways affects lifespan. Therefore, I hypothesized that insult with an oxidizing agent would be more detrimental to older cells that already have a higher baseline of oxidative damage. Old cells, however, are more resistant to hydrogen peroxide insult than young cells.

One possibility is that, because old cells have already experienced oxidative damage, they have upregulated protective response pathways that confer resistance to further oxidative insult. Transcriptional analyses comparing old and young cells have revealed that many general and specific stress response genes are upregulated in old cells (Henderson and Gottschling, unpublished data). Furthermore, it has been shown in other organisms and with many different types of stress that an initial low-grade insult is protective against future insults (Mattson, 2008). Another possibility is that the resistance is byproduct of another age-associated change in the cell, such as the increased thickness of the cell wall in old cells. Hydrogen peroxide is a very small molecule, but it is possible that increased cell wall thickness is reducing the effective dosage of hydrogen peroxide to the cell, either as a mechanical or chemical barrier. The latter explanation is less attractive because a thicker cell wall would likely reduce the effective concentration of most drugs, but resistance was not generally observed.

What are the implications of the log-phase result?

Time in exponential growth or time since saturation dramatically affected the response of cells to hydrogen peroxide, and suggested that there are growth-related factors that may affect age-associated phenotypes that persist for over 24 hours. This result clearly delineated the effects of time compared to age as each exerted their influence on the hydrogen peroxide tolerance in opposite directions. However, this result also suggests that growth conditions experienced prior to aging analysis is confounding, and can mask true age-associated phenotypes.

In addition, time in log-phase growth also has detrimental effects on lifespan (Appendix E). This was later confirmed by micromanipulation, and found to accelerate vacuolar and mitochondrial dysfunction (Hughes & Gottschling, 2012). Together, these findings suggest that age-associated phenotypes and aging studies should be evaluated in the context of the growth history in addition to replicative age.

Alternative approaches may still be useful in discovering age-dependent changes in DNA repair

While the approaches I took to identify compromised pathways in DNA repair were not wholly successful, many lessons were learned that would be important considerations for future endeavors of this nature. Several alternative approaches will be useful in determining whether DNA repair pathways are altered in replicatively aged cells.

The first approach addresses the unsuccessful attempts to transcriptionally repress highly stable DNA repair genes. It is unlikely that conditional transcriptional repression of genes that encode stable proteins will be effective in rapidly depriving the cell of those proteins. However, if gene repression is combined with a post translational method for destabilizing proteins, such as the addition of degron sequences, it should be possible to eliminate proteins of interest from the cell (Banaszynski et al., 2006; Haruki et al., 2008). Additionally, the use of ligand-dependent protein sequestration techniques, such as the anchor-away technique may be useful in removing proteins from cellular compartments where they function.

A second approach is to determine the mutation frequency and rate and characterize the mutation spectrum of cells at various replicative ages. This method would take advantage of our laboratory's ability to obtain highly pure populations of mother cells in combination with new deep sequencing technology. An increase in mutation rate with replicative age would suggest that the number of mutations acquired is not solely due to steady accumulation over time, but that some DNA metabolism pathway is altered. Characterization of how the mutation spectrum changes from young to old cells will provide insight into DNA repair pathways that have become affected due to age.

Finally, an overexpression screen for genes that extend lifespan will also identify pathways that have become defective with age. Such a screen will not only shed light on the most crucial DNA repair pathways for healthy aging, but also identify other cellular pathways that important in the aging process.

Chapter X: Experimental Procedures

Experimental Procedures for Chapters II, III, IV, and V

Strains and plasmids

All yeast strains and plasmids used are listed in Appendix G, which is arranged by chapter. Unless otherwise indicated, strains are derivatives of the *Saccharomyces cerevisiae* S288c BY strains (Mortimer and Johnston, 1986; Brachmann et al., 1998).

Creating MEP strains with fluorescently-tagged marker proteins

Fluorescently tagged marker strains were created using one of four different methods. The method used to create each strain is indicated in Appendix G:

1) Introduction by mating: A number of GFP-tagged strains were obtained by mating the desired GFP-tagged haploid from the GFP library (mat a) with UCC8774 (mat α MEP haploid), selecting for diploids, inducing sporulation and selecting for haploids that contain both all MEP components and the GFP-tagged gene of interest by random spore analysis (Huh et al., 2003a; Lindstrom and Gottschling, 2009a). Strains created using this method contain the selectable marker *HIS3MX6* (Wach et al., 1997).

2) Introduction by transformation: Other marker proteins were C-terminally fused with fluorescent proteins GFP or mCherry using one-step PCR-mediated gene modification and standard transformation techniques (Gietz and Woods, 2002). The plasmid template and primers used to generate these strains are listed in Appendix G with the corresponding strain. Strains created using this method contain the selectable marker *KANMX* (Goldstein and McCusker, 1999).

3) Introduction using the Chromosome I integration vector: Fluorescently-tagged constructs obtained from other sources were introduced into MEP strains by first cloning into an integration vector, pAG306-Gal-ccdB ChrI, which allows for simple insertion into a gene poor region of chromosome I following digestion with *NotI*. Briefly, pAG306-Gal-ccdB ChrI was generated by ligation of a *SmaI*-digested fusion

PCR product that contained two ~500 base pair regions of chromosome I flanking a *NotI* site into Addgene plasmid 14139 pAG306-Gal-ccdB digested with *BsaI*. The primers used to generate the chromosome I integration site are listed in Appendix G. Fluorescently tagged genes were isolated from their original vectors and ligated into pAG306-Gal-ccdB ChrI to replace the *Gal* promoter and ccdB gene prior to *NotI* digestion and chromosome I integration. A more detailed description of how the Chromosome I integration vector was generated is found in Appendix C.

4) N-terminal GFP fusion: N-terminal tagging of genes with GFP was accomplished using two rounds of PCR followed by transformation and selection on 5-FOA for the loss of the selectable marker *URA3*. Briefly, two amplicons are produced during the first round of PCR: one containing homology to the region immediately upstream of the gene of interest, GFP, and the 5' ~2/3 of the *URA3* gene, and the second containing the 3' ~2/3 of *URA3*, GFP, and homology to the gene of interest beginning immediately after the start codon. The second amplification requires fusion PCR across the two amplicons generating a product containing the *URA3* selectable marker flanked by GFP, flanked by regions of homology to the N-terminus of the gene of interest. This product is then integrated using standard transformation techniques. Once stably integrated, loss of *URA3* by homologous recombination is selected for by plating onto 5-FOA containing media. The final result is a single copy of GFP fused to the N-terminus of the gene of interest. Plasmids and primers used to generate N-terminal GFP fusions are listed in Appendix G.

Gene deletion mutants

Gene deletions were introduced into strains containing either one or two fluorescently-tagged marker proteins using one-step PCR-mediated gene replacement and standard transformation techniques (Rothstein, 1991). The plasmid templates and primers used to generate these strains are listed in Appendix G.

Empty vector and GPD-VMA1 overexpression strains

Strains expressing empty vector or *VMA1* from a high expression *GPD* promoter were created using chromosome I integration vectors pAG306-GPD-empty ChrI and pAG306-GFP-*VMA1* ChrI, respectively. Briefly, the chromosome I *NotI* construct described above was ligated to *AatII*-digested pAG306-GPD-ccdB (Addgene plasmid 14140), which contains the high

expression *GPD* promoter, to create pAG306-GPD-ccdB ChrI. pAG306-GPD-empty ChrI was created by digestion with *HindIII* and *SpeI* followed by blunt religation after filling in overhangs with T4 DNA polymerase (New England Biolabs). pAG306-GPD-*VMA1* was created by insertion of *VMA1* from donor Gateway plasmids pDONR221-*VMA1* (HP ID ScCD00023712) using LR clonase according to manufacturer's instructions (Invitrogen). Diploid strains used in this study are hemizygous for the empty vector and *VMA1* overexpression alleles.

Growth media and conditions

Unless otherwise indicated, cells were grown in rich yeast media, YEPD (1% yeast extract, 2% peptone, 2% glucose) at 30°C. Prior to aging, cells were grown to saturation overnight (O/N) and a small number of these cells were subsequently cultured exponentially for 15+ hours to a maximum density of $6x10^6$ cells/mL. Cells cultured under caloric restriction were grown in YEPD containing only 0.5% glucose.

Live purifications were performed using either yeast complete medium (YC) lacking biotin (Sunrise Science Products) or biotin-depleted YEPD (YEPD-biotin). To make YEPD-biotin, avidin-agarose from egg white in glycerol suspension (Sigma) was gently washed once and resuspended to its original volume with phosphate buffered saline (pH7.4) (1XPBS). Avidin-agarose suspension was added to YEP at 10% v/v and incubated overnight at 4°C with constant gentle mixing. Avidin-agarose was removed from YEP by two iterations of low-speed centrifugation followed by carefully recovering the YEP. Glucose was then added to a final concentration of 2%, and the resulting media filter sterilized prior to use.

For live and high-resolution microscopy, cells were resuspended in YC media and mounted onto 2% agarose pads containing YC media. Cells were maintained at 30°C with a temperature-controlled incubation box surrounding the entire microscope stage.

Labeling mother cells with biotin, rhodamine, and Dylight 350

For imaging, $2.5x10^7$ cells if labeling with biotin or rhodamine, or $1.25x10^7$ cells if labeling with Dylight 350, grown as described above, were washed twice with 1XPBS and resuspended in 1XPBS containing 3 mg/mL EZ-Link Sulfo-NHS-LC-Biotin (Thermo Fisher Scientific Inc.), 0.0225 mg/mL NHS-Rhodamine (Thermo Fisher Scientific Inc.), or 0.52 mg/mL Dylight 350 NHS Ester (Thermo Fisher Scientific Inc.) at a cell density of $5x10^7$ cells/mL for biotin and rhodamine and $1x10^8$ cells/mL for Dylight 350. Cells were labeled at room temperature (RT) for 30 minutes with continuous gentle mixing and washed three times with 1XPBS and resuspended in YEPD at a final cell density of $2.5x10^6$ cells/mL.

For Western blots, $1x10^8$ cells were labeled with biotin as described above, except at $1x10^8$ cells/mL in 1XPBS.

Culturing MEP cells

Following labeling with biotin, rhodamine, or Dylight 350, cells were recovered in YEPD at 30°C for 2 hours with a starting cell density of $2.5x10^6$ cells/mL. These cells were used to inoculate aging cultures at a density of $2x10^4$ labeled cells/mL in YEPD containing 1 μM β-estradiol (Sigma) and 1 μg/mL ampicillin (Sigma). Following induction of the MEP, cells were cultured on a shaker at 30°C until they reached the desired age. Cells were generally visualized at time 0 hours (median replicative age ~3 divisions), time 3 hours (age ~5 divisions), time 24 hours (age ~19 divisions), and time 48 hours (age ~27 divisions). Cells densities never exceeded $5x10^6$ cells/mL and aging media was exchanged every 24 hours to prevent nutrient depletion. At each timepoint ~$5x10^7$ total cells were harvested for purification and microscopy if labeled with biotin, or immediate microscopy if labeled with rhodamine or Dylight 350.

For Western blots, following recovery, $3x10^7$ biotinylated cells were inoculated at a cell density of $7.5x10^5$ cells/mL for time 3-hour cultures and $2x10^4$ cells/mL for time 24-hour cultures in YEPD containing 1 μM β-estradiol and 1 μg/mL ampicillin. Following MEP induction, cells were cultured on a shaker at 100 rpm at 30°C until they reached the desired age.

Purification of aged cells for imaging

For fixed-cell purifications, cells were first fixed in 4% paraformaldehyde (Electron Microscopy Sciences) in 1XPBS for 10 minutes at RT, and washed once with 1XPBS. Cells were then resuspended in 500 μL 1XPBS with 25 μL streptavidin-coated magnetic beads (MicroMACS, Miltenyi Biotec) and incubated at RT for 30 minutes with continuous gentle mixing. Following the bead reaction, cells were washed once with 1XPBS, resuspended in 8 mL 1XPBS, and loaded onto a LS MACS column (Miltenyi Biotec) pre-equilibrated with 5 mL 1XPBS. Labeled cells were allowed to bind the column by gravity flow. The column was then washed twice with 8 mL 1XPBS, removed from the magnet, and the original biotinylated mother cells were eluted by a combination of gravity flow and pressure with 8 mL 1XPBS. Purified aged cells were pelleted and resuspended in a small volume of 1X PBS for imaging.

For live-cell purifications, cells were purified as described above with the following modifications: 1) YEPD (2% glucose) without biotin was used in lieu of 1XPBS for the bead reaction and all subsequent steps; 2) Custom-ordered azide-free magnetic beads were used for

the bead reaction (MicroMACS, Miltenyi Biotec); 3) Purified cells were resuspended in YC or YEPD containing 2% glucose for microscopy.

Fluorescent staining

Calcofluor white (Fluorescent Brightener 28) (Sigma) was used to stain cells for bud scar visualization and quantitation to determine replicative age. 50 µL of a 1 mg/mL solution of calcofluor white in 1XPBS was added to the first column wash during purification.

Nile red (Sigma) was used to stain fixed cells to visualize lipid particles according to standard protocols. Briefly, paraformaldehyde-fixed cells were resuspended in 250 µL 0.4 µg/mL Nile red in 1XPBS (prepared from 1 mg/mL stock solution in DMSO), and incubated at RT for 10 minutes. Cells were washed once with 1XPBS and resuspended in a small volume of 1XPBS for imaging.

Alexafluor 488 phalloidin (Invitrogen) was used to stain cells to visualize actin substructures. Briefly, fixed and purified aged cells were permeabilized with 500 µL 0.2% Triton X-100 (Sigma) at RT for 15 minutes. Cells were washed twice with 1XPBS and stained with 50 µL Alexa Fluor 488 phalloidin solution in 1XPBS at RT in the dark for 1 hour. Cells were washed twice and resuspended in a small volume of 1XPBS for imaging.

Fluorescence microscopy

Unless otherwise indicated, cells were visualized by simple wide-field epifluorescence microscopy using a Nikon Eclipse E800 (Nikon 60X/1.40 oil Plan Apo objective) equipped with a CoolSNAP HQ^2 CCD camera (Photometrics). Images were processed using Metamorph version 7.1.1.0 imaging software.

For quantitation, cells were subjected to high-resolution three-dimensional deconvolution microscopy. Cells were imaged on an inverted Olympus IX71 microscope (Olympus 100X/1.40 Plan S Apo oil objective) equipped with a CoolSNAP HQ^2 (Photometrics). Cells were imaged on pads composed of 2% agarose dissolved in YC. Z-section images were captured at 0.25 µm intervals through the entire cell and using Deltavision SoftWorx software (Applied Precision Inc.) Following deconvolution of the image stacks, quantitative analysis was carried out using Volocity (Perkin Elmer), Softworx (Applied Precision Inc.), and/or ImageJ (Rasband, 2012).

For live, time-lapse microscopy, cells were subjected to high-resolution three-dimensional microscopy. Cells were imaged on an inverted Nikon microscope (Nikon 60X/1.40 Plan S Apo oil objective) equipped with a CoolSNAP HQ^2 (Photometrics). Cells were imaged on pads composed of 2% agarose dissolved in YC. For fluorescent images, Z-sections were

captured throughout the thickness of the entire cell. For brightfield images, a single image corresponding to the central z-stack was captured. Images were obtained every 10 minutes for several hours. Nikon Elements software was used for imaging and for initial processing of the image files (See Appendix F). Appendix F describes how the image files were processed to create .avi movies.

Purification of cells for biochemical analysis

For each timepoint, cells were counted, and all cells harvested by gentle centrifugation. Pellets were resuspended in RNAlater (Ambion) at a density of $6x10^8$ cells/mL and incubated for 30 minutes at room temperature. Following RNAlater treatment, cells, solution, and equipment must be kept on ice and/or at 4°C. Centrifugation must not exceed 660xg. Cells were collected by centrifugation, washed with 1XPBS containing 2mM EDTA, and resuspended in 1XPBS 2mM EDTA at $2x10^8$ cells/mL. Streptavidin-coated magnetic beads were added to cells at $1/20^{th}$ the total volume, and cells were incubated with gentle agitation for 30 minutes at 4°C. Percoll gradients were generated by mixing 8.9 mL Percoll Plus (GE Healthcare) with 1.1 mL 1.5 M NaCl, and subjecting to high-speed centrifugation in a fixed-angle rotor for 15 minutes at 19240xg. Use two Percoll gradients per strain per timepoint for time 24 and 48 hours. Cells were collected following the bead reaction, resuspended in either 1 mL (if time 3 hours or younger) or 4 mL (if time 24 hours or older), and gently layered onto the Percoll gradient. Gradients with cells were subjected to low-speed centrifugation in a swinging bucket rotor (2000 rpm for a Beckman GS-6R) for 20 minutes at 4°C. The very top brown layer contains cellular debris and was very carefully removed by aspiration. Cells were recollected by centrifugation and washed 2X with 1XPBS 2mM EDTA. Young cells (time 3 hours or younger) were resuspended in 10 mL 1XPBS 2mM EDTA and older cells (time 24 hours or older) were resuspended in 40 mL 1XPBS 2mM EDTA, and subjected to automated cell separation using an autoMACS Pro Separator (Miltenyi Biotec). Every sample is separated using the PosselD2 program followed by Qrinse. A small aliquot of purified sample is saved for determination of purity and median replicative age by calcofluor staining. The remaining cells, ideally $5x10^6$-$2x10^7$ cells, are collected by high-speed centrifugation, liquid removed, and the pellet flash frozen and stored at -80°C until used for protein extraction.

Western blot analysis

Whole-cell lysates for Western blot analysis were prepared from frozen cell pellets. Pellets were resuspended with 100 µL water. Cells were lysed by addition of 100 µL 0.2 M NaOH and

incubation for 5 minutes at room temperature. Protein extracts were collected by centrifugation at maximum speed for 10 minutes at 4°C, removal of supernatant, and resuspension with 100 µL SDS lysis buffer with 1X protease inhibitors (10 mM Tris HCl pH 6.8, 100 mM NaCl, 1% SDS, 1 mM EDTA, 1 mM EGTA, 25 ng/µL ALLN, 10 ng/µL leupeptin, 0.028 TIU/mL aprotinin, 5 ng/µL pepstatin A, 0.5 µM PMSF, 1 mM DTT). Aliquots of 4 µL were taken for each sample for quantitation, prior to addition of 25 µL loading dye (150 mM Tris HCl pH 6.8, 15% SDS, 25% glycerol, 0.02% bromophenol blue, and 12.5% β-mercaptoethanol).

Samples were quantitated for total protein using the BCA protein assay. Reserved 4 µL aliquots of each sample were boiled for 5 minutes, cooled, and 96 µL water was added. BSA standards were made to contain 0, 4, 8, 20, and 40 µg BSA and 4 µL of SDS lysis buffer with 1X protease inhibitors for a final volume of 100 µL. The BCA assay was carried out following manufacturers directions (Pierce).

Equal amounts of total protein were loaded and subjected to SDS-PAGE. Proteins were transferred onto a nitrocellulose membrane (Invitrogen) using a semi-dry transfer apparatus (Ellard Instrumentation). Equal loading and efficient transfer was confirmed by Ponceau S stain (0.2% Ponceau S (Sigma), 5% acetic acid). GFP and GFP-tagged proteins were detected using a 1:1000 dilution of mouse anti-GFP antibody (Roche) and a 1:4000 dilution of donkey anti-mouse horseradish peroxidase-conjugated antibody (Jackson ImmunoResearch). α-tubulin was detected using a 1:500 dilution of rat anti-α-tubulin antibody (Santa Cruz) and a 1:1000 dilution of donkey anti-rat horseradish peroxidase-conjugated antibody (Jackson ImmunoResearch). Proteins were detected using SuperSignal West Pico Chemiluminescent Substrate (Pierce) prior to exposure to film.

Experimental procedures for Chapter VIII

Strains and plasmids

All yeast strains, plasmids, and primers used are listed in Appendix G, which is arranged by chapter. Unless othe(Rasband, 2012)rwise indicated, strains are derivatives of the *Saccharomyces cerevisiae* S288c BY strains. Mother-enrichment program containing strains UCC5185 or its constituent haploids, UCC5179 and UCC5181, were used for most studies.

Strains for doxycycline-inducible gene repression

The tetracycline-inducible repression machinery consists for three parts: the tetracycline-responsive promoter (*tetO$_2$*), an activator (VP16-tetR), and a repressor (SSN6-tetR') (Bellí et al., 1998). The promoter is the bacterial Tn10 transposon-derived tetracycline-responsive *tetO* promoter. Here we use the *tetO$_2$* promoter, which contains two tandem copies of *tetO*. The activator is a fusion protein consisting of the *tetO* recognition domain of tetR fused to a strong transcriptional activator VP16. The repressor is comprised of the yeast transcriptional repressor SSN6 fused to a mutated version of tetR that is responsive to tetracycline (tetR'). A schematic of this system is shown and described in **Figure 8.2**.

To construct the strains containing both MEP and tetracycline-inducible repression machinery, each component of the tetracycline-inducible repression machinery was added piece-wise to MEP component containing haploids of both mating types, UCC5179 and UCC5181. Each component was contained on individual plasmids: pKAN-*tetO$_2$* (promoter), pUI-tTA-ADH1term (activator), and pLMI-tetR'S (repressor). The promoter and activator were integrated into the genome using one-step PCR-mediated gene modification and standard transformation techniques. The repressor was integrated following linearization with *PacI* and standard transformation techniques. The *tetO$_2$* promoter contains the selectable marker *KANMX*, and was introduced immediately upstream of *RAD52*. The activator contains the *URA3* selectable marker and was integrated into a gene-poor region of Chromosome I. The repressor contains the *LEU2* selectable marker and was integrated into the *met15Δ* designer deletion locus (Brachmann et al., 1998).

Gene deletion mutants were used to assess repression of the corresponding gene of interest. Gene deletions were introduced into strains using one-step PCR-mediated gene replacement and standard transformation techniques. The plasmid templates and primers used to generate these strains are listed in Appendix G.

Strains for drug treatment

The MEP diploid UCC5185 was used to determine the effects of DNA-damaging agents on aging cells.

Growth media and conditions and MEP induction

Unless otherwise indicated, cells were grown in rich yeast media, YEPD (1% yeast extract, 2% peptone, 2% glucose) at 30°C. Prior to aging, cells were grown to saturation overnight (O/N) and a small number of these cells were subsequently cultured exponentially for 3 hours. Cells

were then counted and inoculated at $1x10^3$ cells/mL in prewarmed YEPD and cultured at 30°C for 2 hours, prior to MEP induction. The MEP was induced with YEPD containing 1 μM β-estradiol (Sigma) and 1 μg/mL ampicillin (Sigma).

For the extended log-phase experiments, cells were grown to saturation overnight (O/N) and a small number of these cells were used to inoculate cultures at very low cell densities. These cultures were allowed to grow exponentially and continuously diluted to maintain low cell densities. Cells were removed at time 0, 6, 12, 18, 24, 48, and 72 hours, for MEP induction (described above) and treatment with hydrogen peroxide (described below).

Phenotypic confirmation of Rad52 repression

Adequate *RAD52* repression by doxycycline was phenotypically determined by direct comparison to *rad52Δ* cells. Rad52 is important for DNA-double strand break repair, and cells deficient in Rad52 are lethally sensitive to alkylating agents, such as MMS (Prakash and Prakash, 1977; Prakash et al., 1980). Cells expressing *RAD52* from the $tetO_2$ promoter, cells expressing *RAD52* from its endogenous promoter, and *rad52Δ* cells were spotted on YEPD media alone, YEPD containing 0.08% MMS, YEPD containing 20 μg/mL doxycycline, and YEPD containing both MMS and doxycycline. $tetO_2$*pr-RAD52* cells behaved similarly to *RAD52* cells on YEPD and on YEPD with MMS, and behaved similar to *rad52Δ* cells on YEPD with doxycycline and on YEPD with doxycycline and MMS. This indicates that *RAD52* is normally expressed under non-repressing conditions, and repressed to null-like levels under repressive conditions.

Western blot analysis to determine kinetics of Rad52 repression

Cells containing the tetracycline-inducible gene repression machinery (activator and repressor) with and without $tetO_2$*pr-RAD52* were cultured to saturation overnight, diluted, and grown exponentially for 5 hours to a density of ~$8x\ 10^6$ cells/mL. Doxycycline was added to both cultures at a final concentration of 20 μg/mL. Approximately $1x10^8$ cells were harvested at time 0, 1, 2, 3, and 6 hours, for Western blot analysis. Additionally, *rad52Δ* mutant cells were cultured and harvested for negative control purposes. Cells were pelleted and flash-frozen using liquid nitrogen. Cell pellets were stored at -80°C until whole-cell lysate preparation.

Whole-cell lysates for Western blot analysis were prepared from frozen cell pellets. Pellets were resuspended in 500μL ice-cold sample buffer (0.06 M Tris-HCl pH 6.8, 10% glycerol, 2% SDS, 0.0025% bromophenol blue) containing 5% β-mercaptoethanol (Sigma) and

1X protease inhibitor cocktail (Roche). Following addition of 500 μL glass beads, cells were vortexed 4X, alternating 45 seconds of vortexing with 30 seconds on ice. Tubes were microfuged for 5 minutes at maximum speed at 4°C, and the resulting supernatant transferred to a fresh microfuge tube. The supernatant was boiled for 5 minutes and placed on ice.

Equal volumes of all lysates were loaded and resolved by SDS-PAGE. Proteins were transferred onto a nitrocellulose membrane (Invitrogen) using a semi-dry transfer apparatus (Ellard Instrumentation). Rad52 protein was detected with a 1:500 dilution of Rad52 (y-300) rabbit polyclonal antibody (Santa Cruz) and 1:2000 anti-rabbit horseradish peroxidase-conjugated antibody (Amersham). Rad52 proteins were detected using SuperSignal West Pico Chemiluminescent Substrate (Pierce) prior to exposure to film.

Doxycycline-induced repression of gene expression

Doxycycline (Sigma), a stable analog of tetracycline, was used to repress transcription from the *tetO*$_2$ promoter at a final concentration of 20 μg/mL. For aging experiments, cells were grown and the MEP was induced as described above. For each timepoint, 5 mL aliquots of aging culture were removed for repression with doxycycline and for control. Repressed and unrepressed cells were cultured at 30°C for 6 hours. For each timepoint, approximately 200 viable cells were filtered and washed onto glass filters as described below. The filters were then placed onto solid YEPD plates containing 20 μg/mL doxycycline, cell side up, and counted for colony-forming units after growth at 30°C for several days.

Treatment of cells with DNA damaging agents

All chemical treatments, their manufacturers, and the final concentrations at which they were used can be found on **Table 8.1**. Treatment concentrations were determined by titrating dosage until cells exhibited compromised viability following a 6-hour transient exposure to the drug. Cells were grown and the MEP was induced as described above. Cultures were distributed into 5 mL aliquots for treated and untreated conditions, and for every timepoint. For each timepoint, cells were either treated with drug at the final concentrations noted on **Table 8.1** or mock-treated with 1X PBS for 6 hours. Following treatment, the equivalent amount of culture corresponding to approximately 200 viable untreated mother cells, was filtered and washed onto glass filters, and plated cell side up on solid YEPD media. Plates were assessed for colony forming units following several days incubation at 30°C.

For the extended log-phase experiment, cells were removed from exponentially growing cultures at times 0, 6, 12, 18, 24, 48, and 72 hours of log-phase growth at low cell densities.

The MEP was induced, and cells were either treated or mock-treated for 6 hours prior to filtration and plating, as described above.

Determination of viability by plating with glass filters

Approximately 200 viable original mother cells were collected on a filter for each plate. For a MEP culture started at $1x10^3$ cells/mL and allowed to recover for 2 hours prior to MEP induction, this corresponded to 100 µL for time 0, 250 µL for time 3, 350 µL for time 24, 500 µL for time 48, and 1500 for time 72 hours after MEP induction. Each aliquot of cells was added to 50 mL of 1X PBS. The all-glass filter holder with vacuum connection and 90 mm stainless steel screen (Millipore) was sterilized using a 70% ethanol rinse. An autoclave-sterilized 82 mm glass fiber filter with pore size of 1 micron (GE) is placed on the screen, and the cells and 1X PBS are vacuumed through the filter. The filter is washed with an additional 50 mL 1X PBS to remove any residual estradiol or drug treatment. The filter is then removed from the screen and placed on solid media plates containing the antibiotic doxycycline (Sigma) or hygromycin B (Roche), cell side up. An antibiotic is necessary to prevent growth of contaminating bacteria that remain on the glass filter despite autoclave sterilization. Because of the MEP, only viable mother cells are able to form colonies on the filter. Relative viability is compared between timepoints by counting colonies and adjusting for the volume of culture plated. Colonies were counted by hand or by using ImageJ (Rasband, 2012).

References

Aggarwal, M., and Brosh, R. M. (2009). WRN helicase defective in the premature aging disorder Werner syndrome genetically interacts with topoisomerase 3 and restores the top3 slow growth phenotype of sgs1 top3. Aging *1*, 219–233.

Aguilaniu, H., Gustafsson, L., Rigoulet, M., and Nyström, T. (2003). Asymmetric inheritance of oxidatively damaged proteins during cytokinesis. Science *299*, 1751–1753.

Aitchison, J. D., and Rout, M. P. (2012). The yeast nuclear pore complex and transport through it. Genetics *190*, 855–883.

Alberts, B., Johnson, A., and Lewis, J. (2002). Molecular Biology of the Cell 4th ed. (New York: Garland Science).

Altmann, K., and Westermann, B. (2005). Role of essential genes in mitochondrial morphogenesis in Saccharomyces cerevisiae. Molecular Biology of the Cell *16*, 5410–5417.

Amon, a (1996). Mother and daughter are doing fine: asymmetric cell division in yeast. Cell *84*, 651–654.

Anton, F., Dittmar, G., Langer, T., and Escobar-Henriques, M. (2013). Two deubiquitylases act on mitofusin and regulate mitochondrial fusion along independent pathways. Molecular Cell *49*, 487–498.

Aparicio, O. M., Billington, B. L., and Gottschling, D. E. (1991). Modifiers of position effect are shared between telomeric and silent mating-type loci in S. cerevisiae. Cell *66*, 1279–1287.

Armstrong, J. (2010). Yeast vacuoles: more than a model lysosome. Trends in Cell Biology *20*, 580–585.

Askwith, C., Eide, D., Van Ho, a, Bernard, P. S., Li, L., Davis-Kaplan, S., Sipe, D. M., and Kaplan, J. (1994). The FET3 gene of S. cerevisiae encodes a multicopper oxidase required for ferrous iron uptake. Cell *76*, 403–410.

Austad, S. N. (2004). Is aging programed? Aging Cell *3*, 249–251.

Azevedo, J. E., and Schliebs, W. (2006). Pex14p, more than just a docking protein. Biochimica et Biophysica Acta *1763*, 1574–1584.

Babour, A., Bicknell, A. a, Tourtellotte, J., and Niwa, M. (2010). A surveillance pathway monitors the fitness of the endoplasmic reticulum to control its inheritance. Cell *142*, 256–269.

Babst, M., Katzmann, D. J., Estepa-Sabal, E. J., Meerloo, T., and Emr, S. D. (2002). Escrt-III: an endosome-associated heterooligomeric protein complex required for mvb sorting. Developmental Cell *3*, 271–282.

Ball, D. a, Marchand, J., Poulet, M., Baumann, W. T., Chen, K. C., Tyson, J. J., and Peccoud, J. (2011). Oscillatory dynamics of cell cycle proteins in single yeast cells analyzed by imaging cytometry. PloS One *6*, e26272.

Ballou, C. (1982). Yeast cell wall and cell surface. In The Molecular Biology of the Yeast Saccharomyces (Cold Spring Harbor, NY: Cold Spring Harbor Laboratory Press), pp. 335–360.

Banaszynski, L. a, Chen, L.-C., Maynard-Smith, L. a, Ooi, a G. L., and Wandless, T. J. (2006). A rapid, reversible, and tunable method to regulate protein function in living cells using synthetic small molecules. Cell *126*, 995–1004.

Barton, A. (1950). Some aspects of cell division in Saccharomyces cerevisiae. Journal of General Microbiology *4*, 84–86.

Barzilai, N., Gabriely, I., Atzmon, G., Suh, Y., Rothenberg, D., and Bergman, A. (2010). Genetic studies reveal the role of the endocrine and metabolic systems in aging. The Journal of Clinical Endocrinology and Metabolism *95*, 4493–4500.

Barzilai, N., Guarente, L., Kirkwood, T. B. L., Partridge, L., Rando, T. a, and Slagboom, P. E. (2012). The place of genetics in ageing research. Nature Reviews. Genetics *13*, 589–594.

Beck, R., Rawet, M., Ravet, M., Wieland, F. T., and Cassel, D. (2009). The COPI system: molecular mechanisms and function. FEBS Letters *583*, 2701–2709.

Beckman, R., and Loeb, L. (2005). Genetic instability in cancer: theory and experiment. Seminars in Cancer Biology *15*, 423–435.

Belle, A., Tanay, A., Bitincka, L., Shamir, R., and O'Shea, E. K. (2006). Quantification of protein half-lives in the budding yeast proteome. Proceedings of the National Academy of Sciences *103*, 13004–13009.

Bellí, G., Garí, E., Piedrafita, L., Aldea, M., and Herrero, E. (1998). An activator/repressor dual system allows tight tetracycline-regulated gene expression in budding yeast. Nucleic Acids Research *26*, 942–947.

Bilinski, T., Zadrag-Tecza, R., and Bartosz, G. (2012). Hypertrophy hypothesis as an alternative explanation of the phenomenon of replicative aging of yeast. FEMS Yeast Research, 97–101.

Bilodeau, P. S., Urbanowski, J. L., Winistorfer, S. C., and Piper, R. C. (2002). The Vps27p Hse1p complex binds ubiquitin and mediates endosomal protein sorting. Nature Cell Biology *4*, 534–539.

Bishop, N. a, and Guarente, L. (2007). Genetic links between diet and lifespan: shared mechanisms from yeast to humans. Nature Reviews. Genetics *8*, 835–844.

Blander, G., and Guarente, L. (2004). The Sir2 family of protein deacetylases. Annual Review of Biochemistry *73*, 417–435.

Bokov, A., Chaudhuri, A., and Richardson, A. (2004). The role of oxidative damage and stress in aging. Mechanisms of Ageing and Development *125*, 811–826.

Botstein, D., and Fink, G. R. (2011). Yeast: an experimental organism for 21st Century biology. Genetics *189*, 695–704.

Brachmann, C. B., Davies, A., Cost, G. J., Caputo, E., Li, J., Hieter, P., and Boeke, J. D. (1998). Designer deletion strains derived from Saccharomyces cerevisiae S288C: a useful set of strains and plasmids for PCR-mediated gene disruption and other applications. Yeast *14*, 115–132.

Brett, C., and Tukaye, D. (2005). The yeast endosomal Na+ (K+)/ H+ exchanger Nhx1 regulates cellular pH to control vesicle trafficking. Molecular Biology of the Cell *16*, 1396–1405.

Cabib, E., Ulane, R., and Bowers, B. (1974). A molecular model for morphogenesis: the primary septum of yeast. Current Topics in Cellular Regulation *8*, 1–32.

Campbell, J., and Lorenz, A. (2006). Yeast nuclear envelope subdomains with distinct abilities to resist membrane expansion. Molecular Biology of the Cell *17*, 1768–1778.

Chan, L. Y., and Amon, A. (2010). Spindle position is coordinated with cell-cycle progression through establishment of mitotic exit-activating and -inhibitory zones. Molecular Cell *39*, 444–454.

Chan, Y.-H. M., and Marshall, W. F. (2010). Scaling properties of cell and organelle size. Organogenesis *6*, 88–96.

Cheeseman, I. M., and Desai, A. (2008). Molecular architecture of the kinetochore-microtubule interface. Nature Reviews Molecular Cell Biology *9*, 33–46.

Chondrogianni, N., Petropoulos, I., Franceschi, C., Friguet, B., and Gonos, E. S. (2000). Fibroblast cultures from healthy centenarians have an active proteasome. Experimental Gerontology *35*, 721–728.

Colman, R. J., Anderson, R. M., Johnson, S. C., Kastman, E. K., Kosmatka, K. J., Beasley, T. M., Allison, D. B., Cruzen, C., Simmons, H. a, Kemnitz, J. W., et al. (2009). Caloric restriction delays disease onset and mortality in rhesus monkeys. Science *325*, 201–204.

David, S. S., O'Shea, V. L., and Kundu, S. (2007). Base-excision repair of oxidative DNA damage. Nature *447*, 941–950.

Defossez, P. a, Prusty, R., Kaeberlein, M., Lin, S. J., Ferrigno, P., Silver, P. a, Keil, R. L., and Guarente, L. (1999). Elimination of replication block protein Fob1 extends the life span of yeast mother cells. Molecular Cell *3*, 447–455.

Delaney, J. R., Chou, A., Olsen, B., Carr, D., Murakami, C., Ahmed, U., Sim, S., An, E. H., Castanza, A. S., Fletcher, M., et al. (2013). End-of-life cell cycle arrest contributes to stochasticity of yeast replicative aging. FEMS Yeast Research.

Delaney, J. R., Murakami, C. J., Olsen, B., Kennedy, B. K., and Kaeberlein, M. (2011). Quantitative evidence for early life fitness defects from 32 longevity-associated alleles in yeast. Cell Cycle *10*, 156–165.

Dimmer, K., Fritz, S., Fuchs, F., Messerschmitt, M., Weinbach, N., Neupert, W., and Westermann, B. (2002). Genetic basis of mitochondrial function and morphology in Saccharomyces cerevisiae. Molecular Biology of the Cell *13*, 847–853.

Drose, S., KU, B., Bowman, E., Siebers, A., Zeeck, A., and Altendorf, K. (1993). Inhibitory effect of modified bafilomycins and concanamycins on P- and V-type adenosinetriphosphatases. Biochemistry *32*, 3902–3906.

Dumitrescu, T., and Saunders, W. (2002). The FEAR before MEN. Cell Cycle *1*, 304–307.

Easlon, E., Tsang, F., Dilova, I., Wang, C., Lu, S.-P., Skinner, C., and Lin, S.-J. (2007). The dihydrolipoamide acetyltransferase is a novel metabolic longevity factor and is required for calorie restriction-mediated life span extension. The Journal of Biological Chemistry *282*, 6161–6171.

Egilmez, N., and Jazwinski, S. (1989). Evidence for the involvement of a cytoplasmic factor in the aging of the yeast Saccharomyces cerevisiae. Journal of Bacteriology *171*.

Eglimez, N., Chen, J., and Jazwinski, S. (1990). Preparation and partial characterization of old yeast cells. Journal of Gerontology *45*, B9–17.

Elbaz, Y., and Schuldiner, M. (2011). Staying in touch: the molecular era of organelle contact sites. Trends in Biochemical Sciences *36*, 616–623.

Eldakak, A., Rancati, G., Rubinstein, B., Paul, P., Conaway, V., and Li, R. (2010). Asymmetrically inherited multidrug resistance transporters are recessive determinants in cellular replicative ageing. Nature Cell Biology *12*, 799–805.

Erdmann, R., and Blobel, G. (1995). Giant peroxisomes in oleic acid-induced Saccharomyces cerevisiae lacking the peroxisomal membrane protein Pmp27p. The Journal of Cell Biology *128*, 509–523.

Erjavec, N., Larsson, L., Grantham, J., and Nyström, T. (2007). Accelerated aging and failure to segregate damaged proteins in Sir2 mutants can be suppressed by overproducing the protein aggregation-remodeling factor Hsp104p. Genes & Development *21*, 2410–2421.

Esposito, M., Piatti, S., Hofmann, L., Frontali, L., Delahodde, A., and Rinaldi, T. (2011). Analysis of the rpn11-m1 proteasomal mutant reveals connection between cell cycle and mitochondrial biogenesis. FEMS Yeast Research *11*, 60–71.

Fagarasanu, A., Fagarasanu, M., and Rachubinski, R. a (2007). Maintaining peroxisome populations: a story of division and inheritance. Annual Review of Cell and Developmental Biology *23*, 321–344.

Falk, J. E., Chan, L. Y., and Amon, A. (2011). Lte1 promotes mitotic exit by controlling the localization of the spindle position checkpoint kinase Kin4. Proceedings of the National Academy of Sciences *108*, 12584–12590.

Fannjiang, Y., Cheng, W., and Lee, S. (2004). Mitochondrial fission proteins regulate programmed cell death in yeast. Genes & Development, 2785–2797.

Finley, D., Ulrich, H. D., Sommer, T., and Kaiser, P. (2012). The ubiquitin-proteasome system of Saccharomyces cerevisiae. Genetics *192*, 319–360.

Flury, I., Garza, R., Shearer, A., Rosen, J., Cronin, S., and Hampton, R. Y. (2005). INSIG: a broadly conserved transmembrane chaperone for sterol-sensing domain proteins. The EMBO Journal *24*, 3917–3926.

Fontana, L., Partridge, L., and Longo, V. D. (2010). Extending healthy life span--from yeast to humans. Science *328*, 321–326.

Fry, R. C., Begley, T. J., and Samson, L. D. (2005). Genome-wide responses to DNA-damaging agents. Annual Review of Microbiology *59*, 357–377.

Fuller, R. S., Brake, a J., and Thorner, J. (1989). Intracellular targeting and structural conservation of a prohormone-processing endoprotease. Science *246*, 482–486.

Ganley, A. R. D., Breitenbach, M., Kennedy, B. K., and Kobayashi, T. (2012). Yeast hypertrophy: cause or consequence of aging? Reply to Bilinski et al. FEMS Yeast Research *12*, 267–268.

Gasch, a P., Huang, M., Metzner, S., Botstein, D., Elledge, S. J., and Brown, P. O. (2001). Genomic expression responses to DNA-damaging agents and the regulatory role of the yeast ATR homolog Mec1p. Molecular Biology of the Cell *12*, 2987–3003.

Gasch, A. P., and Werner-Washburne, M. (2002). The genomics of yeast responses to environmental stress and starvation. Functional & Integrative Genomics *2*, 181–192.

Gautier, T., Bergès, T., Tollervey, D., and Hurt, E. (1997). Nucleolar KKE/D repeat proteins Nop56p and Nop58p interact with Nop1p and are required for ribosome biogenesis. Molecular and Cellular Biology *17*, 7088–7098.

Ghaemmaghami, S., Huh, W.-K., Bower, K., Howson, R. W., Belle, A., Dephoure, N., O'Shea, E. K., and Weissman, J. S. (2003). Global analysis of protein expression in yeast. Nature *425*, 737–741.

Gietz, R. D., and Woods, R. a (2002). Transformation of yeast by lithium acetate/single-stranded carrier DNA/polyethylene glycol method. Methods in Enzymology *350*, 87–96.

Glover, J. R., and Lindquist, S. (1998). Hsp104, Hsp70, and Hsp40: a novel chaperone system that rescues previously aggregated proteins. Cell *94*, 73–82.

Goldstein, a L., and McCusker, J. H. (1999). Three new dominant drug resistance cassettes for gene disruption in Saccharomyces cerevisiae. Yeast *15*, 1541–1553.

Goodman, J. M. (2009). Demonstrated and inferred metabolism associated with cytosolic lipid droplets. Journal of Lipid Research *50*, 2148–2156.

Gould, S. J., Keller, G. a, Hosken, N., Wilkinson, J., and Subramani, S. (1989). A conserved tripeptide sorts proteins to peroxisomes. The Journal of Cell Biology *108*, 1657–1664.

Grava, S., Schaerer, F., Faty, M., Philippsen, P., and Barral, Y. (2006). Asymmetric recruitment of dynein to spindle poles and microtubules promotes proper spindle orientation in yeast. Developmental Cell *10*, 425–439.

Greenspan, P., Mayer, E. P., and Fowler, S. D. (1985). Nile red: a selective fluorescent stain for intracellular lipid droplets. The Journal of Cell Biology *100*, 965–973.

Greer, E. L., and Brunet, A. (2009). Different dietary restriction regimens extend lifespan by both independent and overlapping genetic pathways in C. elegans. Aging Cell *8*, 113–127.

Guarente, L. (2005). Calorie restriction and SIR2 genes--towards a mechanism. Mechanisms of Ageing and Development *126*, 923–928.

Guarente, L. (2012). Sirtuins and calorie restriction. Nature Reviews Molecular Cell Biology *13*, 207.

Gurland, B. J., Page, W. F., and Plassman, B. L. (2004). A twin study of the genetic contribution to age-related functional impairment. The Journal of Gerentology: Medical Sciences *59*, 859–863.

Hampton, R. Y., and Rine, J. (1994). Regulated degradation of HMG-CoA reductase, an integral membrane protein of the endoplasmic reticulum, in yeast. The Journal of Cell Biology *125*, 299–312.

Hanahan, D., and Weinberg, R. (2000). The Hallmarks of cancer. Cell *100*, 57–70.

Hanson, P. I., Shim, S., and Merrill, S. a (2009). Cell biology of the ESCRT machinery. Current Opinion in Cell Biology *21*, 568–574.

Harman, D. (1956). Aging: a theory based on free radical and radiation chemistry. Journal of Gerontology *11*, 298–300.

Harris, N., Bachler, M., Costa, V., Mollapour, M., Moradas-ferreira, P., and Piper, P. W. (2005). Overexpressed Sod1p acts either to reduce or to increase the lifespans and stress resistance of yeast , depending on whether it is Cu 2+ -deficient or an active Cu , Zn-superoxide dismutase. Aging Cell *4*, 41–52.

Harris, N., Costa, V., MacLean, M., Mollapour, M., Moradas-Ferreira, P., and Piper, P. W. (2003). Mnsod overexpression extends the yeast chronological (G0) life span but acts

independently of Sir2p histone deacetylase to shorten the replicative life span of dividing cells. Free Radical Biology and Medicine *34*, 1599–1606.

Harris, S. L., and Waters, M. G. (1996). Localization of a yeast early Golgi mannosyltransferase, Och1p, involves retrograde transport. The Journal of Cell Biology *132*, 985–998.

Hartman, J., Garvik, B., and Hartwell, L. (2001). Principles for the buffering of genetic variation. Science *1001*.

Hartwell, L. H., Culotti, J., Pringle, J. R., and Reid, B. J. (1974). Genetic control of the cell division cycle in yeast. Science *183*, 46–51.

Hartwell, L., and Unger, M. (1977). Unequal division in Saccharomyces cerevisiae and its impliations for the control of cell division. The Journal of Cell Biology *75*, 422–435.

Haruki, H., Nishikawa, J., and Laemmli, U. K. (2008). The anchor-away technique: rapid, conditional establishment of yeast mutant phenotypes. Molecular Cell *31*, 925–932.

Hayflick, L. (1965). The limited in vitro lifetime of human diploid cell strains. Experimental Cell Research, 614–636.

Hellmuth, K., Lau, D. M., Bischoff, F. R., Künzler, M., Hurt, E., and Simos, G. (1998). Yeast Los1p has properties of an exportin-like nucleocytoplasmic transport factor for tRNA. Molecular and Cellular Biology *18*, 6374–6386.

Henderson, K. a, and Gottschling, D. E. (2008a). A mother's sacrifice: what is she keeping for herself? Current Opinion in Cell Biology *20*, 723–728.

Henderson, K. a, and Gottschling, D. E. (2008b). A mother's sacrifice: what is she keeping for herself? Current opinion in cell biology *20*, 723–728.

Herndon, L. a, Schmeissner, P. J., Dudaronek, J. M., Brown, P. a, Listner, K. M., Sakano, Y., Paupard, M. C., Hall, D. H., and Driscoll, M. (2002). Stochastic and genetic factors influence tissue-specific decline in ageing C. elegans. Nature *419*, 808–814.

Hickson, I. D. (2003). RecQ helicases: caretakers of the genome. Nature Reviews Cancer *3*, 169–178.

Hofmann, L., Saunier, R., Cossard, R., Esposito, M., Rinaldi, T., and Delahodde, A. (2009). A nonproteolytic proteasome activity controls organelle fission in yeast. Journal of Cell Science *122*, 3673–3683.

Hotz, M., Leisner, C., Chen, D., Manatschal, C., Wegleiter, T., Ouellet, J., Lindstrom, D., Gottschling, D. E., Vogel, J., and Barral, Y. (2012). Spindle pole bodies exploit the mitotic exit network in metaphase to drive their age-dependent segregation. Cell *148*, 958–972.

Huang, C., and Chang, A. (2011). PH-dependent cargo sorting from the Golgi. The Journal of Biological Chemistry *286*, 10058–10065.

Hughes, A. L., and Gottschling, D. E. (2012a). Age-induced decline in vacuolar acidity causes mitochondrial dysfunction and limits yeast lifespan. manuscript in preparation.

Hughes, A. L., and Gottschling, D. E. (2012b). An early age increase in vacuolar pH limits mitochondrial function and lifespan in yeast. Nature *492*, 261–265.

Huh, W.-K., Falvo, J. V, Gerke, L. C., Carroll, A. S., Howson, R. W., Weissman, J. S., and O'Shea, E. K. (2003a). Global analysis of protein localization in budding yeast. Nature *425*, 686–691.

Huh, W.-K., Falvo, J. V, Gerke, L. C., Carroll, A. S., Howson, R. W., Weissman, J. S., and O'Shea, E. K. (2003b). Global analysis of protein localization in budding yeast. Nature *425*, 686–691.

Hutchins, M. U., Veenhuis, M., and Klionsky, D. J. (1999). Peroxisome degradation in Saccharomyces cerevisiae is dependent on machinery of macroautophagy and the Cvt pathway. Journal of Cell Science *112 (Pt 2*, 4079–4087.

Ivy, J., Klar, A., and Hicks, J. (1986). Cloning and characterization of four SIR genes of Saccharomyces cerevisiae. Molecular and Cellular Biology *6*.

Jacquier, N., Choudhary, V., Mari, M., Toulmay, A., Reggiori, F., and Schneiter, R. (2011). Lipid droplets are functionally connected to the endoplasmic reticulum in Saccharomyces cerevisiae. Journal of Cell Science *124*, 2424–2437.

Jamieson, D. J. (1998). Oxidative stress responses of the yeast Saccharomyces cerevisiae. Yeast *14*, 1511–1527.

Jamieson, D. J. (1992). Saccharomyces cerevisiae has distinct adaptive responses to both hydrogen peroxide and menadione. Journal of Bacteriology *174*.

Jana, N. R. (2012). Protein homeostasis and aging: role of ubiquitin protein ligases. Neurochemistry International *60*, 443–447.

Jaspersen, S. L., and Winey, M. (2004). The budding yeast spindle pole body: structure, duplication, and function. Annual Review of Cell and Developmental Biology *20*, 1–28.

Jazwinski, S. (1998). Genetics of longevity. Experimental Gerontology *33*, 773–783.

Jazwinski, S. M. (2005). Yeast longevity and aging--the mitochondrial connection. Mechanisms of Ageing and Development *126*, 243–248.

Jorgensen, P., Edgington, N. P., Schneider, B. L., Rupes, I., Tyers, M., and Futcher, B. (2007). The size of the nucleus increases as yeast cells grow. Molecular Biology of the Cell *18*, 3523–3532.

Joshi, K. K., Chen, L., Torres, N., Tournier, V., and Madura, K. (2011). A proteasome assembly defect in rpn3 mutants is associated with Rpn11 instability and increased sensitivity to stress. Journal of Molecular Biology *410*, 383–399.

Kaeberlein, M. (2010). Lessons on longevity from budding yeast. Nature *464*, 513–519.

Kaeberlein, M., Kirkland, K. T., Fields, S., and Kennedy, B. K. (2004). Sir2-independent life span extension by calorie restriction in yeast. PLoS Biology *2*, E296.

Kaeberlein, M., McVey, M., and Guarente, L. (1999). The Sir2/3/4 complex and SIR2 alone promote longevity in Saccharomyces cerevisiae by two different mechanisms. Genes & Development, 2570–2580.

Kaeberlein, M., and Powers, R. W. (2007). Sir2 and calorie restriction in yeast: a skeptical perspective. Ageing Research Reviews *6*, 128–140.

Kaeberlein, M., Powers, R. W., Steffen, K. K., Westman, E. a, Hu, D., Dang, N., Kerr, E. O., Kirkland, K. T., Fields, S., and Kennedy, B. K. (2005). Regulation of yeast replicative life span by TOR and Sch9 in response to nutrients. Science *310*, 1193–1196.

Kallman, F. J., and Sander, G. (1947). Twin studies on aging and longevity. Journal of Heredity *39*, 349–357.

Kang, P., and Béven, L. (2010). The Rsr1/Bud1 GTPase interacts with itself and the Cdc42 GTPase during bud-site selection and polarity establishment in budding yeast. Molecular biology of the … *21*, 3007–3016.

Karotki, L., Huiskonen, J. T., Stefan, C. J., Ziółkowska, N. E., Roth, R., Surma, M. a, Krogan, N. J., Emr, S. D., Heuser, J., Grünewald, K., et al. (2011). Eisosome proteins assemble into a membrane scaffold. The Journal of Cell Biology *195*, 889–902.

Kennedy, B. K., Austriaco, N. R., and Guarente, L. (1994). Daughter cells of Saccharomyces cerevisiae from old mothers display a reduced life span. The Journal of Cell Biology *127*, 1985–1993.

Kennedy, B. K., Austriaco, N. R., Zhang, J., and Guarente, L. (1995). Mutation in the silencing gene SIR4 can delay aging in S. cerevisiae. Cell *80*, 485–496.

Kenyon, C. J. (2010). The genetics of ageing. Nature *464*, 504–512.

Kim, J., and Hirsch, J. P. (1998). A nucleolar protein that affects mating efficiency in Saccharomyces cerevisiae by altering the morphological response to pheromone. Genetics *149*, 795–805.

Kim, S. K. (2007). Common aging pathways in worms, flies, mice and humans. The Journal of Experimental Biology *210*, 1607–1612.

Kirkwood, T. B. L. (2008). A systematic look at an old problem. Nature *451*, 644–647.

Kirkwood, T. B. L. (2005). Understanding the odd science of aging. Cell *120*, 437–447.

Kirkwood, T. B. L., and Melov, S. (2011). On the programmed/non-programmed nature of ageing within the life history. Current Biology *21*, R701–7.

Kobayashi, T. (2011). How does genome instability affect lifespan?: roles of rDNA and telomeres. Genes to Cells *16*, 617–624.

Kolodner, R. D., Putnam, C. D., and Myung, K. (2002). Maintenance of genome stability in Saccharomyces cerevisiae. Science *297*, 552–557.

Kruckeberg, A., and Ye, L. (1999). Functional expression, quantification and cellular localization of the Hxt2 hexose transporter of Saccharomyces cerevisiae tagged with the green fluorescent protein. Biochemical Journal, 299–307.

Kruegel, U., Robison, B., Dange, T., Kahlert, G., Delaney, J. R., Kotireddy, S., Tsuchiya, M., Tsuchiyama, S., Murakami, C. J., Schleit, J., et al. (2011). Elevated proteasome capacity extends replicative lifespan in Saccharomyces cerevisiae. PLoS Genetics *7*, e1002253.

Kuravi, K., Nagotu, S., Krikken, A. M., Sjollema, K., Deckers, M., Erdmann, R., Veenhuis, M., and Van der Klei, I. J. (2006). Dynamin-related proteins Vps1p and Dnm1p control peroxisome abundance in Saccharomyces cerevisiae. Journal of Cell Science *119*, 3994–4001.

Lee, S. S., Avalos Vizcarra, I., Huberts, D. H. E. W., Lee, L. P., and Heinemann, M. (2012). Whole lifespan microscopic observation of budding yeast aging through a microfluidic dissection platform. Proceedings of the National Academy of Sciences *109*, 4916–4920.

Levy, D. L., and Heald, R. (2012). Mechanisms of intracellular scaling. Annual Review of Cell and Developmental Biology, 1–23.

Li, S. C., and Kane, P. M. (2009). The yeast lysosome-like vacuole: endpoint and crossroads. Biochimica et Biophysica Acta *1793*, 650–663.

Liakopoulos, D., Kusch, J., Grava, S., Vogel, J., and Barral, Y. (2003). Asymmetric loading of Kar9 onto spindle poles and microtubules ensures proper spindle alignment. Cell *112*, 561–574.

Lin, S.-J., Defossez, P.-A., and Guarente, L. (2000). Requirement of NAD and SIR2 for life-span extension by calorie restriction in Saccharomyces cerevisiae. Science *289*, 2126–2128.

Lindstrom, D. L., and Gottschling, D. E. (2009a). The mother enrichment program: a genetic system for facile replicative life span analysis in Saccharomyces cerevisiae. Genetics *183*, 413–22, 1SI–13SI.

Lindstrom, D. L., and Gottschling, D. E. (2009b). The mother enrichment program: a genetic system for facile replicative life span analysis in Saccharomyces cerevisiae. Genetics *183*, 413–22, 1SI–13SI.

Loeillet, S., Palancade, B., Cartron, M., Thierry, A., Richard, G.-F., Dujon, B., Doye, V., and Nicolas, A. (2005). Genetic network interactions among replication, repair and nuclear pore deficiencies in yeast. DNA repair *4*, 459–468.

Loewith, R., and Hall, M. N. (2011). Target of rapamycin (TOR) in nutrient signaling and growth control. Genetics *189*, 1177–1201.

Longo, V. D., and Kennedy, B. K. (2006). Sirtuins in aging and age-related disease. Cell *126*, 257–268.

Losev, E., Reinke, C. a, Jellen, J., Strongin, D. E., Bevis, B. J., and Glick, B. S. (2006). Golgi maturation visualized in living yeast. Nature *441*, 1002–1006.

Manjithaya, R., Nazarko, T. Y., Farré, J.-C., and Subramani, S. (2010). Molecular mechanism and physiological role of pexophagy. FEBS Letters *584*, 1367–1373.

Manolson, M. F., Proteau, D., and Jones, E. W. (1992). Evidence for a conserved 95-120 kDa subunit associated with and essential for activity of V-ATPases. The Journal of Experimental Biology *172*, 105–112.

Marshall, P. a, Krimkevich, Y. I., Lark, R. H., Dyer, J. M., Veenhuis, M., and Goodman, J. M. (1995). Pmp27 promotes peroxisomal proliferation. The Journal of Cell Biology *129*, 345–355.

Martin, G. M. (2011). The biology of aging: 1985-2010 and beyond. FASEB Journal *25*, 3756–3762.

Martinez, M., Roy, S., Archuletta, A., Wentzell, P., Anna-Arrioloa, S., Rodriguez, A., Aragon, A. D., Quinones, G., Allen, C., and Werner-Washburne, M. (2004). Genomic analysis of stationary-phase and exit in Saccharomyces cerevisiae: gene expression and identification of novel essential genes. Molecular Biology of the Cell *15*, 5295–5305.

Mattson, M. P. (2008). Hormesis defined. Ageing Research Reviews *7*, 1–7.

McDonald, R., and Ramsey, J. (2010). Honoring Clive McCay and 75 years of calorie restriction research. The Journal of Nutrition, 1205–1210.

McMurray, M. a, and Gottschling, D. E. (2003). An age-induced switch to a hyper-recombinational state. Science *301*, 1908–1911.

Merlini, L., and Piatti, S. (2011). The mother-bud neck as a signaling platform for the coordination between spindle position and cytokinesis in budding yeast. Biological Chemistry *392*, 805–812.

Moore, J. K., Stuchell-Brereton, M. D., and Cooper, J. a (2009). Function of dynein in budding yeast: mitotic spindle positioning in a polarized cell. Cell Motility and the Cytoskeleton *66*, 546–555.

Mortimer, R., and Johnston, J. (1959). Life span of individual yeast cells. Nature *183*, 1751–1752.

Mortimer, R. K., and Johnston, J. R. (1986). Genealogy of principal strains of the yeast genetic stock center. Genetics *113*, 35–43.

Moseley, J. B., and Goode, B. L. (2006). The yeast actin cytoskeleton: from cellular function to biochemical mechanism. Microbiology and molecular biology reviews *70*, 605–645.

Motley, A. M., Ward, G. P., and Hettema, E. H. (2008). Dnm1p-dependent peroxisome fission requires Caf4p, Mdv1p and Fis1p. Journal of Cell Science *121*, 1633–1640.

Murabito, J. M., Yuan, R., and Lunetta, K. L. (2012). The search for longevity and healthy aging genes: insights from epidemiological studies and samples of long-lived individuals. The Journal of Gerontology: Medical Sciences *67*, 470–479.

Niedenthal, R., Riles, L., Johnston, M., and Hegemann, J. (1996). Green fluorescent protein as marker for gene expression and subcellular localization in budding yeast. Yeast *12*, 773–786.

Nyström, T. (2005). Role of oxidative carbonylation in protein quality control and senescence. The EMBO Journal *24*, 1311–1317.

Oh, Y., and Bi, E. (2011). Septin structure and function in yeast and beyond. Trends in Cell Biology *21*, 141–148.

Olivera-Couto, A., and Aguilar, P. S. (2012). Eisosomes and plasma membrane organization. Molecular Genetics and Genomics *287*, 607–620.

Osborne, A. R., Rapoport, T. a, and Van den Berg, B. (2005). Protein translocation by the Sec61/SecY channel. Annual Review of Cell and Developmental Biology *21*, 529–550.

Ozcan, S., and Johnston, M. (1995). Three different regulatory mechanisms enable yeast hexose transporter (HXT) genes to be induced by different levels of glucose. Molecular and Cellular Biology *15*, 1564–1572.

Pan, X., Ye, P., Yuan, D. S., Wang, X., Bader, J. S., and Boeke, J. D. (2006). A DNA integrity network in the yeast Saccharomyces cerevisiae. Cell *124*, 1069–1081.

Park, P., McVey, M., and Guarente, L. (2002). Separation of mother and daughter cells. Methods in Enzymology *351*, 468–477.

Pearson, C. G., and Bloom, K. (2004). Dynamic microtubules lead the way for spindle positioning. Nature Reviews Molecular Cell Biology *5*, 481–492.

Pereira, G., and Yamashita, Y. M. (2011). Fly meets yeast: checking the correct orientation of cell division. Trends in Cell Biology *21*, 526–533.

Peters, C., Baars, T. L., Bühler, S., and Mayer, A. (2004). Mutual control of membrane fission and fusion proteins. Cell *119*, 667–678.

Piper, M. D. W., and Partridge, L. (2007). Dietary restriction in Drosophila: delayed aging or experimental artefact? PLoS Genetics *3*, e57.

Piper, M. D. W., Partridge, L., Raubenheimer, D., and Simpson, S. J. (2011). Dietary restriction and aging: a unifying perspective. Cell Metabolism *14*, 154–160.

Prakash, L., and Prakash, S. (1977). Isolation and characterization of MMS-sensitive mutants of Saccharomyces cerevisiae. Genetics, 33–55.

Prakash, S., Prakash, L., Burke, W., and Montelone, B. (1980). Effects of the RAD52 gene on recombination in saccharomyces cerevisiae. Genetics, 31–50.

Preston, C. R., Flores, C., and Engels, W. R. (2006). Age-dependent usage of double-strand-break repair pathways. Current Biology *16*, 2009–2015.

Pu, J., Ha, C. W., Zhang, S., Jung, J. P., Huh, W.-K., and Liu, P. (2011). Interactomic study on interaction between lipid droplets and mitochondria. Protein & Cell *2*, 487–496.

Rando, O. J., and Winston, F. (2012). Chromatin and transcription in yeast. Genetics *190*, 351–387.

Rasband, W. (2012). ImageJ.

Reggiori, F., and Monastyrska, I. (2005). The actin cytoskeleton is required for selective types of autophagy, but not nonspecific autophagy, in the yeast Saccharomyces cerevisiae. Molecular Biology of the Cell *16*, 5843–5856.

Rinaldi, T., and Hofmann, L. (2008). Dissection of the carboxyl-terminal domain of the proteasomal subunit Rpn11 in maintenance of mitochondrial structure and function. Molecular Biology of the Cell *19*, 1022–1031.

Rinaldi, T., Ricci, C., Porro, D., Bolotin-Fukuhara, M., and Frontali, L. (1998). A mutation in a novel yeast proteasomal gene, RPN11/MPR1, produces a cell cycle arrest, overreplication of nuclear and mitochondrial DNA, and an altered mitochondrial morphology. Molecular Biology of the Cell *9*, 2917–2931.

Rine, J., and Herskowitz, I. (1987). Four genes responsible for a position effect on expression from HML and HMR in Saccharomyces cerevisiae. Genetics *22*, 9–22.

Rodriguez, K. a, Edrey, Y. H., Osmulski, P., Gaczynska, M., and Buffenstein, R. (2012). Altered composition of liver proteasome assemblies contributes to enhanced proteasome activity in the exceptionally long-lived naked mole-rat. PloS One *7*, e35890.

Ross, K. E., and Cohen-Fix, O. (2004). A role for the FEAR pathway in nuclear positioning during anaphase. Developmental Cell *6*, 729–735.

Rossanese, O. W., Reinke, C. a, Bevis, B. J., Hammond, a T., Sears, I. B., O'Connor, J., and Glick, B. S. (2001). A role for actin, Cdc1p, and Myo2p in the inheritance of late Golgi elements in Saccharomyces cerevisiae. The Journal of Cell Biology *153*, 47–62.

Rothlisberger, S., Jourdain, I., Johnson, C., Takegawa, K., and Hyames, J. (2009). The dynamin-related protein Vps1 regulates vacuole fission, fusion and tubulation in the fission yeast, Schizosaccharomyces pombe. Fungal Genetics and Biology *46*, 927–935.

Rothstein, R. (1991). Targeting, disruption, replacement, and allele rescue: integrative DNA transformation in yeast. Methods in Enzymology *194*, 281–301.

Rottensteiner, H., and Stein, K. (2003). Conserved function of Pex11p and the novel Pex25p and Pex27p in peroxisome biogenesis. Molecular Biology of the Cell *14*, 4316–4328.

Saeki, Y., and Tanaka, K. (2012). Assumbly and function of the proteasome. In Uniquitin Family Modifiers and the Proteasome: Reviews and Protocols, Methods in Molecular Biology, R. J. Dohmen and M. Scheffner, eds. (Totowa, NJ: Humana Press), pp. 315–336.

Sato, K., and Nakano, A. (2007). Mechanisms of COPII vesicle formation and protein sorting. FEBS Letters *581*, 2076–2082.

Saunders, W. S. (1999). Action at the ends of microtubules. Current Opinion in Cell Biology *11*, 129–133.

Scheckhuber, C. Q., Erjavec, N., Tinazli, A., Hamann, A., Nyström, T., and Osiewacz, H. D. (2007). Reducing mitochondrial fission results in increased life span and fitness of two fungal ageing models. Nature Cell Biology *9*, 99–105.

Sebastiani, P., Solovieff, N., Dewan, A. T., Walsh, K. M., Puca, A., Hartley, S. W., Melista, E., Andersen, S., Dworkis, D. a, Wilk, J. B., et al. (2012). Genetic signatures of exceptional longevity in humans. PloS One *7*, e29848.

Silva, D. De, and Askwith, C. (1995). The FET3 gene product required for high affinity iron transport in yeast is a cell surface ferroxidase. Journal of Biological Chemistry *270*, 1096–1101.

Sinclair, D. a (2005). Toward a unified theory of caloric restriction and longevity regulation. Mechanisms of Ageing and Development *126*, 987–1002.

Sinclair, D. a, and Guarente, L. (1997). Extrachromosomal rDNA circles--a cause of aging in yeast. Cell *91*, 1033–1042.

Sinclair, D., Mills, K., and Guarente, L. (1997). Accelerated aging and nucleolar fragmentation in yeast sgs1 mutants. Science *277*, 1313–1316.

Siniossoglou, S., Peak-Chew, S. Y., and Pelham, H. R. (2000). Ric1p and Rgp1p form a complex that catalyses nucleotide exchange on Ypt6p. The EMBO Journal *19*, 4885–4894.

Smeal, T., Claus, J., Kennedy, B., Cole, F., and Guarente, L. (1996). Loss of transcriptional silencing causes sterility in old mother cells of S. cerevisiae. Cell *84*, 633–642.

Smith, E. D., Tsuchiya, M., Fox, L. a, Dang, N., Hu, D., Kerr, E. O., Johnston, E. D., Tchao, B. N., Pak, D. N., Welton, K. L., et al. (2008). Quantitative evidence for conserved longevity pathways between divergent eukaryotic species. Genome Research *18*, 564–570.

Smith, J. J., Marelli, M., Christmas, R. H., Vizeacoumar, F. J., Dilworth, D. J., Ideker, T., Galitski, T., Dimitrov, K., Rachubinski, R. a, and Aitchison, J. D. (2002). Transcriptome profiling to identify genes involved in peroxisome assembly and function. The Journal of Cell Biology *158*, 259–271.

Steffen, K. K., MacKay, V. L., Kerr, E. O., Tsuchiya, M., Hu, D., Fox, L. a, Dang, N., Johnston, E. D., Oakes, J. a, Tchao, B. N., et al. (2008). Yeast life span extension by depletion of 60s ribosomal subunits is mediated by Gcn4. Cell *133*, 292–302.

Steinkraus, K. a, Kaeberlein, M., and Kennedy, B. K. (2008). Replicative aging in yeast: the means to the end. Annual Review of Cell and Developmental Biology *24*, 29–54.

Suda, Y., and Nakano, A. (2011). The yeast Golgi apparatus. Traffic, 505–510.

Taddei, A., Schober, H., and Gasser, S. M. (2010). The budding yeast nucleus. Cold Spring Harbor Perspectives in Biology *2*, a000612.

Takizawa, P. a. (2000). Plasma membrane compartmentalization in yeast by messenger RNA transport and a septin diffusion barrier. Science *290*, 341–344.

Tanaka, K., Kitamura, E., Kitamura, Y., and Tanaka, T. U. (2007). Molecular mechanisms of microtubule-dependent kinetochore transport toward spindle poles. The Journal of Cell Biology *178*, 269–281.

Tanaka, T. U. (2008). Bi-orienting chromosomes: acrobatics on the mitotic spindle. Chromosoma *117*, 521–533.

Teis, D., Saksena, S., and Emr, S. D. (2008). Ordered assembly of the ESCRT-III complex on endosomes is required to sequester cargo during MVB formation. Developmental Cell *15*, 578–589.

Tissenbaum, H. a (2012). Genetics, life span, health span, and the aging process in Caenorhabditis elegans. The Journal of Gerontology: Medical Sciences *67*, 503–510.

Tissenbaum, H. a, and Guarente, L. (2002). Model organisms as a guide to mammalian aging. Developmental Cell *2*, 9–19.

Tong, Z., Gao, X.-D., Howell, A. S., Bose, I., Lew, D. J., and Bi, E. (2007). Adjacent positioning of cellular structures enabled by a Cdc42 GTPase-activating protein-mediated zone of inhibition. The Journal of Cell Biology *179*, 1375–1384.

Torres-Rosell, J., and Machín, F. (2004). Nucleolar segregation lags behind the rest of the genome and requires Cdc14 activation by the FEAR network. Cell Cycle, 496–502.

Toulmay, A., and Prinz, W. a (2011). Lipid transfer and signaling at organelle contact sites: the tip of the iceberg. Current Opinion in Cell Biology *23*, 458–463.

Valerio-Santiago, M., and Monje-Casas, F. (2011). Tem1 localization to the spindle pole bodies is essential for mitotic exit and impairs spindle checkpoint function. The Journal of Cell Biology *192*, 599–614.

Vallen, E. a, Scherson, T. Y., Roberts, T., Van Zee, K., and Rose, M. D. (1992). Asymmetric mitotic segregation of the yeast spindle pole body. Cell *69*, 505–515.

Vanhooren, V., and Libert, C. (2013). The mouse as a model organism in aging research: usefulness, pitfalls and possibilities. Ageing Research Reviews *12*, 8–21.

Vembar, S. S., and Brodsky, J. L. (2008). One step at a time: endoplasmic reticulum-associated degradation. Nature Reviews Molecular Cell Biology *9*, 944–957.

Verma, L., Kane, M. F., Brassett, C., Schmeits, J., Evans, D. G., Kolodner, R. D., and Maher, E. R. (1999). Mononucleotide microsatellite instability and germline MSH6 mutation analysis in early onset colorectal cancer. Journal of Medical Genetics *36*, 678–682.

Versele, M., and Thorner, J. (2004). Septin collar formation in budding yeast requires GTP binding and direct phosphorylation by the PAK, Cla4. The Journal of Cell Biology *164*, 701–715.

Vijg, J., and Suh, Y. (2005). Genetics of longevity and aging. Annual Review of Medicine *56*, 193–212.

Vyjayanti, V. N., and Rao, K. S. (2006). DNA double strand break repair in brain: reduced NHEJ activity in aging rat neurons. Neuroscience Letters *393*, 18–22.

Wach, a, Brachat, A., Alberti-Segui, C., Rebischung, C., and Philippsen, P. (1997). Heterologous HIS3 marker and GFP reporter modules for PCR-targeting in Saccharomyces cerevisiae. Yeast *13*, 1065–1075.

Walsh, R., Kawasaki, G., and Fraenkel, D. (1983). Cloning of genes that complement yeast hexokinase and glucokinase mutants. Journal of Bacteriology.

Walther, T. C., and Farese, R. V (2009). The life of lipid droplets. Biochimica et Biophysica Acta *1791*, 459–466.

Westermann, B. (2010). Mitochondrial fusion and fission in cell life and death. Nature Reviews Molecular Cell Biology *11*, 872–884.

Witkin, K. L., Chong, Y., Shao, S., Webster, M. T., Lahiri, S., Walters, A. D., Lee, B., Koh, J. L. Y., Prinz, W. a, Andrews, B. J., et al. (2012). The budding yeast nuclear envelope adjacent to the nucleolus serves as a membrane sink during mitotic delay. Current Biology *22*, 1128–1133.

Wolinski, H., and Kohlwein, S. (2008). Microscopic analysis of lipid droplet metabolism and dynamics in yeast. Methods in Molecular Biology *457*, 151–163.

Wu, K., Dawe, J. H., and Aris, J. P. (2000). Expression and subcellular localization of a membrane protein related to Hsp30p in Saccharomyces cerevisiae. Biochimica et Biophysica Acta *1463*, 477–482.

Xie, Z., Zhang, Y., Zou, K., Brandman, O., Luo, C., Ouyang, Q., and Li, H. (2012). Molecular phenotyping of aging in single yeast cells using a novel microfluidic device. Aging Cell *11*, 599–606.

Yamagata, K., and Kato, J. (1998). Bloom's and Werner's syndrome genes suppress hyperrecombination in yeast sgs1 mutant : Implication for genomic instability in human diseases. Proceedings of the National Academy of Sciences *95*, 8733–8738.

Yang, J., Dungrawala, H., and Hua, H. (2011). Cell size and growth rate are major determinants of replicative lifespan. Cell Cycle *10*, 144–155.

Yun, C. W., Tamaki, H., Nakayama, R., Yamamoto, K., and Kumagai, H. (1998). Gpr1p, a putative G-protein coupled receptor, regulates glucose-dependent cellular cAMP level in yeast Saccharomyces cerevisiae. Biochemical and Biophysical Research Communications *252*, 29–33.

Zadrag-Tecza, R., Kwolek-Mirek, M., Bartosz, G., and Bilinski, T. (2009). Cell volume as a factor limiting the replicative lifespan of the yeast Saccharomyces cerevisiae. Biogerontology *10*, 481–488.

Van der Zand, A., Gent, J., Braakman, I., and Tabak, H. F. (2012). Biochemically distinct vesicles from the endoplasmic reticulum fuse to form peroxisomes. Cell *149*, 397–409.

Zhao, R., Davey, M., Hsu, Y.-C., Kaplanek, P., Tong, A., Parsons, A. B., Krogan, N., Cagney, G., Mai, D., Greenblatt, J., et al. (2005). Navigating the chaperone network: an integrative map of physical and genetic interactions mediated by the hsp90 chaperone. Cell *120*, 715–727.

Ziółkowska, N. E., Christiano, R., and Walther, T. C. (2012). Organized living: formation mechanisms and functions of plasma membrane domains in yeast. Trends in Cell Biology *22*, 151–158.

Van Zutphen, T., and Van der Klei, I. J. (2011). Quantitative analysis of organelle abundance, morphology and dynamics. Current Opinion in Biotechnology *22*, 127–132.

Zweytick, D., Hrastnik, C., Kohlwein, S. D., and Daum, G. (2000). Biochemical characterization and subcellular localization of the sterol C-24(28) reductase, erg4p, from the yeast saccharomyces cerevisiae. FEBS Letters *470*, 83–87.

Appendix A: Isolation of Living Replicatively Aged Cells in Media

Highly pure populations of replicatively aged mother cells are often required for assays used to identify cellular and molecular changes that occur with age. While low-resolution cell biological approaches tolerate the presence of "dumb-bells," the arrested daughter cells that accumulate secondary to the Mother Enrichment Program (MEP), most other assays require that the mother cells be further enriched by purification away from the arrested daughter cells. Western blot analysis, high-resolution microscopy, and any global gene or protein analyses are examples of assays that demand highly purified populations of replicatively aged mother cells. The Gottschling lab has developed a protocol to obtain large populations (on the order of 10^7 cells) of aged mother cells with no more than 10% contaminating arrested daughters (Lindstrom et al., 2011). This method, however, is only effective if the cells are fixed prior to purification.

For assays that require the isolation of living replicatively aged cells, cells should be maintained in growth media at all times, including during the purification process. This is critical, as time in 1X PBS can have extreme effects on many different cellular pathways, processes, and functions. Live-cell purifications have not been routinely performed using media due to the unexplained low recovery of original biotinylated mother cells following streptavidin bead attachment and magnetic separation. I hypothesized that the presence of biotin naturally occurring in both rich and yeast complete (YC) media might compete with the biotinylated cells for the streptavidin beads, resulting in the loss of biotinylated mother cells during magnetic separation.

To test this hypothesis, the recovery of aged mother cells carried out in 1XPBS, YC media (Difco, 2 ng/mL biotin), YC-biotin media (Sunrise Science, 0 ng/mL biotin), and YEPD (concentration of biotin unknown) were compared. Briefly, cells that had been grown exponentially overnight were biotinylated and aged in rich YEPD for 9 hours in the absence of MEP induction. Cells were counted and 7.5×10^8 cells (corresponds to 1.25×10^7 original biotinylated cells) were collected by centrifugation for each of the four purification conditions. Cells were washed twice with 1XPBS, YC, YC-biotin, and YEPD. All purification media contains 2% glucose. The streptavidin bead reaction and column purification were carried out as described in Chapter XI: Experimental Procedures in the appropriate media (1X PBS, YC, YC-biotin, and YEPD). The recovered cells were stained with calcofluor to determine replicative age. The percent of cells recovered compared to the original population of cells biotinylated and the percent of cells with >4 bud scars were determined for each purification media and

summarized in **Figure A.1**. The percent recovery of aged mother cells in YEPD is only 2%. In comparison, 74% of cells are recovered in 1XPBS, 102% in YC, and 104% in YC-biotin. Both purification media lacking biotin, 1XPBS and YC-biotin, resulted in 97% purity, whereas YC containing 2 ng/mL biotin yielded 70% purity, and YEPD, which likely contains >>2ng/mL biotin, resulted in a relatively impure population with only 33% aged cells. These results suggest that there is some component in YEPD that interferes with the purification of aged mother cells. Interestingly, recovery is greater in either YC-based media than in 1XPBS. The biotin content of the purification media also appears to have a detrimental effect on the purity of the cell population recovered.

In order to demonstrate that it was likely biotin in the YEPD that was interfering with purification and not any other difference between YEPD and YC media, known quantities of biotin were added to YC-biotin media containing 2% glucose. These media containing increasing concentrations of biotin were used to purify live aged mother cells. Results are shown in **Figure A.2** and suggest that increasing concentrations of biotin in the purification media decreases recovery and purity.

Ideally, live purifications of aged mother cells can be accomplished using YEPD to allow cells to remain alive and to keep their aging conditions constant. This is particularly important if looking at phenotypes that are easily altered by shifts in growth media, for example vacuole morphology and changes in metabolites. In order to perform aged-cell purifications in YEPD, the amount of biotin in YEPD must be determined and that biotin has to be depleted from the media. A vitamin H (biotin) ELISA kit (MDBioproducts) marketed to determine biotin levels in human serum, urine, and plasma was used to quantitate the biotin concentration in 1% yeast extract, 2% peptone, and in YEPD. As shown in **Figure A.3**, the source of the biotin in YEPD is solely from yeast extract, and the concentration of biotin in YEPD is approximately 50-75 ng/mL – over 25-fold higher than the biotin content of YC media. Avidin-conjugated agarose beads (Sigma) were used to bind the biotin in YEP, and then removed from the media by gentle centrifugation as described in Chapter XI: Experimental Methods. Depletion of 45 mL YEP required 500 µL avidin agarose beads for adequate biotin depletion and for significant improvement of aged mother cell purification efficacy and efficiency (**Figure A.4**).

As was described above, the purification protocol routinely used by the Gottschling lab can be modified to obtain pure populations of living replicatively aged mother cells for assays requiring

live cells. In general, the recovery of old mother cells using live purification is greater than that of fixed cells. This is likely due to the unintentional labeling of cellular debris with streptavidin magnetic beads, which then bind to the purification columns and interfere with aged mother cell purification. In situations where the nature of the assay does not tolerate contamination with arrested dumb-bells, as they are metabolically active and exhibit abnormal cellular behaviors, it is now possible to obtain pure populations of live old mother cells by serial purification in biotin-free or biotin-depleted media in the absence of MEP induction. The protocols for the depletion of biotin from YEP and for live purification in the absence of MEP induction are listed below.

Protocol for biotin depletion of YEP

1. Gently wash avidin-agarose from egg white in glycerol suspension (Sigma) with 1XPBS, and resuspend to its original volume with 1XPBS.
2. Treat YEP with 10% v/v avidin-agarose suspension and incubate overnight at 4°C with constant gentle mixing.
3. Remove avidin-agarose by two iterations of low-speed centrifugation followed by carefully recovering the YEP.
4. Add glucose to a final concentration of 2%.
5. Filter sterilize media.
6. Store in dark until ready to use.

Protocol for live cell purification without MEP induction

1. Cells are aged as desired; recommend continual exponential growth at low cell densities to ensure adequate nutrients in media at all times with serial purifications every 12 hours.
2. Count cells
3. Collect cells by centrifugation and wash 1X with 25 mL purification media (YC-biotin or YEPD-biotin).
4. Resuspend cells at $2x10^8$ cells/mL in purification media.
5. Add $1/20^{th}$ volume streptavidin beads.
6. Rock at room temperature for 30 minutes, venting often.
7. Collect cells by centrifugation and wash 1X with 25 mL purification media.
8. Separate biotinylated cells using LS magnetic columns (Miltenyi Biotec) with purification media to wet and wash the column. Load ~$1\text{-}2x10^7$ cells/column.
9. Elute cells off column with growth media.
10. Count cells. Recovery should be >75%.

References:

Lindstrom, D. L., Leverich, C. K., Henderson, K. a, and Gottschling, D. E. (2011). Replicative age induces mitotic recombination in the ribosomal RNA gene cluster of Saccharomyces cerevisiae. PLoS Genetics *7*, e1002015.

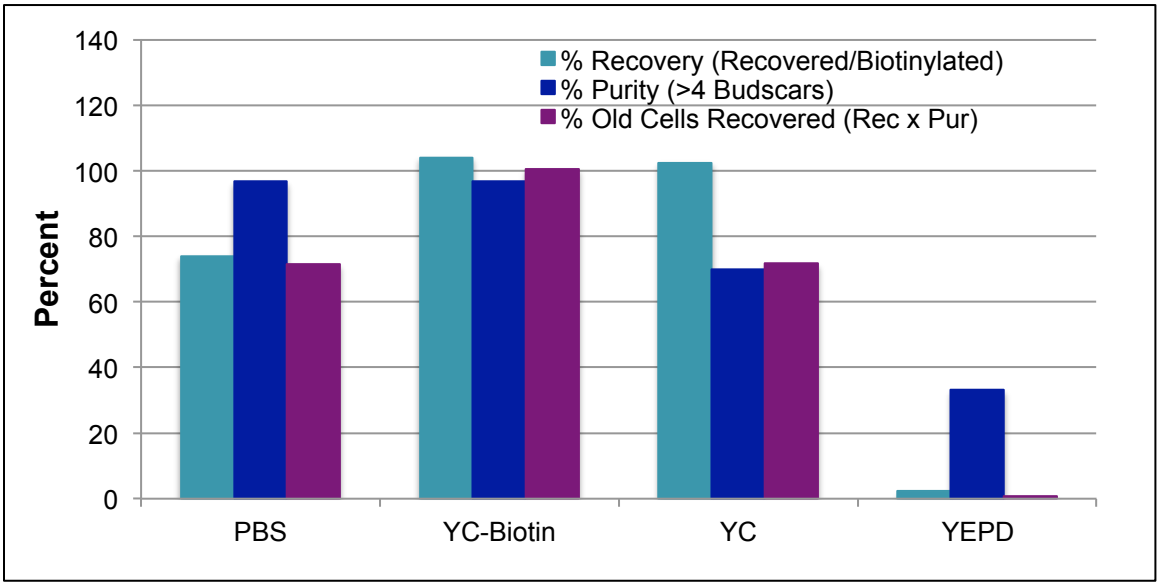

Figure A.1. The recovery of aged mother cells purified in YEPD is extremely low. Cells were grown in YEPD for 9 hours following biotinylation. $7.5x10^8$ cells, containing $1.25x10^7$ original biotinylated cells, were purified using 3.75 mL purification media and 187.5 µL streptavidin magnetic beads. Percent cells recovered, percent purity, and percent aged cells recovered were determined using 1X PBS, YC-biotin, YC, and YEPD as the purification media. Purification in YC-biotin yielded the best recovery of aged cells. Purification using YC, which contains 2 ng/mL biotin, resulted in a high recovery rate but of relatively low purity. Purification with 1X PBS resulted in loss of cells, however the population purified was uniformly aged. Finally, purification using YEPD resulted in a dismally low recovery of a mixed population of young and old cells.

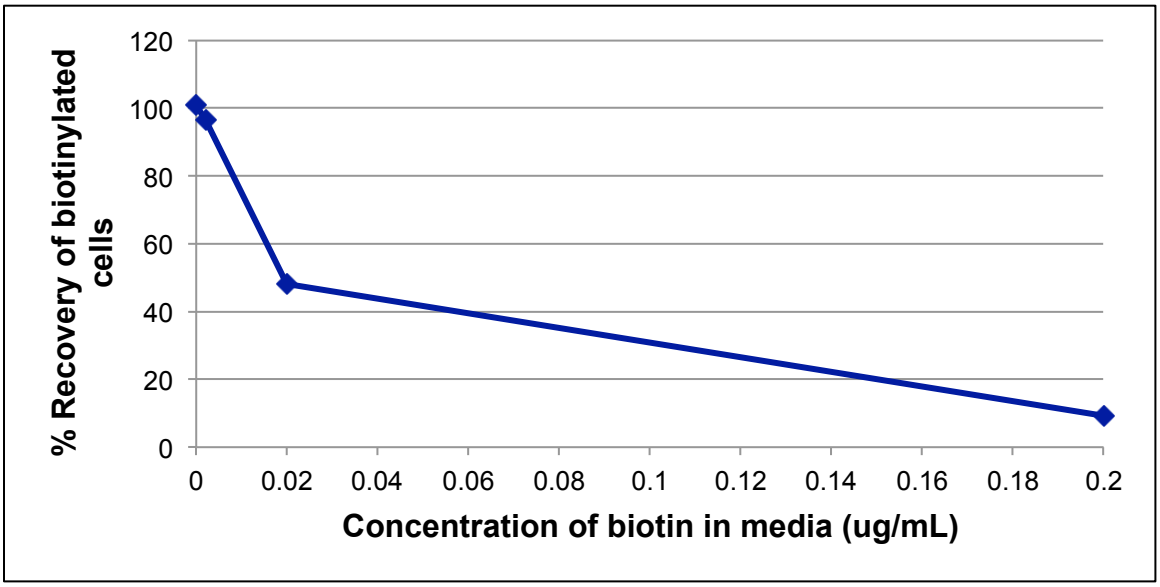

Figure A.2. Biotin in the purification media decreases the recovery of biotinylated cells in a dose-dependent manner. Cells were grown in YEPD for 9 hours following biotinylation. $7.5x10^8$ cells, containing $1.25x10^7$ original biotinylated cells, were purified using 3.75 mL purification media and 187.5 µL streptavidin magnetic beads. The percent of cells recovered was determined using YC-biotin supplemented with 0, 0.002, 0.02, and 0.2 µg/mL biotin as the purification media. Biotin decreased cell recovery in a dose-dependent manner with recovery ~100% in the absence of biotin, ~50% with media containing 0.02 µg/mL biotin, and ~10% when purification was carried out in media containing 0.2 µg/mL biotin.

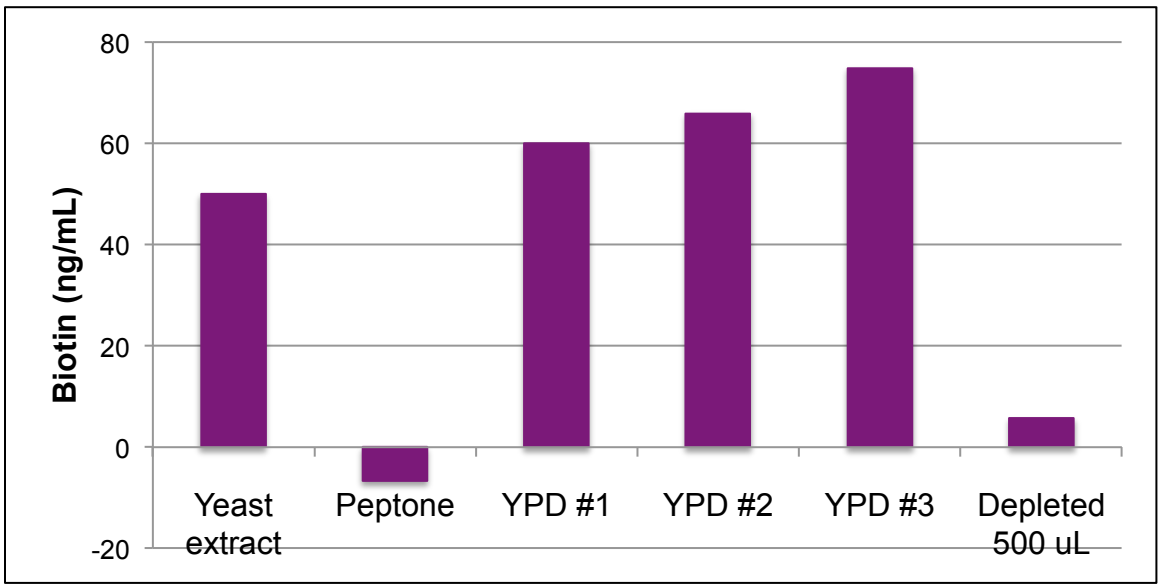

Figure A.3. The biotin in YEPD is primarily from yeast extract and can be depleted from media using avidin agarose beads. Commercially available vitamin H (biotin) ELISA kit from MDBioproducts was used to determine the biotin content of 1% yeast extract, 2% peptone, YEPD from 3 independent preparations, and in YEPD following biotin depletion with avidin agarose beads. YEPD contains 60-80 ng/mL biotin with some variability between preparations. The concentration of biotin in YEPD is dependent on the yeast extract as 2% peptone does not contain detectable quantities of biotin. 500 µL avidin agarose beads was sufficient to greatly reduce the amount of biotin in 45 mL YEP to 6 ng/mL, however did not completely extract all biotin.

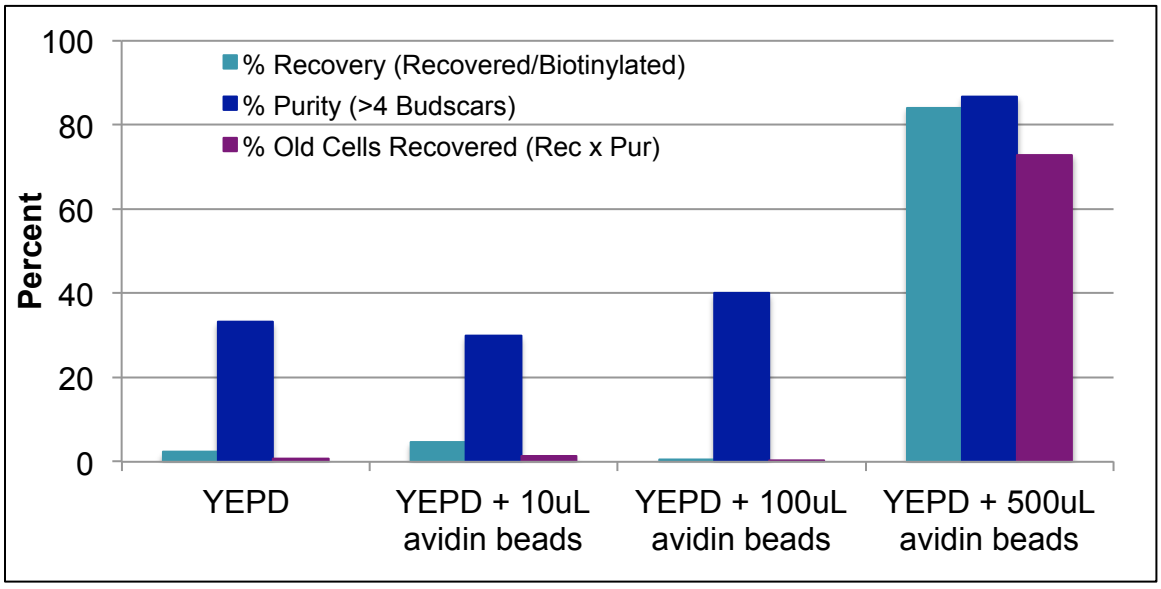

Figure A.4. Depletion of biotin in YEPD to 6 ng/mL is sufficient to allow for adequate recovery and purification of aged cells. Cells were grown in YEPD for 9 hours following biotinylation. $7.5x10^8$ cells, containing $1.25x10^7$ original biotinylated cells, were purified using 3.75 mL purification media and 187.5 µL streptavidin magnetic beads. Percent cells recovered, percent purity, and percent aged cells recovered were determined using YEPD and YEPD depleted with 10 µL, 100 µL, and 500 µL avidin agarose bead per 45 mL media as the purification media. Only depletion with 500 µL avidin agarose beads per 45 mL YEP sufficiently removed enough biotin to allow adequate recovery of biotinylated aged cells.

Appendix B: FM4-64 Internalization Kinetics in Aging Cells

Endocytosis is the process by which material from outside the cell and from the cell's surface is transported within the cell (Alberts et al., 2002). This occurs by invaginations of the plasma membrane that pinch off to form endocytic vesicles (endosomes) that mature and undergo sorting of their cargo (Weinberg and Drubin, 2012; Hanson et al., 2009). The cargo destined for degradation can be found in late endosomes that deliver their contents by fusion to the vacuole. One of the purposes of the endocytic process is to turn over plasma membrane proteins by removing them from the cell surface and transporting them to the vacuole for degradation. This process is heavily dependent on the cell's ability to differentially acidify each compartment within the endocytic pathway with the most acidic compartment being the vacuole and least acidic compartment being the early endosome (Mellman et al., 1986; Kane, 2006; Lafourcade et al., 2008).

Both plasma membrane protein turnover of specific transmembrane proteins and vacuolar acidification are altered in replicatively aged cells (Nelson & Gottschling, unpublished data; Hughes & Gottschling, 2012). It remains unclear at this time whether these two phenomena are causally related (Henderson, unpublished data). Based on these observations and the observation that GFP-tagged endosome markers suggested an increase in endosome number as a function of replicative age, it was reasonable to hypothesize that the endocytic process was also affected by replicative age.

One method for assaying for defects in the endocytic pathway is with the use of vital dye FM4-64 and fluorescence microscopy to visualize internalization of the plasma membrane. It's utility in measuring the kinetics of endocytosis and identifying defects along the endocytic pathway are well-established (Vida and Emr, 1995). FM4-64 exclusively stains the plasma membrane at 0°C. Following removal of the dye and shifting cells to room temperature or 30°C, the dye is internalized and small punctate structures corresponding to early endosomes are seen at 5-10 minutes and full vacuolar rim staining can be seen at 20-40 minutes. Internalization of the dye can be halted at any time by shifting the cells to 0°C and addition of buffer containing azide and fluoride for visualization by fluorescence microscopy.

I used this assay to determine if endocytosis proceeded at a similar rate in replicatively young and old cells with the hypothesis that old cells would have delayed kinetics of endocytosis or experience a block in the endocytic pathway.

Experimental Procedures:

This experiment required the live purification of both young (time 3 hours, corresponding to ~4-7

divisions) and old (time 24 hours, corresponding to ~16-22 divisions) cells with high purity. This was accomplished using serial live purification methods with YC-biotin as the purification medium, as described in Appendix A. Briefly, cells were grown to saturation overnight and a small number of these cells were subsequently cultured exponentially for 15+ hours to a maximum density of $6x10^6$ cells/mL. $5x10^6$ cells were biotinylated for each timepoint and cultured in YEPD. Aging cultures were staggered such at the time 3 hour and time 24 hour cells could be purified, stained and assayed concurrently. Time 24 hour cells underwent intermediate purification at time 12 hours.

The following FM4-64 staining and internalization protocols were adapted from several well-established protocols (Gammie & Rose, 2002; Grote, 2008; Vida & Emr, 1995) $3.5x10^7$ young cells and $3.5x10^7$ old cells were stained with 40 µM FM4-64 on ice for 20 minutes at a cell density of $1x10^7$ cells/mL. $5x10^6$ young and old cells were removed for kinetic timepoint 0 minutes. Internalization of dye was prevented by addition of an equal volume of ice-cold TAF buffer (20 mM Tris pH 7.4, 20 mM NaN_3, 20 mM NaF). Cells were gently centrifuged at 0.3xg, washed twice with ice-cold TAF buffer, and resuspended in 50 µL ice-cold TAF buffer. Cells were placed on ice until visualization by fluorescence microscopy.

For the remaining kinetic timepoints, 5, 10, 15, 20, 30, and 40 minutes, the remaining cells were washed twice with ice-cold YEPD and resuspended in ice-cold YEPD at a cell density of $1x10^8$ cells/mL. For each timepoint $5x10^6$ young and old cells were placed in culture tubes containing 2 mL pre-warmed YEPD and incubated at 30°C for the appropriate amount of time. For each kinetic timepoint, internalization of FM4-64 was halted by addition of 2.5 mL ice-cold TAF buffer. Cells were centrifuged gently at 0.3xg at 4°C and resuspended in 50 µL ice-cold TAF buffer and placed on ice until time of imaging. Cells were visualized by simple wide-field epifluorescence microscopy using a Nikon Eclipse E800 (Nikon 60X/1.40 oil Plan Apo objective) equipped with a CoolSNAP HQ^2 CCD camera (Photometrics). Images were processed using Metamorph version 7.1.1.0 imaging software.

*Note: the fixable form of FM4-64, FM4-64FX (Invitrogen), stained cells variably. The plasma membrane and other artifactual staining was evident at all timepoints regardless of the replicative age of the cell.

Result:

There was no detectable difference in the rate of endocytosis and no identifiable defects along the endocytic pathway in either young or old cells (**Figure B.1**).

Conclusion/Discussion:

Although no difference in the rate of endocytosis was detected using this experimental method, the possibility that the endocytic pathway is altered as a function of age should still be considered. At the time of this experiment, the capability of purifying cells using biotin-depleted YEPD had not yet been developed. Young and old cells were therefore purified using YC-biotin, which is a much more acidic medium compared to YEPD. The acidity of media has been shown to have a significant influence on the acidity of the vacuole, particularly if endogenous vacuole acidification is compromised (Plant et al., 1999). Ideally, cells should be aged, purified, and assayed in the same medium.

Furthermore, the finding that plasma membrane proteins are not being turned over in old cells may result from changes in aspects of endocytosis not reflected in the FM4-64 assay. For instance, there may be differences in the cargo being internalized or an age-dependent difference in cargo sorting and cargo fate. This possibility is supported by the finding that cargo sorting from the Golgi is altered in a pH-dependent manner (Huang and Chang, 2011). The loss of vacuolar acidity early in the aging process should predispose old mother cells to derangements of the secretory pathway, including endocytosis and warrants further examination of these cellular processes (Hughes and Gottschling, 2012).

References:

Alberts, B., Johnson, A., and Lewis, J. (2002). Molecular Biology of the Cell 4th ed. (New York: Garland Science).

Gammie, A., and Rose, M. D. (2002). Assays of cell and nuclear fusion. Methods in Enzymology *351*, 477–498.

Grote, E. (2008). Cell fusion assays for yeast mating pairs. Methods in Molecular Biology *475*, 165–196.

Hanson, P. I., Shim, S., and Merrill, S. a (2009). Cell biology of the ESCRT machinery. Current Opinion in Cell Biology *21*, 568–574.

Huang, C., and Chang, A. (2011). PH-dependent cargo sorting from the Golgi. The Journal of Biological Chemistry *286*, 10058–10065.

Hughes, A. L., and Gottschling, D. E. (2012). An early age increase in vacuolar pH limits mitochondrial function and lifespan in yeast. Nature *492*, 261–265.

Kane, P. (2006). The where, when, and how of organelle acidification by the yeast vacuolar H+-ATPase. Microbiology and Molecular Biology Reviews *70*, 177–191.

Lafourcade, C., Sobo, K., Kieffer-Jaquinod, S., Garin, J., and Van der Goot, F. G. (2008). Regulation of the V-ATPase along the endocytic pathway occurs through reversible subunit association and membrane localization. PloS One *3*, e2758.

Mellman, I., Fuchs, R., and Helenius, A. (1986). Acidification of the endocytic and exocytic pathways. Annual Review of Biochemistry.

Plant, P. J., Manolson, M. F., Grinstein, S., and Demaurex, N. (1999). Alternative mechanisms of vacuolar acidification in H(+)-ATPase-deficient yeast. The Journal of Biological Chemistry *274*, 37270–37279.

Vida, T. a, and Emr, S. D. (1995). A new vital stain for visualizing vacuolar membrane dynamics and endocytosis in yeast. The Journal of Cell Biology *128*, 779–792.

Weinberg, J., and Drubin, D. G. (2012). Clathrin-mediated endocytosis in budding yeast. Trends in Cell Biology *22*, 1–13.

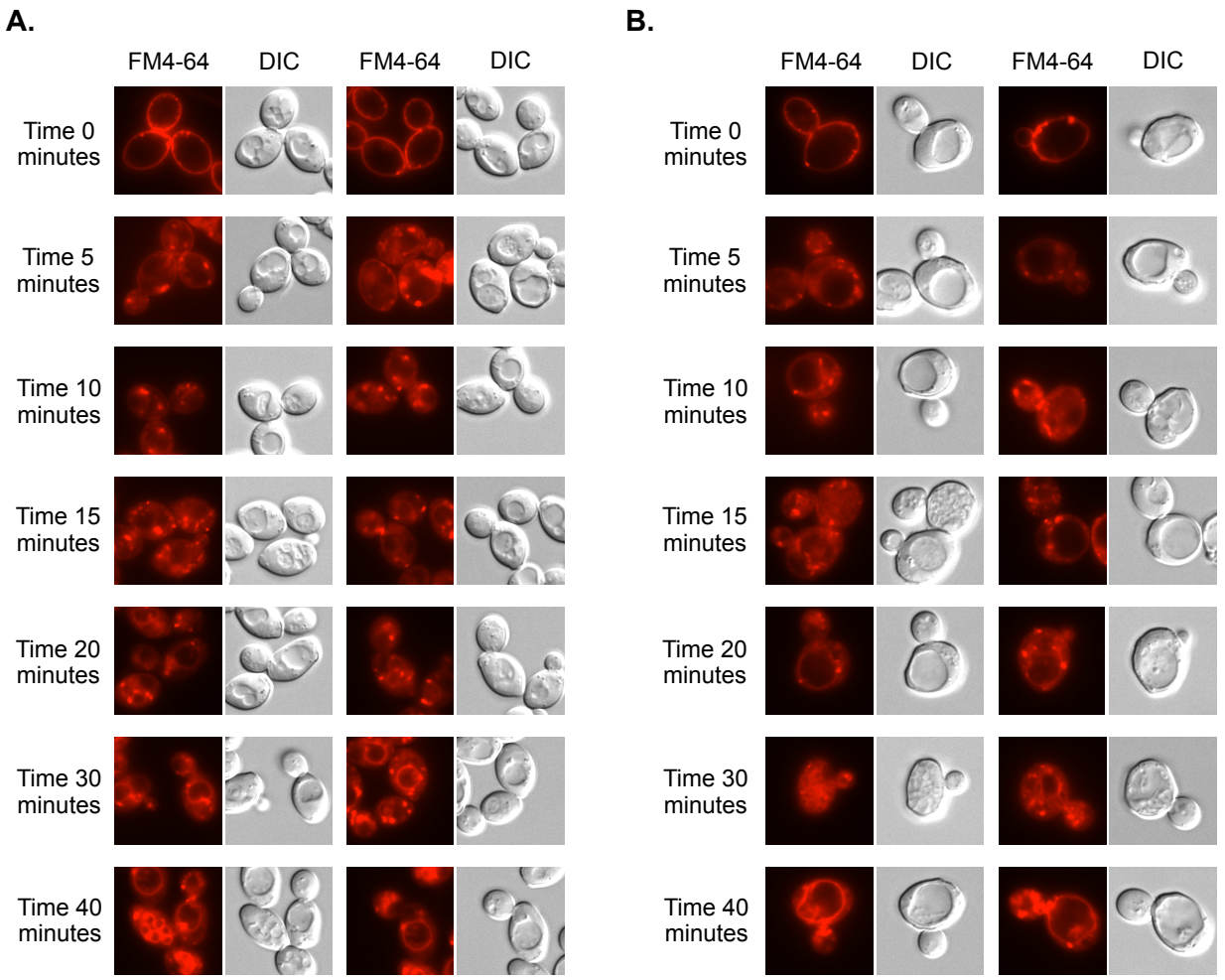

Figure B.1. FM4-64 internalization occurs at similar rates in young and old cells. Young time 3-hour (A) and old time 24-hour (B) cells were live purified in YC-biotin. Internalization of FM4-64 was observed at 0, 5, 10, 15, 20, 30, and 40 minutes after plasma membrane labeling and removal of dye as described in the experiment methods of Appendix B. Two sets of images are shown for young cells (A) and two sets for old cells (B). In each set, the image on the left shows FM4-64 fluorescence and the image on the right shows the DIC image of the same cells. In both young and old cells, plasma membrane and punctate structures along the inside of the plasma membrane are apparent at time 0. Cytoplasmic punctate structures are evident from 5-15 minutes, and vacuolar rim staining is first apparent at 20 minutes. By time 30 and 40 minutes, the majority of FM4-64 is found at the vacuolar rim. This timing is consistent with that reported in the literature for log-phase cells (Ref Emr 1995).

Appendix C: A Gateway-Compatible Integration Vector

One of the major obstacles in using plasmid expression vectors in replicatively aging cells is maintaining consistent expression throughout the aging process. Two-micron and centromeric plasmids have been widely used to study the effects of introducing heterologous genes and altering gene expression. The problem in using plasmids in the context of replicative aging is that two-micron plasmids have a controversial role in lifespan determination and centromeric plasmids are lost from the mother cell at an unknown frequency as a function of replicative age (Falcon, Rios, & Aris, 2005; Falcón & Aris, 2003; Hughes unpublished data). This leaves genomic integration as the only stable method for introducing heterologous genes and/or modifying levels of gene expression. Historically, there are two main methods used to accomplish integration of an expression construct: PCR-mediated gene disruption and the use of integration vectors. The PCR-mediated method requires unique primer sequences and a gene construct that already contains all the material to be introduced. Introduction of genetic material into the yeast genome using an integration vector requires linearization of the vector followed by transformation. However, both of these methods require the time-intensive cloning of constructs and are not amenable to either high-throughput or genome-wide applications.

The Gateway cloning system developed by Invitrogen has enabled a more efficient method for creating constructs that is amenable to high-throughput and genome-wide applications. Briefly, the Gateway cloning system uses recombination enzymes to quickly transfer DNA fragments among different vectors in a single step. This allows for the movement of open reading frames to and from vectors with various expression capabilities. Gateway compatible yeast libraries containing the entire set of yeast open reading frames and Gateway compatible vector backbones that allow constitutive and inducible expression and various protein fusions are now available (Gelperin and White, 2005; Alberti et al., 2007).

My goal was to create an integration vector that is both compatible with the Gateway system for easy gene and promoter exchange and integrates into a neutral ectopic site upon linearization by restriction enzyme digest. The backbone vector used for construction of this integration vector was a centromeric Gateway donor plasmid that contained the galactose inducible overexpression promoter and *URA3* selectable marker (Addgene) (**Figure C.1**). The choice of an ectopic site that was most likely to be neutral and not disrupt the expression of surrounding genes was based on available gene-poor regions in the yeast genome. These are rare, however, chromosome I is generally gene poor, especially on its short arm between coordinates 196185 to 202903 (**Figure C.2**).

Experimental Procedures:

To create a Gateway-compatible vector that allows facile genomic integration into a neutral ectopic site, regions of homology to Chromosome I were inserted into the advanced gateway destination vector pAG306GAL-ccdB such that the entire vector would integrate into Chromosome I following restriction enzyme digestion (Addgene). A fusion product containing reverse tandem regions of homology to a gene-poor region of Chromosome I was ligated into pAG306GAL-ccdB linearized by blunt-end digestion with *BsaAI* as schematized in **Figure C.3** and **Figure C.4A**. The chromosome I homology regions were constructed as follows: Chromosome I Part A was created by amplification of a genomic template with primers *ChrI PartA NotI F* and *ChrI PartA SmaI R* to isolate 450 bp of homology upstream of the integration site of interest (ChI:199456-199457) and to incorporate a *NotI* restriction enzyme site at the 5' end of this region and a *SmaI* restriction enzyme site at the 3' end (Appendix G). Chromosome I Part B was created by amplification of a genomic template with primers *ChrI PartB SmaI F* and *ChrI PartB NotI R* to isolate 450 bp of homology downstream of the integration site of interest (ChI:199456-199457) and to incorporate a *NotI* restriction enzyme site at the 3' end of this region and a *SmaI* restriction enzyme site at the 5' end (Appendix G). Fusion PCR with primers *ChrI PartB SmaI F* and *ChrI PartA SmaI R* using the two amplicons as the template created a single fusion product containing reverse tandem regions of homology to Chromosome I with a *NotI* site separating the two regions of homology and *SmaI* sites at the 5' and 3' ends of the amplicon (Appendix G). The fusion product was blunt-end digested with *SmaI* and inserted into pAG306GAL-ccdB. Proper orientation of the ligation product was verified by unique restriction enzyme digest and electrophoresis.

Result:

The end result was an integration vector that is compatible with the Gateway cloning system and allows the integration of the entire vector into a gene-poor region of chromosome I following *NotI* digestion and transformation.

Conclusion/Discussion:

This is a valuable tool for introducing genetic material into the genome that is stably expressed throughout replicative aging. Additionally, this integration vector can be further modified for the introduction of other cassettes that require stable expression from an ectopic genomic site. Examples of this include the replacement of the galactose-inducible

overexpression promoter and *ccdB* selection gene with *GFP-Tub1* or *ss-GFP-HDEL*, which was used for stable ectopic expression of these constructs for cell biological purposes as shown in Chapters II and III (**Figure C.4B and C**, Appendix G). Furthermore, other members of the Gottschling laboratory have used the chromosome I integration portion of this vector to make other versions that are compatible with the Gateway cloning system and allow the constitutive overexpression of genes.

References:

Alberti, S., Gitler, A., and Lindquist, S. (2007). A suite of Gateway® cloning vectors for high-throughput genetic analysis in Saccharomyces cerevisiae. Yeast, 913–919.

Falcon, A. a, Rios, N., and Aris, J. P. (2005). 2-micron circle plasmids do not reduce yeast life span. FEMS Microbiology Letters *250*, 245–251.

Falcón, A., and Aris, J. (2003). Plasmid accumulation reduces life span in Saccharomyces cerevisiae. Journal of Biological Chemistry *278*, 41607–41617.

Gelperin, D., and White, M. (2005). Biochemical and genetic analysis of the yeast proteome with a movable ORF collection. Genes & Development *19*, 2816–2826.

Hughes, A. L., and Gottschling, D. E. (2012). An early age increase in vacuolar pH limits mitochondrial function and lifespan in yeast. Nature *492*, 261–265.

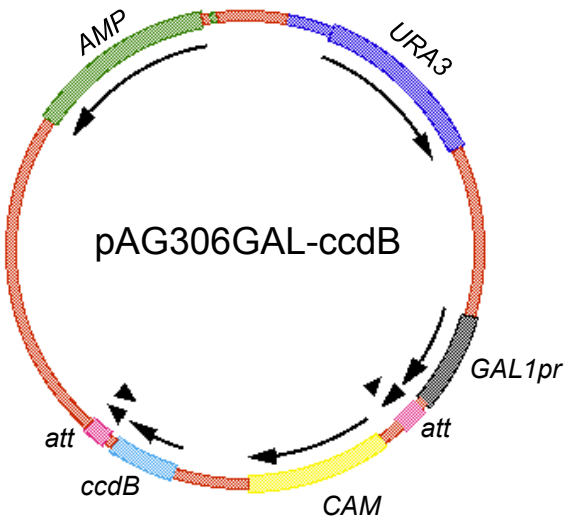

Figure C.1. Schematic of pAG306GAL-ccdB. pAG306GAL-ccdB (Addgene) is an advanced gateway destination vector used as the vector backbone for design of a Gateway-compatible plasmid that allows genomic integration and stable expression of plasmid contents and into a neutral ectopic site on Chromosome I. pAG306GAL-ccdB is itself an integrating vector that contains ampicillin resistance (Amp) and *URA3* selectable markers, and *GAL1* promoter for galactose-inducible gene overexpression . Like all Gateway-compatible destination vectors, pAG306GAL-ccdB contains *att* recombination sites that allow enzyme-mediated exchange of genetic material and the ccdB lethal gene and chloramphenicol resistance marker for counter selection.

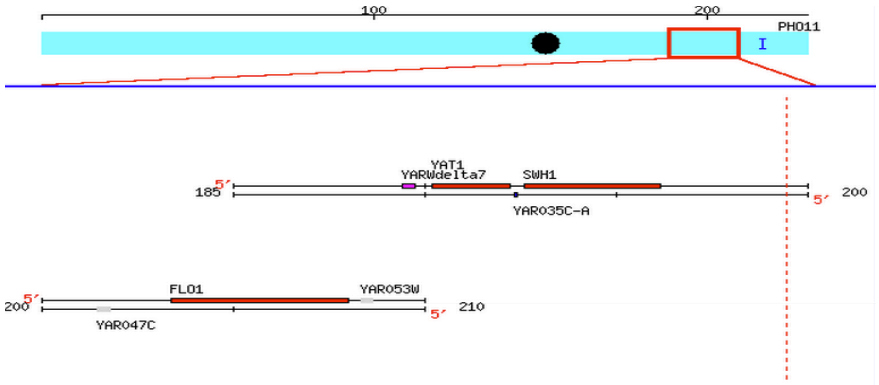

Figure C.2. The target integration site is a gene-poor region on the short arm of Chromosome I. Schematic of chromosome I. Red box indicates region between coordinates 185,000 and 210,000 on the short arm of chromosome I, which are expanded below. The dotted red line indicates coordinate 199,456/7 which is the integration site of interest. It is a gene-poor area with the nearest protein-encoding gene at 196,185 upstream (*SWH1*) and at 202,903 downstream (*FLO1*) (www.yeastgenome.org).

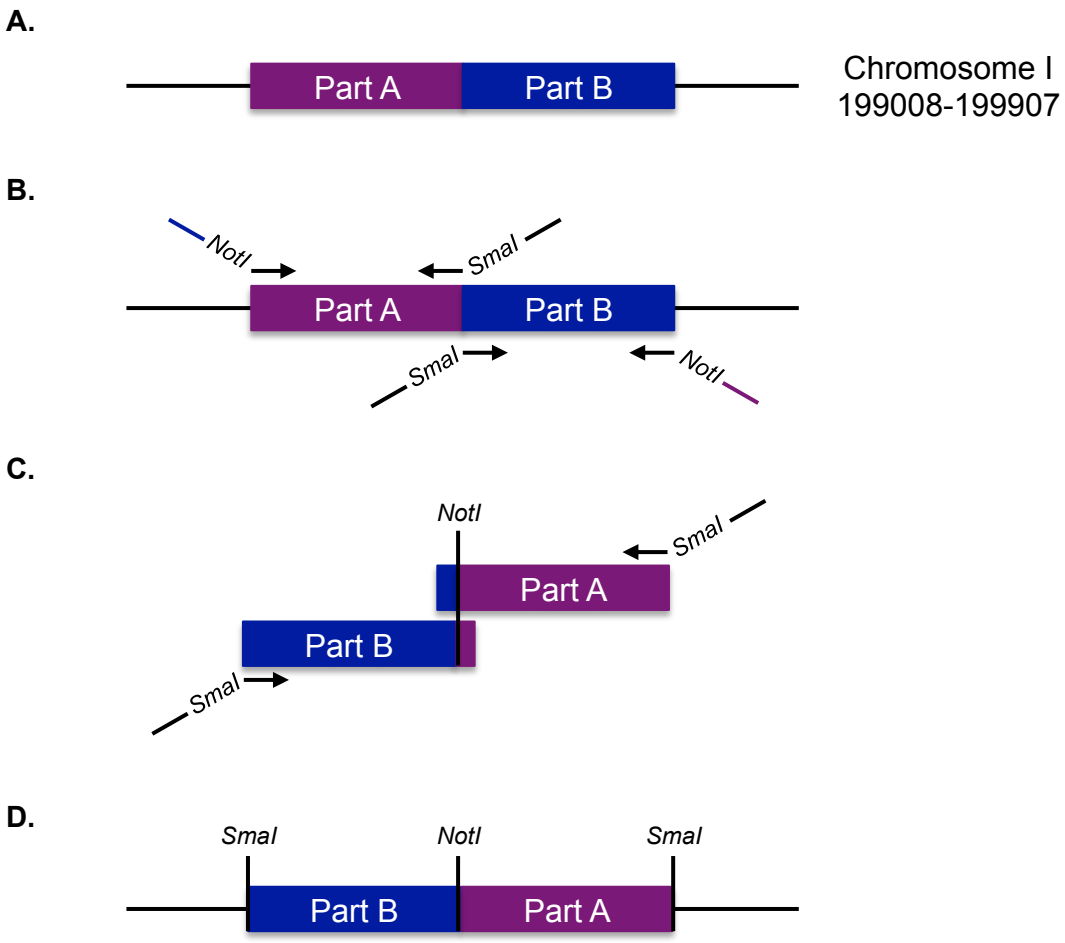

Figure C.3. Schematic of the construction of the Chromosome I integration cassette. (A) Gene-poor region of Chromosome I. A 900 bp region from coordinates 199008 to 199907 divided into two parts, A and B, each 450 bp, was used for regions of homology to facilitate homologous recombination-mediated integration. (B) Part A was isolated by amplification with primers *ChrI PartA NotI F* and *ChrI PartA SmaI R* to provide 450 bp of homology upstream of the integration site of interest (ChI:199456-199457) and to incorporate a *NotI* restriction enzyme site at the 5' end of this region and a *SmaI* restriction enzyme site at the 3' end. Part B was created by amplification of a genomic template with primers *ChrI PartB SmaI F* and *ChrI PartB NotI R* to isolate 450 bp of homology downstream of the integration site of interest (ChI:199456-199457) and to incorporate a *NotI* restriction enzyme site at the 3' end of this region and a *SmaI* restriction enzyme site at the 5' end (Appendix G). (C) Fusion PCR with primers *ChrI PartB SmaI F* and *ChrI PartA SmaI R* using both Part A and Part B amplicons as the template results in (D) single fusion product containing reverse tandem regions of homology to Chromosome I with a *NotI* site separating the two regions of homology and *SmaI* sites at the 5' and 3' ends for insertion into a blunt-end digested, linearized vector backbone.

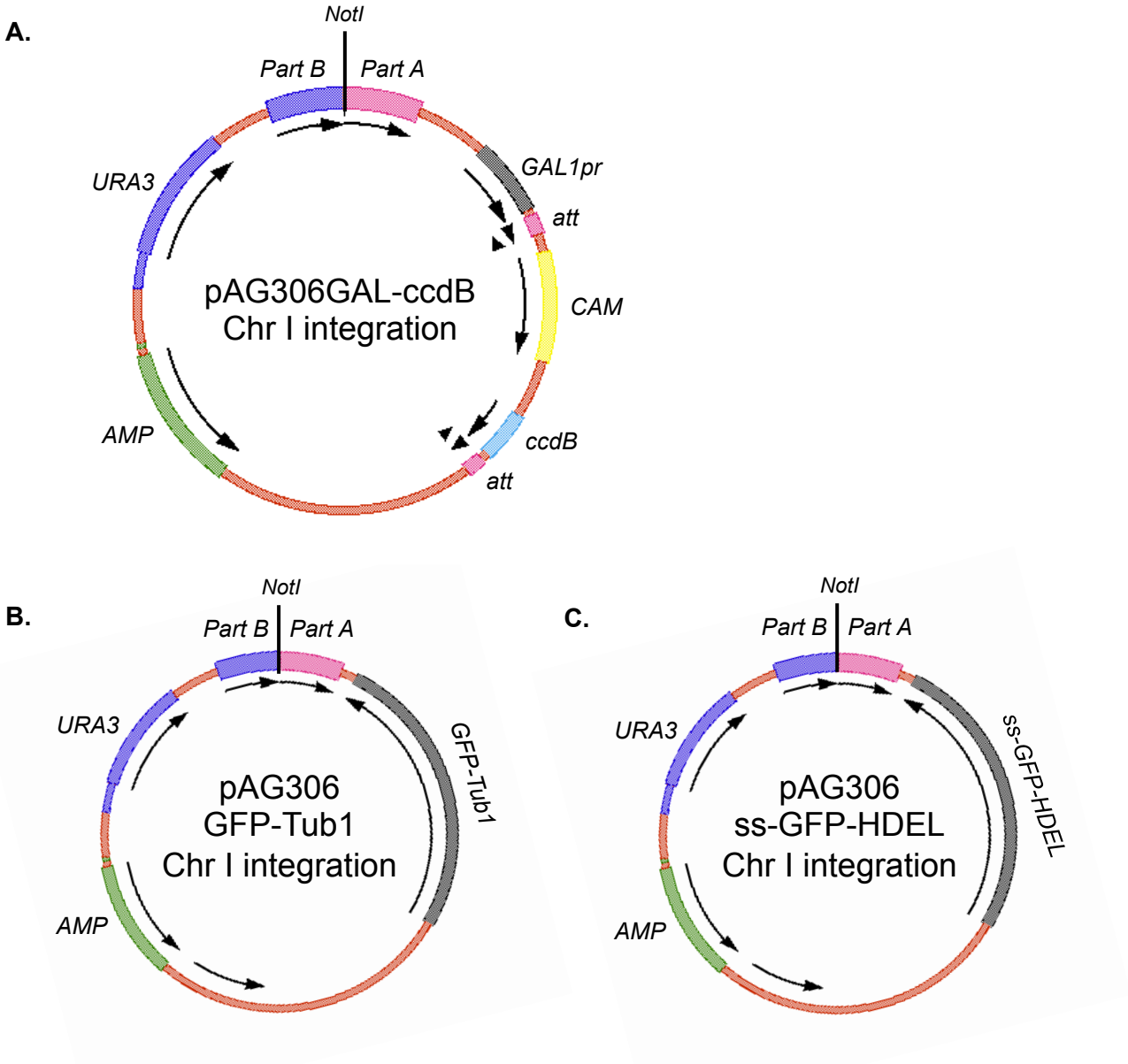

Figure C.4. Chromosome I integration plasmids. (A) Schematic of pAG306GAL-ccdB ChrI integration vector. This is a Gateway-compatible destination vector that allows galactose-inducible overexpression and integration of vector contents into a gene-poor ectopic region of Chromosome I (199456/7) following *NotI* linearization and transformation. (B) Schematic of pAG306 GFP-Tub1 ChrI integration. *GFP-TUB1* cloned to replace *GAL1pr* and Gateway-compatibility region. *NotI* linearization and transformation results in stable expression of GFP-Tub1 from the ectopic Chromosome I site. (C) Schematic of pAG306 ss-GFP-HDEL ChrI integration. *ss-GFP-HDEL* cloned to replace *GAL1pr* and Gateway-compatibility region. *NotI* linearization and transformation results in stable expression of ss-GFP-HDEL (HDEL is the ER retention signal) from the ectopic Chromosome I site.

Appendix D: Mitochondrial DNA Copy Number Increases with Replicative Age

The mitochondria and its dynamics have long been thought to play important roles in cellular decline and the aging process. The mitochondria is an important organelle with multiple crucial functions including cellular energy production, intermediary metabolism, ion and amino acid storage, regulation of apoptosis, and maintenance of its own genome (Alberts et al., 2002). *Saccharomyces cerevisiae* have 30-80 copies of mitochondrial DNA (mtDNA) distributed within its tubular mitochondria, and the mtDNA copy number is thought to change in order to accommodate the metabolic demands of the cell (Solieri, 2010). Interestingly, in yeast, mtDNA is not essential for viability, however it is required for respiration and utilization of non-fermentable carbon sources (Solieri, 2010).

The mitochondria and how it relates to aging has been widely studied since it was first proposed in the 1970's to generate free radicals that damaged the cell and mtDNA, which subsequently led to aging and cell death. Since that time, there have been many studies, both in yeast and in higher organisms, showing various ways the mitochondria contributes to the aging process. These studies have implicated changes in mitochondrial fusion and fission dynamics, mitophagy, and qualitative and quantitative changes in mtDNA as alterations that cause age-associated decline in mitochondrial function and promote aging (Ugidos et al., 2010; Braun and Westermann, 2011; Barros et al., 2010; Seo et al., 2010; Jazwinski, 2005). In higher eukaryotes, somatic mtDNA mutations and deletions have been linked to premature aging phenotypes, suggesting mtDNA replication fidelity and mtDNA quality control pathways are critical processes in preventing age-associated cellular dysfunction. Interestingly, the association between aging and mtDNA copy number is much less clear.

The majority of studies quantitating mtDNA in the context of aging have been done in mammalian model organisms, however consensus has not been reached. Some studies suggest an age-associated increase in mtDNA copy number, possibly secondary to reactive oxygen species production (Lee et al., 2000, 1998; Pesce et al., 2001; Gadaleta et al., 1992). In contrast, there are other studies that support a decline in mtDNA copy number along with mitochondrial dysfunction with advancing age (Barazzoni et al., 2000; Cree et al., 2008; Welle et al., 2003). In yeast, several labs have observed that mitochondria undergo a morphological change from a tubular organelle in young cells to multiple fragmented structures in replicatively aged cells (Scheckhuber et al., 2007; Hughes and Gottschling, 2012). Concomitant abolishment of mitochondrial membrane potential is also observed, however, when cells that are replicatively aged in fermentable media are transferred to a non-fermentable carbon source,

their mitochondria regain their tubular morphology and even replicatively aged cells are able to respire (Adam Hughes, unpublished data). This suggests that mtDNA are still present and mitochondrial function can be rescued. How mtDNA copy number changes with replicative age, however, is unknown. Recent studies have shown that mitochondrial fusion in yeast increases mtDNA copy number (Hori et al., 2011). Because fusion has been shown to be dysfunctional in replicatively aged yeast, one might hypothesize that the mtDNA copy number is reduced in old cells, but not completely absent.

Whether mtDNA copy number changes as function of replicative age has not been previously determined, largely due to limitations in isolating enough replicatively aged cells for Southern blot analysis or quantitative real-time PCR. Here, I sought to determine if mtDNA copy number changes as a function of replicative age using the MEP to isolate replicatively young and replicatively old cells, and quantitative real-time PCR methods to quantify mtDNA copy number.

Experimental Procedures:

Young and old mother cells were purified using the MEP and streptavidin-bead purification process described in the Experimental Procedures chapter. This was done in biological triplicate and mother cells were isolated at time 3 hours (young and corresponding to ~X replications old) and at time 45 hours (old and corresponding to ~ X replications). An aliquot of the resultant dumbbells from the time 45-hour purification was also collected. In addition, log-phase cells of the aging strain, UCC5185, and of a petite strain containing no DNA (UCC835-1) were collected to serve as controls for the experiment and for optimizing the quantitative PCR (Appendix G).

Total cellular nucleic acids were isolated from these cells using standard glass bead and phenol extraction methods, and subsequently treated with RNase A (Hoffman and Winston, 1987). Quantitative real-time PCR was used to determine the number of copies of mtDNA relative to nuclear DNA using two separate reactions: one by amplification of the mitochondrial *COX1* gene (*COX1* forward 5′-CTACAGATACAGCATTTCCAAGA-3′ and *COX1* reverse 5′-GTGCCTGAATAGATGATAATGGT-3′) and one by amplification of the nuclear *ACT1* gene (*ACT1* forward 5′-GTATGTGTAAAGCCGGTTTTG-3′ and *ACT1* reverse 5′-CATGATACCTTGGTGTCTTGG-3′) as designed by Taylor et al. (Taylor et al., 2005). These primer sets showed equal amplification efficiency across a large template dilution series. No amplification of mitochondrial DNA was detected from template derived from UCC835-1. Quantitate real-time PCR was performed with biological triplicates with two different dilutions of

template in duplicate in 25 µL total reaction volume containing 12.5 µL 2X SYBR Green PCR Master Mix (Applied Biosystems), 0.25 µL UDG (New England Biolabs), 5.25 µL ddH_2O, 1 µL of 10 µM forward and reverse primers and 5 µL 1:100 and 1:1000 diluted template from time 3-hour and time 45-hour mother cells and time 45-hour dumbbells.

The mtDNA copy number and the nuclear DNA copy number in young cells, old cells, and dumbbells were calculated using the threshold cycle number (C_T). The relative quantity of mtDNA compared to nuclear genomes was calculated using the equation $2^{\Delta C_T(ACT1\text{-}COX1)}$. The resulting ratio was divided by two in order to determine the number of mtDNA genomes per diploid nuclear genome.

Results:

Young time 3-hour mother cells contained ~8 copies mtDNA per diploid genome, old time 45-hour mother cells contained ~16 copies mtDNA per diploid genome, and time 45-hour dumbbells contained ~38 copies mtDNA per diploid genome. Compared to young time 3-hour cells, replicatively aged cells at time 45 hours were found to have approximately 2-fold more mtDNA and dumbbells contained approximately 4-fold more mtDNA (**Figure D.1**).

Conclusion/Discussion:

Mitochondrial DNA copy number increases as a function of replicative age. This increase is consistent with the finding in mammalian studies where certain tissues and cell types exhibit increased mtDNA copy number with age. The number of copies of mtDNA in replicatively old cells in this study may be an underestimation as accurate quantitation was dependent on the assumption of normal nuclear genome copy number. Based on higher than expected DNA extraction yield from replicatively old cells and the idea that chromosomal instability increases as a function of age, it is possible that old mother cells contain more copies of mtDNA than reported (Henderson, unpublished data).

The finding that mtDNA copy number is increased with replicative age brings up the question of what is the biological significance of this increase, and what, if any, is its role in the aging process? It has been proposed that the increase in mtDNA copy number with age is actually a compensatory mechanism and reflects an accumulation of damaged, mutated, and dysfunctional mtDNA that is ultimately correlated with loss of efficiency in mtDNA transcription

and decline in mitochondrial function. However, other studies have suggested that there is a decline in mtDNA copy number in certain tissues with age. Irrespective, the implications of age-associated changes in mtDNA copy number on transcript levels of mitochondrially encoded genes remain unclear (Barazzoni et al., 2000; Lee et al., 2000; Wei and Lee, 2008). Arguably, yeast is an ideal organism to study these effects, as there is no obligation to retain mtDNA in the presence of a fermentable carbon source.

Another question that remains is where is the mtDNA in a replicatively old cell. The mitochondria in old mother cells are highly fragmented and have lost their membrane potential, however mtDNA must still be present in some form as old yeast cells retain their ability to grow on non-fermentable carbon sources (Hughes unpublished data, Hughes & Gottschling, 2012). Are there mitochondrial structures that contain mtDNA nucleoids, and if so, do these structures maintain some low level of mitochondrial membrane potential? The answers to these questions also have greater implications on other age-associated phenotypes discussed in the body of this work, such as on age-associated peroxisome expansion. It has been shown that peroxisomes proliferate in the setting of mitochondrial dysfunction (Butow and Avadhani, 2004; Motley et al., 2008). The findings that mtDNA copy number increases with replicative age combined with the ability of old mother cells to respire suggests that loss of respiratory capacity is unlikely to be the mechanism by which age-associated peroxisome expansion occurs.

Finally, this technique of using the MEP to isolate pure populations of cells of any replicative age combined with quantitative real-time PCR can be more widely applied to accurately quantify changes in DNA copy number as a function of replicative age. For instance, a similar approach could be used to compare the burden of extrachromosomal rDNA circles in aging cells. The use of quantitate real-time PCR allows for the use of many fewer cells compared to the traditional method of quantifying ERCs, which is by Southern blot.

References:

Alberts, B., Johnson, A., and Lewis, J. (2002). Molecular Biology of the Cell 4th ed. (New York: Garland Science).

Barazzoni, R., Short, K. R., and Nair, K. S. (2000). Effects of aging on mitochondrial DNA copy number and cytochrome c oxidase gene expression in rat skeletal muscle, liver, and heart. The Journal of Biological Chemistry *275*, 3343–3347.

Barros, M. H., Da Cunha, F. M., Oliveira, G. a, Tahara, E. B., and Kowaltowski, A. J. (2010). Yeast as a model to study mitochondrial mechanisms in ageing. Mechanisms of Ageing and Development *131*, 494–502.

Braun, R. J., and Westermann, B. (2011). Mitochondrial dynamics in yeast cell death and aging. Biochemical Society Transactions *39*, 1520–1526.

Butow, R. a, and Avadhani, N. G. (2004). Mitochondrial signaling: the retrograde response. Molecular Cell *14*, 1–15.

Cree, L. M., Patel, S. K., Pyle, a, Lynn, S., Turnbull, D. M., Chinnery, P. F., and Walker, M. (2008). Age-related decline in mitochondrial DNA copy number in isolated human pancreatic islets. Diabetologia *51*, 1440–1443.

Gadaleta, M., Rainaldi, G., Lezza, A., Milella, F., Fracasso, F., and Cantatore, P. (1992). Mitochondrial DNA copy number and mitochondrial DNA deletion in adult and senescent rats. Mutation Research *275*, 181–193.

Hoffman, C., and Winston, F. (1987). A ten-minute DNA preparation from yeast efficiently releases autonomous plasmids for transformation of Escherichia coli. Gene *57*, 267–272.

Hori, A., Yoshida, M., and Ling, F. (2011). Mitochondrial fusion increases the mitochondrial DNA copy number in budding yeast. Genes to Cells *16*, 527–544.

Hughes, A. L., and Gottschling, D. E. (2012). An early age increase in vacuolar pH limits mitochondrial function and lifespan in yeast. Nature *492*, 261–265.

Jazwinski, S. M. (2005). Yeast longevity and aging--the mitochondrial connection. Mechanisms of Ageing and Development *126*, 243–248.

Lee, H. C., Lu, C. Y., Fahn, H. J., and Wei, Y. H. (1998). Aging- and smoking-associated alteration in the relative content of mitochondrial DNA in human lung. FEBS Letters *441*, 292–296.

Lee, H. C., Yin, P. H., Lu, C. Y., Chi, C. W., and Wei, Y. H. (2000). Increase of mitochondria and mitochondrial DNA in response to oxidative stress in human cells. The Biochemical journal *348 Pt 2*, 425–432.

Motley, A. M., Ward, G. P., and Hettema, E. H. (2008). Dnm1p-dependent peroxisome fission requires Caf4p, Mdv1p and Fis1p. Journal of Cell Science *121*, 1633–1640.

Pesce, V., Cormio, A., Fracasso, F., Vecchiet, J., Felzani, G., Lezza, A., Cantatore, P., and Gadaleta, M. (2001). Age-related mitochondrial genotypic and phenotypic alterations in human skeletal muscle. Free Radical Biology and Medicine *30*, 1223–1233.

Scheckhuber, C. Q., Erjavec, N., Tinazli, A., Hamann, A., Nyström, T., and Osiewacz, H. D. (2007). Reducing mitochondrial fission results in increased life span and fitness of two fungal ageing models. Nature Cell Biology *9*, 99–105.

Seo, A. Y., Joseph, A.-M., Dutta, D., Hwang, J. C. Y., Aris, J. P., and Leeuwenburgh, C. (2010). New insights into the role of mitochondria in aging: mitochondrial dynamics and more. Journal of Cell Science *123*, 2533–2542.

Solieri, L. (2010). Mitochondrial inheritance in budding yeasts: towards an integrated understanding. Trends in Microbiology *18*, 521–530.

Taylor, S. D., Zhang, H., Eaton, J. S., Rodeheffer, M. S., Lebedeva, M. A., Rourke, T. W. O., Siede, W., and Shadel, G. S. (2005). The conserved Mec1/Rad53 nuclear checkpoint pathway regulates mitochondrial DNA copy number in Saccharomyces cerevisiae. Molecular Biology of the Cell *16*, 3010–3018.

Ugidos, A., Nyström, T., and Caballero, A. (2010). Perspectives on the mitochondrial etiology of replicative aging in yeast. Experimental Gerontology *45*, 512–515.

Wei, Y., and Lee, H. (2008). Oxidative stress, mitochondrial DNA mutation, and impairment of antioxidant enzymes in aging. Experimental Biology and Medicine *227*, 671–682.

Welle, S., Bhatt, K., Shah, B., Needler, N., Delehanty, J. M., and Thornton, C. a (2003). Reduced amount of mitochondrial DNA in aged human muscle. Journal of Applied Physiology *94*, 1479–1484.

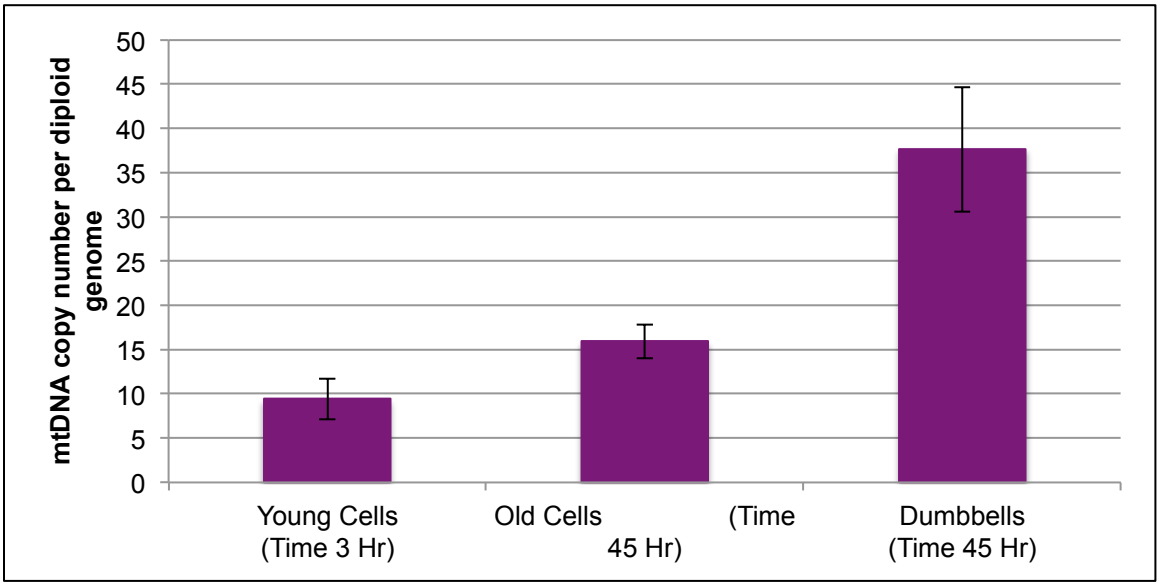

Figure D.1. mtDNA copy number is increased in replicatively old cells. mtDNA copy number was measured relative to genomic DNA copy number by quantitative real-time PCR in purified populations of replicatively young and old cells. Young (time 3-hour) mother cells contained ~8 copies of mtDNA per diploid genome compared to old (time 45-hour) mother cells, which contained ~2-fold more mtDNA. Eluted dumbbells from the time 45-hour purification contained ~38 copies of mtDNA per diploid genome.

Appendix E: Time in Exponential Growth Decreases Replicative Lifespan and Affects Age-Associated Phenotypes

The transition from exponential growth to stationary phase is associated with a change in gene expression of over 1/3 of all genes in *Saccharomyces cerevisiae* (Martinez et al., 2004). This transition is also accompanied by many metabolic changes as nutrients become depleted, including a shift from fermentative growth to respiration, and finally to quiescence (Gray et al., 2004; Smets et al., 2010; Werner-Washburne et al., 1993). In most yeast studies, cells are typically inoculated in culture and grown overnight to saturation, which corresponds to early stationary phase. Cultures are then diluted back with fresh media and incubated for several hours to allow cells to enter the exponential growth phase. While this set-up is perfectly adequate for many assays, additional considerations must be made for experiments studying metabolism, stress response, and replicative aging.

One significant difference between cells in stationary phase and exponential phase is their tolerance to various stresses. Cells that have undergone the diauxic shift in response to dwindling nutrients in the media and have begun to enter stationary phase exhibit increased resistance to heat, osmotic stress, and to oxidative stress (Smets et al., 2010; Jamieson, 1992, 1998; Aragon et al., 2006). This effect was most apparent in the experiments to determine if tolerance to oxidative stress was altered as a function of replicative age. Initially, cells were grown as described above by culturing overnight to saturation and diluted to a lower cell density using fresh media to obtain cells in exponential phase. Cells growing exponentially were used to seed MEP aging cultures and exposed to oxidative stress at various replicative ages as described in Chapter VIII. The result was a dramatic susceptibility to oxidizing agent in the first 24 hours of aging followed by age-associated resistance (**Figure 8.8**). Interestingly, the initial sensitivity to oxidizing agent could be abrogated by growing cells in exponential phase for a longer period of time prior to initiating the aging experiment (**Figure 8.10**). This suggests that sensitivity to oxidizing agent is a result of the culture's growth history and likely due to the transition from stationary to exponential phase, and that aging cells are indeed resistant to oxidizing agent (**Figure 8.10**).

Using increasing sensitivity to hydrogen peroxide as an indication for residual stationary-phase effects, the amount of time required to be truly in exponential phase is ~24 hour from dilution from saturated culture. This is a much longer period of exponential growth than most laboratories use prior to starting their experiments, however, pre-growth for less than 24 hours may have dramatic and potentially confounding effects, especially when attempting to identify

age-associated phenotypes. These findings also suggest that extended time in the exponential growth phase may have detrimental effects on replicative lifespan. Decreased viability due to extended time exponential growth was later confirmed by micromanipulation, and found to accelerate age-associated mitochondrial fragmentation and dysfunction (Hughes unpublished data, Hughes & Gottschling, 2012). Together, these findings suggest that age-associated phenotypes and aging studies should be evaluated in the context of the growth history in addition to replicative age.

The likely explanation for why cells are resistant to insult in stationary phase is the upregulation of heat shock proteins and stress response pathways during the diauxic shift (Werner-Washburne et al., 1993; Gray et al., 2004; Jamieson, 1992, 1998). This upregulation is significant and may have long-lasting effects that persist for quite some time after the transition from stationary phase to exponential growth. In addition, the pathways required for nutrient depletion signaling and required for the shift into respiration are the same pathways that have been found to be important in the regulation of yeast replicative lifespan. These include the PKA, Tor1, and Sch9 signaling kinases and support a relationship between replicative aging and the metabolic changes that occur with growth phase transitions (Smets et al., 2010).

The question that remains to be answered is how is extended exponential phase growth associated with replicative aging? Clearly, the time in log-phase result in some similar phenotypes as seen with advanced replicative age, such as mitochondrial fragmentation and decreased viability. However, there are also differences, such as hydrogen peroxide sensitivity with extended exponential phase growth and hydrogen peroxide resistance as a function of replicative age. Which pathways that are involved in exponential phase growth may also be involved in replicative aging? In other words, do aging cells, either appropriately or inappropriately, upregulate pathways that are upregulated in response to nutrient starvation?

References:

Aragon, A. D., Quiñones, G. a, Thomas, E. V, Roy, S., and Werner-Washburne, M. (2006). Release of extraction-resistant mRNA in stationary phase Saccharomyces cerevisiae produces a massive increase in transcript abundance in response to stress. Genome Biology *7*, R9.1–13.

Gray, J., Petsko, G., Johnston, G., Ringe, D., Singer, R., and Werner-Washburne, M. (2004). "Sleeping beauty": quiescence in Saccharomyces cerevisiae. Microbiology and Molecular Biology Reviews *68*, 187.

Hughes, A. L., and Gottschling, D. E. (2012). An early age increase in vacuolar pH limits mitochondrial function and lifespan in yeast. Nature *492*, 261–265.

Jamieson, D. J. (1998). Oxidative stress responses of the yeast Saccharomyces cerevisiae. Yeast *14*, 1511–1527.

Jamieson, D. J. (1992). Saccharomyces cerevisiae has distinct adaptive responses to both hydrogen peroxide and menadione. Journal of Bacteriology *174*.

Martinez, M., Roy, S., Archuletta, A., Wentzell, P., Anna-Arrioloa, S., Rodriguez, A., Aragon, A. D., Quinones, G., Allen, C., and Werner-Washburne, M. (2004). Genomic analysis of stationary-phase and exit in Saccharomyces cerevisiae: gene expression and identification of novel essential genes. Molecular Biology of the Cell *15*, 5295–5305.

Smets, B., Ghillebert, R., De Snijder, P., Binda, M., Swinnen, E., De Virgilio, C., and Winderickx, J. (2010). Life in the midst of scarcity: adaptations to nutrient availability in Saccharomyces cerevisiae. Current Genetics *56*, 1–32.

Werner-Washburne, M., Braun, E., Johnston, G., and Singer, R. (1993). Stationary phase in the yeast Saccharomyces cerevisiae. Microbiological Reviews *57*, 383–401.

Appendix F: Conversion of Nikon Elements .nd2 Files into Tiffs and Movies Using ImageJ

Introduction:
The goal of this protocol is to take .nd2 live microscopy files that were taken using the Nikon Elements software and convert them into tiffs, make projections of those tiffs, create images combining multiple channels, overlay images with brightfield information, and create movies for each location that contain information from multiple channels, planes, and timepoints. This will be accomplished by using Python script to iterate ImageJ MacroScript commands, such that all images from a single experiment can be treated identically, and in a semi-automated manner.

Requirements:
Nikon NIS Elements Software (brief access needed only)
General text editor (i.e. Text Wrangler for Mac OSX)
ImageJ (http://imagej.nih.gov/ij/index.html)
LOCI plugin (http://www.loci.wisc.edu/bio-formats/imagej)
Bash (UNIX shell)
Python (may need to download from http://www.python.org/)
Microsoft Excel (optional)

Useful terminal commands:

ls – lists contents of a directory
cd – changes working directory
mkdir – makes a new directory
sh – runs a .sh shell script
python – runs a .py script
control z – stops current process

Note:

- Shell environments are case sensitive!!
- Shell environments do not handle spaces correctly so use underscore

Table of Contents:

Step 1: Splitting into multipoints

The purpose of this step is to take an experiment that contains images from multiple xy locations and split them by location. The file format will remain .nd2. This step will: 1) reduce file sizes so that computer memory (RAM) will not be limiting; 2) make separating files by xy position much easier, which will be necessary to make movies that each contain a single xy position. This step needs to be done using the Nikon NIS Elements software available in shared resources.

1. Open file using Nikon NIS Elements

2. Select File, then ND, then Split Multipoints

3. Click Browse and create a new folder for your split .nd2 files
   ***Use underscores instead of spaces!**
   Later, you will be using a shell environment (Terminal) to run scripts, and it will not handle spaces appropriately
   *Example: mrh1_122110_multipoints

4. Files will be automatically incremented (xy1, xy2, etc.)

5. Transfer split files onto FRED

6. Transfer split files from FRED into a working folder (i.e mrh1_122110) in your Folks folder on the Gottschling lab server

7. At this time, also copy and paste (do not move) makedirectories.sh and all the .py templates (see table of contents on p. 2) you will need into that same working folder

Step 2: Creating directories for converted files (makedirectories.sh)

Because of the huge number of image files that will be generated once an .nd2 file is converted into tiffs, it is necessary to create folders and subfolders to organize your data. You can run a shell script to make all the subfolders you need within each main folder, which you will create:

1. Using Finder, manually create main folders in your working folder in Folks for all the types of files you will eventually create
   *** Use underscores instead of spaces!**
   *Example: mrh1_122110_rawtiffs
   *Example: mrh1_122110_BCtiffs (Brightness/Contrast adjusted)
   *Example: mrh1_122110_maxstacks
   *Example: mrh1_122110_sumstacks
   *Example: mrh1_122110_colormerged
   *Example: mrh1_122110_overlays
   *Example: mrh1_122110_movies

2. Open makedirectories.sh from your working folder using Text Wrangler

3. Open Excel
   a. Excel can be used to quickly increment numbers, i.e. xy1, xy2, xy3
   b. Excel can be used to quickly find and replace changes in folder name, i.e. replacing “rawtiffs” with “BCtiffs”

I suggest making subfolders for every channel for every xy location. For example for rawtiffs, make rawtiffs_green_xy1, 2, 3…, then rawtiffs_red_xy1, 2, 3… then rawtiffs_dic_xy1, 2, 3… Do this for all folders except the colormerged, overlays and movies folders. For the colormerged and overlays folder, you only need to make subfolders for the locations because all the colors/channels will already be combined into a single image.

4. Make commands to make all the subfolders you need in makedirectories.sh in Text Wrangler

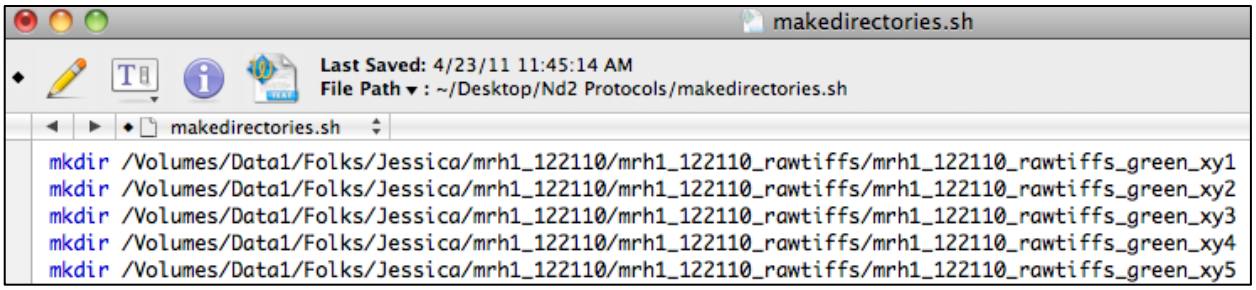

   a. mkdir is the command to make a directory
      i. Note: there must be a space after mkdir and before the location
   b. /Volumes/Data1/Folks/Jessica/mrh1_122110/mrh1_122110_rawtiffs/ is the location of the folder in which you will make subfolders
      i. The location of a folder can be found by copying the folder and pasting in the terminal. The resulting location can then be copied and pasted into Text Wrangler

ii. **Make sure you are NOT logged into the Gottschling lab server yet!**
    1. The paths for the directories you want to create will not match if you are already logged in

c. mrh1_122110_rawtiffs_green_xy1 is the name of the subfolder
    i. Excel can be used to increment these folders quickly
    ii. Copy and paste the entire line into a cell in Excel
    iii. Position your mouse on the bottom right hand corner of that cell until crosshairs appear
    iv. Drag downwards until it has incremented to your last xy location
    v. Copy and paste this into makedirectories.sh in Text Wrangler

d. In Excel, you can use find and replace to make commands for all the other subfolders in that folder, and paste them into makedirectories.sh
    i. Find and replace green to red and dic

e. Now that you have commands to make all the subfolders in one folder, copy and paste that into Excel and use find and replace to make commands for subfolders that go in other folders
    i. Find and replace rawtiffs to BCtiffs or maxstacks, etc.

f. Remember for overlays, you only need subfolders for the locations since all the channels (colors) will already be merged into a single image

g. Save makedirectories.sh

5. Using Finder, find the file makedirectories.sh, which should be in your working folder, in Folks, on the Gottschling server

6. Double click makedirectories.sh
    a. This should bring up a terminal window that says “process complete”
    b. Alternatively, makedirectories.sh can be run from the terminal (if not logged into Gottschling server) by typing: sh, then spacebar, then pasting the location of makedirectories.sh into the terminal

7. Verify that subdirectories were created in all folders intended

Step 2.5: Using ImageJ macro recorder: an example

ImageJ can work in two modes. It has a user interface where tasks can be performed by selecting and clicking functions. ImageJ can also perform the same tasks if given the proper commands in ImageJ Macro Script. The advantages of giving commands by ImageJ Macro Script are that 1) you do not actually have to have ImageJ visibly display images to process them, saving memory, 2) it allows for processing of batches of images in an automated way. ImageJ macro recorder is used to record and display the ImageJ Macro Script commands as the user uses ImageJ. By processing a single image with the macro recorder on, you can get all the ImageJ Macro Script command lines you need to process all of the rest of your images. The reason to use Python is just to iterate the ImageJ macro you recorded. For example, ImageJ macro recorder will give you the ImageJ Macro Script to adjust the brightness/contrast for image xy1_z001, and Python will allow you to generate the ImageJ Macro Script for all other xy positions and all z positions in a text file that can be run through ImageJ through the terminal.

1. Using the terminal, access the Gottschling lab server (the Gottschling lab server has 4 GB memory available and by using that to run everything, it will not affect the computer you are currently on)
    a. Type: ssh gottschlinglab –l jjhsu –X
    b. Use your login after –l
    c. –X, the X must be capitalized
    d. Hit enter
    e. Enter your password, and hit enter again

2. Using Finder, verify that all the folders, subfolders, and .py files that you need are in your working directory in Folks

3. Access that working directory using the terminal
    a. Type: cd /media/Data1/Folks/Jessica (or your Folks folder name)
        i. cd enters you into a directory
    b. Hit enter
    c. Type : ls
        i. ls lists all the contents within the directory you are in
    d. Hit enter
    e. Type: cd, space bar, then the name of your working folder as it appears from the list

```
jjhsu@Gottschling-Server:~$ cd /media/Data1/Folks/Jessica
jjhsu@Gottschling-Server:/media/Data1/Folks/Jessica$ ls
Budscars.ppt          Jessica's Grant Apps     LOH 2009 JH Edits   Nd2_Protocols
Calendar              Jessica's Lab Meetings   Medical School      Papers
Jessica's Classes     Jessica's Meetings       mrh1_122110         Primers
Jessica's Data        Jessica's Protocols      MSTP                Random
jjhsu@Gottschling-Server:/media/Data1/Folks/Jessica$ cd mrh1_122110
jjhsu@Gottschling-Server:/media/Data1/Folks/Jessica/mrh1_122110$
```

4. Open ImageJ from the terminal
    a. Type: imagej –x 3000
    b. This command opens ImageJ using 3000 MB of memory

   c. You should see a program called X11 appear in the dock, and the ImageJ user panel appear on the screen

5. Click Plugins

6. Mouse over Macros, then Record
   *Note: starting now, ImageJ is recording ImageJ Macro Script for EVERY click and EVERY command, so only do what you want ImageJ to do for all images. Be deliberate.

7. Perform all the tasks and functions on a single image that you want performed on all images

8. If you make a mistake, either start over, or note the unintentional commands and remove them later

9. When finished, copy and paste everything from the Macro Recorder into the appropriate Text Wrangler file

10. Use Python to assign ranges for locations, stacks, color, etc.
    a. An example will follow

11. Every line of ImageJ Macro Script command should be preceded by: fout.write(‘

12. Every line of ImageJ Macro Script command should be followed by: \n’)

13. Find and replace specific locations, stacks, or colors, etc. with variables
    a. Example: xy**1** with xy**’+location+’**

14. Save these Text Wrangler files as .py
    a. This .py file should already be in your working folder

15. Select #!, then Run, which will produce a .txt file with all the iterations of the ImageJ commands. This text file will be in the same directory as the .py file
    a. Alternatively, the .py file can be run from terminal if you are logged into the directory containing the .py file, and type: python, then spacebar, then name of the .py file

Again, the goal is to produce commands for ImageJ using ImageJ macro recorder, and then use Python to iterate those commands to all locations, stacks, or colors, etc. A simple example follows for changing the brightness and contrast of an image for multiple locations, and saving it:

ImageJ macro recorder after opening, adjusting brightness/contrast, saving, and closing for one image:

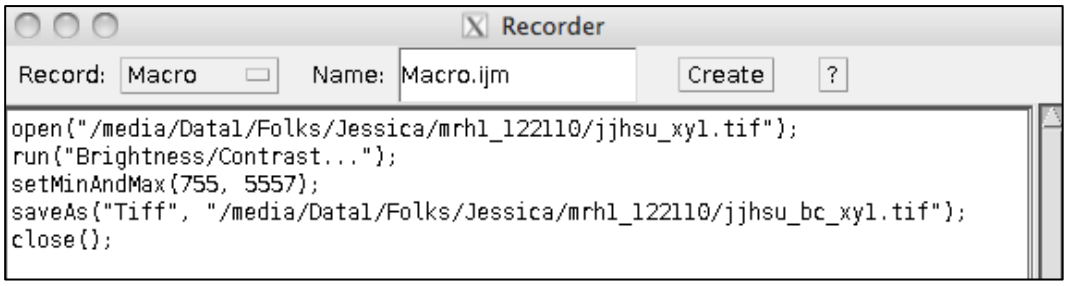

Text Wrangler showing how to use Python to iterate ImageJ commands for ImageJ. This particular example will iterate 20 times, incrementing the xy locations.

```
locations=[]
temploc=range(1,21)
for i in temploc:
    locations.append(str(i))

fout=open("example.txt",'w')

for location in locations:
    fout.write('open("/media/Data1/Folks/Jessica/mrh1_122110/jjhsu_xy'+location+'.tif");\n')
    fout.write('run("Brightness/Contrast...");\n')
    fout.write('setMinAndMax(755, 5557);\n')
    fout.write('saveAs("Tiff", "/media/Data1/Folks/Jessica/mrh1_122110/jjhsu_bc_xy'+location+'.tif");\n')
    fout.write('close();\n')
```

The beginning of the text file produced by running the script shown below. This text file consists of ImageJ Macro Script commands for ImageJ that is repeated for all xy locations, 1-20. Using the terminal, you can then have ImageJ run all the commands in this text file without visibly opening a single image!

example.txt

```
open("/media/Data1/Folks/Jessica/mrh1_122110/jjhsu_xy1.tif");
run("Brightness/Contrast...");
setMinAndMax(755, 5557);
saveAs("Tiff", "/media/Data1/Folks/Jessica/mrh1_122110/jjhsu_bc_xy1.tif");
close();
open("/media/Data1/Folks/Jessica/mrh1_122110/jjhsu_xy2.tif");
run("Brightness/Contrast...");
setMinAndMax(755, 5557);
saveAs("Tiff", "/media/Data1/Folks/Jessica/mrh1_122110/jjhsu_bc_xy2.tif");
close();
open("/media/Data1/Folks/Jessica/mrh1_122110/jjhsu_xy3.tif");
run("Brightness/Contrast...");
```

Step 3: Converting .nd2 files into raw tiffs (Nd2opener.py)

The purpose of this step is to take .nd2 files that have already been split by xy location (step 1) and convert all the images into tiffs. There are two ways to do this: you can do one by hand using ImageJ with macro recorder (recommended), and then incorporate all the commands into Python script as described above (Step 2.5). The second way is to make the appropriate adjustments to an existing script, i.e. change the file names etc.

The first way, which is recommended, will be described below. The second way is noted in the commented version of Nd2opener.py.

1. Verify that all the folders, subfolders, and .py files that you will need are in a common working folder within your Folks folder

2. If not done so already, access the Gottschling server using the terminal
    a. Open terminal
    b. Using the terminal, access the Gottschling lab server
        i. Type: ssh gottschlinglab –l jjhsu –X
        ii. Use your login after –l

iii. –X, the X must be capitalized
iv. Hit enter
v. Enter your password, and hit enter again

c. Access your working directory using the terminal
   i. Type: cd /media/Data1/Folks/Jessica (or your Folks folder name)
      1. cd enters you into a directory
   ii. Hit enter
   iii. Type : ls
      1. ls lists all the contents within the directory you are in
   iv. Hit enter
   v. Type: cd, space bar, then the name of your working folder as it appears from the list

3. Open ImageJ from the terminal
   b. Type: imagej –x 3000
   c. This command opens ImageJ using 3000 MB of memory
   d. You should see a program called X11 appear in the dock, and the ImageJ user panel appear on the screen

4. Select Plugins, Macros, Record

5. Select Plugins, LOCI, Bio-formats Importer
   a. If this plugin is not available, you need to download it

6. Select the first .nd2 file you want to convert (xy1)

7. An Import Options window will pop up
   a. Everything should be **unchecked** with the following exceptions
   b. View stack with: Hyperstack
   c. Color mode: Default
   d. Split channels: checked
   e. Click OK

8. Windows corresponding to each of the channels should appear
   a. It is important to know the order in which you acquired your data
   b. ImageJ numbers the channels starting with 0

9. Select File, Save As, Image Sequence
   a. Format: Tiff
   b. Name: xxxxx_green(or whatever color)_xy1
   c. Digits: 3
   d. Click OK

10. Select rawtiffs folder and appropriate subfolder (xxxxx_rawtiffs_green_xy1)

11. Save

12. Close the window of the channel of images that you just saved as tiffs

13. Repeat with remaining windows (channels)

14. Remember to close last window after saving the last channel as tiffs

15. Copy and paste ImageJ Macro Script commands from the Macro Recorder into a Nd2opener.py template

16. Follow directions from Step 2.5 #7-12
    a. Remember to tell it the range of locations, i.e xy 1-4 means range (1,5)
    b. Remember to give the output text file a name
    c. Remember to replace all xy**1** with xy**'+location+'** to increment
    d. Remember to save
    e. Remember to run the script
    f. Verify that an output text file is generated in the working folder

17. Go back to the terminal (it should still be logged into your working folder in Folks)
    a. If it is not, see #2
    b. If ImageJ is running, hit control z to stop ImageJ

18. Execute Nd2opener.txt using ImageJ though the terminal
    a. Type: imagej –x 3000 –b Nd2opener.txt
    b. imagej –x 3000 means to use imageJ with 3000 MB memory
    c. –b means batch
    d. Nd2opener.txt is the text file that contains iterated ImageJ commands
    e. Hit enter
    f. The terminal should look like this:

```
jjhsu@Gottschling-Server:/media/Data1/Folks/Jessica/mrh1_122110$ imagej -x 3000
-b Nd2opener.txt
Open other images in this ImageJ panel as follows:
  imagej -p 1 <image1> [<image2> ... <imageN>]

log4j:WARN No appenders could be found for logger (loci.common.NIOByteBufferProv
ider).
log4j:WARN Please initialize the log4j system properly.
```

19. As you wait, you can use Finder to look to see if tiffs are being saved where they should be, but do not attempt to open any files until ImageJ is finished converting all files.

20. When the task is completed, the terminal will return to this:

```
jjhsu@Gottschling-Server:/media/Data1/Folks/Jessica/mrh1_122110$
```

Step 4: Adjusting the brightness and contrast of raw tiffs (BCadjuster.py)

The purpose of this step is to adjust the brightness and contrast of the raw tiffs created from the .nd2 file. This step is separate because the raw images should be retained if additional adjustments are to be made later. This step is necessary as the raw images are often not at optimal brightness and/or contrast. The levels of adjustments are determined manually by taking a few images from each channel (preferably from the middle of a stack) and adjusting the brightness and contrast until the image looks as desired. These settings are then recorded and placed in the script such that every image from that channel is adjusted in the exact same way.

1. Open ImageJ using the terminal, as described before
    a. Type: imagej –x 3000
    b. This command opens ImageJ using 3000 MB of memory
    c. You should see a program called X11 appear in the dock, and the ImageJ user panel appear on the screen

2. Open one or two raw tiffs, preferably from the middle of a stack

3. Adjust the brightness and contrast to your liking
    a. Select Image, Adjust, Brightness/Contrast
    b. Adjust image using arrows or scroll bar
    c. Click Set
    d. Record the two numbers that are displayed

4. Repeat for one or two tiffs in every channel

5. Close all images

6. Select Plugins, Macros, Record

7. Select File, Import, Image Sequence

8. Select the first raw tiff in one channel
    a. For example, mrh1_122110_green_xy1_t001_z001.tif

9. A sequence options window will pop up, click OK

10. Select Image, Adjust, Brightness/Contrast

11. Click Set, enter numbers you previously recorded for this channel

12. Select File, Save As, Image Sequence

13. **Select “Use slice labels as file names”, click OK**

14. Select the appropriate directory for saving your brightness/contrast adjusted tiff
    a. For example, mrh1_122110_BCtiffs_green_xy1

15. Click Save

16. Close that image

17. Repeat for the first image in every channel

18. After closing last image, copy and paste all commands from the Macro Recorder into a BCadjuster.py template
    a. Remember BCadjuster.py must be in your working folder

19. Follow directions from Step 2.5 #7-12
    a. Remember to tell it the range of locations, i.e xy 1-4 means range (1,5)
    b. Remember to give the output text file a name
    c. Remember to replace all xy**1** with xy**'+location+'** to increment
    d. Remember to save, then run

20. Go back to the terminal (it should still be in your working folder in Folks)

21. Execute BCadjuster.txt using ImageJ though the terminal
    a. Type: imagej –x 3000 –b BCadjuster.txt
    b. Hit enter

22. Verify that images are located and look as expected

Step 5: Creating projections from multiple Z stacks (Maxstacker.py and Sumstacker.py)

The purpose of this step is to make projections from images taken at the same location and time, but in different planes. Scripts have been written to make two types of projections: maximum intensity projections and sum slice projections. A maximum intensity projection is the image that is created when each pixel location takes on the intensity of the most intense pixel for that location considering all images in a stack. A sum slice projection is the image that is created when all the images in a stack are summed. Projections should only be made from the colored channels here. Brightfield or DIC images will be overlayed onto these projections in Step 7.

1. Open ImageJ using the terminal, as described before
    a. Type: imagej –x 3000
    b. This command opens ImageJ using 3000 MB of memory
    c. You should see a program called X11 appear in the dock, and the ImageJ user panel appear on the screen

2. Select Plugins, Macros, Record

3. Select File, Import, Image Sequence

4. Select first image in BCtiffs
    a. Example: mrh1_122110_green_xy1_t001_z001

5. A sequence options window should appear
    a. Under “Number of images” enter the number of planes in each stack
        i. Example: 7
    b. Under “File Name Contains” enter t001
    c. Sort Names Numerically should be the only box that is checked
    d. Click OK

6. Select Image, Stacks, Z project…

7. Z projection window should appear
    a. Start slice should be 1
    b. Stop slice should be the number of stacks acquired for each location
    c. Projection type:
        i. Max intensity if doing maxstacks
        ii. Sum Slices if doing sumstacks
    d. Click OK

8. The image of the projection should appear

9. Select File, Save As, Tiff
    a. Select appropriate folder
        i. Example mrh1_122110_maxstacks_green_xy1
    b. Alter the file name so that it reflects time and does not say BCtiffs
        i. Example MAX_mrh1_122110_green_xy1_t001
    c. Click Save

10. Close both windows

11. After closing last image, copy and paste all commands from the macro recorder into a Maxstacker.py or Sumstacker.py template
    a. Remember Maxstacker.py or Sumstacker.py must be in your working folder

12. Follow directions from Step 2.5 #7-12
    a. Remember to tell it the range of locations, i.e xy 1-4 means range (1,5)
    b. Remember to give the output text file a name
    c. Remember to replace all xy**1** with xy**'+location+'** to increment
    d. Remember to replace all t0**01** with t0**'+time+'** to increment
    e. Remember to give it all the colors you are using
        i. Example: 'red', 'green'
    f. Remember to save, then run

13. Go back to the terminal (it should still be in your working folder in Folks)

14. Execute Maxstacker.txt or Sumstacker.txt using ImageJ though the terminal
    a. Type: imagej –x 3000 –b Maxstacker.txt (or Sumstacker.txt)
    b. Hit enter

15. Verify that images are located and look as expected

Step 6: Merging channels (Colormerger.py)

The purpose of this step is to combine images from different channels (colors) into a single image. Note that merging two channels reduces the intensity of each of those channels by half. Merging three channels reduces the intensity of each channel by a third, etc. This can be compensated for by multiplying the image by 2 or 3, depending on how many channels are being merged together (optional steps #10, 11).

1. Open ImageJ using the terminal, as described before
    a. Type: imagej –x 3000
    b. This command opens ImageJ using 3000 MB of memory
    c. You should see a program called X11 appear in the dock, and the ImageJ user panel appear on the screen

2. Select Plugins, Macros, Record

3. Select File, Open, first projection in one channel
    a. Example: MAX_mrh1_122110_green_xy1_t001

4. Select File, Open, first projection in the next channel, etc.
    a. Example: MAX_mrh1_122110_red_xy1_t001

5. Select Image, Color, Merge Channels

6. Color Merge window should appear
    a. Red: Select red projection file
    b. Green: Select green projection file
    c. Do for all channels you have color for
    d. Make sure that channels you do not have say *None*
    e. Create Composite should be the only thing checked
    f. Click OK

7. The composite image should appear

8. Select Image, Overlay, Flatten

9. A new flattened image should appear

10. (optional) Select Process, Math, Multiply

11. (optional) Multiply window should appear
    a. Multiply by the number of channels you are merging together
    b. Example: red and green merge, multiply by 2
    c. Click OK

12. Select File, Save As, Tiff
    a. Select appropriate folder
        i. For example: mrh1_122110_colormerged_xy1
    b. Enter file name
        i. For example: MAX_mrh1_122110_colormerged_xy1_t001

   c. Click Save

13. Close all windows

14. Repeat steps 3-13 for sum sum slices projections

15. Remember to close all windows

16. After closing last image, copy and paste all commands from the Macro Recorder into a Colormerger.py template
    a. Remember Colormerger.py must be in your working folder

17. Follow directions from Step 2.5 #7-12
    a. Remember to tell it the range of locations, i.e xy 1-4 means range (1,5)
    b. Remember to give the output text file a name
    c. Remember to replace all xy**1** with xy**'+location+'** to increment
    d. Remember to replace all t0**01** with t0**'+time+'** to increment
    e. Remember to save, then run

18. Go back to the terminal (it should still be in your working folder in Folks)

19. Execute Colormerger.txt using ImageJ though the terminal
    a. Type: imagej –x 3000 –b Colormerger.txt
    b. Hit enter

20. Verify that images are located and look as expected

Step 7: Creating overlays with DIC or brightfield images (Overlayer.py)

The purpose of this step is to overlay brightfield or DIC images over color-combined projections. This is usually done so the boundaries of the cells are apparent.

1. Open ImageJ using the terminal, as described before
    a. Type: imagej –x 3000
    b. This command opens ImageJ using 3000 MB of memory
    c. You should see a program called X11 appear in the dock, and the ImageJ user panel appear on the screen

2. Select Plugins, Macros, Record

3. Select File, Open, first dic image in BCtiffs **(z should be the home slice!)**
    a. Example: mrh1_122110_dic_xy1_t001_z004 (if 7 slices total)

4. Select File, Open, first colormerged image
    a. Example: MAX_mrh1_122110_colormerged_xy1_t001

5. Select Image, Overlay, Add Image

6. Add Image window should appear
    a. X should be 0
    b. Y should be 0
    c. Opacity: 15% (however much you want your brightfield image to show)
    d. Create Image Selection should be checked
    e. Click OK

7. Select Image, Overlay, Flatten

8. Select File, Save As, Tiff
    a. Select the appropriate folder
        i. Example: mrh1_122110_overlay_xy1
    b. Enter the file name
        i. Example: MAX_mrh1_122110_overlay_xy1_t001
        ii. The time is important!
    c. Click Save

9. Close all windows except original DIC image

10. Repeat steps 4-8 with the SUM colormerged file

11. Close all images

12. After closing last image, copy and paste all commands from the macro recorder into a Colormerger.py template
    a. Remember Colormerger.py must be in your working folder

13. Follow directions from Step 2.5 #7-12
    a. Remember to tell it the range of locations, i.e xy 1-4 means range (1,5)

b. Remember to give the output text file a name
c. Remember to replace all xy**1** with xy**'+location+'** to increment
d. Remember to replace all t0**01** with t0**'+time+'** to increment
e. Remember to save, then run

14. Go back to the terminal (it should still be in your working folder in Folks)

15. Execute Overlayer.txt using ImageJ though the terminal
    a. Type: imagej –x 3000 –b Overlayer.txt
    b. Hit enter

16. Verify that images are located and look as expected

Step 8: Creating movies (Moviemaker.py)

The purpose of this step is to create .avi movies from all the colormerged images and overlayed images of both types of projections: sum slice projections and maximum intensity projections.

1. Open ImageJ using the terminal, as described before
    a. Type: imagej –x 3000
    b. This command opens ImageJ using 3000 MB of memory
    c. You should see a program called X11 appear in the dock, and the ImageJ user panel appear on the screen

2. Select Plugins, Macros, Record

3. Select File, Import, Image Sequence, open first MAX colormerged file
    a. Example: MAX_mrh1_122110_colormerged_xy1_t001

4. Sequence options window should appear
    a. Number of images: enter the number of timepoints you acquired
    b. File contains: MAX
    c. Sort numerically should be checked
    d. Click OK

5. Select File, Save As, AVI

6. Save AVI window should appear
    a. Compression: uncompressed
    b. JPEG quality: 100
    c. Frame Rate: 2 fps
    d. Click OK

7. Find the appropriate folder
    a. Example: mrh1_122110_movies

8. Change the file name
    a. Example: MAX_mrh1_122110_colormerged_xy1
    b. Save

9. Close windows

10. Repeat steps 3-8 with SUM colormerged file, MAX overlay file, and SUM overlay file
    a. Remember to enter the appropriate SUM or MAX in the sequence options window when importing the image sequence
    b. Remember to alter the file name being saved appropriately
11. After closing last image, copy and paste all commands from the macro recorder into a Moviemaker.py template
    a. Remember Moviemaker.py must be in your working folder

12. Follow directions from Step 2.5 #7-12
    a. Remember to tell it the range of locations, i.e xy 1-4 means range (1,5)
    b. Remember to give the output text file a name

c. Remember that the dic image should be from the middle of the stack, i.e. z004 if 7 slices were taken
d. Remember that the number of images imported should be the number of timepoints acquired
e. Remember to save, then run

13. Go back to the terminal (it should still be in your working folder in Folks)

14. Execute Moviemaker.txt using ImageJ though the terminal
    a. Type: imagej –x 3000 –b Moviemaker.txt
    b. Hit enter

15. Verify that movies are located and look as expected

Appendix G: Strains, primers, and plasmids

Chapter II strains

Strain	Strain Description	Source	Genotype
UCC8773	MEP haploid mat a	Lindstrom	*MATa his3D1 leu2D0 ura3D0 lys2D0 hoD::SCW11pr-Cre-EBD78-NATMX loxP-CDC20-Intron-loxP-HPHMX loxP-UBC9-loxP-LEU2*
UCC8774	MEP haploid mat α	Lindstrom	*MAT@ his3D1 leu2D0 ura3D0 trp1D63 hoD::SCW11pr-Cre-EBD78-NATMX loxP-CDC20-Intron-loxP-HPHMX loxP-UBC9-loxP-LEU2*
UCC4925	MEP diploid	Hughes	*Mat a/@ his3D1/his3D1 leu2D0/leu2D0 lys2D0/LYS2 TRP1/trp1d63 ura3D0/ura3D0 hoD::SCW11pr-Cre-EBD78-NatMX/hoD::SCW11pr-Cre-EBD78-NatMX loxP-UBC9-loxP-LEU2/loxP-UBC9-loxP-LEU2 loxP-CDC20-Intron-loxP-HPHMX/loxP-CDC20-Intron-loxP-HPHMX*
Basic MEP genotype			*Mat a/@ his3D1/his3D1 leu2D0/leu2D0 ura3D0/ura3D0 hoD::SCW11pr-Cre-EBD78-NatMX/hoD::SCW11pr-Cre-EBD78-NatMX loxP-UBC9-loxP-LEU2/loxP-UBC9-loxP-LEU2 loxP-CDC20-Intron-loxP-HPHMX/loxP-CDC20-Intron-loxP-HPHMX*
UCC9522	Ymr295cp-GFP	Henderson GFP collection	*MATa/@ his3/his3 leu2/leu2 met15/met15 ura3D0/ura3DΔ0 hoD::SCW11pr-Cre-EBD78-NatMX/hoD::SCW11pr-Cre-EBD78-NatMX loxP-UBC9-loxP-LEU2/loxP-UBC9-loxP-LEU2 loxP-CDC20-Intron-loxP-HPHMX/loxP-CDC20-Intron-loxP-HPHMX YMR295C-GFP-HIS3MX/YMR295C-GFP-HIS3MX*
UCC10006	Bni4p-GFP	GFP collection	Basic MEP + *BNI4-GFP-HIS3MX/BNI4-GFP-HIS3MX*
UCC10297	Cdc10p-GFP		UCC4925 + *CDC10-GFP-KANMX/CDC10-GFP-KANMX*
UCC10298	Cdc11p-GFP		UCC4925 + *CDC11-GFP-KANMX/CDC11-GFP-KANMX*
UCC10299	Cdc12p-GFP		UCC4925 + *CDC12-GFP-KANMX/CDC12-GFP-KANMX*
UCC5418	Cin8p-GFP	Nelson GFP collection	Basic MEP + *CIN8-GFP-HIS3MX/CIN8-GFP-HIS3MX*
UCC10004	Dyn1p-GFP	GFP collection	Basic MEP + *DYN1-GFP-HIS3MX/ DYN1-GFP-HIS3MX*
UCC9533	Kip3p-GFP	Henderson GFP collection	*MATa/@ his3/his3 leu2/leu2 trp1D63/TRP1 met15/met15 ura3D0/ura3DΔ0 hoD::SCW11pr-Cre-EBD78-NatMX/hoD::SCW11pr-Cre-EBD78-NatMX loxP-UBC9-loxP-LEU2/loxP-UBC9-loxP-LEU2 loxP-CDC20-Intron-loxP-HPHMX/loxP-CDC20-Intron-loxP-HPHMX KIP3-GFP-HIS3MX/KIP3-GFP-HIS3MX*
UCC5411	Abp140p-GFP	Nelson GFP collection	Basic MEP + *ABP140-GFP-HIS3MX/ABP140-GFP-HIS3MX*
UCC4957	Hof1p-GFP	GFP collection	Basic MEP + *HOF1-GFP-HIS3MX/HOF1-GFP-HIS3MX*
UCC10002	Myo1p-GFP	GFP collection	Basic MEP + *MYO1-GFP-HIS3MX/MYO1-GFP-HIS3MX*

Chapter II strains (cont.)

Strain	Strain Description	Source	Genotype
UCC9520	Sac6p-GFP	Henderson GFP collection	*MATa/@ his3/his3 leu2/leu2 met15/met15 ura3D0/ura3DΔ0 hoD::SCW11pr-Cre-EBD78-NatMX/hoD::SCW11pr-Cre-EBD78-NatMX loxP-UBC9-loxP-LEU2/loxP-UBC9-loxP-LEU2 loxP-CDC20-Intron-loxP-HPHMX/loxP-CDC20-Intron-loxP-HPHMX SAC6-GFP-HIS3MX/SAC6-GFP-HIS3MX*
UCC10080	Cap1p-GFP		UCC4925 + *CAP1-GFP-KANMX/CAP1-GFP-KANMX*
UCC10121	GFP-Cap2p		UCC4925 + *GFP-CAP2/GFP-CAP2*
UCC10016	Htb1p-GFP	GFP collection	Basic MEP + *HTB1-GFP-HIS3MX/HTB1*
UCC10014	Hhf2p-GFP	GFP collection	Basic MEP + *HHF2-GFP-HIS3MX/HHF2*
UCC10303	Nup1p-GFP		UCC4925 + *NUP1-GFP-KANMX/NUP1-GFP-KANMX*
UCC3469	Nup49p-GFP	Nelson GFP collection	Basic MEP + *NUP49-GFP-HIS3MX/NUP49-GFP-HIS3MX*
UCC10664	Nup82p-GFP		UCC4925 + *NUP82-GFP-KANMX/NUP82-GFP-KANMX*
UCC10666	Nup188p-GFP		UCC4925 + *NUP188-GFP-KANMX/NUP188-GFP-KANMX*
UCC10662	Nic96p-GFP		UCC4925 + *NIC96-GFP-KANMX/NIC96-GFP-KANMX*
UCC10670	GFP-Pus1p		*MATa/@ his3D1/his3D1 leu2D0/leu2D0 ura3D0/ura3D0 LYS2/lys2d0 trp1D63/TRP1 hoD::SCW11pr-Cre-EBD78-NATMX/hoD::SCW11pr-Cre-EBD78-NATMX loxP-CDC20-Intron-loxP-HPHMX/loxP-CDC20-Intron-loxP-HPHMX loxP-UBC9-loxP-LEU2/loxP-UBC9-loxP-LEU2 GFP-PUS1/GFP-PUS1*
UCC3449	Sec21p-GFP	Nelson GFP collection	Basic MEP + *SEC21-GFP-HIS3MX/SEC21-GFP-HIS3MX*
UCC10054	Glo3p-GFP	GFP collection	Basic MEP + *GLO3-GFP-HIS3MX/GLO3-GFP-HIS3MX*
UCC10052	Sec27p-GFP	GFP collection	Basic MEP + *SEC27-GFP-HIS3MX/SEC27-GFP-HIS3MX*
UCC10084	Sec28p-GFP		UCC4925 + *SEC28-GFP-KANMX/ SEC28-GFP-KANMX*
UCC10159	Sec23p-GFP		UCC4925 + *SEC23-GFP-KANMX/ SEC23-GFP-KANMX*
UCC10165	Sec24p-GFP		UCC4925 + *SEC24-GFP-KANMX/ SEC24-GFP-KANMX*
UCC9482	Sec13p-GFP	GFP collection	Basic MEP + *SEC13-GFP-HIS3MX/SEC13-GFP-HIS3MX*
UCC5435	Sec31p-GFP	Nelson GFP collection	Basic MEP + *SEC31-GFP-HIS3MX/SEC31-GFP-HIS3MX*
UCC3467	Ncp1p-GFP	Nelson GFP collection	Basic MEP + *NCP1-GFP-HIS3MX/NCP1-GFP-HIS3MX*
UCC5426	Nsg1p-GFP	Nelson GFP collection	Basic MEP + *NSG1-GFP-HIS3MX/NSG1-GFP-HIS3MX*

Chapter II strains (cont.)

Strain	Strain Description	Source	Genotype
UCC10115	Hmg1p-GFP	Maho Niwa	*MATa/@ ADE2/ade2-1 leu2-3,112/leu2-3,112 trp1-1/trp1-1 can1-100/can1-100 ura3-1::HMG1-GFP-URA3/ura3-1::HMG1-GFP-URA3 his3-11,15/his3-11,15 hoΔ::SCW11pr-CRE-EBD78-NatMX/hoΔ::SCW11pr-CRE-EBD78-NatMX loxP-CDC20-Intron-loxP-HPHMX/loxP-CDC20-Intron-loxP-HPHMX loxP-UBC9-loxP-LEU2/loxP-UBC9-loxP-LEU2*
UCC5428	Hmg2p-GFP	Nelson GFP collection	Basic MEP + *HMG2-GFP-HIS3MX/HMG2-GFP-HIS3MX*
UCC9496	Erg4p-GFP	GFP collection	Basic MEP + *ERG4-GFP-HIS3MX/ERG4-GFP-HIS3MX*
UCC10189	Sec61p-GFP		UCC4925 + *SEC61-GFP-KANMX/ SEC61-GFP-KANMX*
UCC10193	Sec63p-GFP		UCC4925 + *SEC63-GFP-KANMX/ SEC63-GFP-KANMX*
UCC10139	ss-GFP-HDEL		UCC4925 + *CHRI(199456-199457)::SS-GFP-HDEL-URA3/CHRI(199456-199457)::SS-GFP-HDEL-URA3*
UCC10197	Sec7p-GFP		UCC4925 + *SEC7-GFP-KANMX/ SEC7-GFP-KANMX*
UCC9494	Och1p-GFP	GFP collection	Basic MEP + *OCH1-GFP-HIS3MX/OCH1-GFP-HIS3MX*
UCC5436	Ric1p-GFP	Nelson GFP collection	Basic MEP + *RIC1-GFP-HIS3MX/RIC1-GFP-HIS3MX*
UCC5440	Rgp1-GFP	Nelson GFP collection	Basic MEP + *RGP1-GFP-HIS3MX/RGP1-GFP-HIS3MX*
UCC10058	Vrg4p-GFP	GFP collection	Basic MEP + *VRG4-GFP-HIS3MX/VRG4-GFP-HIS3MX*
UCC5442	Erg6p-GFP	Nelson GFP collection	Basic MEP + *ERG6-GFP-HIS3MX/ERG6-GFP-HIS3MX*
UCC9484	Erg7p-GFP		UCC4925 + *ERG7-GFP-KANMX/ERG7-GFP-KANMX*
UCC9535	Pil1p-GFP	Henderson GFP collection	*MATa/@ his3/his3 leu2/leu2 met15/met15 ura3D0/ura3DΔ0 hoD::SCW11pr-Cre-EBD78-NatMX/hoD::SCW11pr-Cre-EBD78-NatMX loxP-UBC9-loxP-LEU2/loxP-UBC9-loxP-LEU2 loxP-CDC20-Intron-loxP-HPHMX/loxP-CDC20-Intron-loxP-HPHMX PIL1-GFP-HIS3MX/PIL1-GFP-HIS3MX*
UCC9517	Sur7p-GFP	Henderson GFP collection	*MATa/@ his3/his3 leu2/leu2 met15/met15 ura3D0/ura3DΔ0 hoD::SCW11pr-Cre-EBD78-NatMX/hoD::SCW11pr-Cre-EBD78-NatMX loxP-UBC9-loxP-LEU2/loxP-UBC9-loxP-LEU2 loxP-CDC20-Intron-loxP-HPHMX/loxP-CDC20-Intron-loxP-HPHMX SUR7-GFP-HIS3MX/SUR7-GFP-HIS3MX*
UCC9498	Hse1p-GFP	GFP collection	Basic MEP + *HSE1-GFP-HIS3MX/HSE1-GFP-HIS3MX*
UCC5424	Snf7p-GFP	Nelson GFP collection	Basic MEP + *SNF7-GFP-HIS3MX/SNF7-GFP-HIS3MX*
UCC5444	Kex2p-GFP	Nelson GFP collection	Basic MEP + *KEX2-GFP-HIS3MX/KEX2-GFP-HIS3MX*
UCC10082	Nhx1p-GFP		UCC4925 + *NHX1-GFP-KANMX/ NHX1-GFP-KANMX*

Chapter II strains (cont.)

Strain	Strain Description	Source	Genotype
UCC5489	Fet3p-GFP	Nelson GFP collection	Basic MEP + *FET3-GFP-HIS3MX/FET3-GFP-HIS3MX*
UCC5408	Hxt2p-GFP	Nelson GFP collection	Basic MEP + *HXT2-GFP-HIS3MX/HXT2-GFP-HIS3MX*
UCC3471	Ylr413wp-GFP	Nelson GFP collection	Basic MEP + *YLR413W-GFP-HIS3MX/YLR413W-GFP-HIS3MX*
UCC10141	Mrh1p-GFP		UCC4925 + *MRH1-GFP-KANMX/ MRH1-GFP-KANMX*

Chapter II primers

Primer name	Primer sequence
GFP check	GTAAGTAGCATCACCTTCACCTTC
Cdc10 pKT F	TCGTTCCTCAGCTCATATGTCTAGCAACGCCATTCAACGTGGTGACGGTGCTGGTTTA
Cdc10 pKT R	AATAACATAAGATATATAATCACCACCATTCTTATGAGATTCGATGAATTCGAGCTCG
Cdc10 pKT check	TACCAGTTATTGGCAAGTCGGATACATTGA
Cdc11 pKT F	AGCCAGGTTGGAAAAAGAGGCGAAAATCAAACAGGAAGAAGGTGACGGTGCTGGTTTA
Cdc11 pKT R	ATAGAGAAAGAAGAAATAAGTGAGGAAGCCAAAAGCGGACTCGATGAATTCGAGCTCG
Cdc11 pKT check	CATGGGGCATACTGGACGTGGAAGATTCAT
Cdc12 pKT F	GCAGGTCAAAAGCTTGCAAGTAAAAAAATCCCATTTAAAAGGTGACGGTGCTGGTTTA
Cdc12 pKT R	TTGAAATTGACGAGACAAAGAGGAAGACATTAATTAATCATCGATGAATTCGAGCTCG
Cdc12 pKT check	CAAGGCACTCAGGTAGTTGCAAGGAAGTAT
Cap1 GFP F	TGGCAGTTATAGATTGGGTAAGAATGCGGCAGAAGGCAAAGGTGACGGTGCTGGTTTA
Cap1 GFP R	AAGAAATAGGAAGAGAATGGAATAAGGCAGGCATGAAATTTCGATGAATTCGAGCTCG
Cap1 GFP check	GATGTCAGTTTTGCTGTTTACCCAG
Cap2 upstream	CTTGCTAAACGATTTGCCCAGAC
Cap2 downstream	GCAGAATGATTGTAGTGGTGACTCT
5’ GFP Cap2 R	AATTCTTCACCTTTAGACATTACGGTGGTGATTGTAGAGTTGGA
3’ GFP Cap2 F	GGTATGGATGAATTGTACAAATCTGATGCTCAATTCGATGCTGCT
Nup1 pKT F	GGCGAACAGAAAGATTGCAAGAATGAGGCACTCTAAAAGGGGTGACGGTGCTGGTTTA
Nup1 pKT R	TTCAGAAAAGCAACACAATACCTAATTACATAACCGATATTCGATGAATTCGAGCTCG
Nup1 check	TATGAACGGCAACACTAATGCTAATACGGT
Nup82 F5	ATTGTTACAAGTTTCTCAGGAATTTACTACTAAAACTCAAGGTGACGGTGCTGGTTTA
Nup82 R3	TAGCGTACATATATGATAGCAGACTATGCAAGTCGCTTACTCGATGAATTCGAGCTCG
Nup82 check	TCCACAATAGAATTCATGAGCAACAGTTCG
Nup188 F5	AGACATTAAAGCATTACAAGATTCACTATTTAAGGACGTTGGTGACGGTGCTGGTTTA
Nup188 R3	ATTATTATATTATGTAGCTTTACATAACCTGCAAAATAAGTCGATGAATTCGAGCTCG
Nup188 check	ATATAACTGGGGTGACAACAAGTTAGCAGT
Nic96 F5	GGAAACGTACAGCACTTTAATTAATATAGACGTCTCTCTAGGTGACGGTGCTGGTTTA
NIc96 R3	ATATATAGATATAAACAAAAATATACAATATTTAAAAAAATCGATGAATTCGAGCTCG
Nic96 check	GGTTGGACCTGATGACAATAGCGAGACGAA
Pus1 upstream	AATACCCAGAGACATCAAGTTAGGTCTTGC
Pus1 downstream	TGATCTTCTGCTTGATATCAGGATCTTCAA
3’ GFP Pus1 F	GGTATGGATGAATTGTACAAATCTGAAGAGAATTTGAGGCCTGCC
5’ GFP Pus1 R	AATTCTTCACCTTTAGACATCCTTGATATCACTTATAATTGTTA
Sec28 GFP F	CAAAATTCGATGAATTAGTGAGGAAATATGATACGTCCAACGGTGACGGTGCTGGTTTA
Sec28 GFP R	TCTAAAAAACCTACATGTTTAATGTGAGATATTACGTAAATCGATGAATTCGAGCTCG
Sec28 GFP check	GCAACATCCAACTTTTACTACTATGAAG
Sec23 GFP F	CCTAATAACGATCAAATAAAACAAAAGAAAGCCGTTGCTCTCGATGAATTCGAGCTCG
Sec23 GFP R	CATGACTCACTTACAACAAGTAGCCGTCTCTGGTCAGGCAGGTGACGGTGCTGGTTTA
Sec23 GFP check	CAACCAACTCTAACTTCTTTCTCAATG
Sec24 GFP F	AAAATATACAGTTTCTTTTTATCATTGATTCCCTTTTAGCCTCGATGAATTCGAGCTCG
Sec24 GFP R	CAGAGAATTCTTACAAATCATGAAAGCCAGAATTAGCAAAGGTGACGGTGCTGGTTTA
Sec24 GFP check	ATACTTGATAGATAATGGTAACGAAT

Chapter II primers (cont.)

Primer name	Primer sequence
Sec61 GFP F	ATGCGATTTTTTTTTTCTTTGGATATTATTTTCATTTTATATTCGATGAATTCGAGCTCG
Sec61 GFP R	GGGTTTACTAAGAACCTCGTTCCAGGATTTTCTGATTTGATGGGTGACGGTGCTGGTTTA
Sec61 GFP check	ATCATTCCAACTGCTGCTGCTTTC
Sec63 GFP F	TCTAAGAGCTAAAATGAAAAACTATACTAATCACTTATATTCGATGAATTCGAGCTCG
Sec63 GFP R	ATACGGATACAGAAGCTGAAGATGATGAATCACCAGAAGGTGACGGTGCTGGTTTAATTA
Sec63 GFP check	CAAAAAGATGGTAAAATACTTCAAACGCC
ChrI Part A NotI F	GTCCCATTCGAAGAAGCGGCCGCTTTAGCTCATTGAGATATGTG
ChrI Part A SmaI R	GTATTCTACGACCCCGGGGGTGCTAATTATGGCATTGAT
ChrI Part B SmaI F	CGTCAATGCAAGCCCGGGCCATGGATGGTCGTTTAAGGC
ChrI Part B NotI R	TCTCAATGAGCTAAAGCGGCCGCTTCTTCGAATGGGACCAGCTA
Sec7 GFP F	AACTAAGCATATTTTAATCTGCTGGACCATTCAACAAAGCCTCGATGAATTCGAGCTCG
Sec7 GFP R	CAATTTCTAAGCAGAGTTGGTGAATTATACCTTTCTACTGATGGTGACGGTGCTGGTTTA
Sec7 GFP check	GTAGTATCAATGCCTGGCGTTCAG
Erg7 pKT F	ATTAGGTATGTACAGCAGGGCATATGAAACACATACGCTTGGTGACGGTGCTGGTTTA
Erg7 pKT R	TCTAATTGTTGCAGCCTCTAACAACACTTATAAATAAAACTCGATGAATTCGAGCTCG
Erg7 check	GGTCAGTAAACAGATGAAGGATGG
Nhx1 GFP F	GGCTACGCAATCACCTGCAGATTTCTCTTCCCAAAACCACGGTGACGGTGCTGGTTTA
Nhx1 GFP R	ATATTTATATTAGAAACAAGGAAACCATACACTTTAAAGTTCGATGAATTCGAGCTCG
Nhx1 GFP check	CAGTAACAAGAATCTCCCCAATAAC
Mrh1 F5	GAAGAGCAAGAAATCTAAGAAGTCTAAGAAGTCTGAAGAAGGTGACGGTGCTGGTTTA
Mrh1 R3	AGAAAGAAGAAAGTAGCACATAATTGACATGACGATTGGCTCGATGAATTCGAGCTCG
Mrh1 check	AATGGGGTTACTACACCATCGGTCTAGGTG

Chapter II plasmids

Plasmid	Source	Plasmid Description
pKT127	Euroscarf	pFA6a-link-yEGFP-KAN
GFP 3' ura3 upstream	Gottschling	Contains 3' portion of *URA3* upstream of *GFP* For N-terminal fusion
GFP 5' ura3 downstream	Gottschling	Contains 5' portion of *URA3* downstream of *GFP* For N-terminal fusion
pAG306gal-ccdB	Addgene	pAdvanced Gateway Destination Vector, integrating plasmid containing *URA3* selectable marker, ccdB lethal gene, and inducible *GAL1* promoter
pAG306gal-ccdB chrI	See Appendix C	pAG306gal-ccdB chrI was constructed from pAG306GAL-ccdB, and is designed for integration into Chromosome I (199456-199457) following NotI digestion of the plasmid
YIPlac204TKC-GFP-HDEL	Addgene	Plasmid contains ss-GFP-HDEL construct used for visualizing ER lumen. Plasmid originally from Glick lab.
pAG306 ss-GFP-HDEL chrI int	See Appendix C	Integrating plasmid that inserts SS-GFP-HDEL into Chromosome I (199456-199457) when digested with NotI and transformed. This plasmid was constructed by digesting pAG306gal ccDB ChrI with NaeI and AatII and ligating with YIPlac204TKC-GFP-HDEL digested with SfoI and AatII

Chapter III strains

Strain	Strain Description	Source	Genotype
UCC4925	MEP diploid	Hughes (2012)	*Mat a/@ his3D1/his3D1 leu2D0/leu2D0 ura3D0/ura3D0 hoD::SCW11pr-Cre-EBD78-NatMX/hoD::SCW11pr-Cre-EBD78-NatMX loxP-UBC9-loxP-LEU2/loxP-UBC9-loxP-LEU2 loxP-CDC20-Intron-loxP-HPHMX/loxP-CDC20-Intron-loxP-HPHMX*
Basic MEP genotype			*Mat a/@ his3D1/his3D1 leu2D0/leu2D0 ura3D0/ura3D0 hoD::SCW11pr-Cre-EBD78-NatMX/hoD::SCW11pr-Cre-EBD78-NatMX loxP-UBC9-loxP-LEU2/loxP-UBC9-loxP-LEU2 loxP-CDC20-Intron-loxP-HPHMX/loxP-CDC20-Intron-loxP-HPHMX*
UCC10000	Nop58p-GFP	GFP collection	Basic MEP + *NOP58-GFP-HIS3MX/NOP58-GFP-HIS3MX*
UCC5420	Ssf1p-GFP	Nelson GFP collection	Basic MEP + *SSF1-GFP-HIS3MX/SSF1-GFP-HIS3MX*
UCC10458	Pex11p-GFP		UCC4925 + *PEX11-GFP-KANMX/ PEX11-GFP-KANMX*
UCC10471	Pex25p-GFP Pex11p-mCherry		*MATa/@ his3D1/his3D1 leu2D0/leu2D0 ura3D0/ura3D0 lys2D0/LYS2 trp1d63/trp1D63 hoD::SCW11pr-Cre-EBD78-NATMX/hoD::SCW11pr-Cre-EBD78-NATMX loxP-CDC20-Intron-loxP-HPHMX/loxP-CDC20-Intron-loxP-HPHMX loxP-UBC9-loxP-LEU2/loxP-UBC9-loxP-LEU2 PEX25-GFP-KANMX/PEX25-GFP-KANMX PEX11-mCherry-KANMX/PEX11-mCherry-KANMX*
UCC10628	Pex14p-GFP Pex11p-mCherry		UCC4925 + *PEX14-GFP-KANMX/PEX14 PEX11/PEX11-mCherry-KANMX*
UCC10752	Pex11p-GFP mCherry-PTS1		UCC4925 + *PEX11-GFP-KANMX/PEX11 CHRI/CHRI::MCHERRY-PTS1-URA3*
UCC10497	Pex11p-GFP *dnm1Δ*		UCC4925 + *PEX11-GFP-KANMX/PEX11-GFP-KANMX dnm1::URA3/dnm1::URA3*
UCC10511	Pex11p-GFP *vps1Δ*		UCC4925 + *PEX11-GFP-KANMX/PEX11-GFP-KANMX vps1::URA3/vps1::URA3*
UCC10507	Pex11p-GFP *pep4Δ*		UCC4925 + *PEX11-GFP-KANMX/PEX11-GFP-KANMX pep4::URA3/pep4::URA3*
UCC10624	Pex11p-GFP *GPD-VMA1*		UCC4925 + *PEX11-GFP-KANMX/PEX11-GFP-KANMX CHRI/CHRI(199456-199457)::GPD1pr-VMA1-CYC1term-URA3*
UCC10626	Pex11p-GFP GPD-empty vector		UCC4925 + *PEX11-GFP-KANMX/PEX11-GFP-KANMX CHRI/CHRI(199456-199457)::GPD1pr-CYC1term-URA3*
UCC5444	Kex2p-GFP	Nelson GFP collection	Basic MEP + *KEX2-GFP-HIS3MX/KEX2-GFP-HIS3MX*
UCC10436	Vph1p-GFP		UCC4925 + *VPH1-GFP-KANMX/ VPH1-GFP-KANMX*
UCC5412	Spc42p-GFP	Nelson GFP collection	Basic MEP + *SPC42-GFP-HIS3MX/SPC42-GFP-HIS3MX*

Chapter III strains (cont.)

Strain	Strain Description	Source	Genotype
UCC4959	Spc72p-GFP	GFP collection	Basic MEP + *SPC72-GFP-HIS3MX/SPC72-GFP-HIS3MX*
UCC10008	Nud1p-GFP	GFP collection	Basic MEP + *NUD1-GFP-HIS3MX/NUD1-GFP-HIS3MX*
UCC10314	GFP-Tub1p		UCC4925 + *CHRI::GFP-TUB1-URA3/CHRI::GFP-TUB1-URA3*
UCC10129	Mtw1p-GFP	GFP collection	Basic MEP + *MTW1-GFP-HIS3MX/MTW1-GFP-HIS3MX*
UCC10131	Nuf2p-GFP	GFP collection	Basic MEP + *NUF2-GFP-HIS3MX /NUF2-GFP-HIS3MX*
UCC10670	GFP-Pus1p		UCC4925 + *GFP-PUS1/GFP-PUS1*

Chapter III primers

Primer name	Primer sequence
GFP check	GTAAGTAGCATCACCTTCACCTTC
URA3-4	AGAAAAGCAGGCTGGGAAGC
Pex11 F5	CACATCTATCCTTGGTATGCAAGACATGTGGAAAGCTACAGGTGACGGTGCTGGTTTA
Pex11 R3	GCGGAGAATAGCCAAATAAAAAAAAAAGATGAAAAGAAAGTCGATGAATTCGAGCTCG
Pex11 check	AAGTGGTCTGGCTATGGATCTTCGTAA
Pex25 F5	TTGGATAACAACAAAGAGGTCACTTTGCTCTTCAAAAGATGGTGACGGTGCTGGTTTA
Pex25 R	TATATATGTACATATCTATATGTATACATATTTTTATATATCGATGAATTCGAGCTCG
Pex25 check	CAGGCCCATAAAGACGATGGCTC
Pex14 F5	CCCTGACTGGCAAAATGGACAGGTCGAAGACTCCATCCCAGGTGACGGTGCTGGTTTA
Pex14 R3	CAATTTCCGTTAAAAAACTAATTACTTACATAGAATTGCGTCGATGAATTCGAGCTCG
Pex14 check	AGCTTAATGAATAACCGTATGGAATCCGGT
Dnm1 pRS KO F	TTAAGTAGCTACCAGCGAATCTAAATACGACGGATAAAGACTGTGCGGTATTTCACACCG
Dnm1 pRS KO R	CAATGTTGAAGTAAGATCAAAAATGAGATGAATTATGCAAAGATTGTACTGAGAGTGCAC
Dnm1 KO check	GAGAGGAATACGATACAGAGGAAGGCGCAA
Vps1 pRS KO F	GGACCGTACGAAAACTGCACATTTTATATTATCAGATATCCTGTGCGGTATTTCACACCG
Vps1 pRS KO R	CAAAACCAAGCTTGAGTCGACCGGTATAGATGAGGAAAACAGATTGTACTGAGAGTGCAC
Vps1 KO check	TTCATCCAGTTCCTTCCTCTCTCTCAGTAG
Pep4 D5	ATTTAATCCAAATAAAATTCAAACAAAAACCAAAACTAACGATTGTACTGAGAGTGCACC
Pep4 D3	GGCAGAAAAGGATAGGGCGGAGAAGTAAGAAAAGTTTAGCCTGTGCGGTATTTCACACCG
Pep4 D check	GCCTAGTGACCTAGTATTTAATCC
Vph1 F5	GGAAGTCGCTGTTGCTAGTGCAAGCTCTTCCGCTTCAAGCGGTGACGGTGCTGGTTTA
Vph1 R3	AGTACTTAAATGTTTCGCTTTTTTTAAAAGTCCTCAAAATTCGATGAATTCGAGCTCG
Vph1 GFP check	ACATGCTCAATTGTCTAGTGTTTTATGG

Chapter III plasmids

Plasmid	Source	Plasmid Description
pKT127	Euroscarf	pFA6a-link-yEGFP-KAN
pRS306-TDH3pr-mCherry-SKL (PTS1)	Lazar Dmitrov Schekman lab	pRS306 plasmid containing mCherry fluorescent protein with the peroxisome targeting signal, expressed under the *TDH3* promoter. *URA3* selectable marker.
pAG306 TDH3pr-mCherry-SKL chrI int		Integrating plasmid that inserts TDH3pr-mCherry-SKL into Chromosome I (199456-199457) when digested with NotI and transformed. This plasmid was constructed by digesting pAG306gal ccdB ChrI with NaeI and KpnI and ligating with pRS306-TDH3pr-mCherry-SKL digested with SmaI and KpnI. *URA3* selectable marker.
pAG306-GPD-VMA1 xsome I	Hughes	Integrating plasmid that inserts *GPD1pr-VMA1-URA3* into Chromosome I (199456-199457) when digested with NotI and transformed.
pAG306-GPD xsome I empty	Hughes	Integrating plasmid that inserts *GPD1pr-URA3* into Chromosome I (199456-199457) when digested with NotI and transformed.
pSB298	Biggins lab	Contains GFP-Tub1.
pAG306 GFP-Tub1		Integrating plasmid that inserts GFP-Tub1 into Chromosome I (199456-199457) when digested with NotI and transformed. This plasmid was constructed by digesting pAG306gal ccdB ChrI with NaeI and KpnI and ligating with pSB298 digested with KpnI and NotI.
pRS306	Heiter 1989	Integrating plasmid with *URA3* selectable marker.

Chapter IV strains

Strain	Strain Description	Source	Genotype
UCC10748	Pex11p-GFP Tom70p-mCherry		UCC4925 + *PEX11-GFP-KANMX/PEX11-GFP-KANMX TOM70-MCHERRY-KANMX/TOM70-MCHERRY-KANMX*
UCC10738	Pex11p-GFP Vph1p-mCherry		UCC4925 + *PEX11-GFP-KANMX/PEX11-GFP-KANMX VPH1-MCHERRY-KANMX/VPH1-MCHERRY-KANMX*
UCC10742	GFP-Pus1p Nop58p-mCherry		UCC4925 + *GFP-PUS1/GFP-PUS1 NOP58-MCHERRY-KANMX/NOP58-MCHERRY-KANMX*
UCC10754	GFP-Pus1p Tom70p-mCherry		*MATa/@ his3D1/his3D1 leu2D0/leu2D0 ura3D0/ura3D0 trp1D63/trp1D63 hoD::SCW11pr-Cre-EBD78-NATMX/hoD::SCW11pr-Cre-EBD78-NATMX loxP-CDC20-Intron-loxP-HPHMX/loxP-CDC20-Intron-loxP-HPHMX loxP-UBC9-loxP-LEU2/loxP-UBC9-loxP-LEU2 GFP-PUS1/GFP-PUS1 TOM70-MCHERRY-KANMX/TOM70-MCHERRY-KANMX*
UCC10756	GFP-Pus1p Vph1p-mCherry		*MATa/@ his3D1/his3D1 leu2D0/leu2D0 ura3D0/ura3D0 trp1D63/trp1D63 hoD::SCW11pr-Cre-EBD78-NATMX/hoD::SCW11pr-Cre-EBD78-NATMX loxP-CDC20-Intron-loxP-HPHMX/loxP-CDC20-Intron-loxP-HPHMX loxP-UBC9-loxP-LEU2/loxP-UBC9-loxP-LEU2 GFP-PUS1/GFP-PUS1 VPH1-MCHERRY-KANMX/VPH1-MCHERRY-KANMX*
UCC10760	Nop58p-GFP Tom70p-mCherry		Basic MEP + *NOP58-GFP-HIS3MX/NOP58-GFP-HIS3MX TOM70-MCHERRY-KANMX/TOM70-MCHERRY-KANMX*
UCC10815	Nop58p-GFP Vph1p-mCherry		UCC4925 + *NOP58-GFP-HIS3MX/NOP58-GFP-HIS3MX VPH1-MCHERRY-KANMX/VPH1-MCHERRY-KANMX*
UCC10750	Tom70p-GFP Vph1p-mCherry		UCC4925 + *TOM70-GFP-KANMX/TOM70-GFP-KANMX VPH1-MCHERRY-KANMX/VPH1-MCHERRY-KANMX*
UCC10813	Spc42p-GFP Nop58p-mCherry		UCC4925 + *SPC42-GFP-HIS3MX/SPC42-GFP-HIS3MX NOP58-MCHERRY-KANMX/NOP58-MCHERRY-KANMX*
UCC10428	GFP-Tub1p Spc42p-mCherry		UCC4925 + *CHRI(199456-199457)::GFP-TUB1-URA3/ CHRI(199456-199457)::GFP-TUB1-URA3 SPC42-MCHERRY-KANMX/SPC42-MCHERRY-KANMX*

Chapter IV primers

Primer name	Primer sequence
GFP check	GTAAGTAGCATCACCTTCACCTTC
mCherry check	CGCATGAACTCCTTGATGATGG
Tom70 F5	TCAAGAAACTTTAGCTAAATTACGCGAACAGGGTTTAATGGGTGACGGTGCTGGTTTA
Tom70 R3	TTTGTCTTCTCCTAAAAGTTTTTAAGTTTATGTTTACTGTTCGATGAATTCGAGCTCG
Tom70 check	TGAAGCCACGAATTTATTAGAAAAAGCGTC
Nop58 F5	GAAGGAAAAGAAGTCCAAGAAAGAGAAGAAAGAGAAGAAAGGTGACGGTGCTGGTTTA
Nop58 R3	ACGCGAGGGGTCACTAATTATTAAAATGTAAAATGCATCCTCGATGAATTCGAGCTCG
Nop58 check	CTCTTGTTGGTCAAGCTACTGGTAAGAACA
Spc42 pKT F	TATGTCAGAAACATTCGCAACTCCCACTCCCAATAATCGAGGTGACGGTGCTGGTTTA
Spc42 pKT R	TTTAAGAATGCGCCATACTCCTTAACTGCTTTTTAAATCATCGATGAATTCGAGCTCG
Spc42 check	ATGAGGTCAGAAGACGGTAATAACGACAGG

Chapter IV plasmids

Plasmid	Source	Plasmid Description
pKT127	Euroscarf	pFA6a-link-yEGFP-KAN
pKT mCherry	Adam Waite Shou lab	Plasmid contains mCherry-KANMX with common pKT common oligo sites.

Chapter V strains

Strain	Strain Description	Source	Genotype
UCC11167	Pex11p-GFP Nop58p-mCherry *gpa2Δ*		UCC4925 + *PEX11-GFP-KANMX/PEX11* *NOP58-MCHERRY-KANMX/NOP58* *gpa2Δ::URA3/ gpa2Δ::URA3*
UCC11169	Pex11p-GFP Tom70p-mCherry *gpa2Δ*		UCC4925 + *PEX11-GFP-KANMX/PEX11* *TOM70-MCHERRY-KANMX/TOM70* *gpa2Δ::URA3/ gpa2Δ::URA3*
UCC11171	Pex11p-GFP Vph1p-mCherry *gpa2Δ*		UCC4925 + *PEX11-GFP-KANMX/PEX11* *VPH1-MCHERRY-KANMX/VPH1* *gpa2Δ::URA3/ gpa2Δ::URA3*
UCC11173	GFP-Pus1p Nop58p-mCherry *gpa2Δ*		UCC4925 + *GFP-PUS1/PUS1* *NOP58-MCHERRY-KANMX/NOP58* *gpa2Δ::URA3/ gpa2Δ::URA3*
UCC11175	GFP-Pus1p Tom70p-mCherry *gpa2Δ*		UCC4925 + *GFP-PUS1/PUS1* *TOM70-MCHERRY-KANMX/TOM70* *gpa2Δ::URA3/ gpa2Δ::URA3*
UCC11177	GFP-Pus1p Vph1p-mCherry *gpa2Δ*		UCC4925 + *GFP-PUS1/PUS1* *VPH1-MCHERRY-KANMX/VPH1* *gpa2Δ::URA3/ gpa2Δ::URA3*
UCC11179	Spc42p-GFP Nop58p-mCherry *gpa2Δ*		UCC4925 + *SPC42-GFP-HIS3MX/SPC42* *NOP58-MCHERRY-KANMX/NOP58* *gpa2Δ::URA3/ gpa2Δ::URA3*

Chapter V strains (cont.)

Strain	Strain Description	Source	Genotype
UCC11181	Tom70p-GFP Nop58p-mCherry *gpa2Δ*		UCC4925 + *TOM70-GFP-KANMX/TOM70 NOP58-MCHERRY-KANMX/NOP58 gpa2Δ::URA3/ gpa2Δ::URA3*
UCC11183	Tom70p-GFP Vph1p-mCherry *gpa2Δ*		UCC4925 + *TOM70-GFP-KANMX/TOM70 VPH1-MCHERRY-KANMX/VPH1 gpa2Δ::URA3/ gpa2Δ::URA3*
UCC10784	Nop58p-GFP Tom70p-mCherry GPDpr-empty vector		UCC4925 + *NOP58-GFP-HIS3MX/NOP58 TOM70-MCHERRY-KANMX/TOM70 ChrI(199456-199457)::prGPD1-termCYC1-URA3/ChrI*
UCC10780	Nop58p-GFP Vph1p-mCherry GPDpr-empty vector		UCC4925 + *NOP58-GFP-HIS3MX/NOP58 VPH1-MCHERRY-KANMX/VPH1 ChrI(199456-199457)::prGPD1-termCYC1-URA3/ChrI*
UCC11044	Pex11p-GFP Nop58p-mCherry GPDpr-empty vector		UCC4925 + *PEX11-GFP-KANMX/PEX11 NOP58-MCHERRY-KANMX/NOP58 ChrI(199456-199457)::prGPD1-termCYC1-URA3/ChrI*
UCC10796	Pex11p-GFP Tom70p-mCherry GPDpr-empty vector		UCC4925 + *PEX11-GFP-KANMX/PEX11 TOM70-MCHERRY-KANMX/TOM70 ChrI(199456-199457)::prGPD1-termCYC1-URA3/ChrI*
UCC10776	Pex11p-GFP Vph1p-mCherry GPDpr-empty vector		UCC4925 + *PEX11-GFP-KANMX/PEX11 VPH1-MCHERRY-KANMX/VPH1 ChrI(199456-199457)::prGPD1-termCYC1-URA3/ChrI*
UCC11070	GFP-Pus1p Nop58p-mCherry GPDpr-empty vector		*MATa/@ his3D1/his3D1 leu2D0/leu2D0 ura3D0/ura3D0 trp1d63/trp1D63 hoD::SCW11pr-Cre-EBD78-NATMX/hoD::SCW11pr-Cre-EBD78-NATMX loxP-CDC20-Intron-loxP-HPHMX/loxP-CDC20-Intron-loxP-HPHMX loxP-UBC9-loxP-LEU2/loxP-UBC9-loxP-LEU2 GFP-PUS1/PUS1 NOP58-MCHERRY-KANMX/NOP58 ChrI(199456-199457)::prGPD1-termCYC1-URA3/ChrI*
UCC10772	GFP-Pus1p Tom70p-mCherry GPDpr-empty vector		*MATa/@ his3D1/his3D1 leu2D0/leu2D0 ura3D0/ura3D0 trp1d63/trp1D63 hoD::SCW11pr-Cre-EBD78-NATMX/hoD::SCW11pr-Cre-EBD78-NATMX loxP-CDC20-Intron-loxP-HPHMX/loxP-CDC20-Intron-loxP-HPHMX loxP-UBC9-loxP-LEU2/loxP-UBC9-loxP-LEU2 GFP-PUS1/PUS1 TOM70-MCHERRY-KANMX/TOM70 ChrI(199456-199457)::prGPD1-termCYC1-URA3/ChrI*
UCC10768	GFP-Pus1p Vph1p-mCherry GPDpr-empty vector		*MATa/@ his3D1/his3D1 leu2D0/leu2D0 ura3D0/ura3D0 trp1d63/trp1D63 hoD::SCW11pr-Cre-EBD78-NATMX/hoD::SCW11pr-Cre-EBD78-NATMX loxP-CDC20-Intron-loxP-HPHMX/loxP-CDC20-Intron-loxP-HPHMX loxP-UBC9-loxP-LEU2/loxP-UBC9-loxP-LEU2 GFP-PUS1/PUS1 VPH1-MCHERRY-KANMX/VPH1 ChrI(199456-199457)::prGPD1-termCYC1-URA3/ChrI*

Chapter V strains (cont.)

Strain	Strain Description	Source	Genotype
UCC11079	Spc42p-GFP Nop58p-mCherry GPDpr-empty vector		*MATa/@ his3D1/his3D1 leu2D0/leu2D0 ura3D0/ura3D0 hoD::SCW11pr-Cre-EBD78-NATMX/hoD::SCW11pr-Cre-EBD78-NATMX loxP-CDC20-Intron-loxP-HPHMX/loxP-CDC20-Intron-loxP-HPHMX loxP-UBC9-loxP-LEU2/loxP-UBC9-loxP-LEU2 SPC42-GFP-HIS3MX/SPC42 NOP58-MCHERRY-KANMX/NOP58 ChrI(199456-199457)::prGPD1-termCYC1-URA3/ChrI*
UCC10792	Tom70p-GFP Vph1p-mCherry GPDpr-empty vector		UCC4925 + *TOM70-GFP-KANMX/TOM70 VPH1-MCHERRY-KANMX/VPH1 ChrI(199456-199457)::prGPD1-termCYC1-URA3/ChrI*
UCC10788	Vph1p-GFP Pex11p-mCherry GPDpr-empty vector		UCC4925 + *VPH1-GFP-KANMX/VPH1 PEX11-MCHERRY-KANMX/PEX11 ChrI(199456-199457)::prGPD1-termCYC1-URA3/ChrI*
UCC10800	Vph1p-GFP Tom70p-mCherry GPDpr-empty vector		UCC4925 + *VPH1-GFP-KANMX/VPH1 TOM70-MCHERRY-KANMX/TOM70 ChrI(199456-199457)::prGPD1-termCYC1-URA3/ChrI*
UCC11071	GFP-Tub1p Spc42p-mCherry GPDpr-empty vector		*MATa/@ his3D1/his3D1 leu2D0/leu2D0 ura3D0/ura3D0 trp1d63/trp1D63 hoD::SCW11pr-Cre-EBD78-NATMX/hoD::SCW11pr-Cre-EBD78-NATMX loxP-CDC20-Intron-loxP-HPHMX/loxP-CDC20-Intron-loxP-HPHMX loxP-UBC9-loxP-LEU2/loxP-UBC9-loxP-LEU2 SPC42-MCHERRY-KANMX/SPC42 ChrI(199456-199457)::prGPD1-termCYC1-URA3/ChrI(199456-199457)::GFP-TUB1-URA3*
UCC10786	Nop58p-GFP Tom70p-mCherry GPDpr-VMA1		UCC4925 + *NOP58-GFP-HIS3MX/NOP58 TOM70-MCHERRY-KANMX/TOM70 ChrI(199456-199457)::prGPD1-VMA1-termCYC1-URA3/ChrI*
UCC10782	Nop58p-GFP Vph1p-mCherry GPDpr-VMA1		UCC4925 + *NOP58-GFP-HIS3MX/NOP58 VPH1-MCHERRY-KANMX/VPH1 ChrI(199456-199457)::prGPD1-VMA1-termCYC1-URA3/ChrI*
UCC11087	Pex11p-GFP Nop58p-mCherry GPDpr-VMA1		UCC4925 + *PEX11-GFP-KANMX/PEX11 NOP58-MCHERRY-KANMX/NOP58 ChrI(199456-199457)::prGPD1-VMA1-termCYC1-URA3/ChrI*
UCC10798	Pex11p-GFP Tom70p-mCherry GPDpr-VMA1		UCC4925 + *PEX11-GFP-KANMX/PEX11 TOM70-MCHERRY-KANMX/TOM70 ChrI(199456-199457)::prGPD1-VMA1-termCYC1-URA3/ChrI*
UCC10778	Pex11p-GFP Vph1p-mCherry GPDpr-VMA1		UCC4925 + *PEX11-GFP-KANMX/PEX11 VPH1-MCHERRY-KANMX/VPH1 ChrI(199456-199457)::prGPD1-VMA1-termCYC1-URA3/ChrI*

Chapter V strains (cont.)

Strain	Strain Description	Source	Genotype
UCC11081	GFP-Pus1p Nop58p-mCherry GPDpr-VMA1		*MATa/@ his3D1/his3D1 leu2D0/leu2D0 ura3D0/ura3D0 trp1d63/trp1D63 hoD::SCW11pr-Cre-EBD78-NATMX/hoD::SCW11pr-Cre-EBD78-NATMX loxP-CDC20-Intron-loxP-HPHMX/loxP-CDC20-Intron-loxP-HPHMX loxP-UBC9-loxP-LEU2/loxP-UBC9-loxP-LEU2 GFP-PUS1/PUS1 NOP58-MCHERRY-KANMX/NOP58 ChrI(199456-199457)::prGPD1-VMA1-termCYC1-URA3/ChrI*
UCC10774	GFP-Pus1p Tom70p-mCherry GPDpr-VMA1		*MATa/@ his3D1/his3D1 leu2D0/leu2D0 ura3D0/ura3D0 trp1d63/trp1D63 hoD::SCW11pr-Cre-EBD78-NATMX/hoD::SCW11pr-Cre-EBD78-NATMX loxP-CDC20-Intron-loxP-HPHMX/loxP-CDC20-Intron-loxP-HPHMX loxP-UBC9-loxP-LEU2/loxP-UBC9-loxP-LEU2 GFP-PUS1/PUS1 TOM70-MCHERRY-KANMX/TOM70 ChrI(199456-199457)::prGPD1-VMA1-termCYC1-URA3/ChrI*
UCC10770	GFP-Pus1p Vph1p-mCherry GPDpr-VMA1		*MATa/@ his3D1/his3D1 leu2D0/leu2D0 ura3D0/ura3D0 trp1d63/trp1D63 hoD::SCW11pr-Cre-EBD78-NATMX/hoD::SCW11pr-Cre-EBD78-NATMX loxP-CDC20-Intron-loxP-HPHMX/loxP-CDC20-Intron-loxP-HPHMX loxP-UBC9-loxP-LEU2/loxP-UBC9-loxP-LEU2 GFP-PUS1/PUS1 VPH1-MCHERRY-KANMX/VPH1 ChrI(199456-199457)::prGPD1-VMA1-termCYC1-URA3/ChrI*
UCC11083	Spc42p-GFP Nop58p-mCherry GPDpr-VMA1		*MATa/@ his3D1/his3D1 leu2D0/leu2D0 ura3D0/ura3D0 hoD::SCW11pr-Cre-EBD78-NATMX/hoD::SCW11pr-Cre-EBD78-NATMX loxP-CDC20-Intron-loxP-HPHMX/loxP-CDC20-Intron-loxP-HPHMX loxP-UBC9-loxP-LEU2/loxP-UBC9-loxP-LEU2 SPC42-GFP-HIS3MX/SPC42 NOP58-MCHERRY-KANMX/NOP58 ChrI(199456-199457)::prGPD1-VMA1-termCYC1-URA3/ChrI*
UCC10794	Tom70p-GFP Vph1p-mCherry GPDpr-VMA1		UCC4925 + *TOM70-GFP-KANMX/TOM70 VPH1-MCHERRY-KANMX/VPH1 ChrI(199456-199457)::prGPD1-VMA1-termCYC1-URA3/ChrI*
UCC10790	Vph1p-GFP Pex11p-mCherry GPDpr-VMA1		UCC4925 + *VPH1-GFP-KANMX/VPH1 PEX11-MCHERRY-KANMX/PEX11 ChrI(199456-199457)::prGPD1-VMA1-termCYC1-URA3/ChrI*
UCC10802	Vph1p-GFP Tom70p-mCherry GPDpr-VMA1		UCC4925 + *VPH1-GFP-KANMX/VPH1 TOM70-MCHERRY-KANMX/TOM70 ChrI(199456-199457)::prGPD1-VMA1-termCYC1-URA3/ChrI*
UCC11085	GFP-Tub1p Spc42p-mCherry GPDpr-VMA1		*MATa/@ his3D1/his3D1 leu2D0/leu2D0 ura3D0/ura3D0 trp1d63/trp1D63 hoD::SCW11pr-Cre-EBD78-NATMX/hoD::SCW11pr-Cre-EBD78-NATMX loxP-CDC20-Intron-loxP-HPHMX/loxP-CDC20-Intron-loxP-HPHMX loxP-UBC9-loxP-LEU2/loxP-UBC9-loxP-LEU2 SPC42-MCHERRY-KANMX/SPC42 ChrI(199456-199457)::prGPD1-VMA1-termCYC1-URA3/ChrI(199456-199457)::GFP-TUB1-URA3*

Chapter V strains (cont.)

Strain	Strain Description	Source	Genotype
UCC11149	Pex11p-GFP Nop58p-mCherry *fob1Δ*		UCC4925 + *PEX11-GFP-KANMX/PEX11* *NOP58-MCHERRY-KANMX/NOP58* *fob1Δ::URA3/ fob1Δ::URA3*
UCC11151	Pex11p-GFP Tom70p-mCherry *fob1Δ*		UCC4925 + *PEX11-GFP-KANMX/PEX11* *TOM70-MCHERRY-KANMX/TOM70* *fob1Δ::URA3/ fob1Δ::URA3*
UCC11153	Pex11p-GFP Vph1p-mCherry *fob1Δ*		UCC4925 + *PEX11-GFP-KANMX/PEX11* *VPH1-MCHERRY-KANMX/VPH1* *fob1Δ::URA3/ fob1Δ::URA3*
UCC11155	GFP-Pus1p Nop58p-mCherry *fob1Δ*		UCC4925 + *GFP-PUS1/PUS1* *NOP58-MCHERRY-KANMX/NOP58* *fob1Δ::URA3/ fob1Δ::URA3*
UCC11157	GFP-Pus1p Tom70p-mCherry *fob1Δ*		UCC4925 + *GFP-PUS1/PUS1* *TOM70-MCHERRY-KANMX/TOM70* *fob1Δ::URA3/ fob1Δ::URA3*
UCC11159	GFP-Pus1p Vph1p-mCherry *fob1Δ*		UCC4925 + *GFP-PUS1/PUS1* *VPH1-MCHERRY-KANMX/VPH1* *fob1Δ::URA3/ fob1Δ::URA3*
UCC11161	Spc42p-GFP Nop58p-mCherry *fob1Δ*		UCC4925 + *SPC42-GFP-HIS3MX/SPC42* *NOP58-MCHERRY-KANMX/NOP58* *fob1Δ::URA3/ fob1Δ::URA3*
UCC11163	Tom70p-GFP Nop58p-mCherry *fob1Δ*		UCC4925 + *TOM70-GFP-KANMX/TOM70* *NOP58-MCHERRY-KANMX/NOP58* *fob1Δ::URA3/ fob1Δ::URA3*
UCC11165	Tom70p-GFP Vph1p-mCherry *fob1Δ*		UCC4925 + *TOM70-GFP-KANMX/TOM70* *VPH1-MCHERRY-KANMX/VPH1* *fob1Δ::URA3/ fob1Δ::URA3*
UCC11185	Pex11p-GFP Nop58p-mCherry *ubr2Δ*		UCC4925 + *PEX11-GFP-KANMX/PEX11* *NOP58-MCHERRY-KANMX/NOP58* *ubr2Δ::URA3/ ubr2Δ::URA3*
UCC11187	Pex11p-GFP Tom70p-mCherry *ubr2Δ*		UCC4925 + *PEX11-GFP-KANMX/PEX11* *TOM70-MCHERRY-KANMX/TOM70* *ubr2Δ::URA3/ ubr2Δ::URA3*
UCC11189	Pex11p-GFP Vph1p-mCherry *ubr2Δ*		UCC4925 + *PEX11-GFP-KANMX/PEX11* *VPH1-MCHERRY-KANMX/VPH1* *ubr2Δ::URA3/ ubr2Δ::URA3*
UCC11191	GFP-Pus1p Nop58p-mCherry *ubr2Δ*		UCC4925 + *GFP-PUS1/PUS1* *NOP58-MCHERRY-KANMX/NOP58* *ubr2Δ::URA3/ ubr2Δ::URA3*

Chapter V strains (cont.)

Strain	Strain Description	Source	Genotype
UCC11193	GFP-Pus1p Tom70p-mCherry *ubr2Δ*		UCC4925 + *GFP-PUS1/PUS1* *TOM70-MCHERRY-KANMX/TOM70* *ubr2Δ::URA3/ ubr2Δ::URA3*
UCC11195	GFP-Pus1p Vph1p-mCherry *ubr2Δ*		UCC4925 + *GFP-PUS1/PUS1* *VPH1-MCHERRY-KANMX/VPH1* *ubr2Δ::URA3/ ubr2Δ::URA3*
UCC11197	Spc42p-GFP Nop58p-mCherry *ubr2Δ*		UCC4925 + *SPC42-GFP-HIS3MX/SPC42* *NOP58-MCHERRY-KANMX/NOP58* *ubr2Δ::URA3/ ubr2Δ::URA3*
UCC11199	Tom70p-GFP Nop58p-mCherry *ubr2Δ*		UCC4925 + *TOM70-GFP-KANMX/TOM70* *NOP58-MCHERRY-KANMX/NOP58* *ubr2Δ::URA3/ ubr2Δ::URA3*
UCC11201	Tom70p-GFP Vph1p-mCherry *ubr2Δ*		UCC4925 + *TOM70-GFP-KANMX/TOM70* *VPH1-MCHERRY-KANMX/VPH1* *ubr2Δ::URA3/ ubr2Δ::URA3*

Chapter V primers

Primer name	Primer sequence
URA3-4	AGAAAAGCAGGCTGGGAAGC
Gpa2 D5	GAGCCTTATTGTTACAGCACAAATCACGCGTATTTTCAAGCGATTGTACTGAGAGTGCAC
Gpa2 D3	GAAGAGGCATGCAGTTTTGTCTCTGTTTTAGCTGTGCATTCCTGTGCGGTATTTCACACC
Gpa2 KO check	GTGATTACTAGTACAATGGTCATGAG
Fob1 KO F	TTAACGATTGTGTGAGTGTGAATTTGTGCTGAGGATAACAGATTGTACTGAGAGTGCACC
Fob1 KO R	ACCTATGGTGACTCCTCCTTTCATTCTATCCTACATATTA CTGTGCGGTATTTCACACCG
Fob1 KO check	GTCATATACAGGAAGAGCTTTCAAC
Ubr2 KO F	AGATTCGTTAACTAAATTAATAGCTACTTAACAAGCACGCCTGTGCGGTATTTCACACCG
Ubr2 KO R	TTTCGTAGCAATTTTGAATGACTAGACATTTGTTGGATAAAGATTGTACTGAGAGTGCAC
Ubr2 KO check	TTAGAGGAAGGTGATGACTCGACTCATCAA

Chapter V plasmids

Plasmid	Source	Plasmid Description
pRS306	Heiter 1989	Integrating plasmid with *URA3* selectable marker.

Chapter VIII strains

Strain	Strain Description	Source	Genotype
UCC5179	MEP haploid Mat a	Lindstrom (2009)	*MATa ade2::hisG his3 leu2 lys2 ura3D0 trp1D63 hoD::SCW11pr-Cre-EBD78-NatMX loxP-UBC9-loxP-LEU2 loxP-CDC20-Intron-loxP-HPHMX*
UCC5181	MEP haploid Mat α	Lindstrom (2009)	*MAT@ ade2::hisG his3 leu2 met15D::ADE2 trp1D63 ura3D0 hoD::SCW11pr-Cre-EBD78-NatMX loxP-UBC9-loxP-LEU2 loxP-CDC20-Intron-loxP-HPHMX*
UCC5185	MEP diploid	Liindstrom (2009)	*MATa/@ ade2::hisG/ade2::hisG his3/his3 leu2/leu2 lys2/+ met15D::ADE2/+ ura3D0/ura3Δ0 trp1D63/trp1D63 hoD::SCW11pr-Cre-EBD78-NatMX/hoD::SCW11pr-Cre-EBD78-NatMX loxP-UBC9-loxP-LEU2/loxP-UBC9-loxP-LEU2 loxP-CDC20-Intron-loxP-HPHMX/loxP-CDC20-Intron-loxP-HPHMX*
UCC9110	MEP diploid with tetracycline-induced activator and repressor		*MATa/@ his3D200/his3D200 leu2D0/leu2D0 lys2D0/lys2D0 trp1d63/trp1d63 ura3D0/ura3D0 hoD::SCW11pr-Cre-EBD78-NATMX/hoD::SCW11pr-Cre-EBD78-NATMX loxP-CDC20-intron-loxP-HPHMX/loxP-CDC20-intron-loxP-HPHMX loxP-UBC9-loxP-LEU2/loxP-UBC9-loxP-LEU2 met15D0::tetR'-SSN6-LEU2/met15D0::tetR'-SSN6-LEU2 CHR1::tTA-ADH1term-URA3/CHR1::tTA-ADH1term-URA3*
UCC9104	MEP diploid with tetracycline-induced activator and repressor and *RAD52* with tetracycline-repressible promotor		*MATa/@ his3D200/his3D200 leu2D0/leu2D0 lys2D0/ys2D0 trp1d63/trp1d63 ura3D0/ura3D0 hoD::SCW11pr-Cre-EBD78-NATMX/hoD::SCW11pr-Cre-EBD78-NATMX loxP-CDC20-intron-loxP-HPHMX/loxP-CDC20-intron-loxP-HPHMX loxP-UBC9-loxP-LEU2/loxP-UBC9-loxP-LEU2 met15D0::tetR'-SSN6-LEU2/met15D0::tetR'-SSN6-LEU2 CHR1::tTA-ADH1term-URA3/CHR1::tTA-ADH1term-URA3 KanMX-tet02-RAD52/KanMX-tet02-RAD52*
UCC9102	MEP *rad52Δ* Strain		*MATa/@ his3D200/his3D200 leu2D0/leu2D0 lys2D0/lys2D0 met15D0/met15D0 trp1D63/trp1D63 hoD::SCW11pr-Cre-EBD78-NATMX/hoD::SCW11pr-Cre-EBD78-NATMX loxP-CDC20-intron-loxP-HPHMX/loxP-CDC20-intron-loxP-HPHMX loxP-UBC9-loxP-LEU2/loxP-UBC9-loxP-LEU2 rad52::URA3/rad52::URA3*

Chapter VIII primers

Primer name	Primer sequence
Rad52tetO-F	GAAAAATATAGCGGCGGGCGGGTTACGCGACCGGTATCGACAGCTGAAGCTTCGTACGC
Rad52tetO-R	TTTGTTGATTCTCAGTGGCAAAATAGCTTAAAAACGCCATATAGGCCACTAGTGGATCTG
Rad52tetOchkF	CAACAACACACCAAAGCC
Rad52tetOchkR	CTCTTCCCGTTAGTGATTC
5D Rad52	GAAAAATATAGCGGCGGGCGGGTTACGCGACCGGTATCGAAGATTGTACTGAGAGTGCAC
3D Rad52	AATGATGCAAATTTTTTATTTGTTTCGGCCAGGAAGCGTTCTGTGCGGTATTTCACACCG
5RAD52	GAGTCTGCTCTTCCCGTTAGTGATTCTCG
3RAD52	GATGCAAATTTTTTATTTGTTTCGGCCAGGAAGCG

Chapter VIII plasmids

Plasmid	Source	Plasmid Description
pUI-tTA-ADH1term-URA3		Plasmid contains tTA (tetracycline repression system activator) with ADH1 terminator and URA3 marker.
pLMI-tetR'S		Plasmid used to integrate tetR'-SSN6 into the met15Δ0 locus with the LEU2 selectable marker. Digest with PacI to integrate. Pair with pUI-tTA to create a tet repressible strain.
pKAN-Tet02		Use for placing 2 copies of the tet operator in front of a gene by PCR.
pRS306	Heiter 1989	Integrating plasmid with *URA3* selectable marker.

Appendix A strain

Strain	Strain Description	Source	Genotype
UCC4925		Hughes (2012)	*MATa/@ his3D1/hisD1 leu2D0/leu2D0 ura3D0/ura3D0 lys2D0/+ trp1D63/+ hoD::SCW11pr-Cre-EBD78-NATMX/hoD::SCW11pr-Cre-EBD78-NATMX loxP-CDC20-Intron-loxP-HPHMX/loxP-CDC20-Intron-loxP-HPHMX loxP-UBC9-loxP-LEU2/loxP-UBC9-loxP-LEU2*

Appendix B strain

Strain	Strain Description	Source	Genotype
UCC4925		Hughes (2012)	*MATa/@ his3D1/hisD1 leu2D0/leu2D0 ura3D0/ura3D0 lys2D0/+ trp1D63/+ hoD::SCW11pr-Cre-EBD78-NATMX/hoD::SCW11pr-Cre-EBD78-NATMX loxP-CDC20-Intron-loxP-HPHMX/loxP-CDC20-Intron-loxP-HPHMX loxP-UBC9-loxP-LEU2/loxP-UBC9-loxP-LEU2*

Appendix C strain

Strain	Strain Description	Source	Genotype
UCC4925		Hughes (2012)	*MATa/@ his3D1/hisD1 leu2D0/leu2D0 ura3D0/ura3D0 lys2D0/+ trp1D63/+ hoD::SCW11pr-Cre-EBD78-NATMX/hoD::SCW11pr-Cre-EBD78-NATMX loxP-CDC20-Intron-loxP-HPHMX/loxP-CDC20-Intron-loxP-HPHMX loxP-UBC9-loxP-LEU2/loxP-UBC9-loxP-LEU2*

Appendix C primers

Primer name	Primer sequence
ChrI Part A NotI F	GTCCCATTCGAAGAAGCGGCCGCTTTAGCTCATTGAGATATGTG
ChrI Part A SmaI R	GTATTCTACGACCCCGGGGGTGCTAATTATGGCATTGAT
ChrI Part B SmaI F	CGTCAATGCAAGCCCGGGCCATGGATGGTCGTTTAAGGC
ChrI Part B NotI R	TCTCAATGAGCTAAAGCGGCCGCTTCTTCGAATGGGACCAGCTA
pAG306 ChrI int chk F	GTTTGCTACAACCATCTCAGGTC
pAG306 ChrI int chk R	GTAATAGCGAAGAGGCCCGCAC

Appendix C plasmids

Plasmid	Source	Plasmid Description
pAG306gal-ccdB	Addgene	pAdvanced Gateway Destination Vector, integrating plasmid containing *URA3* selectable marker, ccdB lethal gene, and inducible *GAL1* promoter
pAG306gal-ccdB chrI	See Appendix C	pAG306gal-ccdB chrI was constructed from pAG306GAL-ccdB, and is designed for integration into Chromosome I (199456-199457) following NotI digestion of the plasmid

Appendix D strain

Strain	Strain Description	Source	Genotype
UCC5185	MEP diploid	Lindstrom (2009)	*MATa/@ ade2::hisG/ade2::hisG his3/his3 leu2/leu2 lys2/+ met15D::ADE2/+ ura3D0/ura3Δ0 trp1D63/trp1D63 hoD::SCW11pr-Cre-EBD78-NatMX/hoD::SCW11pr-Cre-EBD78-NatMX loxP-UBC9-loxP-LEU2/loxP-UBC9-loxP-LEU2 loxP-CDC20-Intron-loxP-HPHMX/loxP-CDC20-Intron-loxP-HPHMX*
UCC835-1	Petite rho- diploid	McMurray	*MATa/@ his3-1/his3-1 leu2-0/leu2-0 ura3-0/ura3-0 met15d::URA3/+ lys2-0/+ [rho0]*

Appendix D primers

Primer name	Primer sequence
ActI Forward	GTATGTGTAAAGCCGGTTTTG
ActI Reverse	CATGATACCTTGGTGTCTTGG
Cox1 Forward	CTACAGATACAGCATTTCCAAGA
Cox1 Reverse	GTGCCTGAATAGATGATAATGGT

Appendix E strain

Strain	Strain Description	Source	Genotype
UCC5185		Lindstrom (2009)	*MATa/@ ade2::hisG/ade2::hisG his3/his3 leu2/leu2 lys2/+ met15D::ADE2/+ ura3D0/ura3Δ0 trp1D63/trp1D63 hoD::SCW11pr-Cre-EBD78-NatMX/hoD::SCW11pr-Cre-EBD78-NatMX loxP-UBC9-loxP-LEU2/loxP-UBC9-loxP-LEU2 loxP-CDC20-Intron-loxP-HPHMX/loxP-CDC20-Intron-loxP-HPHMX*